

Purcell-enhanced emission and collective effects of nitrogen-vacancy centers in diamond coupled to a microcavity

Maximilian Benedikt Pallmann



Karlsruhe 2023

Purcell-enhanced emission and collective effects of nitrogen-vacancy centers in diamond coupled to a microcavity

Zur Erlangung des akademischen Grades eines
DOKTORS DER NATURWISSENSCHAFTEN (Dr. rer. nat.)

von der KIT-Fakultät für Physik des
Karlsruher Instituts für Technologie (KIT)
angenommene

DISSERTATION

von

Dipl.-Phys. Maximilian Benedikt Pallmann

Tag der mündlichen Prüfung: 30.06.2023

Erster Gutachter: Prof. Dr. David Hunger

Zweiter Gutachter: Prof. Dr. Wolfgang Wernsdorfer

meinen Eltern

Zusammenfassung

Das wachsende Interesse an Quantentechnologien in der jüngsten Vergangenheit hat die Wichtigkeit geeigneter Quantenemitter und der Fähigkeit, mit ihnen auf sehr effiziente Weise zu interagieren, verdeutlicht. Das Stickstoff-Fehlstellen-Zentrum (NV) in Diamant ist ein vielversprechender Kandidat hierfür, da es sowohl einen optisch adressierbaren Elektronenspin, als auch die Möglichkeit bietet, an nahe gelegene Kernspins zu koppeln. Das NV-Zentrum weist sehr gute Spin-Kohärenzzeiten auf, selbst bei Raumtemperatur. NV-Zentren besitzen jedoch keine optimalen optischen Eigenschaften, auch bei sorgfältig hergestellten Diamantproben. Dies ist zum einen auf die Kopplung der optischen Übergänge an Phononen im Diamantgitter zurückzuführen, die zu einer Verschiebung der Emissions- und Absorptionsfrequenzen führt. Nur $\sim 3\%$ der Emission wird nicht von Phononen beeinflusst und bildet die Null-Phononen-Linie (engl. *zero-phonon line*, ZPL). Darüber hinaus ist die Aufsammlung von Photonen, die im Diamant emittiert werden, ineffizient, da die Emission räumlich ungerichtet ist und zusätzlich durch die totale interne Reflexion im Diamant beeinflusst wird. Die Integration von NV-Zentren in einen optischen Resonator kann dazu beitragen, diese Einschränkungen unter Ausnutzung des Purcell-Effekts zu überwinden. Die erhöhte Zustandsdichte im Resonator führt zu einer verbesserten Emissionsrate der ZPL in die gut aufsammlbare Resonatormode.

In dieser Arbeit wird die Integration von mikrometerdicken Diamantmembranen in einen faserbasierten Mikroresonator demonstriert. Wir präsentieren eine vollständig orts aufgelöste Analyse des Einflusses, den eine Diamantmembran innerhalb eines Resonators auf dessen optische Eigenschaften hat. Dazu führen wir *Scanning-Cavity*-Messungen mit einer selbstentwickelten Resonatorplattform durch. Wir erreichen dabei eine maximale Finesse von über 16 000 für den Hybridresonator und identifizieren den Einfluss der Diamantdicke und der Oberflächenqualität der Probe auf die Gesamtverluste.

Des Weiteren wird die Entwicklung einer mechanisch stabilen Resonatorplattform beschrieben, die für den Betrieb in einem für Anwendungen in der Quantentechnologie besonders relevanten *Closed-cycle*-Kryostaten geeignet ist. Das Design ermöglicht dabei eine vollständige räumliche und spektrale Abstimmbarkeit im kalten Zustand. Die verschiedenen Rauschbeiträge, die den Resonator beeinflussen, werden analysiert und quantifiziert. Wir erreichen eine Stabilität des Abstands zwischen den beiden Resonatorspiegeln von bis zu 1,2 pm rms. Während der Ruhephase zwischen den Pumphüben des Kaltkopfes ist diese Stabilität sogar noch weiter verbessert und erreicht Werte bis zu 0,8 pm rms. Dies ist die höchste Stabilität, die für einen abstimmbaren Resonator in einem *Closed-cycle*-Kryostaten erreicht wurde.

Die Resonatorplattform wird dann verwendet, um die Purcell-verstärkte Emission von

Ensembles mit ~ 15 resonanten NV-Zentren zu untersuchen. Die Fluoreszenz der ZPL zeigt eine superlineare Leistungsabhängigkeit, was auf kollektive Effekte im Resonator hinweist. Zur näheren Untersuchung wird die Autokorrelation zweiter Ordnung $g^{(2)}(\tau)$ des emittierten Lichts aufgezeichnet. In der ZPL zeigt sich bei kurzen Zeitverzögerungen (< 400 ps) ein Photonen-Bunching, zusätzlich zum charakteristischen Anti-Bunching der einzelnen Emitter. Letzteres wird verwendet, um die Lebensdauer des angeregten Zustands im Resonator im Vergleich zu jener in einem Konfokalmikroskop zu ermitteln. Die Messungen zeigen, dass die Lebensdauer um einen Faktor 2 reduziert ist, was einem Purcell-Faktor von 36 für die ZPL entspricht. Der Bunching-Peak erweist sich als robust gegenüber Dephasierung, was experimentell durch eine Erhöhung der Proben temperatur gezeigt wird. Ein theoretisches Modell deutet darauf hin, dass das Bunching durch Interferenzeffekte zwischen den Emittern im Resonator verursacht wird. Unser Ansatz legt die technischen Grundlagen für vielfältige Anwendungen im Bereich der Quantentechnologie, insbesondere für die Realisierung von Quantenrepeatern und verteilten Quantenrechnern.

Abstract

The growing interest in quantum technologies in the recent past highlighted the need for suitable quantum emitters and the ability to interact with them in a very efficient way. The nitrogen-vacancy (NV) center in diamond is a very promising candidate as it offers an optically addressable electron spin and the option to couple to nearby nuclear spins. The NV center thereby shows very good spin coherence times, even at room temperature. However, NV centers have less-than-ideal optical properties, even for carefully engineered diamond samples. This is on the one hand caused by the coupling of optical transitions to phonons in the diamond lattice that leads to a shift of the emission and absorption frequencies. Only $\sim 3\%$ of the emission is not affected by phonons, forming the zero-phonon line (ZPL). Furthermore, the collection of photons that are emitted within the diamond host is inefficient due to it being non-directional with the additional influence of total internal reflection in the diamond. Integrating the NV center into an optical cavity can help to overcome these limitations through the use of the Purcell effect. The increased density of states in the cavity leads to an improved branching ratio of the ZPL and the emission into the well-collectable cavity mode.

In this thesis, the integration of micrometer thick diamond-membranes into a fiber-based microcavity is demonstrated. We present a full spatially resolved analysis of the influence that a diamond membrane inside of a cavity has on its optical properties. For this, we perform scanning cavity measurements using a home-built resonator platform. We achieve a maximum finesse of over 16 000 for the hybrid cavity and identify the impact of the diamond thickness and its surface quality on the cavity losses.

Furthermore, the development of a mechanically stable cavity platform that is suitable for the operation in a closed-cycle cryostat, which is particularly relevant for applications in quantum technology, is described. The design thereby allows for full tunability when cooled down. The different noise components affecting the cavity are analyzed and quantified. We achieve a stability of the distance between the two cavity mirrors of down to 1.2 pm rms. During the quiet phase between the pump strokes of the cold head, this stability was improved even more, reaching values as low as 0.8 pm rms. This is the highest achieved stability for a tunable cavity in a closed-cycle cryostat.

The cavity-platform is then used to investigate the Purcell-enhanced emission from ensembles containing ~ 15 resonant NV centers. The fluorescence of the ZPL shows a super-linear power dependence, indicating collective effects in the cavity. For a closer examination, the second-order correlation function $g^{(2)}(\tau)$ of the emitted light is recorded. In the ZPL, it features a photon bunching at short time delays (< 400 ps) in addition to the characteristic antibunching from the individual emitters. The latter is

used to extract the lifetime of the excited state in the cavity compared to the one in a confocal microscope. The measurements reveal that the lifetime is reduced by a factor of 2, which corresponds to a Purcell factor of 36 for the ZPL.

The bunching peak proves to be robust against dephasing, which is shown experimentally by an increase of the sample temperature. A theoretical model indicates that the bunching is caused by interference effects between the emitters in the cavity.

Our approach lays the foundation for a variety of applications in the field of quantum technology, especially for the realization of quantum repeaters and distributed quantum computers.

Contents

1. Introduction	1
2. The nitrogen-vacancy center in diamond	9
2.1. Level structure and photoluminescence spectra	9
2.1.1. Electronic structure	9
2.1.2. Vibronic structure	11
2.1.3. ZPL broadening and temperature effects	12
2.2. Spin initialization and readout	14
2.2.1. Optical spin initialization	14
2.2.2. Optical spin readout	15
2.3. Influence of sample properties	16
2.3.1. Bulk diamond	17
2.3.2. Nanodiamonds	17
2.3.3. Diamond Membranes	18
2.4. Creation of NV centers	18
3. Light-matter interaction in optical microcavities	23
3.1. Optical resonators	23
3.1.1. Plane-mirror resonator	23
3.1.2. Plane-concave resonator	26
3.2. Fundamentals of light-matter interaction	30
3.2.1. Strong coupling	32
3.2.2. Weak coupling and the Purcell effect	33
3.3. Collective cavity-emitter coupling and superfluorescence	40
3.3.1. Multiple emitters in a cavity and the Dicke formalism	41
3.3.2. Superradiance, superfluorescence and the distinction to similar effects	43
4. Integration of a diamond membrane into an optical cavity	47
4.1. Fiber-based microcavities	47
4.1.1. Motivation	47
4.1.2. Technical aspects	48
4.1.3. Distributed Bragg reflector	53
4.1.4. Limiting factors	55
4.2. Mode hybridization and membrane-induced loss	57

4.3.	Technical aspects of the sample integration	65
4.3.1.	Samples and Mirror coatings used in this thesis	65
4.3.2.	Cleaning and bonding procedure	66
4.4.	Room temperature scanning cavity microscope	69
4.4.1.	Mechanical Setup	69
4.4.2.	Optical setup	72
4.4.3.	Cavity transmission scans	74
4.5.	Scanning cavity microscopy of diamond membranes	76
4.5.1.	Transmission and finesse maps	76
4.5.2.	Modeling the cavity loss	81
4.5.3.	Increased polarization mode splitting and diamond-induced birefringence	89
5.	A highly stable, fiber-based Fabry-Pérot microcavity for cryogenic environments	93
5.1.	Stability requirements and cryogenic adaptations	94
5.1.1.	Theoretical considerations	94
5.1.2.	Redesign of the cavity stage for the use in a closed-cycle cryostat	95
5.2.	Tunability	99
5.2.1.	Cavity transmission scans during a cooldown	100
5.3.	Cavity stability	102
5.3.1.	Active stabilization	102
5.3.2.	Stability evaluation	107
6.	Collective Purcell enhancement of Nitrogen Vacancy centers	119
6.1.	Membrane characterization	119
6.1.1.	Material properties of the sample	120
6.1.2.	Performance of the sample in the cavity and modeling of losses	122
6.2.	Cavity-enhanced ensemble fluorescence from NV centers	125
6.2.1.	Optical setup	125
6.2.2.	Fluorescence spectra	128
6.3.	Cavity-mediated collective emission from few NV centers in a diamond membrane	133
6.3.1.	Superfluorescence in an optical cavity	133
6.3.2.	Rate equations and the second-order correlation function	135
6.3.3.	$g^{(2)}$ -measurements: photon bunching and the Purcell effect	140
6.3.4.	Interpretation of the collective bunching peak	145
6.3.5.	Outlook	149
7.	Conclusion	151
Appendices	Appendices	155
A.	Transmission scans during a cooldown	157
B.	Dispersion measurement	158
C.	Overview of the cavity parameters	159

D.	Abbreviations and symbols	160
E.	Publications and conference contributions	165
	Bibliography	167
	List of Figures	185
	List of Tables	189

1. Introduction

Quantum is everywhere! Since the introduction of quantum physics over a century ago, researchers have proceeded to gain an understanding of quantum theory and utilize it for novel applications. A significant and widely-known application is the laser, which was proposed by Charles H. Townes and Arthur Leonard Schawlow in 1958 [1] and realized experimentally two years later by Theodore Maiman. The invention of the laser facilitated a variety of possible applications and today, many devices cannot be imagined without it. Another groundbreaking invention based on quantum mechanics is the transistor which ranges back to the 1920s [2] and is the most essential building block for any electronic circuit on which our computers and other technical devices are based on.

While these are some of the most important inventions of the last century, quantum physics has opened up many improvements both in applications as well as for basic research. Quantum systems can be utilized for various research fields such as metrology [3], quantum computing [4, 5, 6] and communication [7, 8, 9, 10]. All these new developments of quantum technology are labeled as the "second quantum revolution" [11]. The common requirement of these applications is to manipulate, control and read out the physical state of individual or ensembles of quantum systems. A quantum system which features such a state that has two possible configurations is called a quantum bit or short, "qubit", referring to the bit known from classical computing. Typically, the most convenient way to manipulate or read out a qubit is by using photons, as they can be created, measured and analyzed very precisely.

Quantum information processing: the perfect quantum emitter Any quantum application involving photons of a specific frequency require emitters that fulfill several conditions. Ideally, a qubit is represented by an optical or spin transition which is as isolated as possible. Any additional transition that translates to a similar energy disturbs the qubit and leads to unwanted information loss. Many quantum emitters provide a spin transition that can be manipulated and read out optically. Such a system is thus called a "spin-photon interface". Finding a suitable quantum emitter has been a goal for many researchers in the last decades. One approach is to isolate single qubits by trapping single atoms or ions. In 1995, Cirac and Zoller proposed to use cold trapped ions as a basis for quantum computing [12]. While these systems offer a high level of control, they require a significant technological effort which limits their applicability. Much easier to integrate are quantum systems in solid-state environments. These emit-

ters have the advantage that they can be embedded into integrated optical devices and thus have a much better scalability. Many solid-state emitters have been investigated in the past, such as quantum dots [13, 14], impurity molecules [15, 16], rare earth ion doped crystals [17], carbon nanotubes [18], color centers in silicon carbide [19] or hexagonal boron nitride (hBN) [20] and color centers in diamond [21, 22]. Since the latter arise from defects in the carbon lattice of diamond, a variety of impurities can form color centers that provide promising optical transitions. The most prominent color centers are the nitrogen-vacancy (NV) [23, 24], the silicon-vacancy (SiV) [25], and the more recently emerging tin-vacancy (SnV) [26, 27, 28] and germanium-vacancy (GeV) [29, 30] centers.

The nitrogen-vacancy center in diamond Among the above-mentioned color centers, the NV center is the one that has been studied the most. NV centers feature highly coherent spins (coherence time > 1 s [31]), even at room temperature (1.8 ms [32]), that can be addressed optically. This makes them a great candidate for quantum applications such as quantum communication. Recently, a quantum network consisting of three nodes has been realized [33], showing the enormous potential that NV centers offer, which is essential for all entanglement-based quantum applications. However, the photonic properties of NV centers are not ideal, caused by strong coupling to lattice vibrations (phonons). The probability to emit coherent photons into the zero-phonon line (ZPL) is only $\sim 3\%$ which hinders the overall efficiency of any device it is used in [34]. The majority of emitted photons is red-shifted and forms the phonon-side band (PSB). Due to their incoherent nature, they lack the indistinguishability that lifetime-limited, coherent photons can offer. The indistinguishability of photons is a fundamental feature for the application in quantum networks.

Moreover, the NV center (as any other color center) emits photons with an almost random spatial direction into the diamond environment. Additionally, the high refractive index of diamond leads to a high amount of total internal reflection on the interface to the surrounding air. This poses a challenge since one aims to collect a significant fraction of the photons emitted by the NV center. One way to improve the directionality of the emission and the collection efficiency is by machining a solid immersion lens (SIL) onto the diamond surface [35]. This can improve the collection efficiency by an order of magnitude [36, 37]. The poor branching ratio of the ZPL, however, remains unaffected. Coupling the NV center to an optical high-finesse cavity can improve the optical properties like the collection efficiency and the branching ratio of the NV center due to the Purcell effect.

Diamond membranes coupled to fiber-based microcavities The Purcell effect describes the enhancement of any light-matter interaction in a cavity due to the increased density of states [38]. The extent of this enhancement is thereby given by the ratio of the quality factor of the cavity and its mode volume. The quality factor is a metric for the energy in the cavity that is lost per round trip, e.g. due to transmission through one of the mirrors.

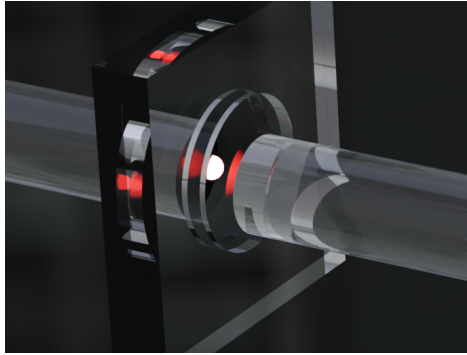


Figure 1.1: 3D rendering of the fiber-based microcavity used in this thesis. The model is not to scale and omits the mechanical setup that surrounds the cavity, but shows the basic principle of a fiber-based cavity. The model shows the fiber onto which the concave mirror profile is machined. The macroscopic mirror is shown together with the diamond membrane that is thinned down in the center region to allow for shorter mirror separations. This technique is also used in the experiment.

The most beneficial geometry for a cavity-based spin-photon interface is therefore a high-finesse cavity with a very small mode volume. A promising approach for this is a fiber-based microcavity, where a concave mirror profile is machined onto the end facet of an optical fiber, as it combines a small mode volume of down to one wavelength cubed with a high degree of tunability and the possibility to achieve high quality factors [39, 40, 41]. Other cavity designs like photonic crystal cavities can reach even smaller mode volumes but lack the tunability [42], while macroscopic cavities can reach very high quality factors but are limited to rather large mode volumes.

The fiber-based cavity used in this work consists of one fiber mirror and a second, macroscopic planar mirror. In most experiments, the sample that shall be investigated is placed onto the planar mirror such that one can use the fiber mirror to probe different positions on the sample. The presence of such a sample can thereby modify the mode structure of the cavity and introduce additional sources of loss to the system. Especially micrometer-thick diamond membranes, as used in this work, can have a major impact on the cavity due to the high refractive index of diamond [43, 44, 45]. Depending on the thickness of the diamond membrane, a hybridized mode can be present that is either confined primarily in the air gap between the fiber mirror and the membrane, or in the membrane itself. As most sources of loss as well as other surface-induced effects scale with the local electric field strength, the mode structure of the cavity is crucial for its performance. A rendered model of the cavity geometry used in this thesis is shown in fig. 1.1 (not to scale).

Mechanical stability While the Purcell effect in an optical cavity improves the optical properties of an emitter greatly by increasing the branching ratio of the ZPL and the

fraction of collectable photons, it cannot fully terminate the phonon-induced dephasing that can increase the natural linewidth by several orders of magnitude. In many cases, this can be overcome by integrating the emitter into a cryogenic environment. The required temperature thereby varies between the different emitters. In the case of NV centers, temperatures below 10 K are suitable to facilitate the emission of lifetime-limited photons [46]. The integration of a sensitive device such as a high-finesse cavity into a cryostat poses major challenges. Since the emission into a cavity mode is only possible if the resonance frequency of both the emitter and the cavity overlap, it is limited by mechanical noise. Depending on the type of the cryostat, the environmental noise level can be heavily increased by the cryostat. The best mechanical stability for tunable cavities was achieved in bath cryostats [47]. Applications in the field of quantum technologies, however, benefit clearly from the use of a closed-cycle cryostat. While the mechanical vibrations caused by such a cryostat are severe, it is superior in terms of usability, since no helium has to be refilled, as opposed to bath or flow cryostats. A mechanical stability of under one picometer has been reached for a monolithic cavity [48]. For tunable cavities, the so far reached cavity length jitter is on the order of a few tens of picometers [49, 50, 51], which is not sufficient for many experiments and thus remains a major challenge.

Collective effects The mechanical stability of a cavity as well as its optical properties heavily influences the efficiency with which quantum emitters can interact with the cavity mode. For ensembles containing multiple emitters that are coupled to a microcavity, interesting effects such as superradiance or superfluorescence can arise and open up a different route for novel technology. Superradiance (SR), proposed already 1954 by R. H. Dicke [52] and experimentally shown in 1973 [53], is a collective effect where N emitters are excited coherently by a laser pulse such that their polarization dipoles are synchronized. This leads to the build-up of a macroscopic dipole which scales with the number of emitters and emits photons in the form of short, intense photon bursts with an increased emission rate. If the excitation is incoherent such that the phases of the dipole oscillations are initially randomly distributed, the emitters can synchronize spontaneously via a common radiation field and thereby form the macroscopic dipole. This effect is then called superfluorescence (SF) and was first mentioned by Bonifacio et al. [54, 55]. The very intense and fast emission of superradiant or superfluorescent ensembles allows for new applications such as ultra-narrow, superradiant lasers [56, 57], long-lived quantum memories [58, 59, 60, 61] or new techniques in quantum metrology [62]. In fact, there are multiple regimes that one can classify collective effects in, e.g. amplified spontaneous emission [63], or interference effects between the emitters [64]. As these effects usually require ensembles with a high density of indistinguishable, yet spatially overlapping emitters, it proved to be very challenging to demonstrate them in solid state environments. While symmetrical group-IV color centers like the SiV center face a smaller spread of transition frequencies for large numbers of emitters and could therefore be more suitable for SR experiments, color centers with permanent electric dipoles like the NV center are rather unlikely to show SR. Collective effects were

successfully shown with cold atoms in cavities [65, 66], rare earth ions [60], or quantum dots [67, 68]. Experiments on NV centers, however, are still very rare. Angerer et al. have shown superradiance for NV centers in a cavity for the electron spin transition in the microwave regime [69]. Bradac et al. demonstrated superradiant emission from diamond nanocrystals containing a large number ($\sim 10^3$) NV centers at room temperature [70]. Cavity-mediated collective effects of NV centers at cryogenic temperatures, especially in tunable cavities, are yet to be shown to our knowledge.

Scope of this work In the course of this dissertation, I shall demonstrate the integration of ensembles of NV centers into a fully tunable, fiber-based microcavity. The technological developments that were essential - both for the cavity itself as well as for the sample integration - are presented in detail. The performance of the setup is analyzed thoroughly and finally, the Purcell effect is exploited to show evidence of collectively enhanced emission rates and interference effects.

In the **second chapter**, I will briefly introduce the theoretical and technological background of NV centers. The main focus will thereby be on the energy level structure of NV centers as well as the different types of diamond samples and their creation. Broadening effects like phonon coupling or temperature effects and their impact on the optical and spin properties of NV centers will be discussed. Moreover, the techniques that allow for an efficient spin initialization and readout are introduced. Different possible approaches for diamond samples are furthermore discussed, highlighting the influence of the geometry on the NV properties. Finally, promising techniques to form coherent NV centers in a diamond sample are considered.

In **chapter 3**, the theoretical description of optical cavities is shown. Their basic principles are derived, followed by the discussion of light-matter interaction in a cavity. The different coupling regimes are highlighted, and the central physical aspect of this work, the Purcell effect, is introduced. In addition to the theoretical model of a single emitter in a cavity, I shall address collective cavity-emitter coupling and its description via the Dicke formalism. The terminology of different collective effects is discussed. Furthermore, the technical realization of the cavity which was used in this thesis, the fiber-based microcavity, is presented. I will discuss the technical aspects such as the machining of concave mirror profiles on the end facet of an optical fiber as well as the limiting factors of such a setup, e.g. by transverse mode coupling or imperfect mirror profiles.

In the **fourth chapter**, the integration of a micrometer thick diamond membrane into such a fiber-based microcavity is described theoretically and quantified experimentally afterwards. I will thereby focus on the influence which the presence of a dielectric membrane has on the mode structure and the optical properties of a cavity. This implies the effective integration of the membrane into the cavity which is realized by van der Waals bonding. The recipe that was used in this work is described in detail. The mode hybridization effect is first simulated and then shown in measurements using a scanning cavity setup at room temperature. As this altered mode structure also affects the electric field strength at the different interfaces and inside the membrane, one expects an alter-

nation of cavity-induced losses which defines the finesse and therefore the quality factor that can be reached. A theoretical model is introduced that aims to predict the expected losses in the cavity, depending on factors like the diamond thickness i.e. the mode structure, the surface quality and other influences like the curvature of the cavity mode or the previously discussed transverse mode coupling. Lastly, the altered polarization axes of the cavity modes by diamond properties like strain are shown.

Chapter 5 deals with the second technological challenge that this experiment poses, the realization of a mechanically stable, fully tunable cavity platform, designed for cryogenic temperatures. As the mechanical stability has a crucial influence on the efficiency of the light-matter interaction, I shall describe the technical aspects of the setup in detail. The development of the stage is mainly based on the work of Thomas Hümmer [71] and Julia Benedikter [72] and will focus on the improvements that were made in order to reach the desired stability on the few picometer range. I shall demonstrate the tunability of the setup during a cooldown, using cavity transmission maps. The theoretical principles that are used to quantify the mechanical stability are introduced. Afterwards, the setup that is used to realize an efficient active stabilization is described. The achieved stability is then evaluated in depth, covering the passive stability of the setup, the improvements that are possible with the active stabilization and the performance of the setup when the fiber mirror is brought into mechanical contact with the plane mirror. Finally, the temporal progress of the cavity length jitter over a pump cycle of the cryostat is analyzed, followed by an overview and possible further improvements.

In the **sixth chapter**, the cavity-enhanced ensemble spectroscopy of NV centers, enabled by the technological developments shown in the previous chapters, is presented. These are the central results of this thesis. The diamond membrane, which contains the NV centers, is first tested for its optical performance, similarly to chapter 4. The spectroscopy section is split into two main parts. The optical setup that was used for the following measurements is first described, followed by cavity-enhanced fluorescence spectra. I shall thereby highlight the effect of the cavity as opposed to measurements in a confocal microscope. Furthermore, the full mode dispersion with its characteristic avoided-crossing structure is shown. Afterwards, the fluorescence measurements are performed for different laser excitation powers, revealing a super-linear power dependence of the count rate due to superfluorescent emission. The second part focuses on the temporal structure of the emitted light. Therefore, second-order correlation measurements are performed, which are defined by the time constants of the different decay channels of the emitters. The dependence of the correlation function on the excitation laser power is used to extract the time constants at zero laser power, yielding the lifetimes of the excited and metastable states of the NV center. These results are compared to a similar measurement series in a confocal microscope, revealing the lifetime reduction that is caused by the Purcell enhancement in the cavity. Finally, the collective behavior of the NV ensembles is analyzed and described theoretically. I shall describe the limiting factors of the measurement and evaluate our findings with respect to theoretical predictions. In the **last chapter**, a short summary of the work is given.

The results that are shown in this thesis have been published in the following papers¹:

- *"Fabrication and Characterization of Single-Crystal Diamond Membranes for Quantum Photonics with Tunable Microcavities"*
J. Heupel, M. Pallmann, J. Körber, R. Merz, M. Kopnarski, R. Stöhr, J. Reithmaier, D. Hunger, C. Popov
2020, Micromachines 11(12) (2020) [73]
- *„Scanning cavity microscopy of a single-crystal diamond“*
J. Körber, M. Pallmann, J. Heupel, R. Stöhr, E. Vasilenko, T. Hümmer, L. Kohler, C. Popov, D. Hunger
Preprint (2022), DOI:10.48550/arXiv.2210.05514 [45]
- *„Fabrication of High-Quality Thin Single-Crystal Diamond Membranes with Low Surface Roughness“*
J. Heupel, M. Pallmann, J. Körber, D. Hunger, J. Reithmaier, C. Popov
Physica Status Solidi (A) Application and Materials (2022) [74]
- *„A highly stable and fully tunable open microcavity platform at cryogenic temperatures“*
M. Pallmann, T. Eichhorn, J. Benedikter, B. Casabone, T. Hümmer, D. Hunger
APL Photonics (2022) [75]
- *“Cavity-mediated collective emission from few inhomogeneous color centers in a diamond membrane”*
M. Pallmann, K. Köster, Y. Zhang, J. Heupel, C. Popov, K. Mølmer, D. Hunger
currently being prepared for publication (2023)

¹ A full list of publications and conference contributions can be found in the appendix.

2. The nitrogen-vacancy center in diamond

The nitrogen-vacancy (NV) center in diamond is a color center and a point defect in diamond. Diamond is a very suitable host for color centers due to its wide band gap of 5.5 eV [76] and the high rigidity of the lattice [77]. In the case of the NV center, two adjacent carbon atoms are removed from the diamond lattice and replaced with a nitrogen atom and a vacancy, respectively. The NV center is shown schematically in fig. 2.1(a). It can occur naturally, as nitrogen is the most common impurity that can be found in diamond [78], or be created artificially using various techniques that shall be presented in this chapter. I will present the electronic structure of NV centers, the resulting optical and spin properties and how they can be manipulated and read out. Furthermore, a short overview over the different approaches is given in which NV centers can be integrated into photonic devices.

2.1. Level structure and photoluminescence spectra

2.1.1. Electronic structure

The electronic structure can be derived using a group-theoretical approach which utilizes the symmetry properties of the NV center [79, 80]. Removing two carbon atoms from the diamond lattice and replacing one with a nitrogen atom leaves behind four unsaturated covalent sp³-hybridized bonds, the so called dangling bonds. The symmetry of the lattice thereby changes from the O_h symmetry of the diamond to a C_{3v} symmetry along the NV axis, which is defined as the axis that connects the vacancy and the nitrogen atom. In the following, the bonding orbitals of the NV center are called σ_1 , σ_2 , σ_3 and σ_N whereby

2. The nitrogen-vacancy center in diamond

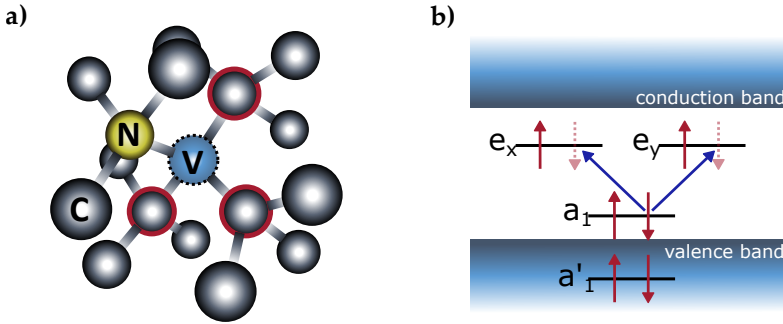


Figure 2.1: (a) Schematic sketch of the NV center. The vacancy (V) is shown as a substitational atom for the sake of clarity. (b) Electronic states of the negatively charged NV center. The respective states are described by linear combinations of the atomic orbitals that emerge from the dangling bonds of the adjacent carbon atoms (marked with red circles in (a)) and the nitrogen atom. The occupation of e_x and e_y as shown here ($\uparrow\uparrow$) results in the $m_s = +1$ ground state. Adapted from [81].

σ_N corresponds to the dangling bond of the nitrogen atom. The electronic states, shown in fig. 2.1(b), are then given by the linear combination of atomic orbitals (LCAO),

$$a'_1 = \alpha \frac{\sigma_1 + \sigma_2 + \sigma_3}{2} + \beta \sigma_N, \quad (2.1.1)$$

$$a_1 = \alpha \sigma_N + \beta \frac{\sigma_1 + \sigma_2 + \sigma_3}{2}, \quad (2.1.2)$$

$$e_x = \frac{2\sigma_1 - \sigma_2 - \sigma_3}{\sqrt{6}} \quad \text{and} \quad (2.1.3)$$

$$e_y = \frac{\sigma_2 - \sigma_3}{\sqrt{2}}. \quad (2.1.4)$$

The states a_1 , e_x and e_y are located in the band gap, while a'_1 is positioned in the valence band. These states are then occupied by the dangling electrons, i.e. one electron from each carbon atom and two electrons from the nitrogen atom, respectively. This describes the neutrally charged NV^0 center. If an additional electron is added to the system, e.g. from nearby nitrogen atoms, the NV center becomes negatively charged and is then called NV^- . Since the NV^- center is the configuration that is of most interest, including the experiments in this work, the term "NV center" will in the following describe the negatively charged version, if not stated otherwise. Following Hund's rules, the a_1 and a'_1 states are filled first with two electrons each since they have the lowest energy level, such that their total spin is zero. The two remaining electrons are split and occupy the e_x and e_y states. Hence, the overall quantum system has then a total spin of $S = 1$ and therefore forms a spin triplet with $m_s = 0, \pm 1$. The symmetry of the spin triplet state is A_2 , the state is thus described as $|^3A_2\rangle$. Due to the parallel orientation of the electron spins in the $m_s = \pm 1$ states, spin-spin interaction leads to an energy splitting between the $m_s = 0$ and the $m_s = \pm 1$ states at zero magnetic field of $D = 2.87$ GHz.

When the NV center is optically excited, one electron is transferred from the a_1 to one of the $e_{x,y}$ states [25]. The resulting electronic configuration again forms a spin triplet and has a higher total energy that is separated from the optical ground state by 1.95 eV ($\lambda_0 = 637$ nm). Hereby, the excited state changes its symmetry and is hence called $|^3E\rangle$. The full level scheme of the NV center is shown in fig. 2.2(a). The decay from the excited triplet states to one of the ground states can either happen via this spin-conserving optical transition or non-radiatively² via additional singlet states $|^1A_1\rangle$ and $|^1E\rangle$ that are located between $|^3A_2\rangle$ and $|^3E\rangle$ [80]. While the lifetime of the excited state $|^3E, 0\rangle$ is ~ 12 ns [24] and thus relatively short, compared to other solid state emitters [22], the lower singlet state $|^1E\rangle$ has a much longer lifetime of ~ 219 ns at room temperature [82, 83]. The singlet states are therefore also called "shelving states", since an electron that decays via this channel is shelved in the $|^1E\rangle$ state and does hence not contribute to the fluorescence.

2.1.2. Vibronic structure

As opposed to some other emitters, NV centers in diamond are heavily influenced by their interaction with their surrounding diamond lattice. In particular, vibrations in the lattice, i.e. phonons, can couple to the electronic states and therefore alter the optical transitions and energy levels. This interaction is described by the Huang-Rhys model [85, 86] and is schematically shown in fig. 2.2(b). It states that an electronic transition couples to the vibrational modes equally in the electronic ground and the excited state. The influence of vibrations to the emission and absorption bands thus only depends on the difference ΔQ of the nuclear equilibrium positions in the ground and excited state, respectively. The optical transition between the vibronic ground states of the electronic ground and the excited state, i.e. without any involved phonons is called zero-phonon line (ZPL). Due to the small Debye-Waller factor, only 3 % of the emission is confined in the ZPL [34]. All other transitions, that couple to vibrations, form the phonon sideband (PSB). If one takes into account the Born-Oppenheimer approximation [87], the motion of the electron during a transition can be assumed to be instantaneous such that only vertical transitions in the picture of fig. 2.2(b) are allowed.

Furthermore, the Frank-Condon principle [88] describes that the probability for any electronic transition that involves a change in vibrational energy depends on the overlap of the respective vibrational wave functions. Hence, the transition corresponding to the ZPL is not the most likely transition, as the nuclear offset lowers the wave function overlap. Consequently, the majority of the emission spectrum is red-shifted, while the absorption spectrum is equally blue-shifted.

² The term "non-radiatively" is a bit misleading here, since the transition from $|^1A_1\rangle$ to $|^1E\rangle$ can produce an infrared photon, but as its wavelength is much larger than the typical transitions of the NV center, it is convenient to call it non-radiative.

2. The nitrogen-vacancy center in diamond

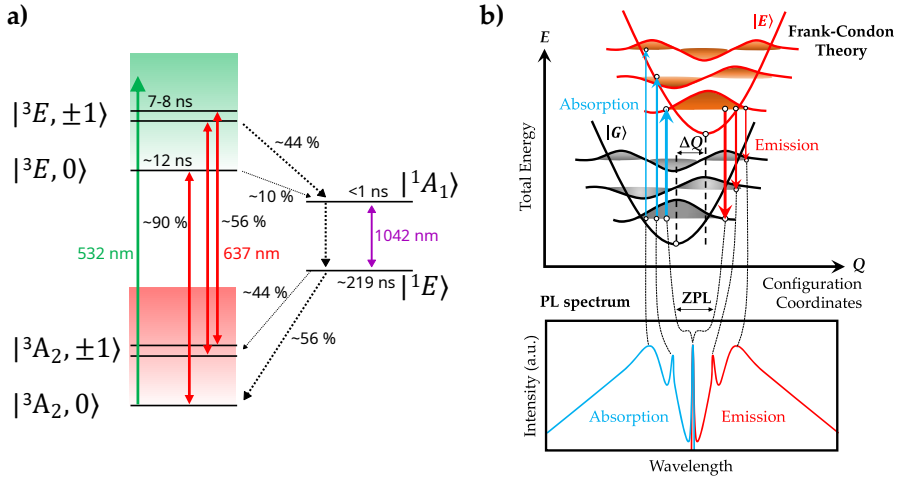


Figure 2.2: (a) Relevant level scheme of the NV center, showing the triplet spin states in the electronic ground and excited state as well as the singlet states that form a non-radiative decay channel. The shaded areas indicate the coupling to phonons in the diamond lattice. The red arrows refer to the resonant excitation and emission wavelength, the green arrow refers to an exemplary wavelength for non-resonant excitation. The lifetimes (branching ratios) are notated for the respective states (transitions). (b) Upper panel: vibronic structure of the NV center, highlighting the emergence of the phonon side band, as described by the Frank-Condon principle. Lower panel: the resulting absorption and emission spectrum. Due to the shift between the electronic states, transitions that involve a change of the vibronic state can be favored, resulting in mirrored absorption and emission spectra around the ZPL. Taken from [84].

This opens up new approaches to optically excite the NV center, despite these vibronic states being barely occupied at room temperature due to the high Debye temperature of diamond [89]. In order to drive the optical transition, one can not only use the coherent wavelength of 637 nm, but also use a blue-detuned laser and excite the NV center into one of the higher vibronic states in the excited electronic state. As the lifetime of the vibronic states are on the picosecond range and therefore much shorter than the optical lifetime [90], the NV center is virtually always in its vibronic ground state. The optical deexcitation under the emission of a photon hence always starts at this state.

2.1.3. ZPL broadening and temperature effects

Since most applications involve the creation of indistinguishable photons, the main focus usually lies on the emission into the ZPL. In order to gain indistinguishability, the spectral linewidth of the ZPL has to be as close as possible to the lifetime limited linewidth

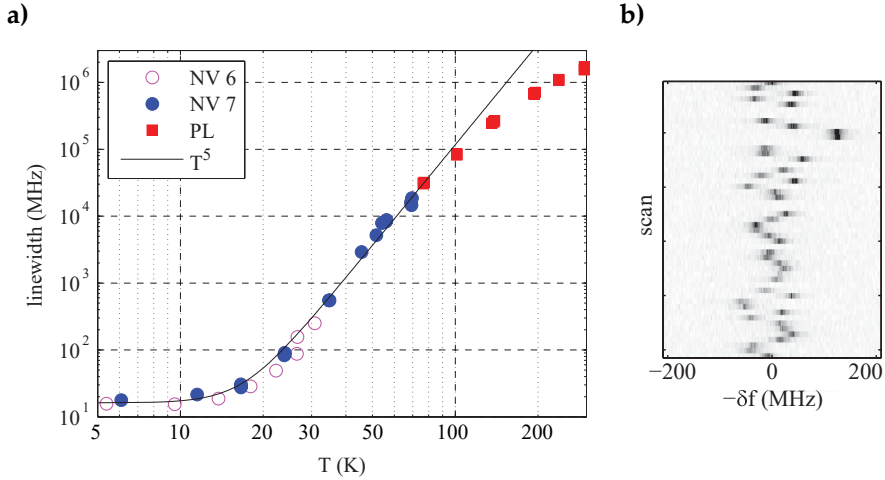


Figure 2.3: (a) Temperature dependence of the ZPL of three different NV centers. The solid black line shows the $\propto T^5$ dependence which fits the data well up to 100 K. (b) Multiple photoluminescence excitation (PLE) scans of the same NV center, showing the frequency jumps of the ZPL due to spectral diffusion. The time average of the individual scans yields the inhomogeneous ZPL. Taken from [93]

of 13 MHz [91]. However, there are several effects that cause spectral broadening of the ZPL. The two main effects are dephasing of the optically excited state caused by the dynamic Jahn-Teller effect [92] and spectral diffusion.

The excited state $|^3E\rangle$ is an orbitally degenerate electronic state, forming the doublet (E_x, E_y) , which describes whether the e_x or e_y orbital is occupied by the excited electron. These doublet states can couple to lattice vibrations with rising temperature. This is mediated by a two-phonon Raman scattering process [93]. The E_x and E_y states can then mix and allow transitions between the two, leading to a reduced electronic lifetime, i.e. an increased dephasing of the optical transition, hence to a broadening of the ZPL. As this effect directly depends on the available energy via lattice vibrations, it shows a strong temperature dependence ($\propto T^5$ up to 100 K), as depicted in fig. 2.3(a). At room temperature, the linewidth can be in the THz regime.

Spectral diffusion originates from fluctuating electric fields in the diamond environment that can be induced by strain, nearby crystal defects or trapped charges [46, 94] as applying an electric field shifts the emission wavelength due to the DC Stark effect. Charge traps in the surrounding diamond host are thereby a main contributor to electric field fluctuations as they can become ionized by the field of the excitation laser [95]. These ionization processes usually happen on a much shorter timescale than the recording of an emission spectrum such that they cannot be resolved directly but instead

lead to a time-averaged Gaussian broadening of the emission line. Fig. 2.3(b) shows consecutive PLE scans of the same NV center, revealing the frequency shifts by spectral diffusion. In this case, the shift is on the order of a few 100 MHz, leading to a significant inhomogeneous broadening. If the NV center is close to the surface, this effect is typically enhanced by a higher occurrence of nearby charge traps due to surface defects [96]. The Stark shift for shallow NV centers can be on the order of several hundred GHz [94]. Similar to the broadening via Jahn-Teller coupling, spectral diffusion by ionization also shows a temperature dependence. For temperatures between 5 – 20 K, the diffusion rate stays constant [94]. This is consistent with the picture that the ionization of charge traps is mainly caused by the excitation laser light (which is usually chosen to be at 532 nm), since their ionization energy is higher than the thermal energy k_bT at this temperature. While the occurrence of Stark shifts is mainly an unwanted effect, it can also be used to actively tune [46] or stabilize [97] the resonance frequency of a NV center. This can be very helpful if one wants to overlap two distinct NV centers spectrally in order to gain indistinguishability.

2.2. Spin initialization and readout

2.2.1. Optical spin initialization

If we recall the level scheme of the NV center in fig. 2.2(a), it becomes apparent that the non-radiative decay channel via the singlet states can be possible for all states of the excited state spin triplet. Also, a system in $|^1E\rangle$ can decay to either of the spin states in the electronic ground state. However, the transition from $|^3E\rangle$ to $|^1A_1\rangle$ has a much higher branching ratio for $m_s = \pm 1$ compared to $m_s = 0$ [98]. It can hence be seen as a spin-selective transition. The reason for this spin-selectivity is still under debate [24, 79]. Again, when decaying back into the ground state, the transition into the $m_s = 0$ state is more likely than $m_s = \pm 1$. This phenomenon opens up some useful features: if one drives the transition into the optically excited state using a blue-shifted laser with respect to the coherent transition, it will conserve the spin state and therefore populate the excited state spin triplet. The NV center then decays either optically under the creation of a photon or via the shelving states. Since the transition from the $m_s = \pm 1$ states to the shelving states is more likely than from the $m_s = 0$ state, it will preferably decay back to the optical and spin ground state $|^3A_2, 0\rangle$. If the transition is pumped constantly, the NV center will eventually always end up in the $m_s = 0$ state. This is called optical spin initialization as it makes it possible to initialize the spin state of the NV center into $m_s = 0$ just by the use of green excitation light. This is a useful tool as it is simple to perform and to implement in the experiment.

Optical initialization by resonant excitation If the NV center is cooled down to cryogenic temperatures, the ZPL transition becomes narrow enough such that the spin-conserving transitions from $|^3A_2\rangle$ to $|^3E\rangle$ can be driven separately for the respective spin configurations, whereas E_x is spin-conserving for $m_s = 0$ and A_1 connects the $m_s = \pm 1$ states. This is because the zero field splitting of the excited state spin triplet is slightly smaller than the one of the ground state (1.423 GHz compared to the 2.87 GHz of the ground state) [99]. Hence, if one only drives the A_1 -transition resonantly, the $m_s = \pm 1$ states will be constantly excited while the $m_s = 0$ state stays unaffected. The high likeliness for the $m_s = \pm 1$ states to decay via the shelving states eventually leads to a spin initialization into $m_s = 0$, which is a more effective way compared to off-resonant excitation [100].

2.2.2. Optical spin readout

The spin-selective optical transition in the NV center does not only enable optical spin initialization, but it can also be used to read out the electron spin state optically. Since the non-radiative decay via the shelving states is more likely if the electron spin is $m_s = \pm 1$, this case will result in less PL emission. The fluorescence rate can hence provide information about the electron spin state. To do so, one commonly uses optically detected magnetic resonance (ODMR) measurements.

Optically detected magnetic resonance To perform an ODMR measurement, the NV spin state is first initialized into the $m_s = 0$ state by continuous irradiation with an off-resonant laser. While doing so, the emission rate is recorded continuously. Additionally, a microwave signal is applied to the NV center whereas the microwave frequency ν_{mw} is swept over the spin transition frequency of 2.87 GHz. While the electron spin stays unaffected most of the time, the transition is driven resonantly when $\nu_{\text{mw}} = 2.87$ GHz. The $m_s \pm 1$ states then become populated, leading to a reduction in the fluorescence rate. The simplified level scheme and an exemplary measurement are shown in fig. 2.4. Furthermore, when a magnetic field is applied to the NV center, the degeneracy of $m_s = \pm 1$ is lifted, and the two spin states split up due to the Zeeman effect that shifts the energy of each spin state by [101]

$$E_Z = \pm g\mu_B B_{\text{NV}} \quad (2.2.1)$$

whereby $g \approx 2$ is the Landé g -factor, μ_B the Bohr magneton and B_{NV} the projection of the magnetic field onto the NV axis. Consequently, the energy difference between the $m_s = \pm 1$ states also becomes visible in the ODMR measurement, two distinct emission drops arise. Fig. 2.4(b) shows several consecutive ODMR measurements of the same emitter for different (external) magnetic fields. Applying an external magnetic field can thus be used to split the spin states and address them individually. Since E_Z scales

2. The nitrogen-vacancy center in diamond

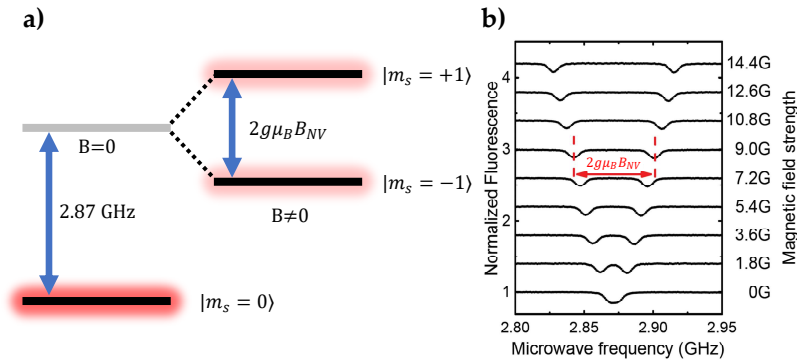


Figure 2.4: (a) Level scheme of the electronic ground state $|^3A_2\rangle$ including the effect of an external magnetic field along the NV axis. The darker, initially degenerate $m_s = \pm 1$ levels split up due to the Zeeman effect. (b) ODMR measurements of an NV center for different applied magnetic fields. The frequency splitting between the two dips in the signal arises from the magnet field strength. Adapted from [101].

linearly with the magnetic field, ODMR is furthermore a great tool to use the NV center as a magnetic field sensor [101, 102, 103].

Photoelectric readout In more recent experiments, the spin readout by photoelectric detected magnetic resonance (PDMR) has been shown as an alternative to ODMR. The idea is that instead of driving the optical transition of the NV center and measuring the fluorescence rate, one can make use of the spin-selective ionization probability of the NV^- center [104]. For this technique, a bias voltage is applied to electrodes on the diamond to extract the ionization-induced electrons in the diamond, leading to a current that reveals the electron spin state of the NV center. The ionization can be realized via single- or two-photon excitation, depending on the wavelength of the excitation laser. The main advantages over ODMR are that close-to-unity collection efficiency as well as an easy on-chip integration can be realized [105].

2.3. Influence of sample properties

The shape of a diamond crystal that acts as a host for NV centers is a crucial criterion for the optical and spin properties of the NV center as well as the practicality in terms of integration into an experiment or potential devices. In the following, I shall discuss the most prevalent approaches and their advantages or drawbacks.

2.3.1. Bulk diamond

A bulk sample is diamond in its macroscopic form. Since diamond effectively shields the color center from external perturbations, it is advantageous to have the emitter surrounded by a sufficient amount of material. For this reason, the longest spin coherence times have been achieved using NV centers in bulk diamond, both at cryogenic temperatures (> 1 s [31]) as well as at room temperature (1.8 ms [32]). Their optical and spin properties are thereby dictated by the purity of the diamond, i.e. whether impurities such as crystal defects or nuclear spins of naturally occurring nitrogen are close to the emitter. Furthermore, samples made from bulk diamond are fairly easy to handle and to process.

Their biggest disadvantage, however, is their very limited collection efficiency. Due to the high refractive index of diamond ($n_d = 2.41$), photons are lost by total internal reflection at the diamond-air interface. For this reason, it is crucial to improve the outcoupling efficiency. Suitable ways to do so are e.g. solid immersion lenses (SIL) that can be fabricated on top of the diamond, coupling to waveguides or antennas, or, as in this work, integrating the diamond into an optical cavity. While SILs can heavily improve the collection efficiency to near-unity, reaching a 10-fold increase to up to 1 Mcounts/s [36] from single NV centers, optical cavities are often preferred in recent NV experiments, since they can simultaneously improve the branching ratio into the ZPL (see sec. 3.2 for more detail). Especially for cavity applications, the integration of bulk diamond is not possible. One way to overcome this limitation is to fabricate nano-cavities inside of the diamond which can reach very high Q-factors and excellent outcoupling efficiencies paired with a strong Purcell enhancement [106, 107]. A major drawback of these platforms is the lack of tunability in terms of the cavity length.

2.3.2. Nanodiamonds

Nanodiamonds (ND) are small pieces of diamond that usually have a size of < 100 nm and can host a high density of color centers [108]. Due to their small size, they can easily be integrated into optical cavities, e.g. via spin coating [109], and are compatible with biotechnological and biomedical applications [110]. Hence, they enable the use of cavities with ultra small mode volumes. Opposed to that, their small size has several consequences: firstly, the excited state lifetime of NV centers in nanodiamonds is longer than the lifetime in bulk diamond. This is caused by the dielectric environment of the color center, which has a significantly lower refractive index for NDs as the emitter is effectively surrounded by air and/or the surface that holds the ND [111]. This leads to a lower emission rate.

Secondly, color centers in NDs are always very close to the surface and therefore suffer from surface-induced effects like increased strain or electric noise [96]. The extent of these effects varies for different kinds of color centers. Group-IV defects like the silicon-vacancy (SiV) center, for example, have a different symmetry and hence do not

show a permanent electric dipole, in contrast to NV centers. If NV centers are close to the surface, however, they are heavily impacted by the above-mentioned effects.

2.3.3. Diamond Membranes

Diamond membranes are thin slabs of diamond whose thickness can vary between a few 100 nm up to tens of micrometers. They are very interesting candidates as a host of NV centers since they combine bulk-like properties such as good spin coherence times with sufficiently small sizes that allow one to integrate them into optical cavities. While group-IV color centers can be easily integrated into very thin membranes, the optimal thickness for NV centers seems to be in the few micrometer regime [112]. If the membrane is much thinner than this, surface effects like spectral diffusion will have a larger impact and limit the optical and spin properties of the emitter. A much thicker membrane, on the other side, limits the smallest possible cavity mode volume and thus the potential gain via the Purcell effect.

The most common way to fabricate such μm -thick membranes is by cutting a bulk sample into thinner pieces, followed by mechanical or chemical polishing processes and finally, the use of reactive-ion etching (RIE) to reduce the membrane down to the desired thickness [73, 74, 112].

In this work, the integration into the cavity is realized by attaching the membrane to a macroscopic plane mirror by van der Waals bonding. This process will be discussed in detail in sec. 4.3.2.

2.4. Creation of NV centers

Diamond samples that are used for quantum optical experiments are usually grown by chemical vapor deposition (CVD). The reason for this is that the concentration of impurities in the lattice, especially that of nitrogen, has to be very low, i.e. the diamond has to be extremely pure in order to avoid any unwanted defects that cause decoherence. In carefully grown diamonds, the abundance of impurities can get below 1 ppb for nitrogen and boron [113, 114]. With this starting material, it is possible to observe lifetime-limited NV centers in bulk [46] and close to lifetime-limited NVs in diamond membranes [112]. An ultra high purity of the diamond host, however, leads to a very low density of natural NV centers. Hence, one would ideally start with an ultrapure diamond and create additional NV centers in the diamond while avoiding damage in the lattice. In the following, several methods are presented how this can be achieved.

Ion implantation The most prevalent method to create NV centers is by implantation of nitrogen ions into the diamond [115]. The basic idea is to bombard the diamond with single nitrogen ions with kinetic energies up to the MeV range such that they get trapped in the lattice and thus increase the nitrogen density. Afterwards, the sample has to be annealed at temperatures up to 1000 °C. This has multiple reasons: firstly, the nitrogen ions have to be placed in lattice positions such that they are able to combine to NV centers. Secondly, the nitrogen implantation alone will not create many NV centers since the intrinsic defects in the diamond are spread randomly in the diamond. By annealing, the lattice defects become mobile and can recombine with nitrogen substitutes to NV centers. Lastly, as the nitrogen ions penetrate the diamond with very high kinetic energies, they leave behind a lot of damage on the crystal lattice, which can be reduced by annealing.

Ion implantation has the big advantage that the depth in which the NV centers are created can be controlled very precisely via the kinetic energy. This is especially beneficial for the integration into optical cavities. As we shall see later, the electric field inside of an optical cavity is a standing wave, i.e. the nodes and anti-nodes of the field are at constant positions in the sample. It is thus of great importance that the emitters are positioned such that they are at or close to an electric field maximum in order to maximize the interaction with the cavity field.

While this technique can be used on bulk samples to create close to lifetime-limited NV centers [116], it poses problems for diamond membranes and limits the NV linewidth, as emitters in these environments are more sensitive to the crystal damage [117].

Electron or laser irradiation The creation of NV centers by electron irradiation offers a much more gentle option compared to ion implantation. The typical procedure, as presented by Ruf et al. [112] is shown in fig. 2.5. Instead of introducing additional nitrogen into the diamond, one makes use of the natural abundant nitrogen in the diamond which is randomly distributed in the lattice. The starting material is an ultrapure, CVD-grown bulk diamond. The irradiation with high-energy electrons then leads to the formation of lattice vacancies. By annealing the diamond at high temperatures, similar to the creation by ion implantation, the vacancies again become mobile and can recombine with the naturally occurring nitrogen impurities in the diamond. Due to the much lower mass of electrons, compared to nitrogen ions, the resulting lattice damage is much lower, thus leading to a purer and less noisy environment. Afterwards, the sample is sliced into thinner slabs, polished, and finally thinned down to the desired thickness by RIE. After the sample is cleaned, this technique can improve the dephasing linewidth of the NV centers by over one order of magnitude, reaching linewidths of < 100 MHz [112]. Recently, yet unpublished experiments have indicated that the creation of NV centers by electron irradiation does not reliably succeed for regions close to the diamond surface (i.e. a few micrometers deep). It is believed that this is caused by near-surface lattice defects that can recombine with the emerging vacancies and thus hinder the creation of NV centers.

Contrary to ion implantation, the depth in which NV centers are created, is here com-

2. The nitrogen-vacancy center in diamond

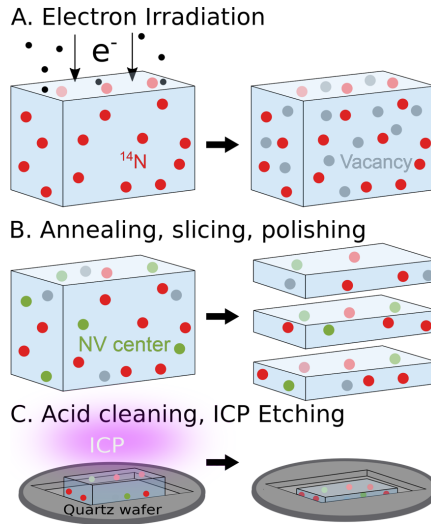


Figure 2.5: Creation of NV centers by electron irradiation. **A.** Vacancies are created by electron irradiation of a bulk diamond. **B.** By annealing at high temperatures, the vacancies become mobile and recombine with naturally abundant nitrogen. Afterwards, the sample is sliced and polished in order to obtain thin slabs. **C.** The sample is cleaned and etched down to the desired thickness by (inductively coupled plasma) reactive-ion etching. Taken from [112].

pletely random such that they are homogeneously distributed over the whole volume. This can be convenient, if the bulk diamond is sliced afterwards into multiple membranes such that all pieces contain a sufficient amount of NV centers, but it poses an additional challenge when integrating the membranes into cavities. A large fraction of NV centers in the membranes will not be suitable for cavity experiments, since they are not located at a field maximum in the standing wave.

An alternative method to create NV centers is by laser irradiation. This technique has the advantage over electron irradiation that the position of created NV centers is much more deterministic such that the sample can be tailored to the experiment. These NV centers have shown ZPL linewidths in the range of a few tens of MHz so far [118].

High temperature annealing All of the above techniques require some kind of irradiation or direct impact of particles on the diamond which always leads to damage in the lattice. More recently, it was shown that high temperature annealing (HTA) at 1700°C can lead to the creation of NV centers without the need of introducing nitrogen ions or vacancies into the sample [119]. While the natural density of NV centers in ultra pure diamond samples is extremely low, the nitrogen abundance is sufficient to create enough NV centers, if the process is efficient. Besides these electronic grade diamond samples, also general grade samples with a higher nitrogen abundance have been used

lately to yield NV centers with narrow linewidths [120]. HTA at 1700 °C thereby has several effects: at these high temperatures, not only defects in the lattice become mobile (which was already exploited in the other methods) [121], but especially near-surface defects can move into the bulk and recombine with naturally abundant nitrogen [122]. Furthermore, at 1500 °C, nitrogen in the diamond can slowly diffuse and hence become mobile as well. This makes the recombination process significantly easier and more likely. With this technique, NV centers with a Fourier-transform-limited linewidth of 24 MHz have been shown [119].

Not only does this method enable the creation of NV centers without damaging the diamond crystal, it is also viable for diamond membranes as a starting material. This would lower the additional lattice damage caused by slicing and polishing the diamond.

3. Light-matter interaction in optical microcavities

As described in the previous chapter, the nitrogen vacancy center suffers from its very low branching ratio into the ZPL. This, however, is not an exclusive property of NV centers, but of many other quantum emitters, too. The most popular way of increasing the fraction of photons emitted into the ZPL is by coupling the NV center emission to an optical cavity, thereby making use of the Purcell effect [38]. This does not only enhance the branching ratio of resonant emitters, it also increases the detection efficiency, as the major part of the emission is confined in a well-defined cavity mode that can be collected efficiently. In fact, any interaction between the light fields and matter can be enhanced using optical resonators, e.g. weak absorption or scattering of nanoparticles [71, 123]. Even though the Purcell effect was predicted over 70 years ago and all kinds of experiments have been realized showcasing the effect, it is a very attractive field of interest up to the present day.

In this chapter, I will briefly discuss the theoretical fundamentals of optical resonators, their interaction with quantum emitters and how they can be characterized.

3.1. Optical resonators

3.1.1. Plane-mirror resonator

In the following, I will summarize the most important properties of optical resonators. More detailed descriptions can be found in several textbooks [124, 125, 126], or in the theses of Matthias Mader [127] or Hanno Kaupp [128].

The simplest form of an optical resonator is a Fabry-Pérot interferometer which consists of two highly reflective, planar mirrors, separated by d . A plane wave that travels back and forth between the two mirrors accumulates a phase of

$$\phi = 2dk \tag{3.1.1}$$

where $k = \omega/c$ is the wave vector of the plane wave. For a mirror separation that is an integer multiple of half the wavelength λ , the reflected waves can interfere constructively,

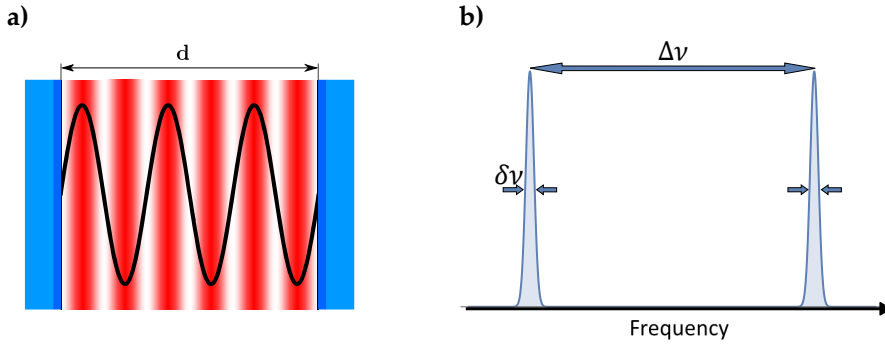


Figure 3.1: (a) The picture of a plane wave in an ideal optical resonator. The standing wave builds up between the mirrors when the resonance condition is fulfilled. Both the electric field (black curve) and the intensity distribution (red) then show nodes at the mirror surfaces. Taken from [127]. (b) Two consecutive resonances for a cavity with mirrors that are not perfectly reflective. The otherwise sharp lines become broadened to $\delta\nu$, their separation in units of frequency $\Delta\nu$ stays constant.

and a standing wave forms. A schematic picture is shown in fig. 3.1(a). This resonance condition can be expressed via the spacing between two consecutive frequencies that fulfil the previous condition, the so called free spectral range (FSR),

$$\Delta\nu = \frac{c}{2d}. \quad (3.1.2)$$

If the two mirrors were perfectly reflective, the resonances would consist of infinitely sharp lines. In real life scenarios, however, a cavity will never be completely lossless. The most dominant sources of loss are typically the mirror transmissions T_1 and T_2 , scattering and absorption losses at the mirror surfaces, and other lossy channels in the cavity. The losses that are not caused by mirror transmission can be summarized as \mathcal{L} . All these aspects effectively broaden the cavity resonance, given by the linewidth $\delta\nu$. The connection between the FSR and the linewidth is depicted in fig. 3.1(b). Since the total loss $\mathcal{L}_{\text{tot}} = T_1 + T_2 + \mathcal{L}$ is usually very small ($\mathcal{L}_{\text{tot}} \ll 1$), the line shape can be approximated by a Lorentzian. The linewidth in phase-units is then $\delta\phi = \mathcal{L}_{\text{tot}}/2$, or, in units of frequency,

$$\delta\nu = \frac{c}{2\pi d} \frac{\mathcal{L}_{\text{tot}}}{2} = \Delta\nu \frac{T_1 + T_2 + \mathcal{L}}{2\pi}. \quad (3.1.3)$$

The maximum transmission of the cavity is given by

$$T_{\text{max}} = \frac{4T_1T_2}{\mathcal{L}_{\text{tot}}^2}. \quad (3.1.4)$$

Eqs. 3.1.3 and 3.1.4 can now be used to describe the fraction of the transmitted intensity I_T and the incident intensity I_0 ,

$$\frac{I_T}{I_0} \approx T_{\max} \cdot \frac{(\delta\nu/2)^2}{(\delta\nu/2)^2 + (q\Delta\nu - \nu)^2}, \quad q \in \mathbb{N}. \quad (3.1.5)$$

Equation 3.1.3 shows that the cavity linewidth decreases reciprocally proportional as the mirror separation increases, since all other quantities are independent of the cavity length. A more favourable measure of quality for the resonator should be independent of the cavity geometry. If one puts the cavity linewidth in comparison with the FSR (which likewise scales with the cavity length), one yields the cavity finesse,

$$\mathcal{F} = \frac{\Delta\nu}{\delta\nu} = \frac{2\pi}{\mathcal{L}_{\text{tot}}}. \quad (3.1.6)$$

In experiments, the finesse is a very convenient figure of merit for the cavity performance, since it can easily be gauged via the expected cavity losses. Moreover, the finesse can be understood as the number of round-trips that light undergoes between the cavity mirrors, before it leaves the resonator, either via transmission through one of the mirrors, or other loss channels. It is therefore directly linked to the average time that a photon stays in the cavity, given by the photon ringdown time

$$\tau_{\text{rd}} = \frac{d}{\pi c} \mathcal{F}. \quad (3.1.7)$$

Consequently, the inverse of the ringdown time describes the cavity decay rate, i.e. the rate at which photons leave the cavity,

$$\kappa = 1/\tau_{\text{rd}} = 2\pi\delta\nu. \quad (3.1.8)$$

As we shall see later, this decay rate plays an important role when gauging how strong an emitter can couple to the cavity light field.

A further way to assess the performance of a cavity is by the quality factor Q which describes the amount of energy stored in the cavity compared to the energy that is lost per round trip via either of the loss channels. It is defined as

$$Q = \frac{\nu}{\delta\nu} = q \cdot \mathcal{F}. \quad (3.1.9)$$

Here, $q = d/(\lambda/2)$ is the longitudinal mode order for the resonance frequency ν . Note that the quality factor scales linearly with the mode order and hence with the cavity length. The highest achievable quality factors are therefore mostly realistic for macroscopic cavities with very highly reflective mirrors [129].

Intra-cavity power For a high finesse cavity, the intra-cavity power, i.e. the optical power at an anti-node of the standing wave, can be very high. It is described by

$$P_{\text{peak}} \approx 4T_1 \left(\frac{\mathcal{F}}{\pi} \right)^2 \cdot P_{\text{in}} \quad (3.1.10)$$

where T_1 is the transmissivity of the mirror through which the light is coupled in and P_{in} is the laser power of the incident beam. As the intra-cavity power scales with the finesse, it becomes relevant especially for high finesse cavities. Typical finesse values can be on the range of $10^4 - 10^5$. This finesse-dependence is particularly important for experiments in a cryogenic environment, as a very high intra-cavity power might lead to unwanted heating of the sample. Furthermore, it can affect the passive stability of a cavity in terms of mirror separation, since a change in incident laser power can lead to thermal drifts that have to be taken into account.

Outcoupling efficiency In quantum-optical experiments, a key aspect is the efficiency of the setup. In the case of optical cavities, there are two main questions: how efficient can photons be created in the cavity, and how likely is it that the photon will eventually reach the detector? The figure of merit for the latter is the outcoupling efficiency of the resonator, i.e. how large the fraction of photons is that is transmitted through one particular mirror, compared to the overall losses in the cavity (this implies also the transmission through the second cavity mirror, since measurements are usually performed only one-sided). This is described via the outcoupling efficiency η_c that is given by

$$\eta_c = \frac{T_2}{T_1 + T_2 + \mathcal{L}}. \quad (3.1.11)$$

In order to maximize the outcoupling efficiency, it is therefore beneficial to design a cavity with asymmetric mirror transmissions, i.e. $T_2 > T_1$ such that the transmission out of the cavity is dominated by T_2 .

3.1.2. Plane-concave resonator

Stability range So far, we only considered cavities consisting of two plane mirrors. In a real-life environment, however, these types of resonators are hard to realize since their angular alignment has to be perfect in order to avoid light leaking out of the cavity. Furthermore, diffraction and the mode divergence limits the cavity stability. For this reason, one or both of the mirrors are often replaced by a concave mirror. This allows for slightly angled beams, as they can also be reflected back into the resonator, leading to a more robust cavity. One can define a condition for a stable cavity by considering beams

that are reproducing themselves when being reflected in the resonator. The condition for a stable mode that self-reproduces is given by

$$0 \leq \left(1 - \frac{d}{ROC_1}\right) \left(1 - \frac{d}{ROC_2}\right) \leq 1. \quad (3.1.12)$$

Here ROC_1 and ROC_2 are the radii of curvature of the two mirrors. If only one of the two mirrors is concave, the respective value $ROC_{1,2}$ tends to infinity, and eq. 3.1.12 reduces to

$$0 \leq \left(1 - \frac{d}{ROC}\right) \leq 1. \quad (3.1.13)$$

That implies that the fundamental limit for the mirror separation of a plane-concave cavity is $d = ROC$. This limit plays an important role for the mirror design later in this thesis.

Gaussian beams While the cavity mode could be described by a plane wave for a plane-mirror resonator, this is not possible when one (or both) of the mirrors are curved. As the electromagnetic wave inside the resonator is now spatially limited, it can be described by a Gaussian beam which is the solution for the paraxial Helmholtz equation. The name thereby follows the fact that its lateral intensity distribution is described by a Gaussian function.

The derivation of Gaussian beams is skipped here, but the most important parameters are introduced below and illustrated in fig. 3.2:

- **Beam waist** $2w_0$:

The beam waist is the minimal $1/e^2$ diameter of the intensity distribution³ at the beam focus ($z = 0$). For a plane-concave resonator, it is located at the plane mirror surface.

- **Rayleigh length** z_0 :

$$z_0 = \frac{\pi w_0^2}{\lambda} \quad (3.1.14)$$

The Rayleigh length is the distance from the beam focus at which the beam radius has increased to $\sqrt{2}w_0$. Typically, $z \ll z_0$ is furthermore used to define the region where the Gaussian wave has a very low mode curvature such that it can be treated as a plane wave.

³ The beam waist is defined either as the beam **radius** or **diameter**, depending on the source. The mathematical description thereby stays the same ($w_0 \hat{=}$ beam radius), but the wording might differ.

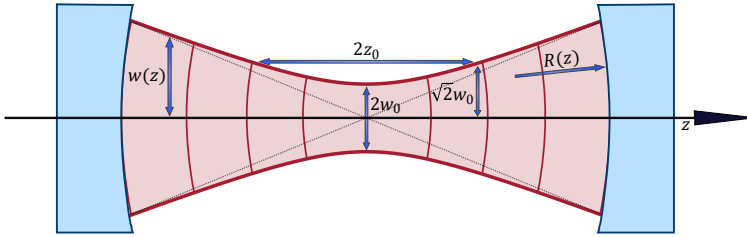


Figure 3.2: Schematic drawing of a Gaussian wave inside a cavity. The sketch highlights the characteristic values of a Gaussian beam, the beam waist ($2w_0$), Rayleigh length (z_0), the beam radius at position z ($w(z)$) and the radius of curvature of the wavefront ($R(z)$).

- **Beam radius $w(z)$:**

$$w(z) = w_0 \sqrt{1 + \left(\frac{z}{z_0}\right)^2} \quad (3.1.15)$$

This describes the $1/e^2$ radius at the position z with respect to the beam waist.

- **Gouy phase shift θ :**

$$\theta = \arctan\left(\frac{z}{z_0}\right) \quad (3.1.16)$$

A Gaussian beam acquires a phase shift while propagating that differs from that of a plane wave. The points of equal phase are thereby not on a plane, but rather show a curved wavefront.

- **Beam radius of curvature $R(z)$:**

$$R(z) = z \left(1 + \left(\frac{z}{z_0}\right)^2\right) \quad (3.1.17)$$

The radius of curvature (ROC) describes the curved wavefront of a Gaussian beam. It approaches infinity for $z \rightarrow 0$, i.e. the wave front is plane. For the far field, the radius becomes $R(z) \approx z$. The smallest radius of curvature (i.e. the strongest curvature) appears at the Rayleigh length z_0 .

Resonance condition As Gaussian modes are solutions for the Helmholtz equation, they can be used to express a resonance condition for a resonator with spherical mirrors (or, as in our case one spherical and one plane mirror). The wavefront curvature thereby has to match the ROC of the curved mirrors at the mirror surface. This already defines all other properties of the Gaussian beam. Furthermore, the wavefront has to accumulate

an integer multiple of 2π per round trip. This leads to the condition for the resonance frequencies of the resonator, taking into account the additional Gouy phase shift θ ,

$$\nu_q = \Delta\nu \left(q + \frac{\Delta\theta}{\pi} \right) \quad (3.1.18)$$

with $\Delta\theta = [\theta(z = d) - \theta(z = 0)]$.

Hermite-Gaussian modes Additionally to the Gaussian modes, Hermite-Gaussian modes are solutions of the Helmholtz equation and therefore eigenmodes of a resonator with spherical mirrors. They are defined by the addition of Hermite polynomials to the purely Gaussian intensity profile. If one defines the electric field distribution in Cartesian coordinates, it is described via

$$\begin{aligned} \mathcal{E}_{mn}(x, y, z) = & \mathcal{E}_0 \frac{w_0}{w(z)} \mathcal{H}_m \frac{\sqrt{2}x}{w(z)} \mathcal{H}_n \frac{\sqrt{2}y}{w(z)} \times \\ & \exp \left\{ - \left(\frac{x^2 + y^2}{w(z)} \right)^2 \right\} \exp \left\{ -ik \frac{x^2 + y^2}{2R(z)} \right\} \times \\ & \exp \{ -i(kz - (m + n + 1)\theta(z)) \}. \end{aligned} \quad (3.1.19)$$

Here, \mathcal{E}_0 is the electric field amplitude, \mathcal{H}_m and \mathcal{H}_n are the respective Hermite polynomials of order m and n . The new resonance condition implying the higher order transverse electromagnetic (TEM) modes then becomes

$$\nu_{(q,m,n)} = \Delta\nu \left(q + (m + n + 1) \frac{\Delta\theta}{\pi} \right). \quad (3.1.20)$$

From eq. 3.1.20, we see that the shift of the resonance frequency of any higher order TEM mode with respect to the fundamental Gaussian mode only depends on the sum of its indices. This leads to a degeneracy of all higher order TEM modes of the same *family*. This, however, is only the case for perfectly spherical and hence symmetrical mirrors. In experiments such as the ones presented in this thesis, this is generally not the case. Especially for the later introduced fiber mirrors, the mirror profile usually shows a slight ellipticity, leading to different radii of curvature $ROC_{(x,y)}$ for the respective Cartesian coordinates. This asymmetry leads to different boundary conditions for the cavity eigenmodes and thus to a difference in the Gouy phase shift. This lifts the degeneracy and the (m, n) modes become distinguishable from the (n, m) modes. This principle is shown in fig. 3.3 which shows real cavity transmission signals measured by Matthias Mader [127].

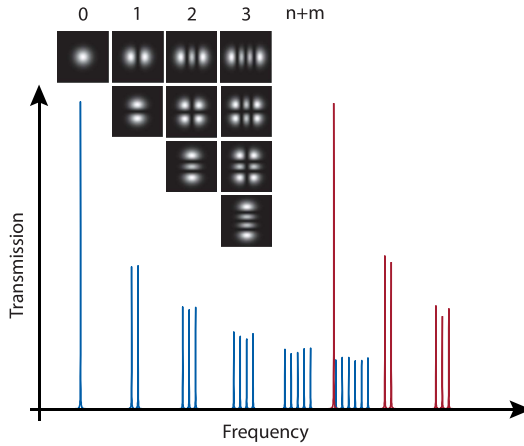


Figure 3.3: Transmitted intensity through the cavity as a function of frequency. The plot shows two consecutive longitudinal mode orders (blue and red), together with their respective higher order TEM modes. Their transverse intensity profile is shown above, showcasing the lifted degeneracy for the different (m, n) configurations. Adapted from [127] and [72].

3.2. Fundamentals of light-matter interaction

Thus far, we discussed the properties of optical cavities that are empty, i.e. neither an alternating refractive index nor a particle or emitter inside the cavity have been considered. While the introduction of a refractive medium changes the optical properties of the resonator (which will be discussed in chapter 4), the implementation of a single quantum emitter or an ensemble opens up the field of cavity quantum electrodynamics (cQED). In the following, I will discuss the basic principles of light-matter interaction inside of an optical cavity and present the various regimes that this interaction can be considered in. I thereby follow the description by M. Fox [126] and A. Meldrum [130], as summarized in the theses of J. Benedikter's [72] and H. Kaupp [128]. The hereafter defined physical measures are visualized in fig. 3.4.

Let us first consider a single emitter that is placed inside the cavity. The cavity light field can be described as a damped harmonic oscillator where the damping constant is its decay rate $\kappa = 2\pi\delta\nu$. The emitter is "damped" by its spontaneous emission rate γ . A classification for the interaction between the cavity light field and the emitter is given by the cavity-emitter coupling strength,

$$g_0 = \sqrt{\frac{\pi\mu_{12}^2\nu}{\epsilon_0\hbar V_m}}. \quad (3.2.1)$$

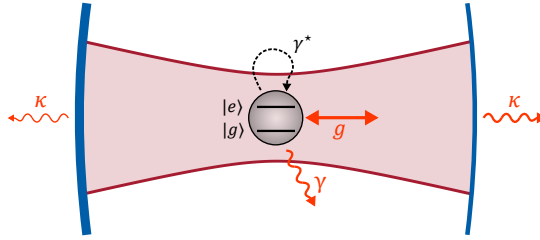


Figure 3.4: Schematic depiction of the relevant cavity parameters for a single two-level system that is coupled to a cavity with an asymmetric transmission profile. Adapted from [131].

Here, ν is the resonance frequency of the cavity mode, μ_{12} is the transition dipole moment from the electric ground state $|g\rangle$ to the excited state $|e\rangle$, given by $\mu_{12} = -e \langle g|x|e\rangle$. V_m denotes the mode volume of the cavity which is given by

$$V_m = \frac{\pi \omega_0^2 d}{4}. \quad (3.2.2)$$

If a number of N emitters couple to the cavity mode, the cavity-emitter coupling strength is modified to $g = \sqrt{N}g_0$. Comparing this coupling strength to the damping parameters lets us identify how strong the interaction between the cavity light field and the emitter is expected to be.

The spontaneous emission rate γ describes the lifetime of the excited state as $T_1 = 1/\gamma$. In experiments, this non-resonant decay rate is not the only limiting factor for the spectral linewidth of an emitter. Especially in solid state environments like diamond, other perturbations like charge fluctuations or lattice vibrations can effectively damp and dephase the oscillator further. They are described via the pure dephasing rate γ^* . For an emitter which is not coupled to the cavity mode, the lineshape would remain Lorentzian with the linewidth given by $\gamma + \gamma^*$.

Here, the additional relaxation term γ^* leads to a total dephasing time of [131, 132, 133]

$$T_2 = \frac{1}{2/T_1 + 1/T_2^*}. \quad (3.2.3)$$

$T_2^* = 2/\gamma^*$ thereby denotes the pure dephasing time of the emitter.

We now have the coupling strength g_0 that is counteracted by all the above mentioned dephasing and relaxation terms. We can thus categorize two different cases:

- **Strong coupling:** $2g \gg \gamma + \gamma^* + \kappa$

Being in the strong coupling regime means that the coupling of the emitter to the cavity is much stronger than the dephasing and cavity decay rates. Photons could be trapped in the cavity long enough to be reabsorbed by the emitter, leading to vacuum Rabi oscillations.

- **Weak coupling:** $2g \ll \gamma + \gamma^* + \kappa$

Contrary to the strong coupling regime, the system is now dominated by

dissipation. The limiting factor can be either transmission out of the cavity or short emitter life- and coherence times. Depending on the lifetime of both the emitter and the cavity, the weak coupling regime can be further specified into three cases:

- **Bad cavity regime:** $\delta\nu_{\text{em}} \ll \delta\nu_{\text{c}}$
Here, the limiting factor is the fast decay rate of photons that are in the cavity.
- **Bad emitter regime:** $\delta\nu_{\text{em}} \gg \delta\nu_{\text{c}}$
In this case, the cavity linewidth is much more narrow than the broad emitter line.
- **Comparable linewidths:** $\delta\nu_{\text{em}} \approx \delta\nu_{\text{c}}$
This is the special case which has to be considered when both the emitter and the cavity have broad lines. Then, the coupling strength is much smaller than the dephasing factors, but neither the cavity or emitter can be neglected.

All of these special cases shall be elaborated further in the following.

3.2.1. Strong coupling

As mentioned above, in the strong coupling regime, the dephasing rates are negligible compared to the cavity-emitter coupling. This case is described by the Jaynes-Cummings (JC) model [134]:

$$\begin{aligned} H &= H_e + H_{\text{cav}} + H_{\text{int}} = \hbar\omega_e\sigma^+\sigma^- + \hbar\omega_c a^\dagger a + \hbar g \hat{\mathbf{E}} \mathbf{d} \\ &= \hbar\omega_e\sigma^+\sigma^- + \hbar\omega_c a^\dagger a + \hbar g_0 \left(a^\dagger \sigma^- + \sigma^+ a \right) \end{aligned} \quad (3.2.4)$$

This Hamiltonian consists of three parts: the two-level system of the quantum emitter H_e , the harmonic oscillator of the cavity H_{cav} , and the interaction Hamiltonian H_{int} . The Hamiltonian of the emitter is given by the energy difference $\hbar\omega_{\text{em}}$ between its ground state $|g\rangle$ and the excited state $|e\rangle$. $\sigma^+ = |e\rangle\langle g|$ and $\sigma^- = |g\rangle\langle e|$ are the creation and annihilation operators, respectively.

Similarly, H_{cav} depends on the angular resonance frequency ω_c and the photon creation and annihilation operators, a^\dagger and a . The Hamiltonian therefore describes the presence of one single photon in the cavity and can be scaled up according to the Tavis-Cummings model via the photon number $n = \langle a^\dagger a \rangle$ [135, 136].

Since H_e and H_{cav} are independent from each other, the interaction term is introduced to represent the fact that the emitter is excited by the annihilation of a single photon, and the emission of a single photon occurs when the emitter relaxes back into the ground state. Note, that this is hence the only term that scales with the coupling strength g_0 .

This coupling leads to a continuous exchange of energy between the emitter and the cavity light field in form of Rabi oscillations, i.e. the emitter-cavity system oscillates between the states $|e, 0\rangle$ and $|g, 1\rangle$. The angular frequency of this oscillation is given by the Rabi frequency $\Omega_0 = 2g_0$, and the eigenenergies of the previously degenerate states split up and form the new eigenstates, also called dressed states. They are given by

$$|+, n\rangle = \frac{|e, n\rangle + |g, n+1\rangle}{\sqrt{2}}, \quad |-, n\rangle = \frac{|e, n\rangle - |g, n+1\rangle}{\sqrt{2}} \quad (3.2.5)$$

and are separated by the energy corresponding to the Rabi frequency, $\sqrt{n}\hbar\Omega_0$. This results in the new eigenenergies

$$E_n^\pm = (n + 1/2) \hbar\omega \pm \sqrt{n}\hbar\frac{\Omega_0}{2}, \quad (3.2.6)$$

assuming that the cavity is exactly resonant with the transition of the emitter. In the optical domain, strong coupling was first observed in the late 1980s [137, 138].

3.2.2. Weak coupling and the Purcell effect

As in the present case of NV centers, which suffer from strong dephasing, or if the photon losses in the cavity are large, the cavity-emitter coupling strength cannot exceed the losses anymore. Thus, a photon emitted by the quantum system is now likely to leave the cavity quickly. This incoherent process is now comparable to the emission in free space, where an emitted photon is lost from the system. Although, the presence of an optical cavity that has the same resonance frequency as the emitter leads to a modified density of states. We shall therefore discuss first the spontaneous emission in free space, and introduce the cavity and its consequences afterwards.

Spontaneous emission in free space The density of states (DoS) ρ for an emitter in free space is the figure of merit for its transition rate γ_0 at a given transition frequency. The spontaneous emission rate can be derived using perturbation theory which considers a fluctuating vacuum field \mathcal{E}_{vac} that causes the excited emitter to emit a photon by coupling to its dipole moment $\mathbf{d} = -e\mathbf{r}$. This interaction can be described via the transition matrix element $M_{12} = \langle \mathbf{d} \cdot \mathcal{E}_{\text{vac}} \rangle$. Perturbation theory yields Fermi's golden rule [139]:

$$\gamma_0 = \frac{2\pi}{\hbar} M_{12}^2 \rho(\omega). \quad (3.2.7)$$

The vacuum electric field \mathcal{E}_{vac} can be expressed as

$$\mathcal{E}_{\text{vac}} = \sqrt{\frac{\hbar\omega}{2\epsilon_0 V_0}} \quad (3.2.8)$$

where V_0 is the mode volume of the vacuum field. Using this expression, the transition matrix element can then be converted to

$$M_{12} = \frac{1}{3} \mu_{12}^2 \mathcal{E}_{\text{vac}}^2 = \frac{\mu_{12}^2 \hbar \omega}{6 \epsilon_0 V_0}. \quad (3.2.9)$$

Note that we added a factor $1/3$ because we have to average over all possible dipole orientations in free space.

For a photon mode in free space, the DoS is given by

$$\rho(\omega) = \frac{\omega^2 V_0}{\pi^2 c^3}. \quad (3.2.10)$$

With these two expressions, Fermi's golden rule simplifies to

$$\gamma_0 \equiv \frac{1}{\tau_r} = \frac{\mu_{12}^2 \omega^3}{3\pi \epsilon_0 \hbar c^3} \quad (3.2.11)$$

where τ_r is the radiative lifetime of the emitter.

Spontaneous emission in a single-mode cavity - the Purcell effect The problem of a single two-level system that is weakly coupled to a resonant single-mode cavity was first considered by E. M. Purcell in 1946 [38] who hence is the name giver for the Purcell effect. In order to express this case mathematically, we shall adapt Fermi's golden rule for the case of a single emitter in a cavity mode.

To treat also emitters with more than two levels or broad emission spectra, the formula has to be extended by the density of states of the emitter $\Lambda(\omega)$, which yields

$$\gamma_0 = \frac{2\pi}{\hbar^2} \int_0^\infty M_{12}^2(\omega) \rho(\omega) \Lambda(\omega) d\omega. \quad (3.2.12)$$

This expression can be categorized into the three previously mentioned cases [130]:

1. The spectrum of the quantum emitter is much more narrow than the cavity linewidth. Then, the DoS of the emitter can be approximated by a delta function, i.e. $\Lambda(\omega) = \delta(\omega - \omega_0)$. Since consequently, the cavity spectrum is much broader than the emitter linewidth, this case is called *bad cavity regime*.
2. The cavity linewidth is much more narrow than the spectrum of the emitter. This is the opposite of the prior case, hence, the delta function can now be applied to the cavity line: $\rho(\omega) = \delta(\omega - \omega_c)$. This case is analogously called *bad emitter regime*.
3. Both linewidths are comparable such that neither can be omitted. In this case, the integral in eq. 3.2.12 cannot be simplified and has to be solved.

All three of these case shall be described in the following.

Bad cavity regime Contrary to the consideration in free space, the density of states for the electric field is now given by the cavity mode which has a Lorentzian line shape:

$$\rho(\omega) = \frac{1}{\pi} \frac{\delta\omega_c/2}{(\omega - \omega_c)^2 + (\delta\omega_c/2)^2}. \quad (3.2.13)$$

As the cavity linewidth is linked to the cavity decay rate by $\delta\omega_c = 2\pi\delta\nu_c = \kappa$, eq. 3.2.13 can be expressed via

$$\rho(\omega_0) = \frac{2}{\pi\kappa} \frac{(\kappa/2)^2}{\Delta^2 + (\kappa/2)^2} \quad (3.2.14)$$

where ω_0 is the transition frequency of the emitter and $\Delta = \omega_0 - \omega_c$ is the detuning of the cavity resonance with respect to this transition. This furthermore satisfies the condition that only one cavity mode is resonant with the emitter, i.e. $\int \rho(\omega)d\omega = 1$. When the cavity is exactly resonant with the transition frequency of the emitter, Δ vanishes, and eq. 3.2.14 becomes

$$\rho(\omega_0) = \frac{2}{\pi\kappa} = \frac{2Q}{\pi\omega_0}. \quad (3.2.15)$$

The transition matrix element is given similarly to the free space situation by

$$M_{12}^2 = \xi^2 \mu_{12}^2 \mathcal{E}_{\text{vac}}^2 = \xi^2 \frac{\mu_{12}^2 \hbar\omega}{2\epsilon_0 V_m}. \quad (3.2.16)$$

The dipole orientation factor ξ^2 , which was previously averaged to 1/3 for an emitter in free space, is generally given by

$$\xi = \frac{|\mathbf{d} \cdot \mathcal{E}|}{|\mathbf{d}||\mathcal{E}|}. \quad (3.2.17)$$

This factor can become especially important in the case of the NV center since the NV axis can be orientated in four different directions. Depending on the crystal plane that the diamond was cut in, ξ has to be taken into account. Eqs. 3.2.14 and 3.2.16 can now be used to find the complete description of Fermi's golden rule in the bad cavity regime:

$$\gamma_c = \frac{2\mu_{12}^2}{\hbar\epsilon_0} \frac{Q}{V_m} \xi^2 \frac{(\kappa/2)^2}{\Delta^2 + (\kappa/2)^2}. \quad (3.2.18)$$

The altered transition rate in the cavity is a manifestation of the Purcell effect and can be quantified by comparing γ_c to the transition rate in free space, yielding the Purcell factor

$$C = \frac{\gamma_c}{\gamma_0} = \frac{3}{4\pi^2} \left(\frac{\lambda}{n}\right)^3 \frac{Q}{V_m} \xi^2 \frac{(\kappa/2)^2}{\Delta^2 + (\kappa/2)^2}. \quad (3.2.19)$$

Here, c/ω was substituted by $(\lambda/n)/2\pi$ where n is the refractive index of the medium inside the cavity. A Purcell factor of $C > 1$ therefore means that the spontaneous emission rate in the cavity is greater compared to the one in free space.

If we again consider a cavity whose resonance frequency exactly matches the transition

frequency of the emitter, the last part of eq. 3.2.19 becomes 1. If we furthermore assume that the dipole of the emitter is aligned with the electric field such that we can omit ξ , we can establish the ideal Purcell factor whose formula reads as

$$C_0 = \frac{3}{4\pi^2} \left(\frac{\lambda}{n}\right)^3 \frac{Q}{V_m}. \quad (3.2.20)$$

If one wants to maximize the transition rate in the cavity, a high Purcell factor is desired. Hence, the cavity should combine a high quality factor with a small mode volume. However, these two quantities are not independent from each other, since Q as well as V_m increases as the cavity length becomes larger. One will therefore always face a trade-off between reaching high quality factors and designing the cavity as small as possible.

Another way to express the Purcell factor is by replacing the mode volume by $V_m = (\pi w_0^2 d)/4$ and the quality factor by $Q = 2d/\lambda\mathcal{F}$, such that one obtains the Purcell factor in dependence of the cavity finesse and the mode waist,

$$C_0 = \frac{6}{\pi^3} \left(\frac{\lambda}{n}\right)^2 \frac{\mathcal{F}}{w_0^2}. \quad (3.2.21)$$

Alternatively, one can define the Purcell factor using the different rates of the cavity-emitter system:

$$C_0 = \frac{4g_0^2}{\kappa\gamma_0}. \quad (3.2.22)$$

This again shows that the emitter mainly profits from a high coupling strength while minimizing losses through any channel.

Bad emitter regime Opposed to the prior case, a commonly arising situation is that the emitter linewidth is very broad while the cavity resonance is overlapping only with a small fraction of the spectrum. As is the case with NV centers, especially solid state emitters can suffer heavily from broadened linewidths. From this follows that $\gamma + \gamma^* \gg \kappa \gg 2g_0$, meaning that the losses in the system are dominated by dephasing of the emitter.

Then, the DoS of the emitter and the cavity swap roles, i.e. the cavity resonance can be considered a delta function $\rho(\omega) = \delta(\omega - \omega_c)$, while the DoS of the emitter with a FWHM of $\delta\omega_0$ is now given by a Lorentzian:

$$\Lambda(\omega) = \frac{1}{\pi} \frac{\delta\omega_0/2}{(\omega - \omega_0)^2 + (\delta\omega_0/2)^2}. \quad (3.2.23)$$

The derivation of the transition rate is analogous to the bad cavity regime, but the quality factor of the cavity has to be replaced by the quality factor of the emitter, given by

$$Q_c = \frac{\omega_0}{\delta\omega_0} = \frac{\omega_0}{\gamma + \gamma^*}. \quad (3.2.24)$$

The transition rate in the cavity is thus

$$\gamma_c = \frac{2\mu_{12}^2}{\hbar\epsilon_0} \frac{Q_e}{V_m} \xi^2 \frac{(\delta\omega_0/2)^2}{\Delta^2 + (\delta\omega_0/2)^2} \quad (3.2.25)$$

which leads to the Purcell factor,

$$C_0 = \frac{3}{4\pi^2} \left(\frac{\lambda}{n}\right)^3 \frac{Q_e}{V_m}. \quad (3.2.26)$$

Interestingly, the Purcell factor for a given wavelength now only depends on the linewidth of the emission spectrum and the cavity mode volume. Consequently, the cavity geometry is of much more importance in the bad emitter regime, compared to the bad cavity regime.

Cavity and emitter with comparable linewidths When the optical transition of the emitter and the cavity have a comparable linewidth, neither of the two can be neglected, meaning that the integral in eq. 3.2.12 has to be solved explicitly. The densities of states $\rho(\omega)$ and $\Lambda(\omega)$ are now both described by Lorentzian's, and the transition rate is

$$\gamma_c(\omega_0, \omega_c) = \frac{\xi^2 \pi \mu_{12}^2}{\epsilon_0 \hbar V_m} \int_0^\infty \frac{1}{\pi^2} \frac{\delta\omega_0/2}{(\omega - \omega_0)^2 + (\delta\omega_0/2)^2} \omega_0 \frac{\delta\omega_c/2}{(\omega - \omega_c)^2 + (\delta\omega_c/2)^2} d\omega. \quad (3.2.27)$$

The solution path for this equation is given in [130] and ultimately yields

$$\gamma_c \approx \frac{2\mu_{12}^2}{\hbar\epsilon_0 V_m} \xi^2 \frac{\omega_0 \delta\omega_c/2 + \omega_c \delta\omega_0/2}{\Delta^2 + (\delta\omega_c/2 + \delta\omega_0/2)^2} \quad (3.2.28)$$

as an approximate solution. Since this is the general description, eq. 3.2.28 includes the previous cases, if one sets $\delta\omega_c = 0$ or $\delta\omega_0 = 0$, respectively.

Yet again, we assume that the cavity is on resonance with the emitter, i.e. $\omega_c = \omega_0$ and that the emitter's dipole is aligned with the electric field axis. Furthermore, by defining an effective quality factor that includes both the emitter and the cavity resonance as

$$Q_{\text{eff}} = \left(\frac{1}{Q_{\text{cav}}} + \frac{1}{Q_e} \right)^{-1}, \quad (3.2.29)$$

we obtain the simplified formula for the transition rate:

$$\gamma_c(\omega_c = \omega_0) = \frac{2}{\hbar\epsilon_0} \mu_{12}^2 \frac{Q_{\text{eff}}}{V_m}. \quad (3.2.30)$$

The (effective) Purcell factor for the general case is then

$$C_{\text{eff}} = \frac{3}{4\pi^2} \left(\frac{\lambda}{n}\right)^3 \frac{Q_{\text{eff}}}{V_m}. \quad (3.2.31)$$

Alternatively, the Purcell factor can be expressed via the cavity parameters. The figure of merit here is the coupling rate of the emitter and the cavity, given by [133]

$$R = \frac{4g_0^2}{\kappa + \gamma + \gamma^*} \frac{1}{1 + \left(\frac{2\Delta}{\kappa + \gamma + \gamma^*}\right)^2}. \quad (3.2.32)$$

The last factor (on the right) describes the effect of a cavity detuning Δ with respect to the emitter frequency which vanishes when the resonances are degenerate. The Purcell factor in this picture is then defined as

$$C = \frac{R}{\gamma}. \quad (3.2.33)$$

Other consequences of the Purcell effect Experimentally, it is often more convenient to determine the Purcell factor via emission rates, as these are the quantities that can easily be measured. The total emission rate γ_{tot} consists of two contributions: the emission rate into the cavity mode γ_c and the emission rate into free space γ_{fs} . The emission into free space itself is not altered by the cavity, but the angle into which the emission can happen is effectively subtended by the geometrical presence of the cavity mirrors, which shields an angle of $\Delta\Omega < 4\pi$ [140]. The emission rate is therefore

$$\gamma_{\text{fs}} = \gamma_0 \left(1 - \frac{3\Delta\Omega}{8\pi}\right) \quad (3.2.34)$$

for a dipole orientation perpendicular to the optical axis. For the total emission rate, we thus obtain

$$\gamma_{\text{tot}} = \gamma_{\text{fs}} + \gamma_c = \gamma_0 \left(1 - \frac{3\Delta\Omega}{8\pi} + C\right). \quad (3.2.35)$$

The shielded angle of course strongly depends on the geometry of the mirrors, i.e. their diameter and their distance from the emitter. In the case of fiber-based microcavities as used in this thesis, this angle can become relevant for short cavity lengths, but is omitted for now. The total emission rate can then be approximated by

$$\gamma_{\text{tot}} \approx \gamma_0(C + 1). \quad (3.2.36)$$

Usually, the photons that are emitted into free space cannot be collected such that the emission rates are not always a sufficient way to gauge the Purcell factor. A more suitable measure can be the lifetime-reduction of the excited state that comes along with the increased emission rate, such that

$$\frac{\tau_0}{\tau_c} = \frac{\gamma_{\text{tot}}}{\gamma_0} \approx C + 1. \quad (3.2.37)$$

From this it follows that

$$\frac{C}{C+1} = \frac{C\gamma_0}{\gamma_{\text{tot}}} = \frac{\gamma_c}{\gamma_c + \gamma_0} \equiv \beta_0. \quad (3.2.38)$$

β_0 is the fraction of the photons that is emitted into the cavity mode. Notably, even for small Purcell factors, β_0 approaches unity and therefore means an almost exclusive emission into the cavity mode. This highlights one major advantage of cQED compared to measurements in free space, as a cavity mode is easily collectable.

When we defined the Purcell factor in eq. 3.2.19, we considered only one single transition that leads to the emission of photons. However, many emitters have multiple states that they can decay into, leading to a fraction of unwanted frequencies, described by γ' . This is expressed by the branching ratio of a certain transition, which is defined as the ratio of emitted photons with the desired frequency and the overall emitted photons:

$$\zeta = \frac{\gamma_0}{\gamma_0 + \gamma'} = \frac{\gamma_0}{\gamma_{\text{all}}}. \quad (3.2.39)$$

From that, one obtains the effective emission rate into the cavity mode

$$\gamma_c = C\zeta\gamma_{\text{all}} \equiv C_{\text{eff}}\gamma_{\text{all}} \quad (3.2.40)$$

where we define $C_{\text{eff}} = \zeta C$ as the effective Purcell factor. Subsequently, the definition via the lifetime-reduction for an emitter with a reduced branching ratio changes to

$$\frac{\tau_0}{\tau_c} = \zeta C + 1 = C_{\text{eff}} + 1. \quad (3.2.41)$$

Moreover, since the emission rate into the transition that is resonant with the cavity gets enhanced while the other transitions stay unaffected, the branching ratio of an emitter inside a cavity is also modified. It can be derived starting with eq. 3.2.39 while using the cavity-enhanced emission rate,

$$\zeta_c = \frac{(C+1)\gamma_0}{(C+1)\gamma_0 + \gamma'} = \frac{C+1}{C + \frac{\gamma_0 + \gamma'}{\gamma_0}} = \frac{C+1}{C+1/\zeta}. \quad (3.2.42)$$

Combining the modified branching ratio with the fraction of photons emitted into the cavity mode lets us describe the overall fraction of photons that are emitted with the desired frequency, into the cavity mode as

$$\beta = \beta_0 \cdot \zeta_c = \frac{C}{C+1} \frac{C+1}{C+1/\zeta} = \frac{C_{\text{eff}}}{C_{\text{eff}} + 1}. \quad (3.2.43)$$

In an experiment, one would mainly be interested in the probability to detect a photon of the desired wavelength on the detector after the emitter has been excited. In this case, β has to be extended by the outcoupling efficiency of the cavity (eq. 3.1.11), the quantum efficiency of the detectors and other sources of loss, like scattering or absorption along the beam path.

Additionally to the reduction of the branching ratio due to unwanted transitions, the emitter can decay completely non-radiatively, e.g. via phonon-assisted decay like the NV center's shelving states. There, these transitions can amount to up to 30 % for shallowly implanted NV centers [141]. The fraction of the radiative decay rate compared to the total decay rate γ is described by the quantum efficiency (QE), given by [142]

$$QE = \frac{\gamma_r}{\gamma} = \frac{\gamma_r}{\gamma_r + \gamma_{nr}}, \quad (3.2.44)$$

where γ_r and γ_{nr} are the radiative and non-radiative decay rates, respectively. Since only the radiative decay of an emitter is enhanced by the Purcell effect, the lifetime reduction is affected by the quantum efficiency via

$$\frac{\tau_0}{\tau_c} = \frac{(C+1)\gamma_r + \gamma_{nr}}{\gamma} = \frac{(C+1)QE\gamma + \gamma - QE\gamma}{\gamma} = CQE + 1. \quad (3.2.45)$$

Furthermore, the enhanced radiative decay rate in the cavity leads to a modified QE as well:

$$QE_c = \frac{(C+1)\gamma_r}{(C+1)\gamma_r + \gamma_{nr}} = \frac{C+1}{C+1/QE}. \quad (3.2.46)$$

3.3. Collective cavity-emitter coupling and superfluorescence

So far, we confined ourselves with considering only a single emitter that is coupled to the cavity mode. In the case of the strong coupling regime, the interaction is described by the Jaynes-Cummings model, as presented in sec. 3.2.1. However, if we replace the single emitter by an ensemble of N identical two-level systems, the Hamiltonian in eq. 3.2.4 has to be adapted. In a free space scenario, this is described by the Dicke model [52] which translates to the Tavis-Cummings (TC) model when a cavity is considered and the rotating-wave approximation is applied [135, 136]. For the description, I shall follow the publications of B. Garraway [143], Cong et al. [144] and the famous publication of Gross and Haroche [145].

3.3.1. Multiple emitters in a cavity and the Dicke formalism

Tavis-Cummings model In the TC model, the excitation and annihilation operators are adapted to an ensemble by the collective operators

$$J_+ = \sum_{n=1}^N \sigma_n^+ \quad , \quad J_- = \sum_{n=1}^N \sigma_n^- \quad \text{and} \quad J_z = \sum_{n=1}^N J_{z,n}. \quad (3.3.1)$$

Here, N is the number of two-level systems in the ensemble, $\sigma_n^+ = |e_n\rangle \langle g_n|$ and $\sigma_n^- = |g_n\rangle \langle e_n|$ are the excitation and annihilation operators for the n -th emitter, respectively. $J_{z,n} = \frac{1}{2}(|e_n\rangle \langle e_n| - |g_n\rangle \langle g_n|)$ makes $J_{+,-,z}$ a complete set of spin-1/2 operators. The resulting Hamiltonian can then be derived analogously to the JC-Hamiltonian and reads as

$$H_{\text{TC}} = \hbar\omega_e J_z + \hbar\omega_{\text{cav}} a^\dagger a + \frac{G}{\sqrt{N}} (a^\dagger J_- + a J_+) \quad (3.3.2)$$

where $G \equiv \omega_e \mu_{12} (2\pi \hbar \omega_{\text{cav}})^{1/2} (\rho_e)^{1/2}$ is the collective coupling constant and $\rho_e = N/V_m$ describes the spatial density of emitters.

Interpretation of the Dicke model Let us first consider the case where an ensemble of N emitters are coupled to a common radiation field in free space. Such a system can be treated as an ensemble of N quasi-spins in $|JM\rangle$ states, where each spin is defined by its eigenstates $|e\rangle$ and $|g\rangle$. Analogous to a spin-1/2 state, there are $N+1$ of such eigenstates with $J = N/2, \dots, J = -N/2$.

The $|JM\rangle$ state in which $J+M$ emitters are in the upper level $|e\rangle$ and $J-M$ in the lower level $|g\rangle$ is then obtained by repeatedly applying the collective annihilation operator J_- on the initial state, where all emitters are excited:

$$|JM\rangle = \sqrt{\frac{(J+M)!}{N!(J-M)!}} \cdot (J_-)^{(J-M)} |e, e, \dots, e\rangle \quad (3.3.3)$$

with $-J \leq M \leq J$.

In order to allow the prior expression, several assumptions have to be made:

1. All emitters have the same transition frequency and coupling strength.
2. The emitters are confined in a volume that is small compared to the transition wavelength λ .
3. The first two assumptions imply that the coupling to the cavity field is symmetrical under exchange for any two emitters in the ensemble.
4. The deexcitation of an emitter is only due to its coupling to the radiation field, i.e. all other decoupling mechanisms like phonon-mediated relaxation are omitted.

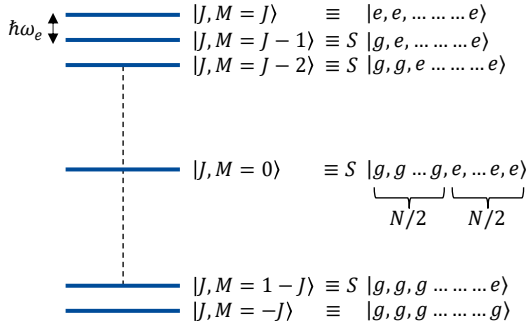


Figure 3.5: Dicke "ladder" of $N + 1$ symmetrical states $|JM\rangle$, respectively separated by $\hbar\omega_0$. The system starts in the fully excited state $|J, M = J\rangle$ and then decays down the ladder until all emitters are in their ground state. $M = 0$ thereby describes the state where half of the emitters are in the excited and in the ground state, respectively. S denotes the symmetrization operator of the system. Adapted from [145].

The evolution of such a system can be compared to the spontaneous emission of an angular momentum J . The different $|JM\rangle$ states form a "ladder" of $2J + 1 = N + 1$ equidistant energy levels which the system cascades down from while exchanging energy with the light field. This principle is depicted schematically in fig. 3.5.

Emission rate The second assumption from above lets us assume that the N emitters behave like a point-like dipole that consists of the sum of the N individual dipoles:

$$\mathcal{D}_e = \sum_n \mathcal{D}_{e,n} = \mu_{12} \cdot \mathbf{d} \sum_n (\sigma_n^+ + \sigma_n^-) \quad (3.3.4)$$

where μ_{12} is the electric matrix element for the transition $|g\rangle \rightarrow |e\rangle$ and \mathbf{d} is its normalized polarization vector.

For a single emitter, it is known that the photon emission rate is given by

$$\gamma_1 = \delta\omega_0 \langle \sigma_n^+ \sigma_n^- \rangle \quad (3.3.5)$$

with $\delta\omega_0$ as the natural linewidth of the transition and $\langle \ \rangle$ as the quantum mechanical average. This can be generalized easily to N emitters via

$$\gamma_N = \delta\omega_0 \langle J_+ J_- \rangle. \quad (3.3.6)$$

The expectation value in eq. 3.3.6 is described analogous to the transverse components of an angular momentum $J = N/2$, yielding

$$\gamma_N = \delta\omega_0(J + M)(J - M + 1). \quad (3.3.7)$$

For this expression, three special cases stand out:

- When the system is fully excited, i.e. $M = J$, the emission rate is $N\delta\omega_0$.
- For the half-deexcited emitter-system ($M = 0$), one obtains $\gamma_N = J(J + 1)\delta\omega_0 = \frac{1}{2}N(\frac{1}{2}N + 1)\delta\omega_0$. This shows that the emission rate strongly increases as the system cascades down the ladder and becomes proportional to N^2 when half of the ensemble is back to its ground state.
- When all the excitations have been transferred to photon energy and the system is in the $M = -J$ level, the emission rate vanishes completely and the emission stops.

The fact that the maximum emission rate scales with N^2 stands in contrast to the expected exponential decay that should show a linear scaling and is a characteristic of a special case of collectively enhanced emission, the so called superradiance, which shall be described in the following.

3.3.2. Superradiance, superfluorescence and the distinction to similar effects

Superradiance The term superradiance (SR) was chosen by R. Dicke "for want of a better term" for "a gas which is radiating strongly because of coherence" [52]. In principle, SR is both a classical and quantum effect; the decay of the ensemble itself is fully classical, but the start of the decay is a quantum effect, since it is caused by the interaction with the vacuum field, i.e. by spontaneous emission. As the system starts in the fully excited state, all N emitters are coherent in the beginning and therefore enable the superradiant emission.

When recalling the progression of the emission rate, we see that overall, the emission of photons in a superradiant ensemble happens at a higher rate than for the "normal" case. Due to energy conservation (the overall stored energy in the ensemble is still $N\hbar\omega_0$), the decay therefore has to occur on a shorter timescale that scales with $1/N$. This means that the emission of a superradiant ensemble happens in form of a short, high intensity photon burst.

As the decay of the ensemble is highly coherent, one can think of it as a large collection of dipoles with moment d that oscillate in phase and thereby form one macroscopic dipole, described by

$$P \propto Nd. \quad (3.3.8)$$

The characteristics of superradiant emission are summarized and illustrated in fig. 3.6. In

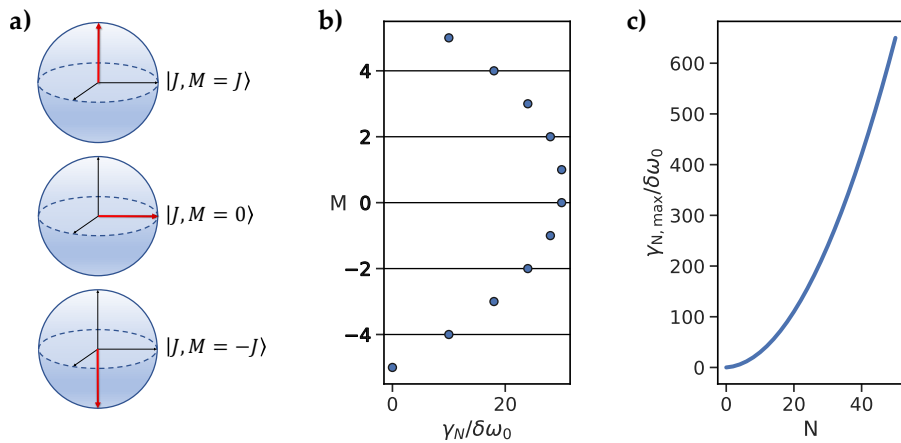


Figure 3.6: (a) Schematic of the most important $|JM\rangle$ states that describe the macroscopic dipole of the ensemble. The system can thereby be visualized by a collective Bloch vector. (b) Spontaneous emission rate of an ensemble of $N = 10$ dipoles in dependence of M , showing the characteristic increase in emission rate that reaches its maximum for $M = 0$. (c) Maximum emission rate depending on the number of emitters in the ensemble, clearly showing the proportionality to N^2 .

such a system, not only the emission rate is enhanced, but also the excitation is affected, leading to a super-linear dependence of the fluorescence rate on the excitation laser power.

Superfluorescence Superfluorescence (SF) often is described as a special case of superradiance (and is often mislabeled as such [146]), but in fact, it is rather a more general case of SR. SF describes a similar coherent decay of N emitters in a common radiation field, but - in contrast to SR - the emitters are initially excited incoherently. This means that the single dipoles are in their excited state, but start oscillating with random phases. Only when the first emitter interacts with the vacuum field and emits a photon, the next nearby oscillators can couple to its phase and spontaneously build up synchronization. Due to its stochastic nature, SF is an intrinsically random process [55]. The decay of the ensemble under emission of a short, coherent light pulse is similar to SR, once the synchronization has been established and the macroscopic dipole has emerged. This self-organization is an exciting phenomenon to discover, but rather hard to realize experimentally. It was first demonstrated by Skribanowitz et al. in 1973 in a gas of hydrogen fluoride molecules [53]. The intrinsic random nature of SF was shown by Florian et al. [147] in 1984, as they observed strong variations of intensity, pulse width and delay time, even under identical excitation.

In order to enable superradiant or superfluorescent radiation, some boundary conditions have to be fulfilled. The mainly limiting factor for SF is the time scale on which the

macroscopic dipole builds up, has to be faster than any phase breaking time scales, in particular, the population lifetime of the emitter T_1 and the polarization relaxation time T_2 :

$$\tau_p, \tau_d < T_1, T_2 \quad (3.3.9)$$

where $\tau_p \propto 1/N$ is the duration of the superradiant pulse and $\tau_d \propto \tau_p \ln N$ is the delay time after which the dipole has been developed.

Furthermore, as described above, the ensemble has to be confined spatially in a volume that is smaller than λ^3 such that the dipoles are invariant under exchange and the origin of each photon is unknown. If the emitter density is significantly lower, the dipoles do not interact with each other and the ensemble undergoes the "normal" emission with rate $\gamma_N \propto N$.

Since the emitters have to interact with each others and share the same (their own) light field, the transition frequency has to be the same for all emitters. While this seems like an obvious requirement, it is one of the main limiting factors for solid state systems, as presented in this thesis.

Lasing Not only SF and SR are often mixed up, but also other similar processes of large quantum ensembles can cause confusion due to their similarities.

SR gets commonly compared to lasing. In fact, a superradiant ensemble can be described as a mirrorless laser that is pumped in a percussional way at $t = 0$. Superradiant lasers are a very attractive application of SR since they can be much more stable and narrow than conventional lasers [57]. Due to the low average number of photons, the coherence in a superradiant laser is not stored in the light field inside the laser, but rather in the lasing medium itself.⁴

Amplified spontaneous emission SR/SF often gets confused with amplified spontaneous emission (ASE) which happens when a laser medium has a very large gain such that emitted photons can cause stimulated emission of other emitters before they leave the medium [63]. This effect is substantially different from SR as it is largely incoherent, i.e. emission and amplification are two sequential events. Therefore, the spectrum of photons created by ASE is usually rather broad which is an unwanted effect for most applications, but can also made use of, e.g. for broadband light sources. Furthermore, SR/SF converts all the stored energy in the ensemble into radiation, while in the case of ASE, only half of the initially stored energy is consumed by the radiation pulse [55].

⁴ Even though a superradiant ensemble can be described as a mirrorless laser, one can of course still couple the medium to an external cavity to further improve the optical properties of the laser.

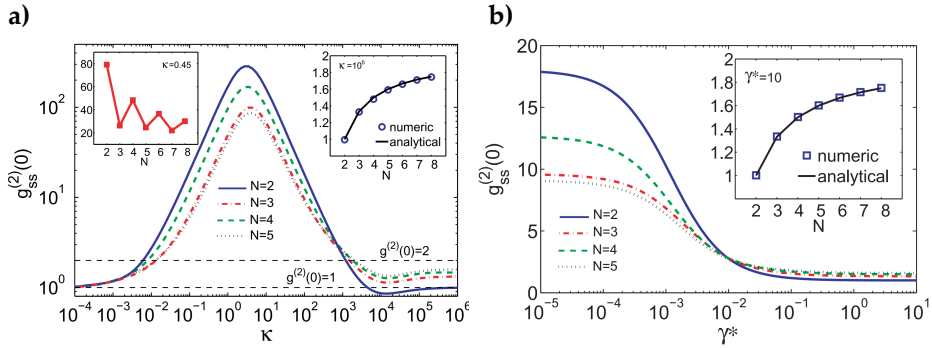


Figure 3.7: Simulation of the second-order correlation function at zero time delay for different (a) cavity decay κ and (b) pure dephasing rates γ^* (both normalized to g). The insets show the results as a function of N . Taken from [64].

Collective effects in the limit of few emitters The aforementioned ensemble effects are mostly valid for ensembles containing a large number of quantum emitters. For small ensembles, especially when coupled to a cavity, the classification of the different regimes is more subtle. Auffèves et al. have derived a theoretical description of a few emitters in a cavity [64]. Figure 3.7(a) shows a numerical simulation of the theoretical second-order correlation function at zero time delay for an ensemble of the emitter-cavity system. Depending on the cavity decay rate κ (normalized to the atom-cavity coupling strength g), the system either enters a subradiant regime, where strong bunching arises, or enters the bad cavity limit, leading to an increasingly uncorrelated behavior. Interestingly, there is an oscillatory dependence of the correlation function on the parity of the number of particles. This arises from additional single-photon cycles that appear in the angular momentum basis for an odd number of emitters. On the other side, when the cavity decay rate is much larger than the atom-cavity coupling, this behavior is lost and the bunching slowly decreases. For large numbers of particles and decay rates, the system behaves like a thermal light source, approaching $g^{(2)}(0) = 2$. The bunching then arises from constructive interference of the emission of pairs of atomic excitations resulting from the indistinguishability of the atoms in the emitting pairs [148]. In fig. 3.7(b), the correlation function at zero time delay is depicted for different pure dephasing rates γ^* (again normalized to g) for a moderate decay rate of $\kappa = 100g$. Here, the simulation shows that the bunching, as well as the oscillatory behavior, vanishes if the pure dephasing is comparable to or higher than the coupling rate. As we shall see in chapter 6, the system that is investigated in this thesis shows $\kappa \approx 6g$ and is therefore located near the peak in fig. 3.7(a). The pure dephasing rate, however, is $\gamma^* > g$, which translates to a much weaker bunching, as shown in fig. 3.7(b).

4. Integration of a diamond membrane into an optical cavity

The efficient integration of thin diamond membranes into an optical cavity is one of the major challenges in this work. The aim is to avoid any additional losses compared to an empty cavity. Additional losses can have a variety of sources such as scattering on either of the surface interfaces, increased absorption in the diamond and transverse mode coupling, among others. In this chapter, I shall describe the technical approach of integrating a membrane into a cavity and discuss all these sources of loss.

First, the special case of fiber-based microcavities, which are used in this thesis, will be presented and discussed in terms of theoretical as well as technical aspects. Afterwards, I will discuss van der Waals bonding - the technique that was used for the sample integration - and describe the recipe that we developed and used in our experiments. The measurements presented in this chapter are recorded on samples S_A , S_B and S_C , which will be described in detail in section 4.3.1. The measurements on samples S_B and S_C have mostly been performed by Jonathan Körber in his master's thesis under my supervision. The experiments on samples S_B and S_C were recorded using a dedicated room temperature setup that has been set up by Evgenij Vasilenko under my supervision.

4.1. Fiber-based microcavities

4.1.1. Motivation

As we have seen in sec. 3.2, the geometry of an optical cavity has a major impact on its applicability for experiments in cQED. The figures of merit are a small mode volume, combined with a high quality factor of the cavity, since $C \propto Q/V_m \propto \mathcal{F}/w_0^2$. Finding the right dimensions for a cavity thus aims to optimize the above-stated proportionality. Therefore, different approaches on macroscopic in addition to small-scale micro- and nanocavities have been investigated in the past.

Some experiments require a macroscopic scale, like trapped atom or ion experiments. Due to their rather large mirror separation, high quality factors on the order of 10^8 are possible, but the reachable Purcell factor is limited by the large mode volume $V_m \approx (10^4 - 10^6)\lambda^3$. This leads to Purcell factors on the order of 10^2 [149, 138].

Micropillar cavities can also reach high quality factors $> 200\,000$ [150] while having a much smaller mode volume, but they lack the tunability that an open cavity provides. The smallest mode volumes possible can be realized e.g. in photonic crystal (PC) cavities that usually consist of structures inside the bulk material. They can reach the limit for the mode volume of λ^3 with decent quality factors and can therefore enable very high Purcell factors [42]. However, like micropillar cavities, they are hard to tune such that a large quantity has to be fabricated until one can find a suitable cavity.

Besides Fabry-Pérot cavities, where the light field builds a standing wave between two mirrors, other geometries are possible. Especially whispering gallery mode (WGM) resonators have been investigated a lot as they can show very high quality factors on the order of $> 10^9$, although the mode volume is larger compared to micropillar or PC cavities [151].

A fiber-based microcavity is an approach that can combine small mode volumes with decent quality factors and a full tunability. This makes them interesting for all kinds of applications like sensing or imaging [152, 153, 154, 155], trapped atoms or ions [156, 157], cavity-enhanced Raman spectroscopy [158], or Purcell-enhanced spectroscopy of solid state emitters like rare earth ions [159, 49, 48], color centers in diamond [109, 160, 161, 50] or 2D materials [20]. Furthermore, fiber-based cavities have the advantage of being already directly fiber-coupled.

In the following, I shall discuss the basic principles of fiber-based microcavities, the technical aspects like production and characterization, and their limitations. The characteristics of fiber-based microcavities are described extensively in the theses of Julia Benedikter, Hanno Kaupp and Matthias Mader [72, 128, 127]. Therefore, I will confine myself to the most important aspects that are relevant for this thesis.

4.1.2. Technical aspects

Basic idea of laser machining In a fiber-based microcavity, one or both cavity mirrors are machined on the end facet of an optical fiber [39, 162]. The light can be coupled into the cavity through the fiber, facilitating an easier alignment of the cavity. Similarly to macroscopic cavities, a fiber-based microcavity is rather hard to align when both mirrors are planar. Therefore, it is desirable that at least one of the mirrors features a concave mirror profile. A sketch of a basic fiber-based microcavity is depicted in fig. 4.1.

The most common way (which was used in this thesis) to fabricate such mirror profiles is by focusing single or multiple pulses of a CO₂ laser⁵ beam onto the cleaved end facet of the fiber. The fused silica material of the fiber has an absorption coefficient in this frequency regime that is about a million times larger than in the optical range [163]. Hence, the high power pulses of the laser that hit the fiber with $> 1\text{ W}$ cause the material to melt and lead to thermal evaporation. Since the absorbed energy depends on the laser

⁵ Synrad firestar v40, $\lambda_{\text{CO}_2} = 10.6\ \mu\text{m}$

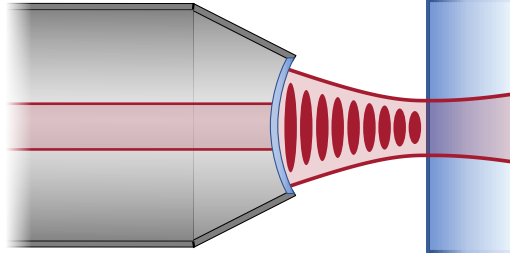


Figure 4.1: Exemplary, simplified sketch of a fiber-based microcavity. A concave profile on the end facet of the fiber acts as a concave mirror and thus improves the stability range of the cavity. When the mirror distance fulfills the resonance condition for the design wavelength, a standing wave emerges, its lateral extent is described by a Gaussian beam. Note that the individual parts in this sketch are not drawn to scale.

power, the lateral power profile of the laser beam will be imprinted into the fiber surface, given by [162]

$$I(r) \propto I_0 \exp -2r^2/w_0^2 \quad (4.1.1)$$

where I_0 is the maximum intensity of the beam, r is the radial position and w_0 is the beam waist which is located at the fiber surface if the beam is focused precisely. This leaves a concave profile on the fiber tip that can be approximated with a Gaussian profile. Its shape thereby depends on multiple factors like the laser power, the number of pulses, the pulse duration, etc.. Via various combinations of these settings, one can control the resulting mirror profile. Although finding the right parameters can be a tedious effort, there are a few rules of thumb for them. For example, a deep profile with a small radius of curvature can be obtained by using many pulses with low laser power, while for a more shallow profile that has a larger diameter, one would rather use fewer pulses with higher power. A very nice side effect of the laser machining is that it can help smoothen the surface down to the Ångström level which greatly reduces cavity loss by scattering on the fiber surface.

Additionally to the concave profile in the middle of the fiber, we use a cropping technique where multiple circles of single, high-power shots and decreasing diameter are applied to the outer region of the fiber. This has two effects: firstly, it narrows down the fiber tip, allowing for shorter mirror distances. If the fiber is still at its full thickness at the tip, the edge might already touch the plane mirror (or the second fiber mirror) when the mirrors are not aligned perfectly perpendicular. This limits the smallest possible cavity length and therefore the mode volume. Secondly, the cleave of the fiber often leads to sharp-edged protrusions in the outer region.⁶ Fig. 4.2 shows optical microscope images of such a machined fiber.

⁶ This strongly depends on the cleaver that is used. Some cleavers "break" the fiber by tearing it apart under an angle. Other cleavers truly cut the fiber slowly while gently pulling both ends of the fiber.

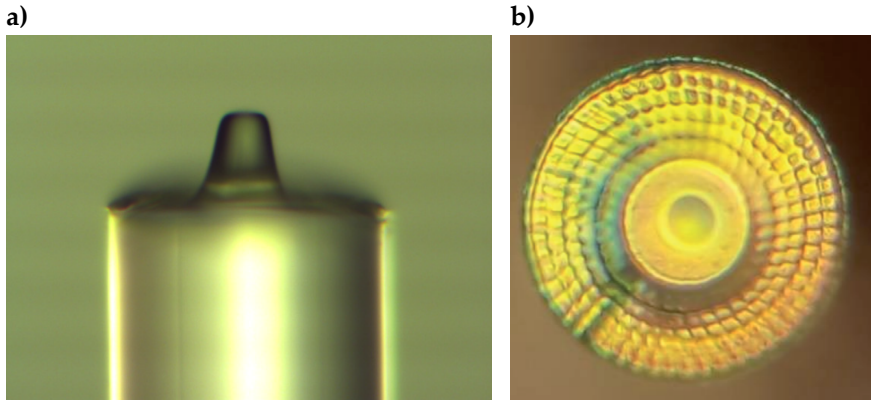


Figure 4.2: Optical microscope images of laser-machined fibers. (a) Side view of the fiber, showing the cropped fiber tip. The fiber diameter is $125\ \mu\text{m}$. The photo was taken by Hanno Kaupp [128]. (b) Top view of a different machined fiber. The single, ring-wise applied cropping shots are clearly visible, as well as the concave mirror profile that was shot onto the plateau in the center region of the fiber. The surface appears yellow because the fiber features a mirror coating with a central wavelength of $585\ \text{nm}$. The photo was taken by Julia Benedikter [72].

Machining setup and characterization For the fiber mirrors, it is crucial to have a very precise alignment of the fiber with respect to the laser beam, in particular for its lateral position. As the fiber core usually has a slightly different absorption coefficient than the cladding, a lateral misalignment will immediately lead to asymmetric profiles. Therefore, we clamp the fibers (after cleaving them) into a home-built holder (designed by Benedikt Schlederer [164] and Matthias Mader [127]) that can be mounted into a micropositioning stage. The stage is then used to adjust the fiber core to the laser beam laterally and to position it such that the fiber surface is in its focal plane. Although the CO_2 laser itself is running in a pulsed mode, an acousto-optic modulator (AOM) is used to gain full control over the pulses.⁷ If one wants to fabricate very small profiles, a beam expander can be used before the focusing lens such that a smaller beam waist can be reached. Additionally, the positioning stage can be moved either to an optical light microscope or a white light interferometer (WLI).⁸ This is useful both for the alignment pre-machining as well as for the characterization of the imprinted profiles afterwards. The microscope is used mainly for the coarse adjustment of the fiber positioning or to identify damages on the fiber surface. The WLI has a much finer lateral resolution and can detect height differences on the sub-nanometer scale. A height difference on the sample leads to a phase difference between reflected beams which can be resolved by interfering the

⁷ The duty-cycle of the laser can be adjusted. A duty-cycle of 100 % means that the laser emits over the whole period between two pulses and is then in a quasi-continuous wave mode.

⁸ The WLI used in this thesis is in fact not a real WLI as it does not use a true white light source. Instead, we use a broadband LED with $\lambda = 463.25\ \text{nm}$. However, the working principle stays unaffected.

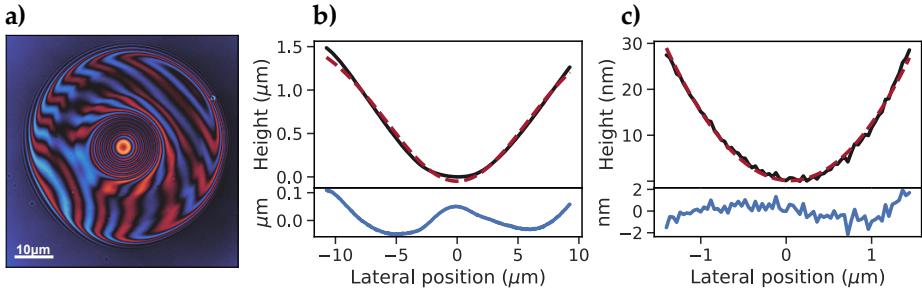


Figure 4.3: (a) WLI image of a machined fiber, F_C . (b) Height profile of (a) along the x-axis through the center of the profile. The WLI data (black) is fitted by a Gaussian (dashed red), the residual is shown in the lower panel (blue). (c) Zoom of the central region of (b), fitted with a parabola.

beam with a reference beam path that has a well defined phase. The light then features interference fringes that can be resolved using a high-resolution camera. The height difference Δh is given by

$$\Delta\phi = \frac{4\pi}{\lambda_{\text{LED}}}\Delta h \quad (4.1.2)$$

where $\Delta\phi$ is the phase difference between a reflected and the reference beam and $\lambda_{\text{LED}} = 463.25 \text{ nm}$ the wavelength of the LED.

Fig. 4.3(a) shows a WLI image of the fiber F_C which was used for measurements in this thesis (for more details, see tab. 4.1). Every fringe (change from red to blue) hence refers to a height difference of $\lambda_{\text{LED}}/4$. Since one is interested in the height map of the profile rather than in the periodic phase, a phase unwrapping algorithm is applied. To do so, multiple camera pictures (typically a few hundred) are averaged and thereby yield the relative phase from each pixel's averaged intensity. This process is repeated five times while moving the objective by $\lambda_{\text{LED}}/4$ along the optical axis between each step. Figs. 4.3(b) and (c) show cuts through the height profile of the fiber shown in (a) that were fitted with a Gaussian (b) and a parabola (c), respectively. As highlighted by their respective residuals, the Gaussian is a good approximation for the whole profile, but it fails to match the center region at the fiber core. This region is described much better by a parabolic function, showing residuals of under 2 nm.

With this setup, radii of curvature as small as a few micrometers and as large as hundreds of micrometers can be reached. The profile depth can be as low as below 100 nm and as deep as a few micrometers.

Fiber machining results The fiber mirrors that were produced in the course of this thesis were aimed to show a variety of geometrical settings such that they match the varying requirements. E.g. for a cavity that includes a micrometer thick diamond membrane, larger profiles are necessary as the cavity length can be tens of micrometers by default. For an empty cavity, smaller radii of curvature can be used in order to minimize the

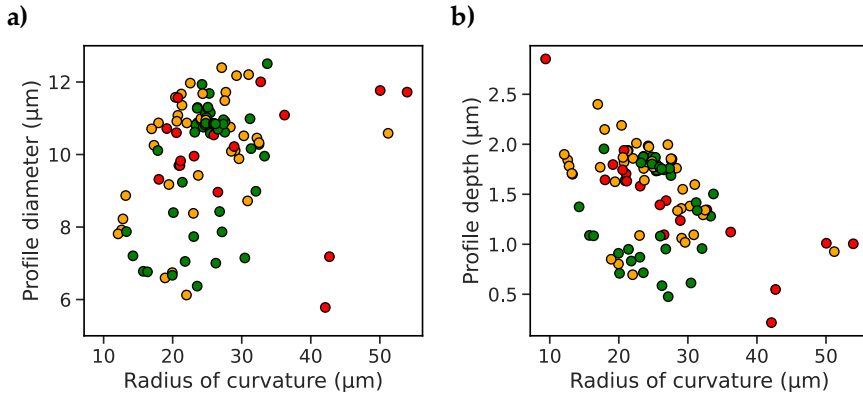


Figure 4.4: Overview of the machined fiber mirror profiles for (a) the profile diameter and (b) the profile depth, with respect to the corresponding radius of curvature. The coloring indicates profiles with an asymmetry of < 10 % (green), 10 – 20 % (orange) and > 20 % (red).

mode volume and reach short mirror separations. An overview of the machined profiles is given in fig. 4.4.

The mirrors were machined onto pure silica single-mode fibers with an aluminium coating⁹. A pure silica fiber has the advantage that its fluorescence when a laser with a wavelength of 532 nm is guided through, has been observed to be significantly reduced, especially at cryogenic temperatures.

The majority of profiles have radii of curvature around 20 – 30 μm , averaged over the two elliptic principal axes. Since we estimated the beam waist of the cavity modes in later experiments to be on the order of 1 – 2 μm , we aimed for profile diameters > 6 μm such that clipping and diffraction losses could be minimized. The profile depth is then chosen to be as shallow as possible while still reaching the desired profile geometry. We thereby aimed to not exceed 2 – 3 μm for the profile depth in order to avoid very steep slopes on the coating. Profiles with smaller radii of curvature tend to be rather deep which is necessary in order to achieve a suitable profile diameter. It became apparent that profiles with a larger ROC were harder to machine with high quality relative to profiles with a moderate ROC.

During the machining of the fibers, the CO_2 laser suffered from significant power fluctuations which directly affects the profile symmetry as the shot settings might not match the expected behaviour. In this thesis, mirror profiles with a parabola asymmetry of < 10 % were considered good, while profiles with an asymmetry of over 20 % were avoided. The intermediate profiles were mostly used for testing purposes.

⁹ *artphotonics SM530-125-160AL*

4.1.3. Distributed Bragg reflector

After the mirror profiles have been machined onto the fibers, a mirror coating has to be added to make them applicable for optical cavities. In this thesis, distributed Bragg reflectors (DBR) were used. DBRs are dielectric mirrors that consist of a sequence of thin layers of optical materials with alternating refractive indices n_H and n_L . The layer thickness is thereby chosen such that their optical length matches a quarter of the design wavelength for normal incidence. As each interface of both materials is partially reflective, the incident light wave splits up into two waves with a path length difference of $\lambda_0/2$. This leads to constructive interference of the reflected waves of each layer, resulting in a high overall reflectivity. The more layers are stacked onto each other, the higher the reflectivity will be. For the design wavelength, the reflectivity R can be approximated via [165]

$$R = \left(\frac{n_0 n_L^N - n_S n_H^N}{n_0 n_L^N + n_S n_H^N} \right)^2 \quad (4.1.3)$$

where n_0 and n_S are the refractive indices of the incident medium and the medium onto which the mirror is added, respectively. N denotes the number of stacks in the DBR. Typically, one uses Ta_2O_5 ($n_H = 2.12$ at 640 nm) and SiO_2 ($n_L = 1.46$). Fig. 4.5 shows two DBR coatings that were used in this thesis (details in tab. 4.1) and a simulation of their resulting transmission profiles. For the simulation, a transfer matrix model was used, which is described in detail in ref. [72]. The first coating (blue) is a rather simple combination of $\lambda/4$ -stacks that results in a reflective band around the center wavelength of $\lambda_0 = 640$ nm. The second coating (orange) has a more sophisticated design, where the layer thickness shows a stronger variation. This can be used to change the shape of the transmission profile or to add additional reflective frequency bands to the coating. In the case of the second coating, the arrangement of layers was changed such that the reflectivity at 640 nm stays about the same while the coating also features a reflectivity of about 99.8 % at 532 nm. These kind of advanced coating designs can be necessary, e.g. if a second laser must be used in the cavity simultaneously, or if one wants to avoid transmission of unwanted frequencies through the mirror. As we shall see later in chapter 4, any additional dielectric layer can modify the mirror's transmission profile further.

Mirror termination The mirror termination of a DBR refers to the final layer of the stack and whether it has a high or low refractive index. Typically, a termination with the high refractive index material is beneficial since the electric field then has a node at the mirror surface. This reduces the penetration depth of the light field into the coating, given by $d_{\text{pen}} = \lambda/(4\Delta n)$ with $\Delta n = n_H - n_L$. Moreover, this mostly prevents scattering at the mirror interface. However, sometimes it can be useful to shift the position of the field

4. Integration of a diamond membrane into an optical cavity

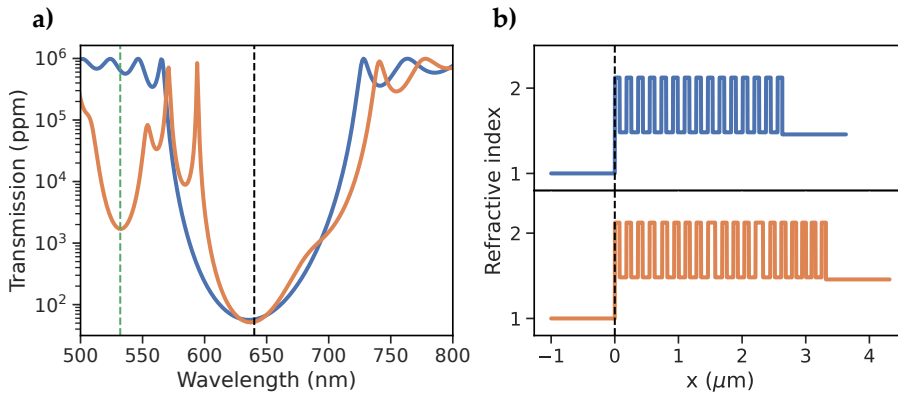


Figure 4.5: (a) Simulated transmission profile of two different coatings, defined by their DBR stack structure shown in (b). Blue: a simple stack containing of $\lambda/4$ -layers, leading to a single center wavelength (coating C_A). Orange: coating with a secondary stop band around 532 nm with a higher transmission. The layer design is now more complicated and deviates from the $\lambda/4$ -structure (coating C_B). Transmission spectra were obtained by transfer matrix simulation.

maximum with respect to the mirror surface, e.g. when a sample is placed either on, or with a defined distance to the mirror surface (typically on the planar mirror). In order to maximize the interaction with the cavity field, it is hence important to adapt the coating such that the sample is located at a field antinode. In the case of a sample that is placed directly on the mirror surface, the phase of the electric field has therefore to be shifted by π , i.e. an additional $\lambda/4$ -layer of the low refractive index material has to be added to the coating, which is then called *spacer layer*. If the sample has a certain distance to the mirror surface (e.g. in a membrane with a particular implantation depth), the thickness of the spacer layer has to be adapted accordingly to shift the field maximum to the location of the emitter. The simulated cavity field intensity of the same coating without a spacer and with an exemplary spacer of 60 nm is shown in fig. 4.6. One can observe that the intensity minimum is located at the high refractive index surface in both cases, but the spacer in the lower panel effectively shifts the physical mirror-air interface, leading to a phase shift at the mirror position (and likewise, any fixed distance from the mirror surface). If, e.g. for practical or financial reasons, a mirror coating has to be used that does not feature a spacer layer, but the sample would require one, one can subsequently add a spacer via spin-coating. Polymethylmethacrylat (*PMMA*) is a common choice for this, as it has good optical properties and has a comparable refractive index to the one of SiO_2 (see sec. 4.3.2 for more detail).

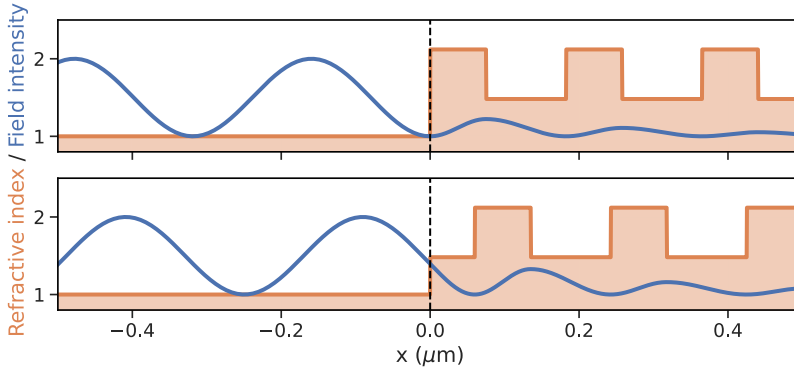


Figure 4.6: Comparison of two DBR coatings where a spacer layer of 60 nm was added (lower panel) on one of the otherwise identical coatings. The dashed line marks the physical surface of the mirror where a potential sample could be located, highlighting the shifted phase of the field intensity.

4.1.4. Limiting factors

In the following, I shall briefly discuss the limiting factors of fiber-based microcavities, mainly due to geometrical reasons. A much more detailed discussion about the effects stated below can be found in refs [166] and [167].

Transverse mode coupling Transverse mode coupling is an effect that arises mostly for longer mirror distances and describes the coupling of higher order transverse modes to a fundamental mode with a different longitudinal mode order. The effect can be understood by recalling eq. 3.1.20:

$$v_{(q,m,n)} = \Delta v \left(q + (m + n + 1) \frac{\Delta\theta}{\pi} \right). \quad (4.1.4)$$

The fundamental modes ($m = n = 0$) are separated in frequency space by the free spectral range Δv . For higher order modes, however, this frequency difference is larger, scaling with $m + n + 1$, i.e. the frequency spacing between the different transverse mode orders increases as the cavity becomes longer. Eventually, the difference will become so large that the (m, n) -mode for a certain q becomes degenerate with the fundamental mode of the subsequent longitudinal mode order $q + 1$. The modes then couple, which typically leads to an avoided crossing behaviour. This means that as the modes are approaching each other, the energy slowly gets transferred from one to the other mode, which leads to a decreasing transmission for the fundamental mode, until both modes are approximately equal when they couple resonantly. In an experiment, this usually shows

4. Integration of a diamond membrane into an optical cavity

in a decrease both in cavity transmission and finesse. As this effect only happens for distinct longitudinal mode orders, one can observe sudden finesse drops when scanning the cavity length.

As mode coupling becomes more severe for longer cavity lengths, it is a limiting factor for experiments which has to be taken into account, especially when a larger mirror separation is required.

Diffraction loss and imperfect mirror profiles For macroscopic cavities, the mode size is usually very small compared to the size of the mirror profiles. However, in the case of fiber-based microcavities, the mirror profiles can be rather small and thus comparable to the mode size. This can cause clipping losses and increased diffraction, which affect mostly higher order transverse modes due to their larger spatial size. Furthermore, the CO₂-laser machined mirror profiles usually have asymmetric and imperfect shapes. While asymmetric, i.e. elliptic mirror profiles lead to a splitting of the fundamental (and higher order transverse) modes, surface deviations and particle-like features in the profile have a higher spatial frequency. These high spatial frequencies couple the fundamental mode to many transverse modes with large mode index, which leads to a smooth decrease in finesse for larger mirror separations. It has been reproducibly shown that the finesse drops rapidly at a cavity length around $d = ROC/2$ for a fiber mirror with the effective radius of curvature ROC which is only half of the theoretical limit of $d = ROC$. This limitation has to be taken into account when designing an experiment. A way to minimize the diffraction and clipping losses is by using mirror profiles that are sufficiently large. As a rule of thumb, it has been found that in order to avoid diffraction loss for mirror separations up to $d = ROC/2$, the profile radius a should fulfill

$$a > 4w_c \quad (4.1.5)$$

where w_c is the mode radius at the curved mirror.

Small radii of curvature If one wants eq. 4.1.5 to be satisfied, one has to adapt the other profile parameters accordingly. As small radii of curvature are usually desired, the profile depth, given by $t = \frac{a^2}{2ROC}$ has to be rather large. This again increases the shortest possible mirror separation and therefore the mode volume of the cavity. Furthermore, if one chooses a smaller profile radius, the curvature can become very steep for small ROC , which can cause deviations of the DBR layer thickness at the edges of the profile.

Mode matching Coupling light into a fiber-based microcavity can be done either via the free space channel (as done in sec. 6) or conveniently through the cavity fiber directly (as done here and in chapter 5). When coupling the light through the fiber mirror, the efficiency is limited by the overlap of the cavity mode and the fiber mode, ϵ :

$$\epsilon = \langle \Psi_F | \Psi_C \rangle = \int_{-\infty}^{\infty} \Psi_F^* \Psi_C \, dx dy. \quad (4.1.6)$$

If the mirror profile is centered at the optical axis of the cavity, this can be expressed as

$$\epsilon = \frac{4}{\left(\frac{w_f}{w_0} + \frac{w_0}{w_f}\right)^2 + \left(\frac{s\lambda}{\pi w_0 w_f}\right)^2} \quad (4.1.7)$$

where w_f is the mode field diameter of the optical fiber and s is the distance between the mode waist position for the fiber and the cavity mode, respectively [39]. Hence, the mode matching is ideal when both beam waists are equal and positioned such that they overlap spatially, i.e. at the plane mirror. Since this is usually not the case, one aims to improve the mode matching, e.g. by adding mode matching optics onto the fiber mirror. This approach has been investigated in the recent past and shows promising results. Gulati et al. have proposed using a concatenation of graded-index (GRIN) and multimode (MM)/core-less fibers spliced together, which lets the fiber mode expand in the GRIN fiber before being focused down to the desired beam waist [168]. If the length of the respective fibers are chosen correctly, the mode matching can be improved drastically. A drawback of such a sophisticated fiber mirror can be that its machining comes with a lot of effort, making it harder to produce a large number of fiber mirrors, e.g. with varying geometrical properties.

4.2. Mode hybridization and membrane-induced loss

In this section, I will discuss the influence that the introduction of an additional refractive layer, such as a diamond membrane, has on the performance of an optical cavity. The extent of this influence thereby depends on multiple factors, such as the refractive index of the added material, the geometry (i.e. thickness, angular alignment, etc...) and the surface quality of all interfaces. The presence of a diamond membrane adds a layer with a high refractive index of $n_d = 2.41$, as shown in the lower panel of fig. 4.7(a). Since the diamond-air interface is a partially reflective surface, the electric field does not only have a resonance condition in the cavity, but also the membrane itself can be considered a bad resonator. The continuity condition at the diamond-air interface then leads to a hybridization of the air cavity mode and the diamond mode, respectively. Thus, the resonance condition has to be described for the coupled system [44, 43]. This configuration has two special cases: when the diamond thickness t_d satisfies the resonance condition for the vacuum wavelength λ_0 for the diamond cavity $t_d = N \cdot \lambda_0 / 2n_d$, the hybridized mode has an anti-node at the diamond-air interface, and the cavity features a so called "diamond-like mode". The opposite case, when the cavity mode has a node on the diamond-air interface, is analogously called an "air-like mode". The latter is shown in the left panel in fig. 4.7(a) and zoomed in to the diamond-air interface in the right panel, the former is depicted in fig. 4.7(c). This nomination comes from the fact that for an air-like mode, the electric field is mostly confined in the cavity air gap and vice versa for the diamond-like mode.

If we treat the modes in the air gap and in the membrane separately, the coupling

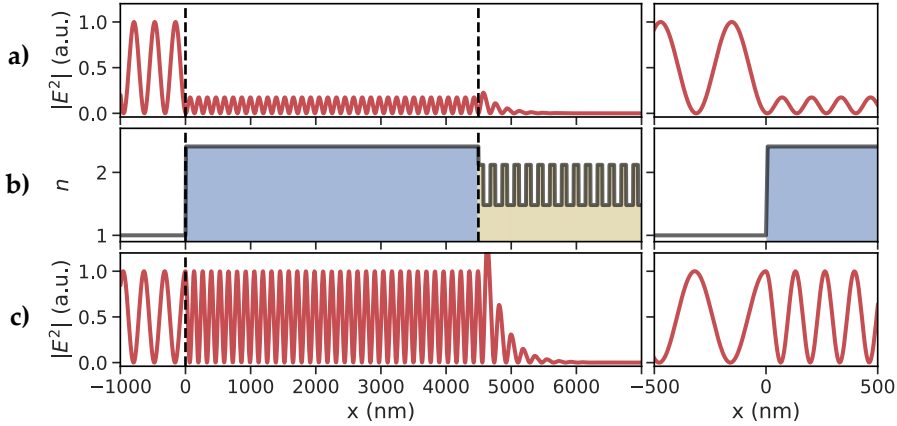


Figure 4.7: Normalized field intensity distribution in a hybrid cavity, depending on the diamond thickness t_d . Simulated using a transfer matrix calculation. **(a)** Air-like mode character. The diamond thickness is chosen such that the electric field has a node at the diamond-air interface (first dashed line). As the coating used in this simulation is terminated by a high-refractive index layer, the electric field is on a node at the mirror-diamond interface (second dashed line). **(b)** The distribution of the refractive indices for the cavity region used in (a) and (c). It shows the diamond membrane ($n_d \approx 2.41$, blue) and the dielectric mirror coating on the planar mirror (n_{SiO_2} ($n_{\text{Ta}_2\text{O}_5}$) ≈ 1.48 (2.12)). **(c)** Diamond-like character, similar to (a). Here, the electric field has an antinode at the diamond-air interface and the intensity in the diamond membrane is equal to that in the air gap. The right panels show a zoom around the diamond-air interface, respectively.

strength of the two modes depends on the reflectivity of the membrane-air interface, given by the refractive index of the membrane material. If the interface was perfectly reflective, the two modes would not couple at all and we simply had an air-cavity and a diamond-cavity. The air-cavity would show the typical linear dispersion of a bare cavity. The resonance wavelength of the diamond-cavity, on the other hand, would obviously not depend on the cavity air gap at all, since the diamond thickness - which is constant - satisfies the resonance condition. By lowering the reflection on the interface, the two modes couple and thereby lead to hybridized cavity modes. Analogous to two coupled mechanical oscillators, this mode hybridization leads to an avoided crossing behavior. The extent of this avoided crossing splitting is given by the refractive index of the membrane material, which, in the case of diamond, is rather strong. The dispersion plots for the two hybridized modes from fig. 4.7(a) and (c) are again simulated using the transfer matrix model, the results are shown in fig. 4.8(a) and (b), respectively. When the cavity is resonant with an air-like (diamond-like) mode, the dispersion at λ_0 has a steep (shallow) slope. If the modes would be completely decoupled, the dispersion would just be a horizontal line for the diamond-like mode, as indicated in fig. 4.8(b).

As stated above, the diamond thickness and thus the hybridized mode structure is of great importance for the cavity and therefore requires different mirror coating designs.

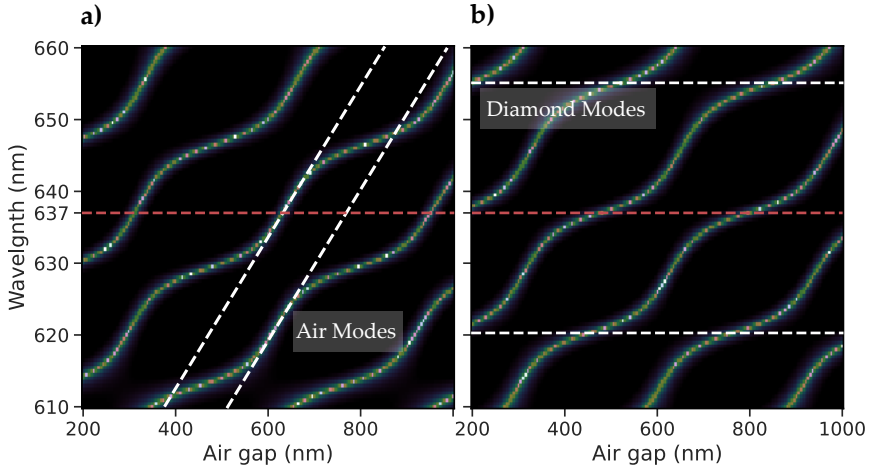


Figure 4.8: Simulated mode dispersion for the two configurations in fig. 4.7. (a,b) Mode dispersion of a hybrid cavity satisfying the (a) air-like and (b) diamond-like condition for $\lambda_0 = 637$ nm (red dashed line). The white dashed lines indicate the dispersion of uncoupled (a) air modes and (b) diamond modes that are then altered by coupling to each other.

In the following, I will discuss different sources of loss that contribute to the cavity performance.

Mirror loss In a bare cavity, the mirror loss \mathcal{L}_M consists of transmission, scattering on and absorption in the coating and is simply given by

$$\mathcal{L}_M = \mathcal{L}^m + \mathcal{L}^f \quad (4.2.1)$$

where \mathcal{L}^m and \mathcal{L}^f describe the mirror losses at the plane mirror and the fiber mirror, respectively. This equation, however, becomes invalid for a diamond-air cavity, since the field intensity at the mirrors changes. In the coupled membrane-air cavity, the relative field intensity depends on the hybridized mode structure, i.e. whether the cavity mode shows an air-like or a diamond-like character.

The continuity condition for the electric field at the diamond-air interface can be described via

$$E_{max,a} \sin\left(\frac{2\pi t_a}{\lambda_0}\right) = E_{max,d} \sin\left(\frac{2\pi t_d n_d}{\lambda_0}\right). \quad (4.2.2)$$

4. Integration of a diamond membrane into an optical cavity

In order to eliminate t_a from this formula, one aims to find an expression for the resonance condition of a hybrid cavity. The resonance frequency ν for the q -th longitudinal mode of such a cavity is given by [43]

$$\nu \approx \frac{c}{2\pi [t_a + (n_d - 1)t_d]} \left\{ \pi q - (-1)^q \times \arcsin \left(\frac{n_d - 1}{n_d + 1} \sin \frac{q\pi [t_a - (n_d + 1)t_d]}{t_a + (n_d - 1)t_d} \right) \right\} \quad (4.2.3)$$

where t_a is the cavity air gap, i.e. the distance between the fiber mirror and the diamond-air interface. From that, we can deduce the expression for the resonance condition for t_a at a given diamond thickness [44],

$$t_a = \frac{\lambda_0}{2\pi} \arctan \left(-\frac{1}{n_d} \tan \left(\frac{2\pi n_d t_d}{\lambda_0} \right) \right) + \frac{q\lambda_0}{2}. \quad (4.2.4)$$

Combining eqs. 4.2.2 and 4.2.4 then yields the relative field intensity in the air gap, given by

$$\frac{E_{max,a}^2}{n_d E_{max,d}^2} = \frac{1}{n_d} \sin^2 \left(\frac{2\pi n_d t_d}{\lambda_0} \right) + n_d \cos^2 \left(\frac{2\pi n_d t_d}{\lambda_0} \right). \quad (4.2.5)$$

Thus, the mirror losses at the fiber mirror have to be scaled with eq. 4.2.5, yielding

$$\mathcal{L}_M = \mathcal{L}^m + \frac{E_{max,a}^2}{n_d E_{max,d}^2} \mathcal{L}^f. \quad (4.2.6)$$

The scaling factor for the fiber mirror transmission $E_{max,a}^2/n_d E_{max,d}^2$ is shown in fig. 4.9(a), as given by the analytical description from eq. 4.2.5, as well as the values obtained from the numerical simulation for several diamond thicknesses. One thus has to take the diamond thickness into account when designing a hybrid cavity. This, however, is not the only influence that the diamond thickness has on the mirror losses. Additionally to the scaling factor, the presence of the diamond membrane also modifies the pure transmission of the plane mirror. This can be understood as adding an additional layer to the dielectric mirror that either increases or lowers the reflectivity of the stack. The result is a periodic alternation of the mirror transmission profile. Fig. 4.9(b) shows three special cases for the same dielectric coating. In the case of the bare mirror, the coating has one single stopband that shows a transmission of 57 ppm for $\lambda_0 = 637$ nm (upper panel). When adding a diamond membrane that satisfies the air-like condition $t_d = N \cdot \lambda_0/2n_d + \lambda_0/4n_d$, the transmission profile shows the periodical alternation described above (center panel). The transmission at $\lambda_0 = 637$ nm stays at 57 ppm¹⁰. When changing the diamond thickness such that the diamond-like condition is fulfilled, the mirror transmission is almost six times higher, reaching 330 ppm for the fully

¹⁰ It is not generally the case that the transmission for an air-like character stays the same as for the bare mirror. Other coatings can show higher or lower transmissions.

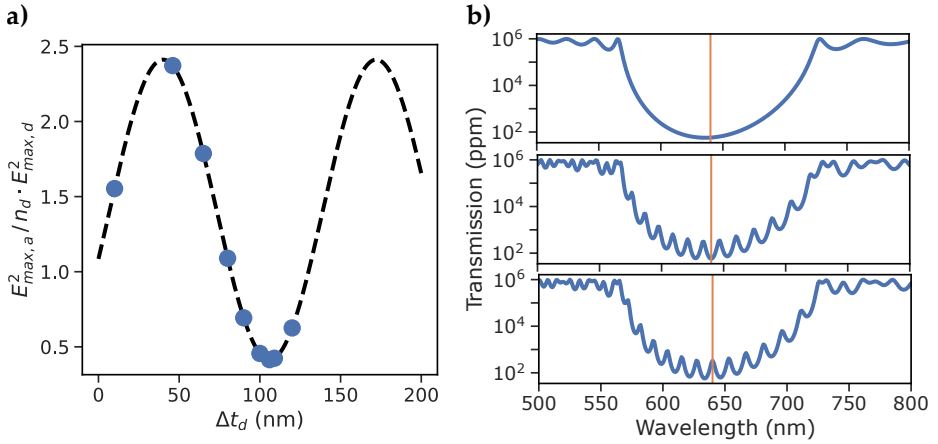


Figure 4.9: (a) Scaling factor for the electric field intensity in the air gap, depending on the diamond thickness t_d . The dashed line thereby describes the analytical formula from eq. 4.2.5, the blue dots are single values obtained from the transfer matrix simulation, showing good agreement. (b) Simulated transmission profile of the dielectric coating used for the simulations in figs. 4.7 and 4.8, designed for $\lambda_0 = 637$ nm. There are three special cases: the plain mirror (upper panel), the diamond-mirror combination in an air-like configuration (central panel) and in a diamond-like configuration (lower panel).

diamond-like configuration. This follows directly from the resonance condition in the diamond. This effect does not only affect the expected finesse of a hybrid cavity, but also has to be taken into account before designing the mirror coatings for experiments that require high collection efficiencies which usually is the case. If one considers a cavity with an air-like character that uses the same coating (e.g. the coating introduced above) for both the plane and the fiber mirror, the transmission of a photon is equally likely to happen at the plane and the fiber mirror. This is not desired for experiments, where the collection optics and measurement modules are only located on one side of the cavity. Thus, a cavity with asymmetric mirror transmissions is usually preferred. This can either be achieved by choosing different mirror coatings for each mirror, or, as it is the case for the coating in fig. 4.9(b), one can make use of the transmission increase on the planar side, if operated in the diamond-like configuration. These considerations highlight that it is of great importance to decide whether the cavity shall be operated on air-like or diamond-like modes before designing the mirror coatings.

Scattering at the membrane interfaces The second major source of additional loss in the system that we discuss is scattering. If we first consider an ideal van der Waals bond (see section 4.3.2), the diamond membrane is in direct contact with the DBR coating at all lateral positions. Thereby, we introduce two additional interfaces to the system that can induce loss, the diamond-air and the diamond-mirror interface. At both interfaces,

scattering can occur, which can greatly limit the performance of the resonator. Scattering generally can be avoided if the electric field has a node at the scattering surface. In the case of the diamond-mirror interface, this can be achieved by using a DBR stack that is terminated with a layer of high refractive index. This interface can then be neglected. However, depending on the layer depth of emitters that are used in the experiment, it can be necessary to add a spacer layer with low refractive index to the coating (as is the case for sample S_A). Then, the field node is shifted away from the interface and scattering reemerges, depending on the spacer layer thickness. Furthermore, a shift of the field node can also happen if the bond is not fully established over the whole contact area of the membrane. This can happen e.g. when the membrane is not perfectly planar - either showing a slightly curved surface or flatness imperfections in the form of small bumps - or when some residual dirt particles are trapped between the two surfaces. Since the phase of the electric field is fixed after the bond has been done, scattering on the diamond-air interface solely depends on the membrane thickness, and, of course, on the surface roughness of the sample. The choice between the operation in an air-like or a diamond-like mode is not so straightforward, unfortunately.

Since the field intensity at the diamond-air interface is maximal for a diamond-like mode while it vanishes completely for an air-like mode, one expects scattering to happen only for the former. The scattering loss in air on a surface with roughness σ_{rms} and refractive index n is given by [169]

$$\mathcal{L}_{\text{scat},0} = \left(\frac{4\pi\sigma_{\text{rms}}n}{\lambda_0} \right)^2. \quad (4.2.7)$$

Since the diamond-air interface is located inside the cavity, the cavity light field gets scattered on the surface in both directions, from the air gap and from inside the diamond. The scattering loss for the field approaching from the air gap thereby has yet to be scaled with the relative field intensity which leads to

$$\mathcal{L}_{\text{scat}} = \mathcal{L}_{\text{scat,DA}} + \frac{E_{\text{max},a}^2}{n_d E_{\text{max},d}^2} \cdot \mathcal{L}_{\text{scat,AD}} \quad (4.2.8)$$

for the total scattering loss per roundtrip. To find the expression for $\mathcal{L}_{\text{scat,AD}}$, one needs to compare the incoming and outgoing field $E_{A,in}$ and $E_{A,out}$ which are related by the transmission and reflection coefficients ρ_{AD} and τ_{DA} via

$$\begin{aligned} \mathcal{L}_{\text{scat,AD}} &= 1 - |E_{A,out}|^2 / |E_{A,in}|^2 \\ &= 1 - |\rho_{AD}E_{A,in} + \tau_{DA}E_{D,in}|^2 / |E_{A,in}|^2. \end{aligned} \quad (4.2.9)$$

Analogously, we can deduce $\mathcal{L}_{\text{scat,DA}}$. By combining equations 4.2.8 and 4.2.9 and simplifying the result as shown in [44], we obtain the expression for the effective scattering loss,

$$\mathcal{L}_{\text{scat}} \approx \sin^2 \left(\frac{2\pi n_d t_d}{\lambda_0} \right) \frac{(1+n_d)}{n_d} (1-n_d)^2 \left(\frac{4\pi\sigma_{\text{rms}}}{\lambda_0} \right)^2. \quad (4.2.10)$$

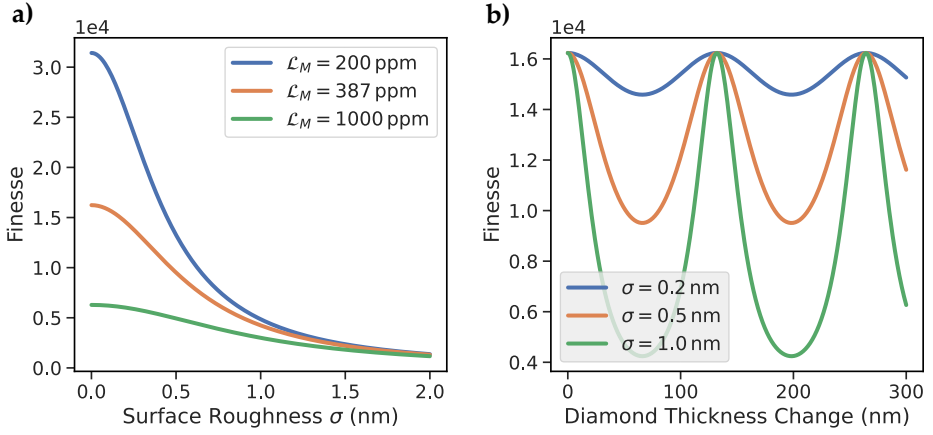


Figure 4.10: Finesse a cavity including mirror transmission and scattering, obtained analytically using eq. 4.2.10 in dependence of (a) the rms surface roughness of the diamond membrane σ_{rms} for a diamond-like mode (the orange line corresponds to the coating used in the previous simulations) and (b) the relative diamond thickness, simulated for $\mathcal{L}_M = 387$ ppm.

From this, we see that the scattering loss only depends on the mode character, given by the diamond thickness, and the surface roughness of the diamond-air interface, scaling quadratically. It is therefore crucial to smoothen the diamond surface as much as possible during the polishing and etching process of the sample preparation. Fig. 4.10(a) shows how scattering impacts the finesse of a diamond-like mode, if only mirror transmission and scattering loss are included. The orange line thereby corresponds to the coating design that has been used for the simulations in fig. 4.9, the other two lines are references for cavities with higher and lower design finesse. It becomes apparent that a low surface roughness is always desirable, but even more essential the higher the design finesse is. While superpolished fused silica substrates and our fiber mirrors can easily reach roughness values of 0.2 nm and below, even a roughness of < 1 nm can be challenging to reach for diamond membranes, depending on the surface quality of the starting material [73]. For the high-reflectivity coating (blue curve), even a surface roughness of 0.5 nm, which can be considered very low, corresponds to scattering loss that leads to an immensely lower finesse. The higher the transmission loss, the less impactful the scattering becomes, consequently. It can thus be advantageous to design mirror coatings that have a higher transmission if one wants to operate the cavity in a diamond-like character.

Absorption in the diamond The absorption loss in an optical medium is given by the Beer-Lambert law which applies to the optical cavity as

4. Integration of a diamond membrane into an optical cavity

$$\mathcal{L}_{abs}(t_d) = I/I_0 = \exp(-2\alpha t_d) \approx -2\alpha t_d \quad (4.2.11)$$

where I_0 and I are the incoming and the transmitted field intensity, respectively, and α describes the material-dependent absorption coefficient. There are literature values for α in diamond, but the absorption coefficient strongly depends on the optical quality, i.e. the purity of the diamond. Also, impurities in the material like implanted ions or color centers have an influence on the predicted absorption. We can therefore only gauge the order of magnitude that we anticipate in our samples, and treat α as a free parameter in our model. As absorption is a bulk effect that, in the case of hybrid cavities, only happens in the diamond membrane, \mathcal{L}_{abs} is independent on the mode character.

Total loss in a hybrid cavity As we now found expressions for the different sources of loss that we expect to be the dominating factors in our cavities, we can combine eqs. 4.2.6, 4.2.10 and 4.2.11 and derive the formula for the total expected loss

$$\mathcal{L}_{tot} = \mathcal{L}_M + \mathcal{L}_{scat}(\sigma_{rms}) + \mathcal{L}_{abs}(\alpha_d) \quad (4.2.12)$$

The expected finesse of a hybrid cavity is therefore given by

$$\mathcal{F} \approx \frac{2\pi}{\mathcal{L}_{tot}}. \quad (4.2.13)$$

Air-like versus Diamond-like - benefits and drawbacks As we have seen, the mode composition in a hybrid cavity is crucial for the expected performance. We now have to gauge the advantages of both air-like and diamond-like modes in order to understand how the experiment has to be designed. Firstly, the stored energy in the diamond membrane is larger for a diamond-like mode, compared to an air-like mode with the same mirror transmission (taking the alternation of the mirror coating into account). This is of course beneficial since the emitters are located in the membrane. However, one has to compare the expected losses for both cases. Here, the absence of scattering at the diamond-air interface for air-like modes has a major impact on the total loss in the system. Depending on the surface roughness of the diamond membrane, we saw that scattering can become dominant, even for a surface roughness of below 1 nm. Hence, a poor sample quality can already be an insuperable problem for the operation in a diamond-like configuration.

Contrary to that, a second major disturbing factor in the form of cavity length fluctuations has a much lower impact for diamond-like modes compared to air-like. Vibrations in this context means any mechanical or electric noise that acts on the longitudinal degree of freedom of the cavity, i.e. changing the mirror separation and thereby the resonance frequency in the cavity. Recalling fig. 4.8, we know that air-like modes (for a specific

wavelength) lead to a steep slope in the cavity dispersion while diamond-like modes feature a shallow slope. This means that air-like modes are much more susceptible to vibrations than diamond-like modes. While this is not a major issue when operating the system at room temperature, the massive mechanical noise introduced by a closed-cycle cryostat - as used in this experiment - can also inhibit any measurements requiring a resonant cavity. A more detailed discussion of vibrations and cavity stability can be found in chapter 5. Since we always have a trade-off between the advantages and disadvantages of hybrid modes and usually do not know which of the sources of loss is more severe when designing a mirror coating, it is convenient that most membranes show a small thickness gradient over the whole lateral size due to an uneven etching speed or a slightly angled cut of the raw material. Thus, one can tune the desired mode composition by changing the lateral position of the fiber mirror with respect to the sample. This will be investigated closely in section 4.5.

4.3. Technical aspects of the sample integration

4.3.1. Samples and Mirror coatings used in this thesis

Before I discuss the technical details of the membrane integration, I will give a brief overview of the different samples and mirrors - both for the planar and the fiber mirrors - that were used in this work. Table 4.1 summarizes their most important properties. Since

Coating	Design Wavelength	\mathcal{L}_M @ Design Wavelength	Spacer
C_A	637 nm	57 ppm	No
C_B	637 nm	52 ppm	No
C_C	620 nm	615 ppm	Yes
Fiber	Applied Coating	Radii of Curvature (R_x, R_y)	Profile Depth
F_A	C_B	(33.1, 30.5) μm	0.6 μm
F_B	C_A	(55.2, 48.7) μm	2 μm
F_C	C_B	(27.8, 27.3) μm	1.7 μm
Sample	Quality	Emitter	Thickness
S_A	Electronic grade	Shallow implanted (10 nm)	3.5 μm
S_B	General grade	None	5 μm
S_C	Electronic grade	None	5 μm

Table 4.1: Overview of the different coatings ($C_{(A,B,C)}$), fibers ($F_{(A,B,C)}$) and diamond samples ($S_{(A,B,C)}$) used in this thesis. The sample thickness describes the minimal thickness in the middle of the etched area. Note that the mirror coating C_C has a different design wavelength that corresponds to the ZPL of Tin-vacancy centers (SnV). Thus, when using the coating for NV experiments, we are using the coating away from its center wavelength, leading to a higher transmission.

sample S_A is the only one that hosts a significant density of NV centers, samples S_B and S_C are solely used for measurements of the optical properties in a hybrid diamond-air cavity that are presented in this section.

As commercially available diamond samples usually have a thickness of a few tens of micrometers, which leads to limitations in terms of optical cavity lengths and minimizing the mode volume in order to enable a strong Purcell enhancement (see sec. 3.2), the sample has to be thinned down to a few μm by an inductively-coupled plasma reactive-ion etching (ICP-RIE) procedure, which is described in detail in ref. [73]. In the case of samples S_B and S_C , this is done before bonding the sample to the plane mirror. For sample S_A , however, the sample is bonded first and the etching is performed afterwards. This has the advantage that the bonding can be done while the sample is thicker and therefore easier to handle, but, as a result, leaves the mirror substrate around the sample uncoated. Conveniently, this etching process is usually not perfectly homogeneous, hence leaving a slight thickness gradient on the etched area of the sample. As described above, this is advantageous, since it allows us to tune the diamond thickness and thereby the mode composition just by moving the fiber laterally over the sample. As shown in fig. 4.9(a), a thickness difference of $\lambda_0/4n_d \approx 66 \text{ nm}$ corresponds to a change from a fully air-like to a fully diamond-like mode and vice versa. Usual thickness gradients are in the μm -regime and thereby more than sufficient for our experiments while still showing a good planarity with respect to the mirror surface.

4.3.2. Cleaning and bonding procedure

Van der Waals bonding Our approach for the sample integration is based on van der Waals bonding, a technique that allows us to bring the diamond membrane in direct contact with the plane mirror surface, thereby avoiding any additional materials in the cavity [170]. The idea of this technique is to make use of van der Waals forces between the diamond surface and the planar mirror. While van der Waals forces are very strong, they only have a short range due to the r^{-6} - scaling of the potential [171]. It is therefore of great importance to bring the two surfaces very close to each other. This implies a very good intrinsic surface roughness for both the mirror coating and the diamond surface, as well as a very clean environment, since every dust particle can hinder the bond. The surface roughness of the mirrors that were used in this thesis are specified by the manufacturer to have a rms surface roughness of $< 0.2 \text{ nm}$. The membranes, however, do not only rely on a high quality starting material, but also strongly on an excellent fabrication process in order to reach a low surface roughness and avoid defects, e.g. by micro masking or polishing damage [172, 173, 112]. We therefore developed a cleaning and bonding procedure that shall be described below [73].

Bonding recipe The cleaning and bonding procedure, which is described in the following, is shown schematically in fig. 4.11. Both the mirrors and samples are cleaned

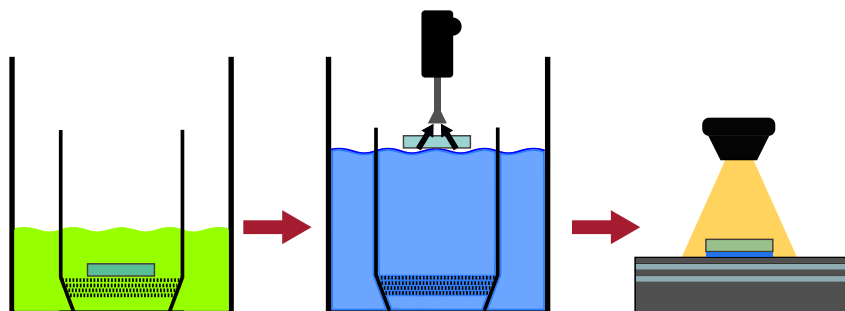


Figure 4.11: Schematic drawing of the cleaning and bonding process. The sketch shows the cleaning in piranha solution (left panel), followed by repeated rinsing in double-distilled water in order to wash away any residual acid from the sample (middle panel). Once the sample is free from any contamination, vacuum-tweezers are used to pick up the sample from the water surface and place it onto the plane mirror where it rests under bright illumination of an optical microscope (right panel). Adapted from [73].

under cleanroom conditions using piranha solution¹¹ for 45 min to remove all organic contamination. Afterwards, the mirrors and samples have to be rinsed multiple times in double-distilled water to remove the piranha solution and all residual non-organic particles. It is crucial to minimize all mechanical interactions with the mirrors and the samples. We therefore use vacuum-tweezers¹² for the samples to place them in a filter crucible that is sitting inside a beaker. This allows for performing the cleaning and rinsing steps without having to touch the samples at any time. The samples are left in the crucible while the mirrors are removed, dried carefully using compressed nitrogen, and are treated in an oxygen plasma¹³. This does not only further remove organic material, but also activates the mirror surface, leaving it hydrophilic. This will facilitate the bonding procedure, as described below.

The sample is raised by gently pouring double-distilled water into the beaker until the water level is high enough to reach the sample with the vacuum-tweezers. This allows us to pick up the sample without ever touching the bottom side of the membrane (that shall be bonded) while leaving a small amount of residual water on the surface which helps mediating the bond. The mirror is placed under an optical microscope with bright illumination. The sample is then dropped onto the hydrophilic mirror surface which leads to an even distribution of the residual water between mirror and sample. Depending on the angle between the two surfaces, interference fringes are visible on the sample (see fig. 4.12). As the water evaporates - sped up by the bright illumination - the fringes move and the surfaces eventually come into contact. When all of the water has evaporated, only very few fringes should be left, indicating a good alignment of

¹¹ 2:1 H₂SO₄ [98%] : H₂O₂ [35%]

¹² POLYVAC-pickup, polyplas

¹³ 5 minutes at 150 W, oxygen flow of 25 sccm

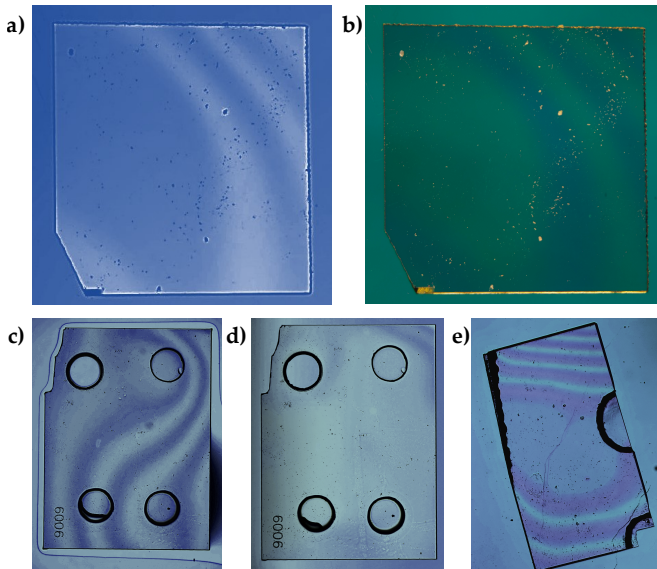


Figure 4.12: Microscope images of different diamond membranes during the bonding process. (a) Sample S_A . One can see a large region on the left hand side of the sample where almost no interference fringes are visible. The membrane was cut with an asymmetric pattern (bottom left corner) such that one can clearly identify the implanted side of the sample. (b) Dark-field microscopic image of sample S_A . (c) Microscope image of sample S_C right after dropping it onto the plane mirror. One can see plenty of fringes and the residual water at the edges of the diamond. (d) After a few minutes of bright illumination, the water evaporates, the bond emerges and the number of fringes decreases. (e) Sample S_B after the bonding process has finished. The sample has been broken in half such that the etched down membrane is located on the edge of the diamond. Even though there are numerous fringes near the top and bottom of the sample, the region around the membrane is almost completely flat. Note that samples S_B and S_C have been etched down before the bonding process while sample S_A was bonded first and then etched down afterwards.

the surfaces. If many interference fringes are visible, it is likely that the bond was not successful, but some regions could still be close enough for van der Waals forces to be effective. This might already be sufficient for some applications, e.g. when the region of interest on the sample is rather small and located in the successfully bonded area. If not, the sample can easily be removed from the mirror using another cleaning step in piranha solution¹⁴.

Bonding with an additional spacer layer While samples S_B and S_C are empty diamond membranes that we solely use to examine the performance of a diamond-air hybrid-cavity,

¹⁴ Note: a successful bond is very strong and cannot be broken mechanically without using brute force.

sample S_A hosts a layer of NV centers at around 10 nm depth, measured from the bottom side. We thus need to make sure that the electric field in the cavity will have an anti-node at this depth. This is achieved by adding an additional low-index layer on top of the DBR that effectively shifts the electric field to the desired position, as described in section 4.2. However, the mirror coating C_C was initially planned for a sample that has a different implantation depth. Therefore, we match the anti-node position again by spin-coating a thin layer of Polymethylmethacrylat (PMMA) onto the mirror¹⁵. We aim for a layer-thickness of 40 nm which should shift the field anti-node near the emitters' location. The sample is then bonded after the PMMA layer has been applied.

4.4. Room temperature scanning cavity microscope

In order to acquire a clear understanding of the different effects discussed in sec. 4.2, that the integration of a diamond membrane in the cavity has, it is crucial to being able to probe the hybrid cavity for different membrane thicknesses. We therefore use a home built scanning cavity microscope, that was developed in the group over the last years and was constantly refined. The general idea is to use the transmitted light of an optical cavity in a similar way to electron or confocal microscopes, that are all based on a probe beam that is moved laterally over the sample. This comes with the advantage compared to other microscopes, that every interaction like absorption or scattering, or fluorescence of emitters, is enhanced by the cavity. In the simplified picture of a photon bouncing back and forth between the cavity mirrors, one can think about the photon being able to interact with the sample \mathcal{F} times on average before leaving the cavity. In this section, the main purpose of the cavity microscope is to probe the performance of the resonator itself by recording laterally resolved cavity scans.

4.4.1. Mechanical Setup

As a starting point, we use the room temperature platform introduced by Thomas Hümmer in his PhD thesis [71] that is based on fiber-based microcavities, as introduced in section 4.1 and make slight adjustments. A schematic of the setup is shown in fig. 4.13 together with photographs of the fiber cavity. Figure 4.14 shows a 3D rendered CAD model of the positioning stage. Although the version shown here already anticipates some of the changes that shall be done for the adaption to the cryogenic environment, the same mechanical working principle applies for the room temperature stage. The cavity platform consists of two parts: the main frame (1) and the mirror holder

¹⁵ 30 s @ 200 rpm, then 60 s @ 2000 rpm with acceleration 1000 rpm/s.

4. Integration of a diamond membrane into an optical cavity

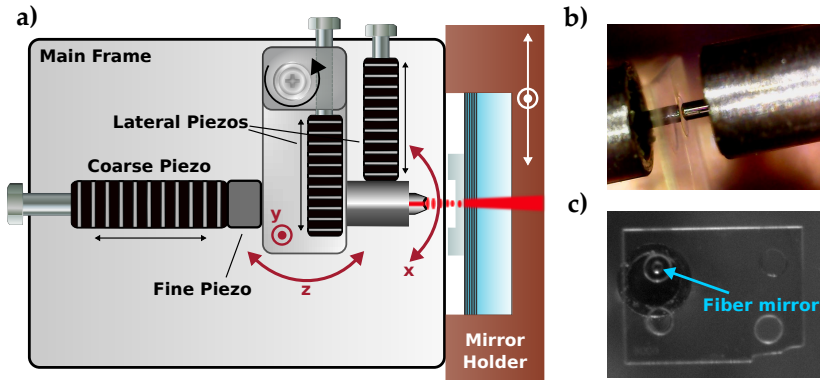


Figure 4.13: (a) Schematic drawing of the mechanical setup of the resonator main frame, visualizing the working principle of the positioning stage. The specific parts are depicted not to scale for better visibility. (b) Photograph of the cavity fiber, glued into the steel needle. The picture further shows the membrane of sample S_C and the reflection in the plane mirror (left hand side). (c) Photograph of the cavity using sample S_C , recorded through the free space optical path (see fig. 4.15).

(2). The main frame is fabricated out of titanium which provides a high stiffness and thereby a good suppression of low frequency noise (which is not of high priority for this section but becomes crucial for later fluorescence measurements). The mirror holder is made of copper which will be important for thermal conduction when moving the experiment to a cryogenic environment (see section 5.1). The key component of the main frame is the lever arm that enables the tunability of the cavity and in which the fiber mirror is fixed (3). The fiber itself is glued into a steel needle¹⁶ (4). This stabilizes the fiber while providing a rigid contact point for the x-axis piezo. Furthermore, the fiber couples quite strongly to mechanical noise, both of acoustic and vibrational origin, which improves with higher mass. For the 3D-scanning, we use a set of piezo actuators that address the spatial position of the fiber mirror. The x-axis direction is controlled by a piezo stack¹⁷ (5) that pushes directly on the steel needle and thereby bends it sideways. The installation of an y-axis piezo is a little more complicated since one wants to keep the design as flat as possible. Therefore, the y-axis piezo¹⁸ (6) is inserted in a shallow ridge at the top side of the lever arm, pushing on an extrusion at the end of the arm. This leads to a downward facing force that bends down the lever arm. To increase the scanning range, a notch is added to the opposite side of the arm where the thickness is lowered from 3 mm to 1 mm. The cavity length, i.e. the distance between the plane

¹⁶ UHU Plus endfest 300

¹⁷ Piezomechanik PSt 150/2x3/20, 460 nF measured capacitance

¹⁸ Piezomechanik PSt 150/3.5x3.5/20, 860 nF measured capacitance

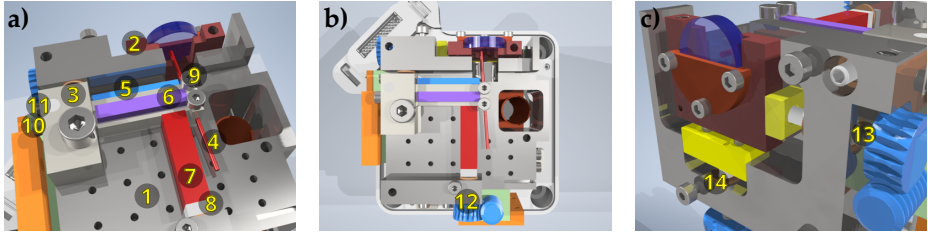


Figure 4.14: 3D rendering of a CAD model of the cavity platform. The drawing shows the lever arm mechanics (a), the top view of the stage (b) and the front view, highlighting the mirror holder together with the coarse positioning mechanics (c). Note that in this model, some changes for the cryogenic environment are already included (see ch. 5) although the essential parts for the room temperature version are the same. Most parts are colored arbitrarily for the sake of visibility.

and fiber mirror, is controlled by a piezo stack, in the following called *coarse piezo*¹⁹ (7) that pushes against the back of the lever, thereby forcing a rotational movement in z-direction. We can therefore probe the cavity length by applying a (usually periodical) voltage signal to the coarse piezo.

It becomes apparent that all three piezo actuators lead to such a rotational movement rather than just a linear displacement. In the case of the z-axis piezo, this leads to a slight angle misalignment and lateral displacement. Since the lever is rather long, this angle and thus the lateral shift are small compared to the x-y-scanning range and are therefore neglected in our setup. The movement in x- and y-direction, however is much more impactful since it indirectly also changes the cavity length. Ideally, one wants to perform a cavity scan without changing the longitudinal mode order of the cavity. The cavity length change should thus be smaller than a free spectral range. To counteract this effect, we add a second piezo stack²⁰ (in the following referred to as *fine piezo* (8)) between the coarse piezo and the lever arm. We then apply a voltage that is inversely proportional to the tilt-induced cavity length change to keep the mirror distance constant. Since the scanning range of the fine piezo is rather small, it is crucial that the scanning-induced tilt is not larger than a few free spectral ranges. To allow for a larger tuning range for the x and y-axis alignment, the bore in the lever arm, that guides the needle, is slightly angled to the upper left such that the resting position of the fiber is not centered already. This is especially helpful e.g. in the case of a tilted mirror profile or if the fiber is glued into the needle at an angle.

Additionally to the piezos, we added screws that are used to fix the piezos or provide a much coarser tuning option for the pre-alignment (9,10,11). This allows us to move the (x, y, z) -volume of $(70 \times 70 \times 10) \mu\text{m}^3$ that the piezos can reach during a scan to cover a few mm per axis. While the screws in the x- and y-direction are mostly used for the angular alignment, the z-axis screw allows us to probe the cavity at a wide range

¹⁹ Piezomechanik PSt 150/5x5/20, 1.6 μm measured capacitance

²⁰ Thorlabs PA4FEW, 195 nF measured capacitance

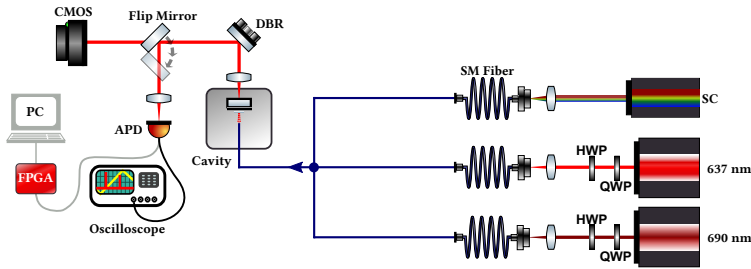


Figure 4.15: Schematic drawing of the optical configuration. The light of two different tunable diode lasers (TDL) are coupled into single mode (SM) fibers, their polarization can be adjusted using half- (HWP) and quarter-wave plates (QWP). Additionally, a supercontinuum laser (SC) is coupled into a third SM fiber. Each laser source can be coupled directly into the cavity fiber. Behind the cavity, a flip mirror is used to either enable the transmission measurement using an avalanche photodiode (APD), or to look at the position of the fiber with respect to the plane mirror using a complementary metal–oxide–semiconductor (CMOS) camera. The APD signal can then be directly displayed on an oscilloscope, or is forwarded to a computer through a FPGA module. DBR: distributed bragg reflector.

of mirror distances. Via a gear (12) which is attached to the end of the z-axis screw, we furthermore connect a simple electric motor²¹ to the stage that allows us to tune the cavity length in a reproducible way. In order to change the coarse position of the plane mirror with respect to the fiber, the mirror holder is mounted loosely on the main frame such that its position can be adjusted with the use of two more screws (13,14) that push the mirror holder in x- and y-direction. Similarly to the z-axis screw, the screws for the mirror holder are connected to electric motors via gears. The mirror holder is pulled back against the main frame using a spring that is mounted diagonally through the titanium block, acting as the restoring force. The importance of the installation of motors is minor for the room temperature setup but will become an essential building block for the cryogenic stage, see sec. 5.1.2.

4.4.2. Optical setup

Optics The optical setup is shown in figure 4.15 (for the sake of simplicity, only the essential parts are depicted here). To probe the cavity, we use three different light sources - two tunable diode lasers (TDL) and one supercontinuum laser. In order to reach the highest possible finesse, we use a TDL that operates at 637 nm²² which matches the center wavelength of coatings C_A and C_B . The laser is guided through a half-wave

²¹ Eckstein Komponente, V-TEC 6V Micro 10x12 mm DC motor with spur gearing, 54 rpm

²² Topica DL pro

plate and a quarter-wave plate in order to control the polarization of the light. This is important to optimize the overlap of the fiber mirror profile with the polarization eigenmodes of the cavity and will become important for measurements on the impact of a membrane on the polarization. We always optimize the wave plates to obtain linear polarized light at the cavity.

Furthermore, a second TDL²³ is used that operates around 690 nm. As this wavelength is off-center for all coatings used in this work, it enables us to intentionally use a lower finesse. This can be advantageous, especially if the cavity is very lossy and a higher mirror transmission is desired. Thirdly, we use a supercontinuum laser²⁴ that features a very broadband emission, allowing us to investigate the cavity dispersion, i.e. determining the hybrid mode composition.

Each of the light sources can be connected to the cavity fiber separately, allowing us to quickly switch between measurement modes. The cavity transmission is collected on the plane mirror side, being led either to an APD²⁵, or to a CMOS camera²⁶. The latter allows us to determine the exact lateral position of the fiber mirror which can be challenging since the only other way to look at the cavity is from above, making it difficult to navigate on a micrometer level. Additionally, one can use the camera to directly see the intensity pattern of the transverse mode structure of the cavity mode, e.g. if it is not clear whether the transmission corresponds to a Gaussian fundamental mode.

Data acquisition and measurement routine It is convenient to connect the APD to an oscilloscope²⁷ in order to quickly display the time-resolved cavity transmission. This, however, is not suitable if one wants to raster the fiber position with high speed while scanning the cavity length. This is necessary to speed up the data acquisition, e.g. if a high scanning resolution is chosen or a large number of scans is recorded. A typical scanning frequency that has been used mostly in this thesis is 200 Hz. Note that a higher z-axis scanning frequency means that the fastest possible lateral scanning speed without skipping resonances increases. This high scanning frequency, combined with a high finesse, i.e. a narrow linewidth of the cavity resonances, can exceed the oscilloscope's resolution, leading to missing data points and thereby lower transmission maxima. Furthermore, one wants to choose a larger z-axis scanning range than one FSR to ensure that the maximum transmission is recorded for every pixel, e.g. for the case that some longitudinal modes suffer from mode mixing (see sec. 4.1.4). Therefore, we are using a field-programmable gate array (FPGA) module²⁸, that runs an algorithm written by

²³ home-built TDL at 690 nm

²⁴ Fianium Whitelase SC450-2-PP

²⁵ Thorlabs APD130A2/M

²⁶ IDS UI-148xLE-M

²⁷ LeCroy Wavesurfer 3024z

²⁸ Red Pitaya StemLab 125-14

Thomas Hümmer [71], which records a single time trace and forwards its maximum value to a data acquisition card²⁹ such that it can be read out by the computer software³⁰. The lateral scanning is realized by feeding a linear voltage ramp to the x- and y-axis piezos using the acquisition card, whereby we choose to use the x-axis to be the fast scanning axis. In order to use the full scanning range of the piezos (-30 - 150 V), we amplify the scanning voltage^{31,32}, which is limited to 0 - 10 V by the acquisition card. It is thereby particularly important to have a suitable bandwidth for the x-axis piezo to avoid distortions in the scan.

4.4.3. Cavity transmission scans

To get an idea of the capability of the scanning cavity setup described above and possible limitations, we start off with an empty mirror that has been marked with a regular marker grid using CO₂ laser shots, similarly to sec. 4.1 (see fig. 4.16(a)). In contrast to optical fibers, CO₂-machining of already coated plane mirrors leads to a bulging of the coating, roughly in the size of the CO₂ laser profile. This adds additional loss to the mirror, leading to a considerably lower cavity transmission that can easily be identified in scanning cavity images. Not only does this grid provide a great starting point for cavity scans in terms of checking the maximum scanning range, highlighting areas with an uneven scanning range, etc.. It also serves as a reference point to reliably find specific emitters on the mirror which can be very challenging without any markers. The grid shown in figs. 4.16(a), (b) and (c) has a pitch of 10 μm, the fiber scanning range is therefore estimated to be between 60 and 70 μm which should be suitable to tune the cavity between multiple air-like and diamond-like modes via lateral movement. Figure 4.16(d) shows a different spot on the mirror that features a coarser grid, with a pitch of 30 μm. Additionally, one can identify several dark spots on the scans which we attribute to small impurities on the mirror. These small scatterers can furthermore be used to gauge the point spread function of the cavity, assumed that the lateral resolution of the scan is fine enough.

The shape of the marked spots can also be used to fine tune the prestress that is applied on the x- and y-axis piezos. If the prestress is too high for one of the piezo actuators, it might not be able to reach the maximum elongation, which is especially crucial for the y-axis piezo, since it has to bend the lever arm and therefore apply a larger force to the stage. If the prestress is too low, on the other side, it could happen that the piezo has to expand a bit before being able to affect the fiber position. A round feature in the transmission scan (marked spots as well as mirror contamination) is thus a sign for an equal scanning range and a good coarse configuration.

²⁹ National Instruments NI 6353, 1 MS/s

³⁰ Python-based scanning cavity software, written by Thomas Hümmer[71]

³¹ PDm200B, PiezoDrive. gain: 10 V/V

³² PDu150CL, PiezoDrive. gain: 10 V/V

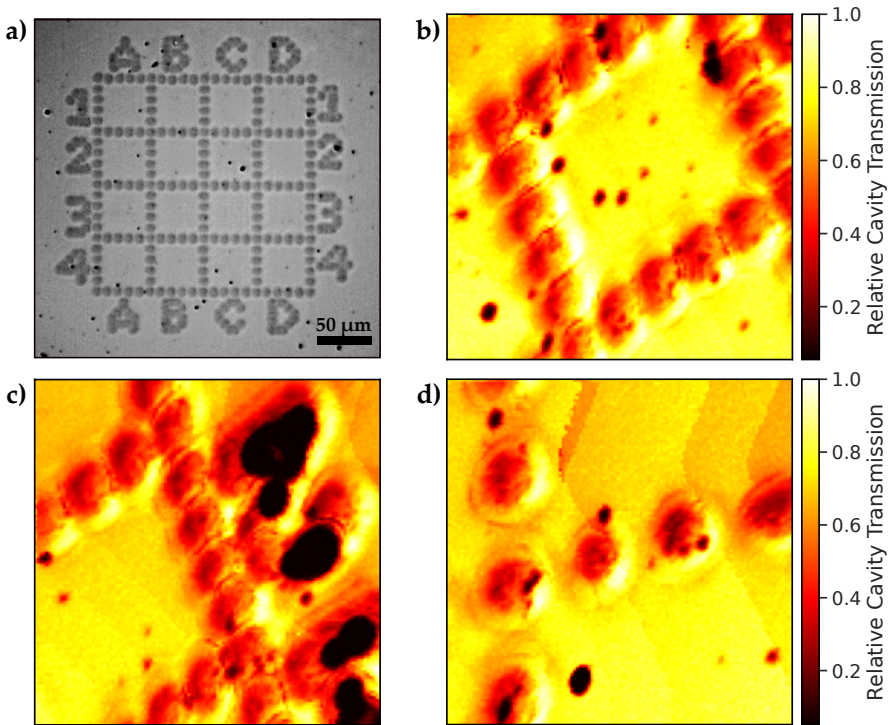


Figure 4.16: Cavity transmission scans of a marked mirror. (a) Microscope image of the marked mirror, showing the marker grid with a pitch of $10\ \mu\text{m}$. The labels outside of the grid facilitate the navigation both by looking at the mirror and via cavity transmission scans. (b) Scanning cavity image of the grid shown in (a). The marked spots become apparent through a lower transmission and can therefore be easily identified. The other (smaller) features in this scan are dirt particles or other scatterers. (c) Cavity scan of the same mirror, now revealing the labels of the checkerboard. Here shown: "1" (partially) and "2"; the mirror is rotated by almost 180 degrees with respect to (a). (d) Cavity transmission scan of a different mirror, marked with a coarser grid where the spots are $30\ \mu\text{m}$ apart from each other.

Moreover, the scan in fig. 4.16(d) features sharp lines that reminds one of contour lines. This is not a feature on the plane mirror, but rather a sign of residual tilt, induced by the curved motion of the fiber when scanning laterally. Even though we are using the fine piezo to correct the tilt length change, the tilt can overwhelm the relatively short scanning range of the fine piezo, e.g. if the resting position of the fiber is not perpendicular to the plane mirror surface. Whenever a fundamental cavity mode leaves the scanning range while being the mode with the highest transmission in the scan, the maximum transmission decreases and a sharp line appears. In the case of the scan presented in fig. 4.16(d), the cavity length increases when the fiber is tuned over the whole scanning range in positive x-direction by roughly 4 free spectral ranges. Usually,

a tilt-induced length change of a few FSR is not very problematic for transmission scans (as long as the z-axis scanning range is larger than one FSR), but can become more severe when other mode properties like the finesse shall be studied.

4.5. Scanning cavity microscopy of diamond membranes

4.5.1. Transmission and finesse maps

As we have seen in sec. 4.2, the presence of a diamond membrane inside an optical cavity can have a major impact on the performance of the device. It is therefore convenient to start off with a bare diamond membrane, i.e. without any implanted emitters, and comprehend the influence of the membrane in an experimental scenario. Most of the measurements presented here have been published in [45] and [73].

The measurements that are shown in figs. 4.17-4.30 have been performed by Jonathan Körber.

Transmission scans We start with cavity transmission scans using fiber F_A and sample S_B . In order to increase the scanning area, we perform 16 transmission scans at different positions, having a slight overlap, and stitch them together. This stitched transmission scan is shown in fig. 4.17(b). The first thing that stands out is the striped structure of the cavity transmission, showing a periodic change from bright to dark areas on the sample. By comparing the cavity transmission scan to a height map of the sample (see fig. 4.17(a)), obtained by white light interferometry (WLI), we see that the transmission stripes match the surface topology of the sample. From the estimates on the lateral scanning range of the cavity, we can gauge the complete size of the stitched scan of $\sim (150 \times 110) \mu\text{m}^2$ and find the respective position on the height map, marked by a blue rectangle in fig. 4.17(a).

One is drawn to the conclusion that the alternation of the cavity transmission arises from the hybridized mode structure, which would explain the periodic nature of the alternation. To confirm this, we gauge the height difference in the scanned region from the left to the right edge of the scan. From the height map, we know that the height difference between these two points is $\Delta t_d^{\text{WLI}} \approx 780 \text{ nm}$. In the transmission scan, we see roughly seven dark fringes; assuming the mode structure being the source of the fringes, and given the periodicity of the mode structure is $\lambda_0/2n_d$, seven fringes correspond to a thickness difference of $\Delta t_d^{\text{cav}} = (7 - 1)\lambda_0/2n_d \approx 800 \text{ nm}$. Considering the very coarse lateral scanning range calibration, this is in very good agreement to the WLI measurement. We thus state that the hybridized mode structure indeed influences the transmitted light intensity in a diamond-air cavity.

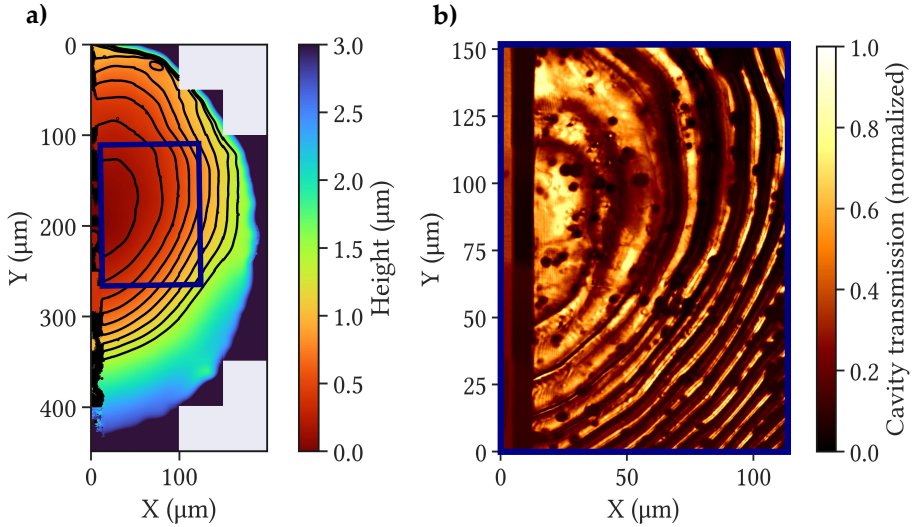


Figure 4.17: (a) Height map of sample S_B , acquired by white light interferometry. The blue area highlights the region where we performed cavity transmission scans in (b). 16 distinct cavity scans were recorded, each with a slight lateral overlap to make it possible to afterwards stitch all measurements together and thereby obtain a large area cavity microscopy image. Taken from [45].

Dispersion measurements The next question that arises is whether the high transmission areas correspond to air-like or diamond-like modes. The answer to that question is given by the respective dispersion at a given position on the sample. With the use of the white light spectrum of the supercontinuum laser (see fig. 4.15), multiple cavity modes can be excited at the same time. By additionally applying a voltage ramp to the coarse piezo, i.e. scanning the cavity length, and feeding the transmitted light into the spectrometer, we can acquire full dispersion plots for the given lateral fiber position. Fig. 4.18(a) shows such a dispersion plot when using a relatively large scanning range, revealing multiple Gaussian fundamental modes. The colorbar is chosen such that some of the much darker higher order transverse modes also become visible. The blue dots in fig. 4.18(a) refer to a transfer matrix simulation of a diamond-air cavity using $t_d = 6.00 \mu\text{m}$ and an air gap range of $6.75 - 5.20 \mu\text{m}$. This is in good agreement with the estimated dimensions in the experiment.

The fiber position is then navigated to a dark spot on the transmission scan. By repeating the dispersion measurement with a lower scanning range, we obtain a more detailed dispersion scan, shown in fig. 4.18(b). The green dashed line indicates the laser wavelength of 639.7 nm that was used for the transmission scans in fig. 4.17(b), where the dispersion has a shallow slope which corresponds to a diamond-like mode character. Opposed to that, when locating the fiber on a bright spot on the sample (fig. 4.18(c)), the

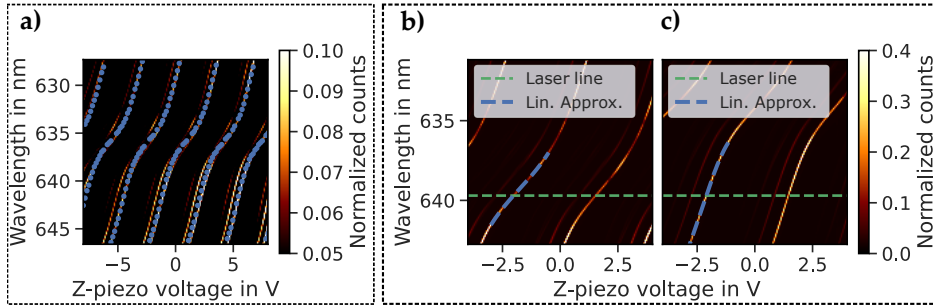


Figure 4.18: Dispersion measurements of the hybrid diamond-air cavity. (a) Large range dispersion scan, spanning over multiple air-like and diamond-like modes. Blue dots are obtained by transfer matrix simulation. Dispersion scans with smaller scanning ranges reveal a (b) diamond-like character and an (c) air-like mode character for different lateral positions on the sample for the laser wavelength of 639.7 nm. The blue dashed lines in (b) and (c) are linear approximations of the recorded data, yielding the exact slope of the dispersion at the desired wavelength. Adapted from [45].

dispersion scan shows a steep slope, i.e. an air-like mode character. One can describe the mode character quantitatively for a general case by approximating the data linearly, yielding the slope at the desired wavelength. We can then denote a value of 0 for a purely diamond-like mode and 1 for a perfect air-like mode. We thus get a measure of value for the mode composition which will be beneficial if one wants to investigate configurations that are not purely air-like or diamond-like. We conclude that for this combination of sample, mirror coating and fiber mirror, diamond-like modes seem to show a higher amount of loss than air-like modes.

Finesse scans In order to rule out the possibility that the total loss per round-trip is still higher at the bright spots, we need to examine the cavity finesse for the different mode structures.

If one wants to get a full image of how the cavity finesse behaves for different mode compositions, the goal is to measure the finesse for every pixel of a transmission scan. For this purpose, the data acquisition routine is slightly changed compared to transmission scans: instead of scanning the x-axis piezo line-wise (which speeds up the measurement), we probe the cavity at each pixel separately. The reason for this is that a finesse measurement takes much longer than a transmission scan, since every Lorentzian mode has to be fully resolved in order to measure the finesse. Depending on the number of pixels used for a scan and the finesse regime, this can prolong the measurement by several orders of magnitude.

We start by recording a transmission map at a position where multiple alternations between air-like and diamond-like modes are observable, see fig. 4.19(a). We then perform

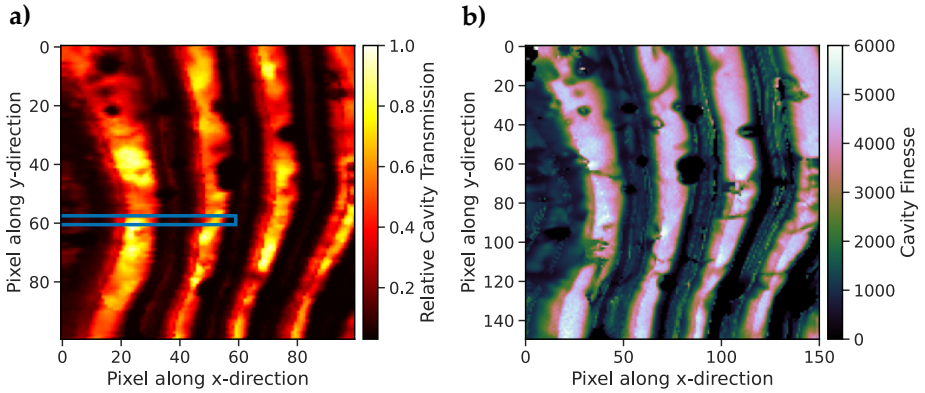


Figure 4.19: (a) Transmission map of a smaller area on sample S_B . The blue rectangle indicates the area that was used to extract a set of pixels that correspond roughly to a perpendicular movement with respect to the height profile of the sample. (b) Finesse map of the same region. The lateral resolution is slightly higher compared to the transmission map. Adapted from [45].

a finesse scan with the same lateral range, such that we can correlate the transmission and the cavity finesse for each pixel (fig. 4.19(b)). Dark spots, arising from scatterers on the plane mirror, can thereby act as reference points to confirm the lateral overlap of both scans. The same structure that we see in the cavity transmission appears in the finesse scan, and the dark stripes in the transmission map indeed match the areas with low finesse. Overall, the finesse map shows values between 200 and 5500.

The correlation between the mode structure and the cavity transmission / finesse becomes even clearer in a 1D cut of the scans. If one chooses a cutting line that lies almost perpendicular to the fringes, the lateral position results in a close-to-linear diamond thickness change. We should therefore be able to directly observe the periodic mode structure and link it to the diamond thickness. We choose the cutting line indicated by the blue box in fig. 4.19(a) which lets us access multiple air-like and diamond-like modes. One obstacle that usually comes with single finesse measurements is that the fluctuation between measurements is usually rather high, leading to a large error. In order to minimize this, we repeat the finesse measurement for several pixels and average them 50 times each. The result - together with the transmission cut along the 59th pixel of fig. 4.19(a) is shown in fig. 4.20(a). This specific pixel is chosen not only to give access to a perpendicular transmission cut, but also to avoid any particle or other lossy feature such that a drop in finesse can purely be attributed to the mode character. We clearly see the correlation between the cavity finesse and transmission. At the dark spots, the finesse drops from values up to 6000 to just a few hundred, while the transmission vanishes almost completely.

4. Integration of a diamond membrane into an optical cavity

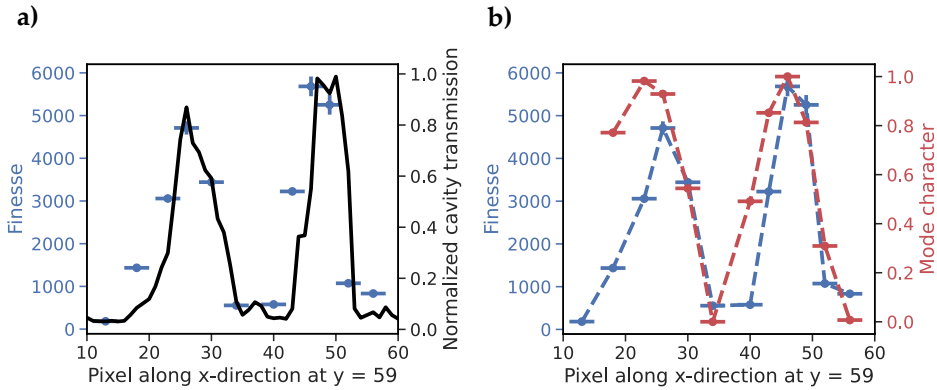


Figure 4.20: (a) Cavity finesse for several pixels along the blue line in fig. 4.19(a) (blue markers) and the transmission cut for the same region (black). (b) Mode character (red) for the hybridized cavity modes at the positions where the finesse (blue) was shown in (a). A mode character of 1 is thereby equivalent to a purely air-like mode, while 0 describes a purely diamond-like mode. Adapted from [45].

We can now extract the mode character at each given position by repeating the dispersion measurement of fig. 4.18(b) for every pixel where we measured the finesse and yield the respective mode character factor. The results are shown in fig. 4.20(b). We observe that not only the positions of diamond-like modes match the low finesse regions (and vice versa for air-like modes), but also their progression in between the maxima is in good agreement. This shows, that the majority of losses in the cavity originates from effects that are affected by the hybridized mode structure. Note that we added an error in x-direction of two pixels, caused by the piezo hysteresis and the nature of the lever arm mechanics which makes it difficult to navigate to an exact pixel in the scan.

What leaps into the experimenter’s eye, is the overall low finesse in the previous measurements, reaching maximum values of 6000, while the expected maximum finesse for the used coating is over 57000. This corresponds to a loss of 1050 ppm which cannot be explained purely by diamond effects (even more so since the finesse is measured for an air-like mode where scattering is negligible). The most likely source of this additional loss is the fiber mirror itself. This is a very common issue that can arise for multiple reasons such as a non-ideal centering of the mirror profile, scattering due to coating defects or diffraction loss [166]. Indeed, we observe that the cavity finesse of an empty cavity drops heavily for longer cavity lengths and only reaches a maximum value of 12000, as shown in fig. 4.21. It is therefore necessary to exchange the fiber mirror before proceeding with the quantitative investigation of the cavity loss. Since the stability range for a plano-concave cavity scales with the radius of curvature of the concave mirror, we now choose a fiber with a larger profile and a higher ROC, fiber F_B .

Even though the fiber coatings are almost equal for the wavelength used here (52 ppm

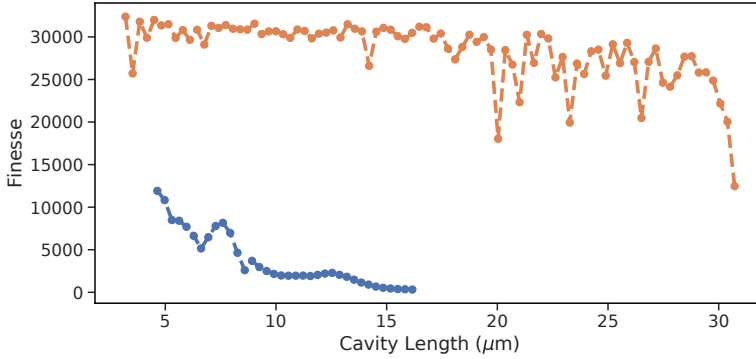


Figure 4.21: Finesse for a bare cavity using a spot on the mirror next to sample S_C for fiber F_A (blue) and F_B (orange). The maximum stability range for fiber F_B is larger due to the larger radii of curvature. Adapted from [45].

vs. 57 ppm at 639.7 nm), the new fiber (orange line in fig. 4.21) leads to a drastic increase in finesse. While the cavity finesse decreased constantly from the already low starting value for fiber F_A , there are almost no severe drops for a cavity length of $< 20 \mu\text{m}$ for fiber F_B , and also the higher longitudinal mode orders work relatively well, up to the stability range of the cavity. This is of course particularly important for our experiments with diamond membranes, since the shortest achievable (optical) cavity length is already limited by the physical thickness of the membrane combined with the high refractive index of diamond.

4.5.2. Modeling the cavity loss

Lateral variation of the finesse Now, we can remeasure the finesse map shown in fig. 4.19(b) using the new fiber mirror. The result is shown in fig. 4.22(a). The achieved finesse is now significantly higher, both for the air-like and the diamond-like modes. For air-like modes, a finesse of over 16000 can be reached, while for diamond-like modes, the finesse is 2000 – 3000. We now use a cut through the finesse map along the dashed line indicated in fig. 4.22(a) and apply the loss model that we developed in section 4.5.2. We use equation 4.2.12 for a fit and choose σ_{rms} and α_d to be free parameters (fig. 4.22(b)). The expected mirror transmission for every pixel can be extracted from the transfer matrix code, acting as a good starting point for the expected loss. In order to gauge the absorption loss as precisely as possible, it is crucial to know the diamond thickness at the position of the measurement. We therefore repeat the dispersion measurement, fit the result using the transfer matrix model and extract the estimated diamond thickness of $t_d = 5.96 \mu\text{m}$. One can then add $\lambda_0/4n_d \approx 66 \text{ nm}$ for every change from diamond-like

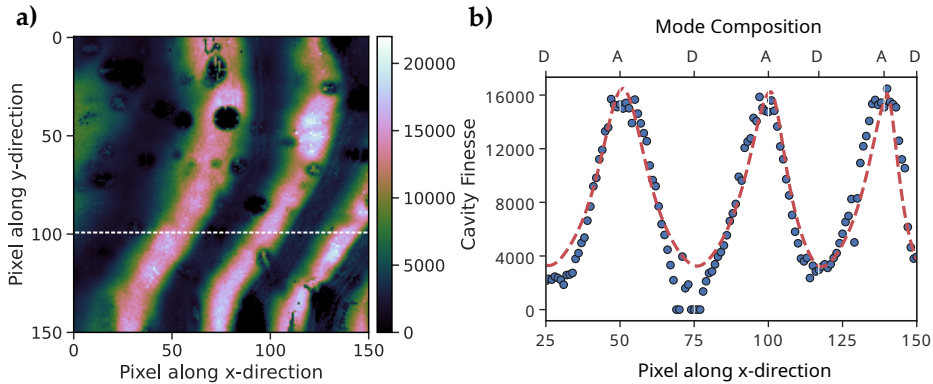


Figure 4.22: (a) Finesse map on sample S_B , now using fiber F_B . The white dashed line indicates the path along which the cut has been made for the loss modeling in **(b)**. The blue dots are the extracted finesse values from the cut through the map, the red dashed line describes the fit using the theoretical model derived in sec. 4.2. Adapted from [45].

to air-like and vice versa, indicated by "A" and "D" in the plot.

We see that the overall finesse trend can nicely be reproduced with the different sources of loss that have been regarded. Around pixel 75 in the cut, the finesse drops completely to zero. This is caused by a contamination on the mirror at this position which is barely visible in the finesse map, causing the transmission to drop almost completely and making it impossible to perform a finesse measurement. The fit yields $\alpha_d = (0.19 \pm 0.01) \text{ cm}^{-1}$ and $\sigma_{\text{rms}} = (1.02 \pm 0.03) \text{ nm}$. The value for the absorption coefficient is in good agreement with the expected value of $\alpha_d = 0.1 - 0.5 \text{ cm}^{-1}$ for a general grade diamond, which contains a higher nitrogen concentration of $> 100 \text{ ppb}$ [174].

The fit value for the surface roughness, however, is significantly higher than the value of $\sigma_{\text{rms}} = 0.4 - 0.5 \text{ nm}$, obtained via atomic force microscopy [73]. The reason for this discrepancy could be unconsidered sources of loss, like scattering at the diamond-mirror interface due to an imperfect van der Waals bond, or surface absorption due to sp^2 carbon and surface defect states.

Increased transverse mode-mixing In most areas on the sample, we observe thin lines in the transmission map that seem to follow the topology of the sample, i.e. the fringes of air-like and diamond-like modes. Interestingly, these lines appear preferably in diamond-like regions. The effects strongly reminds of transverse mode-mixing which can be seen in bare cavities also and has been discussed in section 4.1.4.

The fact that the dark lines match the membrane topology suggests that this effect mostly occurs at the diamond-air interface. Considering the "usual" source of trans-

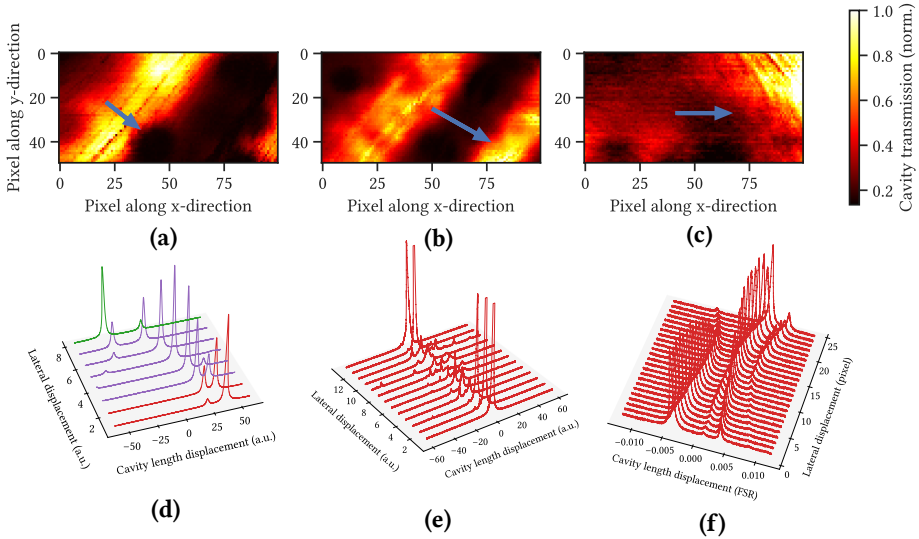


Figure 4.23: (a), (b), (c) Segments of cavity transmission maps on sample S_B where mode-mixing occurs. To reveal the effect, the fiber is moved along the blue arrows in the respective scans while scanning the cavity length. (d), (e), (f) Transmission spectra for several pixels along the blue arrows. Taken from [45].

verse mode-mixing, i.e. a fundamental mode becoming degenerate with a higher order transverse mode due to the different Gouy-phase, one can understand the increased occurrence here by the different mode character of the coupling modes. The different Gouy-phase does not only detune the resonance frequencies of higher-order modes, but it also shifts the diamond thickness that leads to air-like or diamond-like mode character [175]. This means, that a fundamental mode that shows an air-like character, could become degenerate with a higher order transverse mode that is diamond-like for the exact same diamond thickness, leading to a much stronger coupling between the two modes. This would furthermore explain why the severity of mode-mixing is increased for certain diamond thicknesses.

In order to prove that the dark lines indeed originate from mode-mixing, one can record a transmission map, set the fiber position close to a dark line and then move the fiber slowly perpendicularly over the line while scanning the cavity length and recording the transmission on the oscilloscope. Some exemplary transmission scans are shown in fig. 4.23(a, air-like), (b, diamond-like) and (c, general case).

Similarly to ref. [167], the dark lines appear for certain longitudinal mode orders and cavity lengths, when a higher order transverse mode becomes degenerate with a fundamental mode with a different longitudinal mode order. Figures 4.23(d), (e) and (f) show the respective cavity transmission spectra. In the case of fig. 4.23(a, d), one can observe two areas where mode-mixing occurs, showing as avoided crossings in the transmission

4. Integration of a diamond membrane into an optical cavity

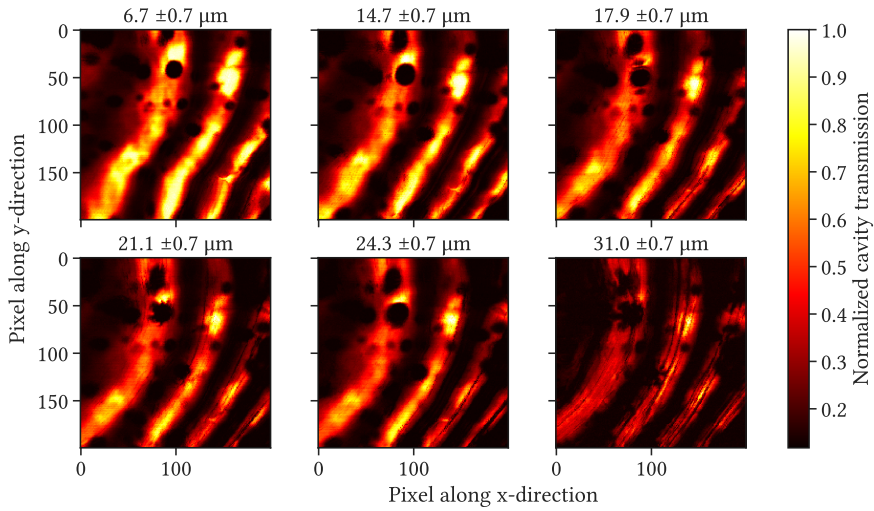


Figure 4.24: Transmission maps of sample S_B for different cavity air gaps. The cavity length thereby increases while leaving the lateral position unaffected. Transmission values are normalized to the maximum value of the upper left panel. Taken from [45].

spectrum. One can clearly see that the higher order transverse mode "approaches" from the left-hand side for the first scan, and then again for the 8th pixel.

In the case of the diamond-like mode (fig. 4.23(b, e)), we see that the mode-mixing is much more severe, leading to an almost complete drop in transmission. Furthermore, not only one higher order transverse mode is coupling to the fundamental mode, but multiple modes couple to each other, causing a wild cavity mode "forest". A further example of mode-mixing is shown in fig. 4.23(c, f), showing clearly the avoided crossing of the two cavity modes.

We now want to investigate, how the severity of mode-mixing changes when different cavity parameters change. Firstly, we record a cavity transmission scan in a region that shows mode-mixing and then change the air gap, i.e. the cavity length. The corresponding transmission maps are shown in fig. 4.24. We see that the bright regions, i.e. the air-like modes, are virtually free from mode-mixing lines for small air gaps. When increasing the mirror separation, we notice that particularly the dark regions start to show mode-mixing, while the bright regions are mostly unaffected. By further increasing the cavity length, we start to see mode-mixing appear also for air-like modes. For the maximum cavity length of $31.0 \mu\text{m}$, the transmission in air-like regions has drastically decreased while cavity measurements in diamond-like regions are almost impossible to perform.

Notably, not only the transmission on small areas drops as mode-mixing becomes more frequent for larger air gaps, but also the overall transmission decreases. This could either be caused by additional loss in the cavity, which should then also affect the cavity

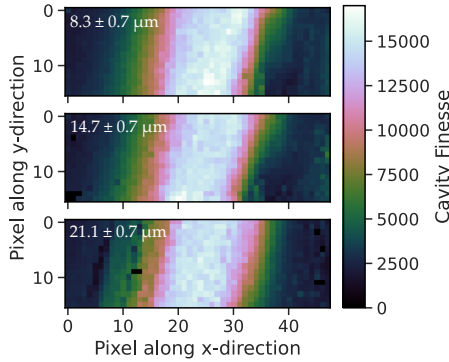


Figure 4.25: Finesse scan for different cavity air gaps at an air-like region. Adapted from [45].

finesse, or be purely dominated by mode-matching, as the mode overlap of the fiber mode and the cavity mode might decrease for larger cavity lengths. This would leave the maximum finesse unaffected for a suitably large scan range.

We therefore position the fiber mirror at an air-like region that is free of mode-mixing in the transmission scan and perform finesse scans for different air gaps. The results are shown in fig. 4.25. Here, we see no drop in finesse whatsoever, which brings us to the conclusion that the transmission drop in fig. 4.24 is indeed caused by mode-matching.

Additional loss by mode curvature So far, we were only able to change the cavity length by tuning the air gap, but the diamond thickness stayed roughly the same, modulo a few tens of nanometers to tune between air-like and diamond-like modes. However, it would be interesting to investigate whether the diamond thickness also has an influence on the the overall cavity performance as well as on the presence of mode-mixing. Therefore, we swap the sample to S_C , an electronic grade sample that features four rather than just one etched membranes that all were etched down to different thicknesses. This allows us to examine the cavity performance for different thickness regimes. We measure the cavity finesse both for air-like and diamond-like modes at different positions, leading to different effective cavity lengths and diamond thicknesses. The average of 100 respective measurements is shown in fig. 4.26. What strikes the eye here, is that the finesse for air-like modes drops way faster than expected. Since we saw that the cavity finesse for a bare cavity stays almost constant for the whole stability range, we would only expect the bulk absorption to increase for thicker diamond membranes. However, absorption loss is expected to increase linearly with diamond thickness, which is not the case here, considering that $\mathcal{F} \sim 1/\mathcal{L}_{\text{tot}}$. Contrarily, the finesse for diamond-like modes is rather low, but stays fairly constant for thicker membranes. Hence, there seems to be an effect that decreases the performance of an air-like mode with increasing diamond thickness while leaving diamond-like modes almost unaffected.

One likely candidate is the influence of the mode curvature at the diamond-air interface,

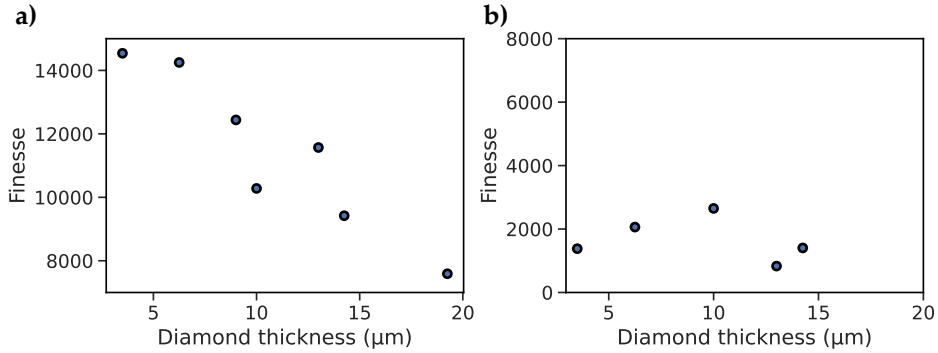


Figure 4.26: Maximum finesse value for different diamond thicknesses in an (a) air-like setting and a (b) diamond-like one. The measurements have been performed on four different regions on the sample that have been etched down to different thickness regimes. Adapted from [45].

which is illustrated in fig. 4.27. Due to the continuity condition at both cavity mirror surfaces, the cavity mode shows a minimal curvature at the plane mirror and is curved at the fiber mirror, matching the mirror curvature. Thus, the cavity mode wavefront shows some curvature at the diamond-air interface, depending on the diamond thickness. While this curvature becomes negligible for thin membranes, it has to be taken into account when the diamond-air interface lies further away from the mode waist. The consequence is that a cavity mode might be air-like at its central region but due to the mode curvature, the outer region of the mode is shifted slightly to the diamond-like character. Following from that, sources of loss that should be exclusively present for diamond-like modes can partially add loss to an air-like mode. This, of course also happens the other way around, i.e. diamond-like modes containing leakage of an air-like mode in the outer region of the cavity mode. This volume is depicted as the red shaded area in fig. 4.27. We therefore need to develop a model with which one can gauge the extent to which a diamond-like mode leaks into an air-like mode and vice versa.

We start with a cavity mode that we assume to be perfectly air-like at the center of the mode, thus facing minimal scattering and transmission loss. The different position of the field node between the center and the edge of the Gaussian mode is then given by

$$\Delta d = R - d = R - \sqrt{R^2 - w^2} \quad (4.5.1)$$

where R is the mode's radius of curvature, d is the projection of R onto the optical axis when pointing to the mode radius and w is the beam radius at height d . For Gaussian beams, the radius of curvature and beam radius are given by

$$R(z) = z \cdot \left(1 + \frac{\pi w_0^2 n_d}{\lambda z} \right)^2, \quad (4.5.2)$$

$$w(z) = \left(w_0^2 \cdot \left(1 + \frac{\lambda z}{\pi w_0^2 n_d} \right)^2 \right)^{1/2} \quad (4.5.3)$$

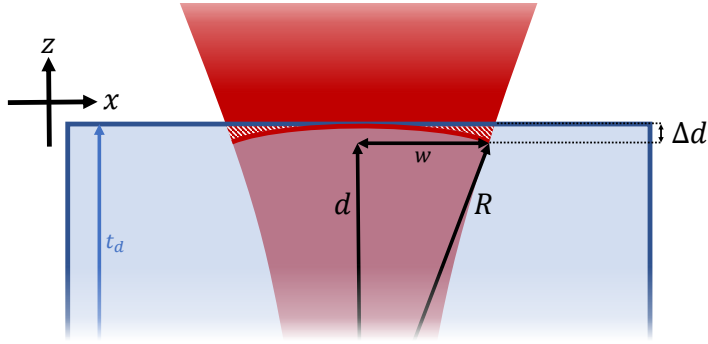


Figure 4.27: Schematic drawing of a Gaussian mode in a diamond-air hybrid cavity with the most important parameters. The shaded red area highlights the mode volume where the effective diamond thickness is altered due to mode curvature, compared to the middle region of the mode. The sketch is not to scale for better visibility.

with w_0 being the beam waist, z the distance to the mirror surface, λ the wavelength and n_d the refractive index of diamond. The beam waist of the cavity mode is altered by the presence of the diamond membrane and can be described via [44]

$$w_0 \approx \sqrt{\frac{\lambda}{\pi}} \left(\left(t_a + \frac{t_d}{n_d^2} \right) \left(ROC - \left(t_a + \frac{t_d}{n_d^2} \right) \right) \right)^{1/4}. \quad (4.5.4)$$

Here, ROC denotes the radius of curvature of the mirror profile on the fiber. We can then define a dimensionless factor $C_{a/d}$ that describes the mode character shift at a given radial distance r with respect to the center where 1 is a full shift from air- to diamond-like and vice versa:

$$C_{a/d}(r) = \frac{4n_d \Delta d}{\lambda} \cdot \frac{r}{w}. \quad (4.5.5)$$

Here, we approximate the mode curvature as linear along r since $r, w \ll d, R$. As loss in our system scales with the field intensity present at the source of the loss, we have to add the mode's Gaussian intensity profile as an additional factor. Integrating over the whole mode then gives us the total amount of diamond-like character in an air-like mode,

$$C_{curv} = \int_0^\infty C_{a/d}(r) \cdot \left(\frac{w_0}{w} \right)^2 \cdot e^{-2r^2/w^2} dr. \quad (4.5.6)$$

Note, that C_{curv} is not the actual loss, but only the scaling factor for losses originating from diamond-like modes leaking into an air-like mode. To include this loss to the experiment data, we use the lowest loss that we measured for diamond-like modes,

4. Integration of a diamond membrane into an optical cavity

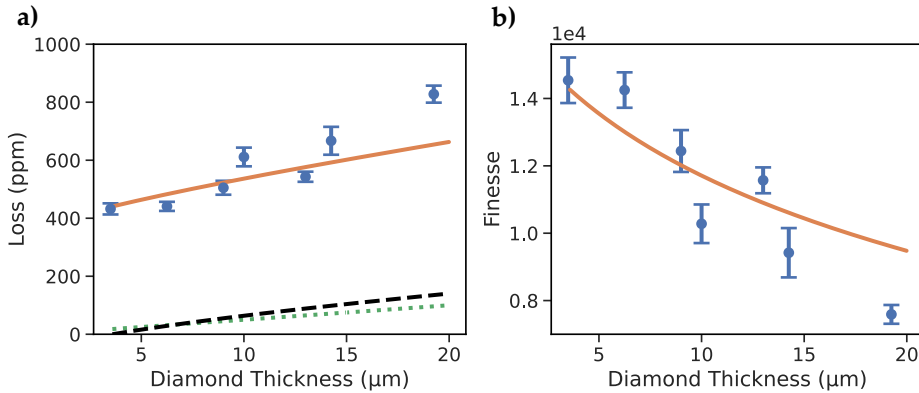


Figure 4.28: (a) Estimated total cavity loss (orange), including loss by mirror transmission (not shown here), absorption loss (green dashed line) and the additional loss by mode curvature (black dashed line). The experimental loss values are extracted from the finesse measurement in fig. 4.26(a). (b) Respective expected Finesse (orange), together with the measured values from fig. 4.26(a).

multiply this with C_{curv} and add it to the total loss. This combined with an estimated absorption loss assuming $\alpha = 0.05 \text{ cm}^{-1}$ [174] and the loss via mirror transmission is in good agreement with the measurement, see fig. 4.28(a), and fig. 4.28(b) for the respective finesse. One inaccuracy of this model is that we set the additional curvature loss to zero for the lowest diamond thickness, which should not be the case for any membrane with a thickness > 0 . The measured loss, however, is in the case of the thinnest membrane already limited by the transmission loss alone, leaving no room for any additional loss to be added.

In total, it has to be stated that even for a perfect air-like mode, contributions from diamond-like-exclusive loss sources have to be taken into account, and vice versa. Another aspect that can be explained qualitatively by the presence of mode curvature is the increased mode-mixing. Even for an air-like mode where we assumed the electric field intensity to be zero at the interface, the outer regions of the cavity mode can scatter. This scattered light can then preferably couple to higher-order transverse modes that have a larger spatial extent. This can then - additionally - lead to increased clipping losses at the fiber mirror surface [166].

This effect gives further emphasis on the importance of keeping the membranes as thin as possible.

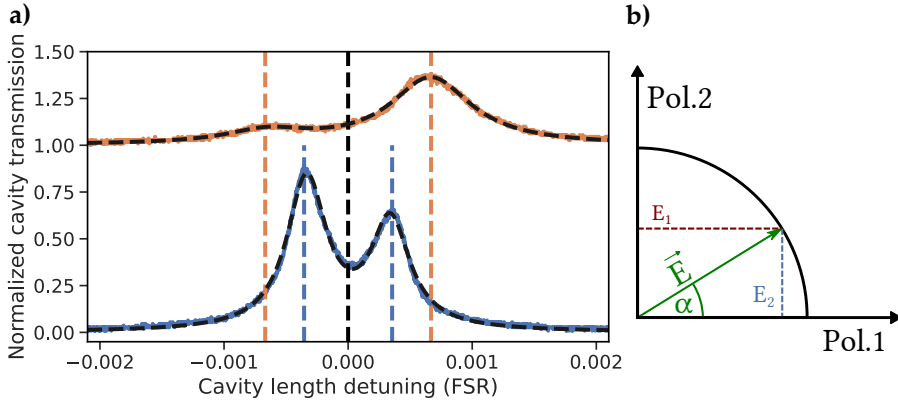


Figure 4.29: (a) Example of the increased polarization mode splitting that occurs on the membrane. The splitting is larger for a diamond-like mode (orange) compared to air-like modes (blue). The relative peak height thereby yields the angle between the two eigenmodes, described schematically in (b). The angle α is defined between 0 and 90° . Adapted from [45].

4.5.3. Increased polarization mode splitting and diamond-induced birefringence

For experiments with concave cavity mirror profiles, especially when they are CO_2 laser-machined as is the case for our fiber mirrors, one often observes the presence of a frequency splitting of the cavity modes (also the fundamental ones). This effect is caused by imperfect mirror shapes, leading to a slight ellipticity, i.e. two different radii of curvature, depending on the axis that is investigated. The degeneracy of the two polarization eigenmodes is then abrogated [176]. One usually anticipates this effect and compensates it by matching the incoming linear polarization axis with one of the half axes of the mirror profile. Thus, one of the polarization modes vanishes and the other one can be used for experiments.

In our experiments on diamond membranes, however, we faced the problem, that the frequency splitting reemerges when changing the lateral position of the fiber mirror with respect to the sample, making it virtually impossible to perform scanning cavity measurements without exciting both polarization modes. We also observe consistently that the splitting does not only vanish and appear, but also shows a larger frequency gap for regions with a low finesse. This is shown for an exemplary measurement in fig. 4.29(a). One can define a polarization angle α that describes the relative amplitude of the two eigenmodes, as depicted in fig. 4.29(b). The angle shown here is defined between 0° and 90° where the two extrema describe the cases of one of the polarization eigenmodes completely vanishing. Mathematically, the angle is described as $\tan \alpha = E_2/E_1 = \sqrt{I_2/I_1}$. In order to confirm the dependence of the frequency splitting on the cavity finesse, we perform a cavity raster scan yet again, now fitting a double Lorentzian to the fundamental

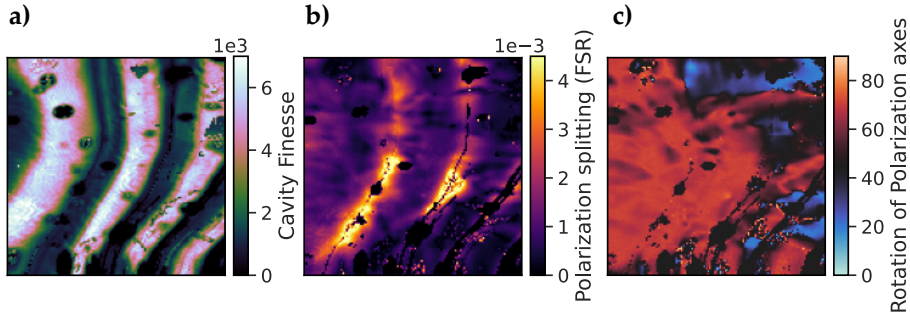


Figure 4.30: Cavity measurements of the polarization splitting. (a) Finesse map of the inspected region on the sample, showing the characteristic fringes. (b) Polarization splitting of the same region. The splitting is normalized to one free spectral range. (c) Polarization angle α for the same area. Pixels where a measurement was not possible or the Lorentzian fit did not converge are set to 45° , i.e. both modes are equal. Adapted from [45].

mode for each position. This then returns the frequency splitting as well as the angle between the two polarization axes, i.e. the two peak intensities of the polarization eigenmodes. The results are shown in fig. 4.30. The finesse map, shown in (a), features the same structure as the previous scans, i.e. a higher finesse for air-like regions and lower finesse values for a diamond-like character. Note that this measurement was performed using fiber F_A , hence the lower finesse maximum. When comparing the finesse map to the measurement of the polarization splitting (fig. 4.30(b)), the same structure appears, following the finesse fringes and thereby confirming the punctual measurements that have shown a stronger polarization splitting for lower finesse i.e. diamond-like modes. The splitting fluctuates around 0.1 % of a FSR for air-like and around 0.3 – 0.4 % for diamond-like modes. This indicates that the increased frequency splitting is again induced by the hybridized mode structure. This is caused by the relative energy in the diamond which is higher for diamond-like modes and thus leads to an additional phase shift.

However, even the lower polarization splitting for air-like modes is much more prominent compared to measurements on bare cavity mirrors which show a splitting of only $\delta = v_{\text{split}}/\Delta\nu = 3.82 \times 10^{-5}$, i.e. up to two orders of magnitude lower. The value for the bare cavity is consistent with the expected polarization splitting caused by the measured ellipticity of the mirror profile, given by [176]

$$\delta_{\text{mirr}} = \frac{\lambda_0}{4\pi^2} \frac{ROC_x - ROC_y}{ROC_x ROC_y}, \quad (4.5.7)$$

where ROC_x and ROC_y are the respective radii of curvature of the fiber mirror. The increased polarization splitting in general can be explained by birefringence, caused by local strain in the sample. If we leave out the higher splitting for diamond-like modes, i.e. consider the air-like splitting as the pure diamond-induced frequency shift, it

corresponds to a change in refractive index Δn_d . We can describe Δn_d via the acquired phase of the two polarization eigenmodes in the diamond, given by

$$\frac{\phi_{(x,y)}}{2\pi} = \frac{t_d}{\lambda_0/n_{d,(x,y)}}. \quad (4.5.8)$$

The relative frequency splitting can then be described as

$$\delta = \frac{\nu_{\text{split}}}{\Delta\nu} = \frac{\phi_x - \phi_y}{2\pi} = \Delta n_d \frac{t_d}{\lambda_0} \quad (4.5.9)$$

with $\Delta n_d = n_{d,x} - n_{d,y}$. The difference in refractive index is hence

$$\Delta n_d = \delta \cdot \frac{\lambda}{t_d}. \quad (4.5.10)$$

The frequency splitting of 0.1 % for the air-like modes thus corresponds to a refractive index difference of $\Delta n_d = 1 \times 10^{-4}$. This is an indication for a high local strain that leads to dislocations in the diamond lattice and therefore to birefringence [177]. On contrast, carefully grown diamond can achieve strain that is two orders of magnitude lower [172]. Repeating the measurement on sample S_C - which is electronic grade - yields a much lower refractive index difference of $\Delta n_d \approx 2.5 \times 10^{-5}$, supporting the assumption that the birefringence is indeed induced by local strain.

When analyzing the polarization angle as shown in fig. 4.30(c), a more differentiated picture arises. One can still see a clear structure on the sample which, however, does not match the sample topology and is thus independent of the mode character. The dark spots from the other scans being visible is caused by the fact that a value of 45° is assumed whenever the double Lorentzian fit is not successful. This is another indicator of strain in the membrane which is not impacted by the diamond thickness, i.e. the mode structure.

The measurements in this chapter show clearly that the integration of a diamond membrane (or any dielectric, e.g. yttrium orthosilicate or silicon carbide) into an optical cavity can massively change the optical properties of the system. While the diamond thickness, i.e. the hybridized mode structure, and the surface quality have the biggest impact on its performance, also effects from the bulk diamond like absorption or strain-induced polarization splitting have to be taken into account. We see that the right choice of material combined with a careful sample preparation are crucial in order to achieve the desired Purcell enhancement.

5. A highly stable, fiber-based Fabry-Pérot microcavity for cryogenic environments

In the last chapter, we discussed the integration of diamond membranes into an optical fiber-based microcavity and the obstacles that the additional optical layer brings with it. We learned that the full tunability of the system is not just a nice feature to have, but rather an essential building block of cavity experiments using dielectric membranes. At the same time, many quantum optical applications require a high cavity finesse, i.e. narrow cavity resonances. A very precise control over the mirror separation is therefore needed in order to keep the cavity resonant with the desired wavelength. Additionally, most quantum emitters require an operation at cryogenic temperatures in order to reach their optimal properties like long coherence times and a Fourier-transform-limited optical linewidth. This adds several technological challenges to the experiments.

The crux thereby is that one usually wants to make the design for a cavity as stiff and monolithic as possible in order to minimize vibrations. At the same time, tunability always comes with the need for movable parts. These two contradicting requirements are very hard to fulfill to a reasonable level simultaneously. One therefore has to carefully choose cryogenic-compatible materials for the setup without sacrificing any features of the system. Cryostats, especially closed-cycle systems like the cryostat used in this thesis, add a high amount of vibrations to the setup. So far, commercially available positioning stages are not able to achieve the mechanical stability that is needed for cryogenic cavity experiments.

In this chapter, I will thus introduce the cryogenic version of the home-built scanning cavity setup that was used in chapter 4. A commercially available version of such a cavity stage, based on the work of Thomas Hümmer and Jonathan Noé, was developed in parallel to this work.³³

The chapter focuses firstly on the adaptations that were done in terms of design and choice of materials. After that, a thorough characterization of the cavity platform is presented while investigating different approaches to suppress any noise, both of mechanical (including acoustic) and electrical nature.

The results presented in this chapter have partly been published, see ref. [75].

³³ Qlibri GmbH, München

5.1. Stability requirements and cryogenic adaptations

5.1.1. Theoretical considerations

Before designing a cryogenic resonator platform, one has to address the theoretical aspects of a cavity, suffering from noise. The figure of merit hereby is the full width at half maximum (FWHM) cavity linewidth which defines the required cavity length stability such that the cavity will stay on resonance for the desired wavelength most of the time. When considering noise, i.e. a jitter of the mirror separation, it is suggestive to express the cavity linewidth in terms of mirror separation as well, which is given by [71]

$$\delta d = \frac{\lambda/2}{\mathcal{F}} \quad (5.1.1)$$

and is thus independent from the cavity length.³⁴ For a cavity with a finesse of 30 000 at 637 nm (which is a realistic scenario for our experiments), the linewidth thus translates to $\delta d = 10.6$ pm. If one wants to gauge how severe the effect of a cavity length jitter on the eventual performance in the experiment is, a good metric is the normalized Purcell factor. For a cavity that is affected by length fluctuations with a Gaussian distribution, this is given by [51]

$$\frac{C(\delta d, \Delta z)}{C_0} = \sqrt{\frac{\pi}{8}} \frac{\delta d}{\Delta z} \exp\left(-\frac{\delta d^2}{8\Delta z^2}\right) \left(1 - \operatorname{erf}\left(\frac{\delta d}{2\sqrt{2}\Delta z}\right)\right). \quad (5.1.2)$$

Here, Δz is the rms cavity length jitter, C_0 describes the ideal Purcell factor without any vibrations. Fig. 5.1 shows the outcome of eq. 5.1.2 for different finesse values. From that, one can derive that a vibration noise level of one linewidth results in a reduction of the achievable Purcell factor to just over 40 %. For a finesse of 100 000, this is already the case for only $\Delta z = 3.2$ pm, which is a demanding challenge, even for a room temperature setup. In order to gain reasonable benefits from the Purcell effect, one rather wants to aim for 80 % of the ideal Purcell factor or higher. This is only possible, if one achieves a cavity length jitter in the low pm regime. If a more conservative cavity finesse is assumed (15000 in this case, which comes close to the values that were measured on the membranes in chapter 4), the acceptable noise level increases by a few pm, but one has to keep in mind that the ideal Purcell factor is then lower, as well.

The few pm regime has so far not been reached with tunable cavities in closed-cycle cryostats, with 14 pm being so lowest noise level reported so far when actively stabilized [51]. In her dissertation [72], Julia Benedikter presented a first cryogenic version of the scanning cavity setup used in chapter 4, reaching an actively controlled stability of 4 pm rms when the cryostat was turned on at room temperature. The noise level, however, increased a lot when cooling down the platform to 12 K, showing a stability of 60 pm.

³⁴ Note that this is only the case if the linewidth is expressed in terms of mirror separation. The linewidth in dependence of the wavelength, however, is more sensitive to changes in wavelength for longer cavities.

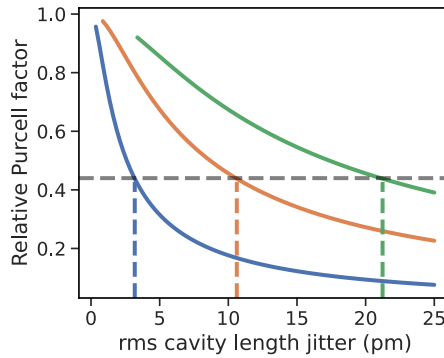


Figure 5.1: Dependence of the normalized Purcell factor to the rms cavity length jitter for a cavity finesse of 100 000 (blue), 30 000 (orange) and 15 000 (green). The vertical dashed lines indicate the respective cavity linewidths in terms of mirror separation for a wavelength of 637 nm.

While the stability at room temperature without the compressor running was already in the sub-pm regime, the significant noise spike at cold temperatures highlights the need of a redesign of the cavity platform, which will be discussed in the following. The design from ref. [72] is thereby used as a starting point with various modifications being applied.

5.1.2. Redesign of the cavity stage for the use in a closed-cycle cryostat

In the following, I will describe the most important aspects of adapting the cavity platform for cryogenic temperatures in a closed-cycle cryostat³⁵. For the basic working principle, see the description in sec. 4.4.

What the new cavity stage should offer A well designed cavity should avoid coupling to any kind of external noise as much as possible. As Thomas Hümmer has shown in his dissertation, the most prominent (acoustic) frequencies in a typical laboratory environment can be found below 2 kHz [71]. One essential aspect is therefore to shift the first eigenfrequency of the system as high as possible such that the coupling to the noise is minimized. For a general mass-spring system, we know that the eigenfrequency is given by $\omega_0 = \sqrt{\frac{k}{m}}$ where k is the spring stiffness and m the mass. Hence, the mass should be as low and the stiffness as high as possible.

³⁵ *Montana Cryostation CS1*

Choice of materials and design changes The design of the updated cavity platform is presented in fig. 5.2(a), highlighting the changes that were made. The upper part of the platform (in the following called *top frame*) caused problems during the cooldown due to the very different thermal expansion coefficient of $23.1 \times 10^{-6} \text{ K}^{-1}$ [178], compared to the one of the used piezo actuators, $-5 \times 10^{-6} \text{ K}^{-1}$ ³⁶. This leads to a strong thermal drift when cooling down the setup of several hundred μm , which has to be taken into account during the cooldown. We therefore changed the massive block of the top frame from aluminium to titanium. This has the advantage that the expansion coefficient of titanium is much closer to the one of the piezo actuators, being $8.6 \times 10^{-6} \text{ K}^{-1}$ [178]. The cavity drift is hence much smaller and easier to compensate.

Even though the density of titanium is 4.5 g/cm^3 and thus higher than the one of aluminum (2.375 g/cm^3), a cavity stage made of titanium is (also mechanically) beneficial nevertheless due to its high stiffness which further minimizes the coupling to external acoustic noise. One disadvantage of titanium is its thermal conduction, which is over a factor of 10 smaller than the one of aluminium. The heat transfer is thus much slower, which increases the importance of an efficient thermal coupling to the cold platform of the sample chamber. The thin copper sheets used in ref. [72] are therefore replaced by super flexible copper braid stripes³⁷. Additionally, we used a higher amount of thermal links to increase the thermal load that can be transported away from the titanium block.

Aside of thermal drifts, the second limiting factor was the connector pieces with which the top frame was mounted to the base frame (the lower block in fig. 5.2). While the mechanical decoupling worked nicely at room temperature, the material of the connection³⁸ apparently became stiff when cooled down, leading to a massively increased coupling of vibrations coming from the cold platform. Therefore, the connection piece is replaced by a set of steel springs³⁹ which act on the top frame as a mechanical low-pass filter. The high frequency noise coming from the cryostat should be converted by the springs to a low frequency motion which can be easily addressed by active stabilization. Furthermore, we changed the base frame from aluminium to copper, improving the thermal conduction from the cold platform to the top frame.

Other minor modifications were also made, e.g. the position on the mirror holder, where the spring is connected that pulls the part back against the titanium block, or the wiring of the piezos, motors and temperature sensors. These changes are discussed in the following. There are several essential parts on the top frame of the cavity stage, some of which have changed compared to the first cryogenic platform, while others have been carried over to the new design, but are of great importance such that I shall discuss them here. Fig. 5.2(b) shows the top view of the updated positioning stage, displaying the most important parts of the top frame:

³⁶ Provided by the manufacturer. Note the negative expansion coefficient, meaning that the piezo expands when being cooled down.

³⁷ *Copper Braid, SuperFlex 0.2 mm*

³⁸ A combination of a thin Teflon sheet and an aluminium slab was used. The Teflon sheet seems to be the likelier reason for the increased coupling.

³⁹ spring constant: 2.909 N/mm, length: 11.18 mm, outer diameter: 6.1 mm, wire diameter: 0.66 mm

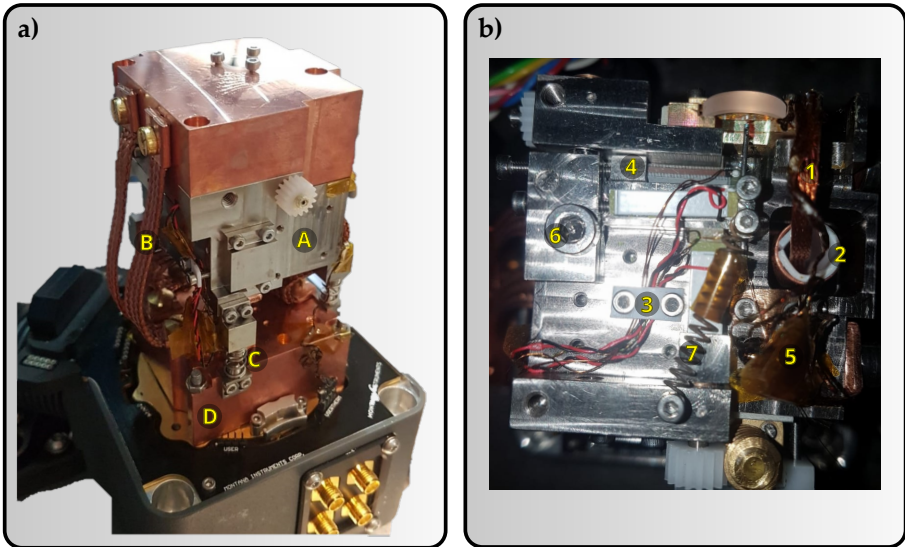


Figure 5.2: Photographs of the cavity stage (a) from the side and (b) from the top. The most essential parts or parts that have faced a major change compared to the version introduced in ref. [72] are highlighted. (A): Top frame. (B): Thermal links. (C): Connector piece between top and base frame. (D): Base frame. (1): Thermal link to mirror holder. (2): Copper tube. (3): Teflon sheet. (4): Piezo jacket. (5): *Kapton* tape. (6): Fixing screw for the lever arm. (7): Steel spring pulling back the lever arm.

- The sample is the only part of the experiment that has to be cooled down to the lowest possible temperature, while the other parts of the setup can remain on higher temperatures. The mirror holder therefore has to be attached to the 4 K cold platform of the cryostat directly while being thermally isolated from the top frame. This is realized by separating the mirror holder from the block using small glass spheres which feature a very low thermal conductivity and almost no expansion. The mirror holder is then thermally linked to the cold platform using a desoldering braid made of copper (1) that is soldered into a hole at the top of the mirror holder. The other end is fed through a copper tube (2), which acts as a thermal shield for the cold copper braid, down to the cold platform. The inside of the tube is coated with a thin Teflon sheet in order to prevent the braid from touching the warmer tube.
- The wires for the piezos are in some cases made from 0.2 mm thin phosphor bronze wires, whereas some others are connected with regular insulated copper

wire⁴⁰. In all cases, the wires are interrupted after a few centimeters and soldered onto additional phosphor bronze wires. This adds a thermal lag to the cables which is essential, in particular for the copper wires, since the electric connectors of the cryostat are thermalized at room temperature. At the top frame, all wires are clamped down onto the titanium block using a Teflon sheet (3). This is a necessary method to avoid vibrations being coupled from the electrical connectors to the piezos via the wires, since the thin cables are excellent mechanical antennas. The connector containing the soldered connections is clamped onto the side of the titanium block, in order to further decouple the connector from the top frame.

- When we move the piezos by either using the motors or the screws directly, a rotational force is applied to the end face of the piezos, possibly forcing the piezo to rotate as well. This can lead to an unpredictable movement of the piezo in the best case, or breaking the piezo completely due to its brittle nature in the worst case. Therefore, we cover the end of the piezo actuators that face towards the screws with home-built jackets made of titanium (4) whose side walls are resting on the top frame and thereby prevent any rotation of the piezo. Using titanium-jackets has the further advantage of adding an additional layer between the screw and the piezo which protects the end face of the piezo.
- As can be seen in fig. 5.2(b), the top frame (and most importantly, the mirror holder) is isolated by a thermal shielding made of copper that is firmly screwed onto the titanium block. This is important since the thermal radiation, which is the main source of heat in a cryostat, scales with T^4 , which leads to a tremendously increased heat load if the cold parts "see" the vacuum chamber at room temperature, or the radiation shield at < 100 K. In order to prevent any soldering connections or possibly uninsulated cables from touching the electrically conducting thermal shield, they are covered using *Kapton* tape (5) which is a cryo-compatible thermal and electric insulator.
- The lever arm that holds the fiber can be clamped down against the titanium block using a screw (6), a steel spring (7) is used to pull it back into its initial position (the lever arm mechanic is described in detail in sec. 4.4). This has already been implemented in the previous version of the cavity platform, but is of great importance for the stability and scanning range of the lever arm. We face a trade-off between clamping the lever down, resulting in a more monolithic, i.e. mechanically stable setting but sacrificing some of its mobility, and leaving the arm as loose as possible, thus utilizing the whole scanning range of the piezo, but being more susceptible to vibrations. In this work, a rather loose setting of the screw was used mainly.

⁴⁰ These wires are pre-soldered by the manufacturer such that a modification is hard to realize.

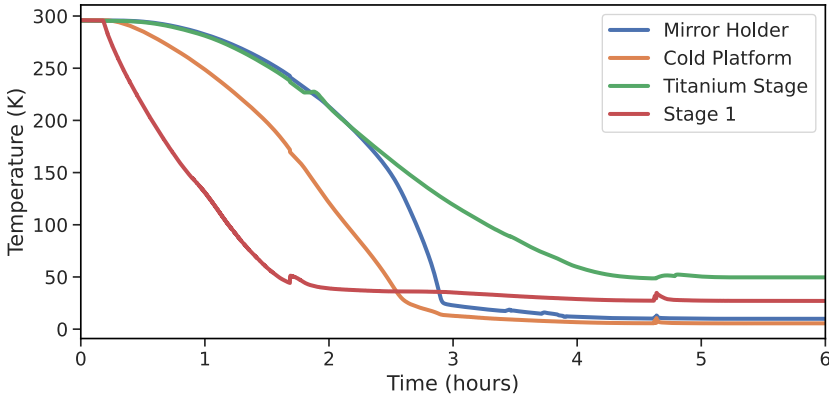


Figure 5.3: Temperature measurements at several parts of the stage during a cooldown. The measurements on *Stage 1* and the cold platform are built-in functions of the cryostat, the measurements on the titanium block and the mirror holder have been performed using additionally installed temperature sensors⁴¹.

- A second way to tune the scanning range versus the mechanical stability could be to utilize the length of the lever arm. A longer arm would result in a longer lever and thus in a larger scanning range. At the same time, this would increase its mass and thereby lower the mechanical eigenfrequency.

5.2. Tunability

Before addressing the mechanical stability of the cavity, we want to investigate whether the full tunability that the room temperature setup allowed for, persists during a cooldown. There are two main aspects that affect the tunability at cold temperatures: the expansion coefficient of the piezo actuators and the mechanical configuration of screws, clamps, and so on.

Fig. 5.3 shows the temperature of different parts of the setup during a typical cooldown. *Stage 1* thereby refers to the part in the cold head that is connected to the titanium block, while *cold platform* is the base plate below the stage that is connected to the mirror holder and has the lowest temperature in the sample chamber. We observe that the highest temperature decrease happens in the first three hours of the cooldown, but it takes another two to three hours until the setup is fully thermalized and (severe) thermal drifts no longer appear.

The low thermal conduction of titanium thereby leads to a very slow adaption to the temperature of *Stage 1*, which approaches its final temperature after just two hours

versus almost five hours for the titanium stage. The mirror holder reaches a temperature of 10.1 K and is therefore noticeably warmer than the cold platform, which stabilizes at 5.6 K. This cooldown was performed with all piezos and motors attached, leading to a rather high heat load on the system. The titanium block reaches a temperature around 50 K. The temperature sensor was thereby attached to the top side of the block. However, the temperature might differ for other positions due to thermal gradients in the material. It should be noted that the minimal temperature of the cryostat of 3.2 K could never be reached on the cold plate, even if all cables are disconnected. This is an indication that the heat load due to radiation cannot be avoided effectively by the radiation shields. The capacitance of a piezo actuator drops by about one order of magnitude when being cooled down below 10 K from room temperature [179]. Hence, the maximum displacement drops by the same amount. Since the piezo actuators used in this experiment are thermalized to the titanium block rather than to the coldest parts, their temperature is expected to be higher and the capacitance drop thus to be smaller. The maximum displacement range becomes crucial e.g. when navigating to a certain emitter on the sample, or attempting to depict the lateral change of the mode structure on a membrane. Even though the smaller scanning range can be counteracted by coarse movements using the electric motors, it is desirable to use as little mechanical movement as possible and focus on the bending mechanics via the piezo actuators in order to avoid irreversible mechanical drifts. While we already used voltage amplifiers for the lateral piezo actuators at room temperature, we now also add amplifiers for the fine and coarse piezos that tune the cavity length^{42 43}, such that the whole voltage range of the actuators can be used.

5.2.1. Cavity transmission scans during a cooldown

In order to investigate how the cooldown influences the cavity, we repeat the cavity transmission scans on the marked mirror used in sec. 4.4.3 and repeatedly record transmission maps while cooling down the stage. This is quite challenging since both the cavity length and the lateral position of the fiber start to drift during the cooldown. One can counteract both drifts using the motors, but in order to gauge the lateral drift, we decide not to adjust the lateral fiber position - or the plane mirror position, respectively - and just keep the cavity length constant. The amount of longitudinal drift, i.e. mirror separation drift, can easily be estimated by marking the screw that pushes the piezo and comparing the setting when both mirrors are in contact at room temperature and during the cooldown. Fig. 5.4 shows cavity transmission maps of the same grid as used in fig. 4.16 for different temperatures. The temperatures thereby refer to the measured temperature on the mirror holder, respectively. The full set of transmission maps can

⁴¹ Lake Shore DT-670C-SD

⁴² Falco Systems, WMA-02

⁴³ Falco Systems, WMA-200

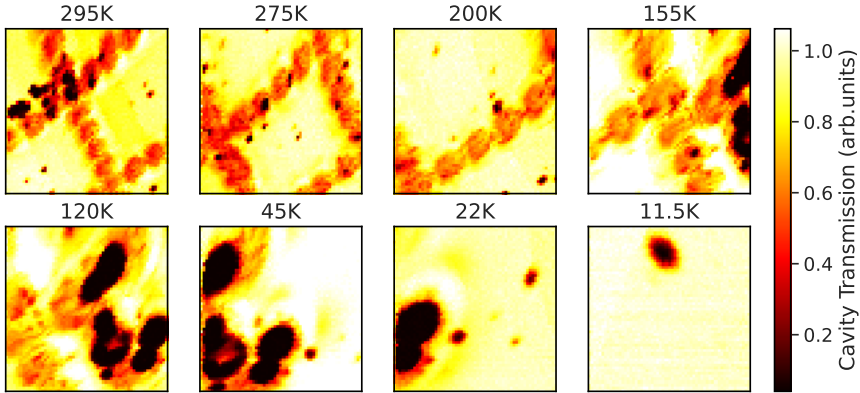


Figure 5.4: Series of cavity transmission maps of a marked mirror, recorded during a cooldown. The temperature thereby refers to the measured temperature on the mirror holder. The markers were machined using a CO₂ laser and are separated by 10 μm . Transmission scans were performed at a finesse of 1300. The full set of transmission maps is shown in appendix A. Adapted from [75].

be found in appendix A. The cavity length is comparable for all the scans. It would normally be easy to make sure that every scan shows exactly the same longitudinal cavity modes. In this case, however, the scans were recorded while the stage is being cooled down such that the drift is a limiting factor and the time window for each cavity scan is very short. Hence, the lateral resolution is chosen to be slightly lower compared to other transmission maps shown in this thesis. The cavity drift in z-direction is usually in the range of a few 10 μm . Due to the lever mechanics, the thermal drift in the lateral directions is larger. During the cooldown, one can observe that the scanned area is moving mainly to the right (x-direction) and slightly upwards (y-direction). Since the scanned area exceeds the marked region for this series of measurements at around 100 K, and since the scanning range decreases, one can only estimate the lateral offset for this cooldown to be 150 – 200 μm ⁴⁴.

The lateral scanning range for the first few scans is given by the marker grid, confirming the scanned area of $70 \times 70 \mu\text{m}$ at room temperature that was described in sec. 4.4.1. As the scanned area leaves the grid for temperatures < 150 K, one can identify the number "1" (rotated by $\sim 130^\circ$) that has been added to the grid for an easier orientation (compare to fig. 4.16(a)). When the stage is at its lowest temperature, i.e. 11.5 K for this very cooldown, there was still a small particle visible that acts as a scatterer and that we assume to appear in the estimated size of the point spread function of the cavity mode of 3 μm . This lets us gauge the scanning range at cold temperatures to be in the range of $\sim (10 \times 10) \mu\text{m}^2$.

Note that the temperature given in fig. 5.4 refers to the temperature on the mirror holder.

⁴⁴ Note that the mechanical setup is slightly different for every cooldown, leading to a varying drift

The limiting factor for the scanning range, however, is the temperature of the piezos, i.e. of the titanium block. It could therefore be possible that the scanning range at the same temperature varies for individual cooldowns, since the piezo temperature might be different.

5.3. Cavity stability

As discussed above, the mechanical stability of the cavity is a crucial sign of quality of a cavity setup that poses a challenge for any cryogenic cavity experiment. The cavity was thereby utilized in two different configurations: as an open cavity (the same as it was used for all the previous measurements) and additionally in the so called contact mode. The latter is realized by carefully bringing the fiber tip into physical contact with the plane mirror. This could improve the overall mechanical stability of the cavity drastically since the setup becomes a lot more monolithic. The advantages and drawbacks of both configurations must be evaluated in terms of passive stability of the system as well as the improvements that can be achieved by active stabilization.

5.3.1. Active stabilization

The features and modifications of the new positioning stage presented in the previous section are essential to improve its passive stability against external vibrations that disturb the cavity. In many cases, however, this is not sufficient, as some strong resonances in the system can still be driven. The most convenient way to further stabilize the cavity is by using an active stabilization scheme. The general idea thereof is mostly the same for all approaches: one needs some sort of error signal that is (ideally) linearly dependent on the degree of freedom that shall be stabilized, in our case the cavity length, i.e. the mirror separation. This error signal can then be fed forward to a proportional–integral–derivative (PID) controller. The PID controller then feeds a signal back to the system - in our case the piezo actuators that control the cavity length - such that the error signal gets minimized. By adding a constant offset to the error signal, one can furthermore choose an arbitrary set point inside the locking range (which is usually given by the peak intensity of the error signal). The aspect where most locking schemes differ is the creation of the error signal. The two locking schemes that are commonly used in cavity experiments are Pound-Drever-Hall (PDH) locking [180, 181] and side of fringe (SOF) locking. Both are depicted for a simulated cavity resonance in figs. 5.5(a, PDH) and (b, SOF).

Pound-Drever-Hall locking For the PDH locking scheme, a second laser is usually used, which has a lower finesse than the probe laser. The locking laser is phase-modulated with

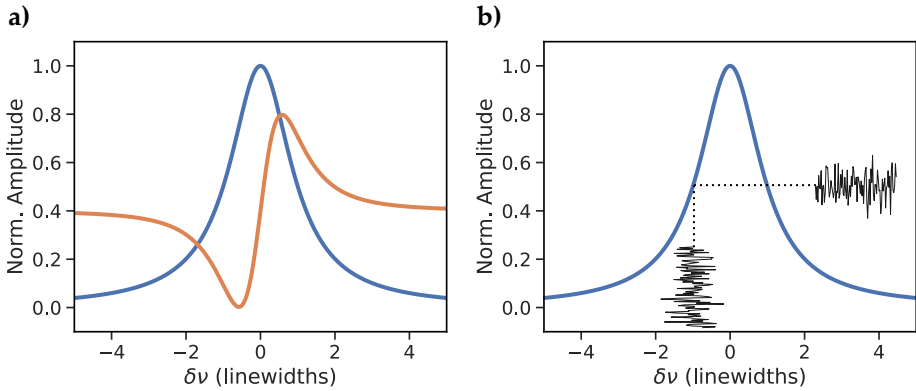


Figure 5.5: Simulation of a cavity transmission signal. (a) The PDH signal is shown (orange) for a slow modulation of the transmission signal (blue). The signal is shifted and rescaled for better visibility. (b) The same transmission signal as in (a), used for side of fringe locking. The black lines indicate random noise that acts on the resonance frequency which can be translated directly to intensity noise when in the linear region of the slope.

an electro-optic modulator (EOM), typically in the GHz range. The light is then coupled into the cavity and the transmitted power is measured using an APD⁴⁵. Afterwards, the APD signal is mixed with the local oscillator that drives the EOM and the resulting signal is low-pass filtered with a cut-off frequency that is much smaller than the modulation frequency. This yields the PDH signal shown in fig. 5.5(a) which is proportional to the derivative of the transmission signal, hence being zero at the center frequency of the cavity resonance. This signal has the advantage of showing a linear behaviour around the center frequency, allowing one to operate the cavity exactly on the peak of the resonance. Furthermore, PDH locking has the advantage of being insensitive to laser intensity fluctuations.

However, this technique firstly has rather high hardware requirements, and secondly, a two-laser setup is needed. This in particular can be hindering, as one needs to tune the lasers and the cavity in such a way, that it shows a double resonance for both wavelengths at the same time. While the PDH locking technique has been used in earlier experiments in the group, we decide to use the subsequently described side of fringe locking due to the priorly described drawbacks of PDH locking.

Side of fringe locking In contrast to the PDH technique, the side of fringe lock uses the transmitted cavity mode itself as an error function. In principle, it therefore has no

⁴⁵ It is also very common to use the cavity reflection signal, instead. Since the transmission signal was used in this experiment as well as in earlier experiments in the research group, I will focus on this case.

need of a dedicated locking laser, even though this might of course still be beneficial, e.g. if one wants to keep the cavity on top of the resonance. As the name hints, the error function in this case is either of the fringes of the cavity mode, where it can be described approximately linearly for small frequency changes, see fig. 5.5(b). The idea hereby is that a longitudinal motion, i.e. a change of the resonance frequency of the cavity, can be directly translated to an optical intensity fluctuation due to the linear slope of the fringe. This intensity fluctuation can then be detected by an APD and used as an error signal by a PID controller. One clear drawback of the operation without a second laser is that the cavity cannot be locked on top of the resonance. Also, the capture range of a side of fringe lock is smaller compared to the one of a PDH lock.

The considerably easier operation although makes side of fringe locking a very good option for cavity systems that already show a reasonably high passive stability. Another useful feature of the SOF locking technique is that the Lorentzian line shape can be used to easily convert a transmission time trace measured by the APD into units of mirror separation, i.e. cavity length change. The only quantities that have to be known are the cavity finesse at the respective locking wavelength (see eq. 5.1.1), and the measured peak voltage of the cavity mode. From that, one can derive the slope K of the Lorentzian at the setpoint I_{set} via

$$K = 4I_{\text{set}}^2 \times \frac{\sqrt{I_0/I_{\text{set}} - 1}}{I_0 \delta d}. \quad (5.3.1)$$

The figure of merit for the achieved cavity stability is the cavity length jitter's root mean square Δz which can be calculated either from the time trace directly, or via the power spectral density (PSD) of the signal. Both can be obtained using an oscilloscope⁴⁶. For the PSD, a fast Fourier transform (FFT) is calculated by the oscilloscope, yielding the spectrum in dBm/Hz. The values in dBm can then be converted to V via

$$[V] = \sqrt{50 \Omega \times 1 \text{ mW} \times 10^{[\text{dBm}]/10}}. \quad (5.3.2)$$

By doing so, the PSD becomes an amplitude spectral density (ASD), and the unit of the spectrum becomes $V/\sqrt{\text{Hz}}$. The length jitter is then expressed as

$$\Delta z = \sqrt{\int \text{ASD} \, d\nu} \quad (5.3.3)$$

or, for the discrete values calculated by the oscilloscope,

$$\Delta z = \sqrt{\sum_i \text{ASD}_i \cdot \Delta \nu_i}, \quad (5.3.4)$$

⁴⁶ LeCroy WaveSurfer 3024z-OFM-DVM, 8-bit, 2 GS/s

where $\Delta\nu$ is the spectral resolution of the ASD.

Finally, this value can be further converted to $\text{pm}/\sqrt{\text{Hz}}$ by applying the slope factor K :

$$\Delta z_{\text{pm}} = \Delta z / K. \quad (5.3.5)$$

If one wants to calculate the rms length jitter directly from the voltage time trace, one can use the standard deviation of the signal and directly apply the conversion factor. This is a much easier method, if only the length jitter is of interest, but using both methods simultaneously allows for a good assessment whether the calculated values are consistent.

Drift compensation How sensitive the lock is to deviations from the set point depends on the slope of the error signal, i.e. the cavity finesse, and on the gain - a linear factor in the case of the proportional and the integral part of the PID - that is applied to the PID controller. Finding the right parameters is always a trade-off between gain and locking bandwidth. Using a higher gain makes it possible to compensate for noise with a higher amplitude, ultimately limited by the linewidth of the error signal and the response of the system. A higher gain, however, shifts the bandwidth of the stabilization to lower values. This underlines the importance of a good passive stability, achieved through mechanical and acoustic decoupling, a careful choice of materials or design, and so on. The ideal case would be that the overall noise level is already very low, allowing us to use a low gain and therefore a high locking bandwidth. Besides acoustic noise, fast vibrations, and electronic noise, a major source of cavity length variations are slow drifts, usually caused by thermal effects or relaxing materials. While those drifts are very slow and generally easy to compensate, their scale can be thousands of linewidths and more. In order to compensate these large cavity length shifts, a piezo actuator with a high travel range, i.e. high capacitance is needed. This is contradictory to the requirements for the active stabilization. It thus makes sense to address the slow drift and the much faster vibrations using two different PID loops, controlling two separate piezo actuators.

Cascaded side of fringe lock Combining the fast SOF lock and the drift compensation is realized using a cascade control, i.e. two PID controllers that both control the same degree of freedom, whereby the output of one controller is simultaneously the error function for the second controller. One of the controllers (in the following called *fast lock*) is hence used for the "actual" lock while the second one (drift compensation, *slow lock*) tries to keep the output of the first PID constant. The locking setup used in this thesis is shown schematically in fig. 5.6. The cavity transmission (i.e. the error signal) is recorded using the APD and the resulting voltage is fed to the fast PID controller. In this work, the fast PID is realized using the python-based software *PyRPL* which runs

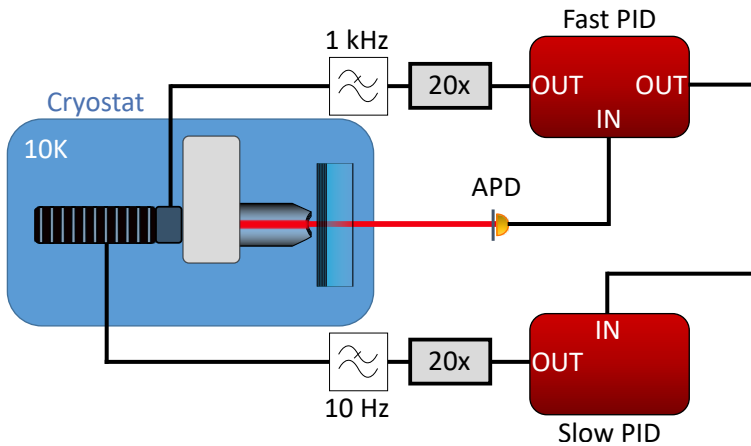


Figure 5.6: Schematic setup of the cascaded side of fringe lock. The output signals of both PID controllers are amplified when used at cryogenic temperatures and low-pass filtered. The drift compensation drives the coarse piezo (striped), the FPGA-based PID is connected to the fine piezo (pale grey). Taken from [75].

on a similar FPGA module⁴⁷ to the one that was used for the data acquisition of cavity scans [182]. Using a software-based PID has various advantages over an analog lockbox, like digital filtering, shaping the gain profile precisely, or being able to quickly switch between different presets. The output signal is split and sent to the fine piezo⁴⁸ after being amplified and low-pass filtered at 1 kHz using an analog filter⁴⁹, and to the input of the second PID. The amplification is only needed for the use at cryogenic temperatures in order to counteract the decreased capacitance of the piezo actuators.

The second, i.e. the slow PID controller is a simple python-based software, written by Thomas Hümmer [71]. The software-signal is converted to an analog signal by the data acquisition card and forwarded to the coarse piezo⁵⁰. Since we only use it for coarse tuning and drift compensation, it can be heavily low-pass filtered, in this case at 10 Hz⁵¹, after also being amplified.

Remark If the drift of the cavity is extremely low, which can be the case when the system has been cold for a long time span especially, the drift compensation might become obsolete (this, of course, also depends on the cavity linewidth). It can then be

⁴⁷ Red Pitaya StemLab 125-14

⁴⁸ Thorlabs PA4FEW, 195 nF measured capacitance, see section 4.4.1

⁴⁹ Thorlabs EF110

⁵⁰ Piezomechanik PS1 150/5x5/20, 1.6 μ F measured capacitance, see section 4.4.1

⁵¹ Home-built filter

advantageous to replace the slow PID by a simple battery, combined with a potentiometer to tune the output voltage. This way, one can manually control the cavity length such that the desired cavity mode is within the voltage range of the fine piezo. This can further improve the cavity stability, since a battery has a very low noise level, compared to the rather noisy output of the data acquisition card.

Sequenced lock A further feature of *PyRPL* that was used to improve the lock performance, are sequenced locking schemes. It allows one to use multiple presets of PID parameters and activate them after a certain time. An exemplary use is when enabling the cavity lock. The locking software scans the output voltage until it passes the cavity mode and then "catches" the resonance. Most commonly, the gain should be rather low, since if the gain is set too high, the software might overshoot the resonance and not be able to establish the stabilization. After the cavity length is locked, the gain can gradually be increased to improve the stability. This can be a very time-consuming procedure, as one has to reset the gain every time the noise level exceeds the capture range of the side of fringe lock and hence has to be reestablished. The sequenced lock can thus be used to automatically use a lower gain to start with, then e.g. slowly increase the gain, shift the setpoint, use a different digital filter, etc.

Servo bandwidth Every closed-loop feedback has a fundamental bandwidth limit, the so called servo bandwidth. Steps like data acquisition, signal processing, the PID controller itself or reaction times of the piezo actuators delay the feedback output with respect to the error signal (i.e. the APD voltage in our case), which leads to a phase shift between both signals that depends on the frequency of the noise that shall be suppressed. As the noise frequency increases, this phase shift increases as well. Once the phase shift becomes 180° , the feedback signal is completely out of phase with the error signal, and the feedback enhances the oscillation instead of suppressing it. This is the servo bandwidth, the resulting noise peak is called "servo bump". When the gain of the PID controller is increased, the response time of the piezo actuator increases as well due to the larger elongation range. This gain limit shows as a ringing in the cavity transmission signal that becomes stronger as the gain is further increased. Avoiding this servo bump is a crucial part of optimizing the PID parameters.

5.3.2. Stability evaluation

Mechanical transfer function Before discussing the optimization of the cavity stability, we want to obtain a clearer picture of the mechanical resonances that are relevant for the expected performance. A good way to do this is by recording the mechanical transfer function of the system, which is a measure for the response of the system to an external perturbation. A transfer function can be recorded by using a lock-in amplifier. In order

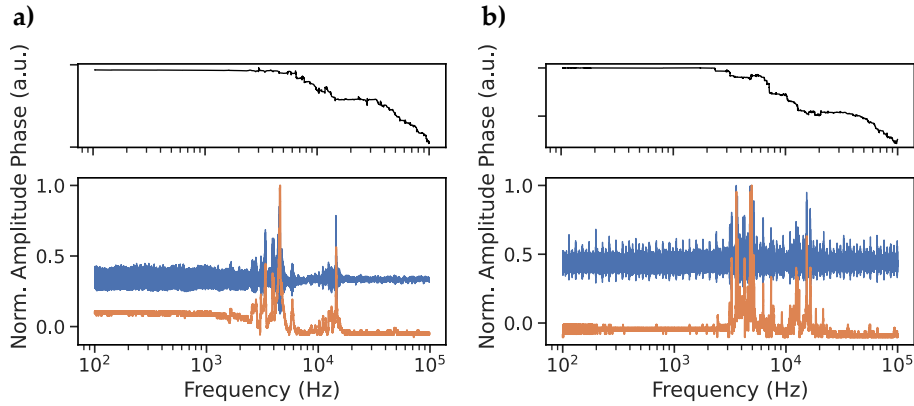


Figure 5.7: Mechanical transfer function (orange) and phase (black) **(a)** at room temperature and **(b)** at 11 K. Both data sets were recorded while the cavity is passively kept resonant with the 690 nm laser, showing a finesse of 3500. The normalized cavity transmission is depicted in blue. Adapted from [75].

to add controlled noise to the longitudinal axis of the cavity, we apply a very small sinusoidal voltage to the fine piezo while the cavity is held passively on resonance. The resulting cavity transmission should then reflect the answer of the system and can be measured using an APD. The transmission signal is then fed forward to the lock-in amplifier, mixed with the local oscillator which is driving the piezo, and finally low-pass filtered to extract the phase and amplitude response of the cavity. The frequency of the sinusoidal signal is swept on a logarithmic scale from 100 Hz to 100 kHz such that we gain a full transfer function for the relevant frequency regime.

The mechanical transfer function is depicted in fig. 5.7(a) at room temperature and (b) at 11 K on the mirror holder. For the scans, the same home-built 690 nm laser as in chapter 4 was used. The first mechanical eigenmodes appear around 3 – 4 kHz. Below that, no resonances are visible (for the longitudinal degree of freedom). The phase matches this behavior, as it stays almost constant for lower frequencies until the first eigenresonance appears. At room temperature, one can observe the rather unexpected trend that the frequency-independent noise is generally higher, compared to the frequency-regime above 10 kHz. It is not entirely clear whether this originates from measurement artifacts or whether it reflects the actual behavior of the stage. The fact that the cavity transmission signal (which is directly measured using the APD) becomes less noisy supports the assumption that the higher amplitude at low frequencies is caused by the inertia of the stage which is suppressing the movement at high frequencies.

When cooling down the stage, new resonances appear and the density of peaks in the range of 3 – 20 kHz overall increases. The cavity transmission signal additionally shows the noise spikes induced by the pump cycles of the cryostat over the time span of this measurement. Interestingly, the lowest eigenfrequency stays about the same as at room

temperature. This is an encouraging result, since one aims to push the first resonance to as high frequencies as possible, or at least above the main regime of external noise in the lab environment, as motivated in sec. 5.1.2.

Note that the cavity resonance for the cryogenic measurement is already extremely stable, showing a noise level of well below one cavity linewidth. This partially anticipates the result of the following sections, where the use of the contact mode in the cavity is introduced. This measurement would be impossible with the passive stability levels that have been reached using the open cavity design, since the lowest noise level is already exceeding one linewidth, hence prohibiting one from extracting the responses to the (much smaller) sinusoidal piezo impulse. This, however, does not change the interpretation of the transfer function but instead strengthens the assumption that the mechanical resonances do not depend on whether the mirrors are in contact or not.

It should also be stated that this method cannot reveal the reaction of the cavity to vibrations that are directed in other orientations, e.g. vibrations that are coupled from the cryostat to the cavity via the titanium block. This could be investigated by attaching an additional piezo actuator to different parts of the stage, that the sinusoidal signal is then applied to, which lets one simulate vibrations that couple to those parts specifically. This has not been done for this redesigned stage for time reasons, but was investigated using the previous design of Julia Benedikter [72]. This measurement revealed (for the old design) that some resonances can appear only for a mechanical stimulus originating from the optical table and being transferred to the top frame of the stage. Nevertheless, this coupling should be minimized in the new design by the usage of the springs between the bottom and top frame.

Passive stability Finding suitable PID parameters is a substantial part of optimizing the mechanical stability of the cavity. However, the active stabilization will always be limited by the passive stability of the cavity. A better passive stability means that a smaller PID gain is needed, and a higher bandwidth is hence possible. A decent stability might thus be misleading, when the active feedback has to modulate the cavity heavily due to excessive noise, since we possibly waste a lot of potential improvement. Therefore, a bad overall stability can be addressed by starting with passive stability only and in doing so, identifying sources of noise before making use of the the active feedback⁵².

Locked cavity We firstly focus on the open cavity design, i.e. without the two cavity mirrors being in physical contact. Thereby, one has to monitor closely, how the noise level changes when turning on the compressor of the cryostat, whether new resonances appear or whether the overall noise rises. Fig. 5.8 shows the best ASD spectra for the to

⁵² In this context, measuring the passive stability means only using the drift compensation or, if possible, a battery such that thermal drifts are negligible.

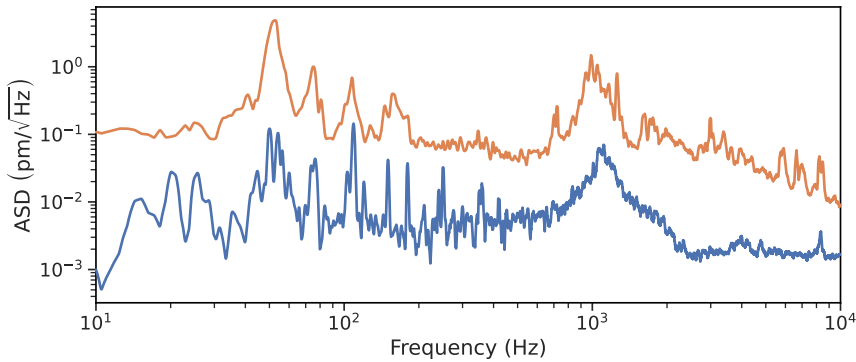


Figure 5.8: Amplitude spectral density of the cavity with a finesse of 3500 when operated at room temperature. Blue spectrum: cavity under vacuum conditions while the compressor of the cryostat is turned off. Orange spectrum: cavity under the same conditions when turning on the compressor while still being at room temperature.

respective cases, both smoothed using a moving average.

When the compressor is turned off (blue spectrum), the vibrations and the acoustic noise level are very low, allowing one to benefit heavily from the active feedback. The spectrum shows two main frequency regimes where the main noise is measured: most resonances are located at low frequencies, i.e. in the few 100 Hz range. They are composed of mechanical resonances as well as some residual electronic noise⁵³. The second contribution originates from the large peak around 1 kHz, which is the servo bump of the feedback. As described earlier, one could completely avoid this oscillation by lowering the PID gain significantly, at cost of the suppression at lower frequencies. The gain level has been optimized by constantly checking the cavity length jitter and we have found this configuration to yield the lowest overall noise.

At higher frequencies, the effect of the stiff cavity design combined with the mechanical decoupling shows its impact. Above the servo bump (where the cavity stability is dominated by its passive stability), no strong resonances appear in the spectrum. Additionally to the cavity design, this is caused by the acoustic shielding of the stage that comes with the closed vacuum chamber. Surprisingly, the vacuum itself only plays a minor role here, since the vacuum chamber itself seems to block most acoustic vibrations already. The effect of the acoustic shielding can nicely be seen in fig. 5.9, where the difference between an open (orange) and a closed (blue) lid is highlighted. For an open vacuum chamber, the cavity is fully exposed to any noise in the lab environment, which then couples to the eigenresonances of the stage at around 3 – 4 kHz, as we have seen in the mechanical transfer function.

Integrating over the whole spectrum yields a cavity length jitter of $\Delta z \approx 0.9$ pm rms.

⁵³ Electronic noise always is a bottleneck and can be addressed by expending an arbitrarily high effort.

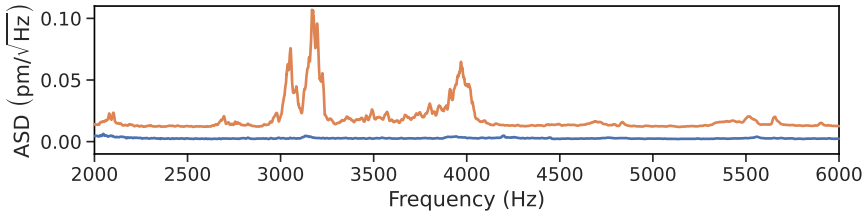


Figure 5.9: Segment of the amplitude spectral density under quiet conditions for a completely open vacuum chamber (orange) and for the case with the lid closed and vacuum (blue). The former curve is shifted by $0.01 \text{ pm}/\sqrt{\text{Hz}}$ for the sake of visibility.

When turning on the compressor of the cryostat, the resonator is exposed to a great amount of additional vibrations, which have a wide range of frequencies. This shows in a higher noise level (orange spectrum in fig. 5.8) in the whole frequency range. The resulting cavity length jitter increases to 15 pm rms . If we recall the cavity linewidth in terms of mirror separation of $\delta d = 10.6 \text{ pm}$ for a finesse of 30000 at 637 nm , this noise level already exceeds this bound, meaning that this setting would not be suitable for such a finesse.

At cryogenic temperatures, such a stability has been achieved previously using this resonator stage with a slightly different electronic setup and a lower finesse of 1000, where the active feedback was realized using a home-built analog lockbox. With this FPGA-based PID, however, these results could not be reproduced in the course of this work, and a stabilization with the open cavity design was not possible when cooled down. While the stability without the use of the cryostat is already more than sufficient for high finesse, the declining stability under cryogenic conditions underlines the need for an even better mechanical decoupling.

Cavity in contact mode In order to further improve the passive stability of the resonator, we increase the stiffness and monolithic character of the design by carefully bringing the fiber into physical contact with the plane mirror, as suggested above. This should heavily damp vibrations of the fiber tip which protrudes the steel needle by a few $100 \mu\text{m}$.

Using the contact mode comes along with several consequences that have to be considered. Firstly, bringing the two cavity mirrors into contact leads to a restriction of possible longitudinal cavity modes i.e. cavity lengths. This is especially important if one wants to use a dedicated locking laser, since the resonance frequencies of both lasers have to overlap very closely. As the tuning range of most lasers is rather small (on the order of a few nm), only specific longitudinal modes allow for this overlap. In most scenarios, this is not the case in contact mode. The probe laser itself thus has to be used for the active stabilization.

Secondly, this technique might be disadvantageous for plane mirrors that hold loose particles or agglomerates of the sample, which might be accidentally picked up by the

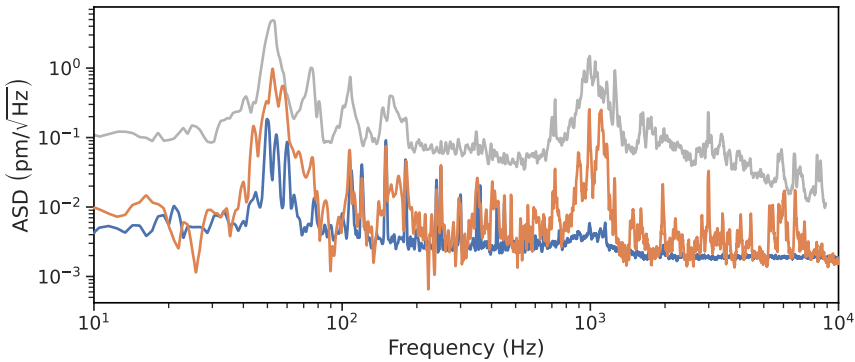


Figure 5.10: Amplitude spectral density of the actively stabilized cavity in contact mode. The measurement is performed at room temperature while the compressor is turned on (orange) and off (blue). The ASD of the open cavity (grey, orange line in fig. 5.8) is added for an easier comparison.

fiber tip. For the use in this very experiment, neither of these restrictions is relevant such that the use of the contact mode is a reasonable attempt.

The approach that led to the best stability was as follows:

1. Carefully bring the fiber tip closer to the plane mirror using the motor-driven screw while constantly sweeping the cavity length using the coarse piezo around 0 V and monitoring the cavity transmission with an APD.
2. When contact is established, the free spectral range abruptly increases due to the mechanical resistance that the piezo is facing. Nevertheless, the cavity length can still be scanned when in contact since the first part to touch the plane mirror usually is the outer region of the fiber. By applying an even higher force, the fiber can bend a little bit and thereby reduce the cavity length further. Tune the cavity to the second next fundamental mode after contact is established.
3. The coarse positioning should be adjusted such that the second contact-mode appears for a low piezo voltage (ca. 0 – 10 V in this case).
4. Stop scanning the piezo voltage and use the drift compensation to manually tune the cavity to the next cavity mode which should appear for a rather high piezo voltage. This makes sure that the piezo is even more rigidly clamped between the screw and the lever.
5. Use the previously described locking scheme to actively stabilize the resonator.

At room temperature, we already see a major improvement of the stability compared to the open cavity, as depicted in fig. 5.10. While the compressor is turned off, one main set of resonances around 50 Hz dominates the noise spectrum. This is composed

of residual characteristic electronic 50 Hz-noise as well as mechanical resonances that we attribute to the eigenresonance of the steel spring that are used for the mechanical decoupling of the top frame. This is consistent with the open cavity measurement that showed the same resonance. Integrating the whole spectrum yields a cavity length jitter of $\Delta z = 0.5$ pm rms, which is partially limited by measurement noise, especially at higher frequencies.

When the compressor is turned on, the overall noise again increases, although the impact on the background noise level is heavily reduced compared to the open cavity approach. While the resonances around 50 Hz only show a slight increase, the servo bump around 1 kHz again becomes more prominent as we have to increase the PID gain in order to counteract the increased vibrations. The biggest impact of the contact mode can be seen at higher frequencies where the ASD is reduced by over one order of magnitude. The total length jitter hereby amounts to 3 pm rms and is thus a significant decrease from the 15 pm rms of the open cavity. It can thus be stated that the contact mode increases the mechanical stability of the cavity such that it would be suitable for the previously mentioned cavity length-change linewidth for a finesse of 30000 at 637 nm of $\delta d = 10.6$ pm. In this case, it would be possible to reach $> 80\%$ of the ideal Purcell factor, according to fig. 5.1, or eq. 5.1.2, respectively.

Contact mode at cryogenic temperatures In previous attempts, we saw that the mechanical properties of the resonator platform change upon cooldown which leads to increased noise, especially at higher frequencies in the kHz-regime. By making use of the contact mode, these frequencies are expected to become less severe. Indeed, when using the same procedure as described above when the cryostat is cooled down to 10 K, we again see massive improvements compared to an open cavity, which could not be stabilized at all at cold temperatures. Due to the heavily improved stability, it is now possible to tune the cavity to the fringe of the mode without the active feedback and examine the passive stability, as well. The respective ASD spectra are shown in fig. 5.11, along with a time trace over eight seconds while the cavity is locked in contact mode. The prominent eigenresonance of the springs from fig. 5.10 is still clearly dominant and contributes the major portion of the cavity length jitter. The frequency is slightly shifted compared to the measurement at room temperature, with its center frequency now at 62 Hz. This is due to the temperature dependence of the springs' shear modulus, which increases at lower temperatures, leads to a higher spring constant and therefore a higher eigenfrequency [183]. The cavity length jitter for the passively stable cavity is 2.5 pm rms which is already suitable for further experiments.

When turning on the feedback, this value decreases further to 1.2 pm rms. This is the lowest value that has been accomplished in any closed-cycle cryostat until now, exceeding previously published results by over an order of magnitude [51, 49]. The main improvement can be seen at low frequencies < 1 kHz, where the active feedback can be used to suppress vibrations (even though the spring eigenresonance is still dominating the noise). For frequencies > 1 kHz, the stability does not exceed the passive stability of the stage, highlighting the limited bandwidth of the feedback loop. Particularly, the

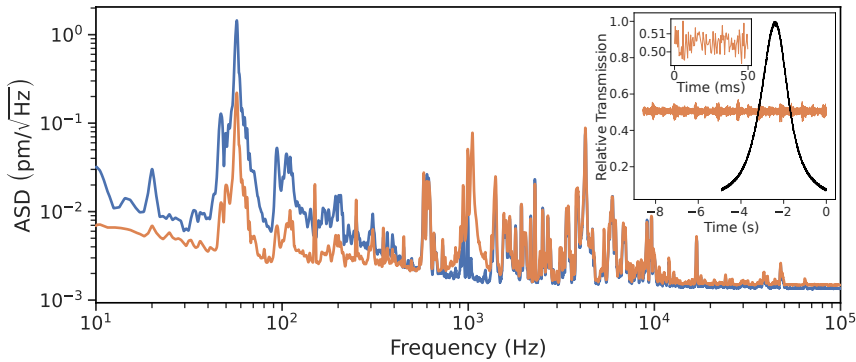


Figure 5.11: Amplitude spectral density of the locked cavity in contact mode when cooled down to 10 K at the mirror holder. Blue: passive stability. Orange: actively stabilized cavity. The inset shows the time trace that corresponds to the measurement of the orange ASD, compared to the respective Lorentzian shape of the cavity transmission when the cavity length is swept over the resonance. Adapted from [75].

servo bump leads to a higher noise level around 1 kHz compared to the passive setting. In order to get a clearer picture of the frequencies that contribute the most to the cavity length jitter, we analyze the cumulative jitter with respect to its frequency, as shown in fig. 5.12(a). Here, three main frequencies clearly stand out: the spring eigenresonance at 62 Hz, the servo bump around 1 kHz and a peak at 4.27 kHz, which matches the eigenfrequency of the lever arm mechanics. Note that the servo bump vanishes when the active feedback is turned off. In this depiction, it becomes apparent that the cavity length jitter in the passively stable setting almost entirely originates from the springs, already adding about 2 pm rms to the cumulative noise. As this is such a low frequency, it can be heavily suppressed (by one order of magnitude) using the active feedback, although it cannot be completely avoided. The lever arm eigenresonance at 4.27 kHz, however, becomes enhanced by the lock. Nevertheless, as we can almost cut the cavity length jitter in half, it is still worth it to implement the active feedback when possible.⁵⁴

As the vibrations induced by the cryostat are linked to the pump cycle of the cold-head and therefore have a very characteristic time dependence, it is highly beneficial to time our experiments such that the measurements are performed during the quiet phase of the pump cycle. Its period can thereby be controlled by changing the operating mode of the compressor. Usually, the time between two pump strokes is on the order of one second.

We now want to investigate how the cavity length jitter changes during one period

⁵⁴ It might catch the reader's eye that that overall cavity length jitter for the contact mode even decreases when cooling down the stage. This is likely to be caused by the low reproducibility of the passive stability for individual attempts and does not reflect a general property of the setup.

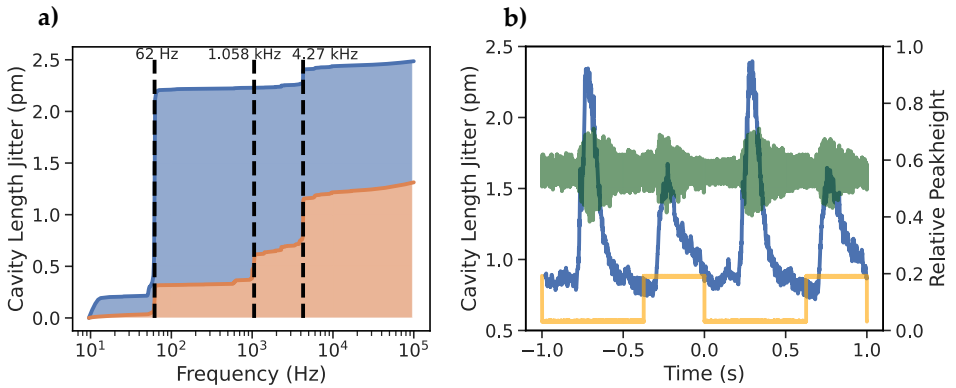


Figure 5.12: (a) Cumulative cavity length jitter of the measurements shown in fig. 5.11, describing the passive stability (blue) and the actively controlled stability (orange). The black dashed lines indicate the frequencies with the highest noise contribution. (b) Time-resolved cavity length jitter of the measurement shown in the orange graph in (a). The plot thereby shows the cavity transmission time trace (green), the trigger signal generated by the cryostat control device (yellow) and the time-resolved jitter of 10 ms long time cuts of the transmission signal (blue). Adapted from [75].

in order to find the best time window for measurements. We again record a cavity transmission time trace and analyze the cavity length jitter via the standard deviation of the APD signal. This time, however, we slice the time trace into time snippets of 10 ms and calculate the cavity length jitter for each snippet individually instead of integrating over the whole pump cycle. In doing so, we can identify the time windows in which the noise is lowest. For this measurement, we use the time trace of the orange graph in fig. 5.11 and fig. 5.12(a) which showed a cavity length jitter of 1.2 pm rms over the whole cycle. The analysis, shown in fig. 5.12(b), reveals that most of the noise contribution is clustered in several short pulses of 100 – 200 ms. These pulses are linked to the pump strokes whose impact affect the cavity stability with a time delay with respect to the trigger signal of the cryostat. As the coldhead movement pulses have an alternating intensity, we observe the same alternation in the noise level. Here, the cavity length jitter peaks at 2.4 pm rms and 1.7 pm rms, respectively.

The time intervals of interest are therefore the quiet phases of the cryostat, which arise shortly before each pulse, when the strong vibrations of the pump have declined. The cavity length jitter then drops to values of $\Delta z < 0.8$ pm rms which can be observed on time scales up to 100 ms. This stability allows for the stabilization of a cavity with a finesse of 40 000, if one sticks to the premise that the jitter should not exceed 10 % of the cavity linewidth. Moreover, 100 ms is a reasonable interval for most experiments that do not rely on long integration times and even this would not pose a problem since any data acquisition can easily be triggered to the pump cycle such that only the quiet phases are used for the measurement.

Discussion and possible improvements While the mechanical stability in the previously presented measurements is extremely high, the main achievement of this chapter is merging these low vibration levels with the full functionality i.e. the tunability of this cavity platform. This is the first open cavity design for the use in a closed-cycle cryostat that combines full three-dimensional tunability with sub-pm noise levels. In order to get a better overview over the noise levels that were measured in this chapter, table 5.1 summarizes the various configurations that have been investigated. While the results that have been accomplished in this chapter are very satisfying, there are still plenty of possible improvements to the passive stability as well as the locking scheme that could be considered in the future:

- Choosing titanium as a material for the setup instead of aluminum has improved the thermal properties of the stage during a cooldown a lot, due to its low thermal expansion coefficient. However, other materials could be even more beneficial, e.g. the lately arising invar. Its thermal expansion coefficient is usually as low as $1.2 \times 10^{-6} \text{ K}^{-1}$ and therefore about seven times smaller than the one of titanium [184]. Even though the density of invar is about a factor of two higher than the one of titanium, it could be an interesting approach for future designs.
- Testing different springs for the mechanical decoupling could very likely improve the stability. For time reasons, only one set of springs has been used in this work. Changing either the spring constant or the material could lead to a significantly increased filtering effect. A reasonable material to use could be copper beryllium as it remains elastic at cryogenic temperatures and thereby makes it easier to gauge the possible performance when working on the resonator at room temperature.

Setting	Temperature @Mirror holder	Cavity length jitter in pm rms
Open cavity, quiet environment	RT	0.9
Open cavity, compressor turned on	RT	15
Open cavity	10 K	Not stable
Contact mode	RT	0.5
Contact mode, compressor turned on	RT	3
Contact mode, passive	10 K	2.5
Contact mode, active	10 K	1.2
Contact mode, quiet phase	10 K	< 0.8

Table 5.1: Summary over the values for the cavity length jitter that have been recorded for different approaches in the course of this work. All values have been acquired using the same cavity stage and the same hardware setup.

- Remove some of the copper braid stripes that are used as thermal links for the titanium block. This could improve the mechanical decoupling, since the thermal links might transfer vibrations to the top frame. This, however, could be rather time-consuming as one has to cool down multiple times to test the cooling capacity.
- Replacing the single 1 kHz low-pass filter at the fast PID output by a more sophisticated combination of electronic filters would make it easier to tailor the PID gain profile more precisely. This would e.g. allow one to choose a higher cut-off frequency for the fast PID controller that is closer to the first mechanical eigenresonance of the lever system.
- Use a locking scheme that is triggered to the coldhead movement cycle. When the active feedback is running constantly, one has to adapt the PID settings to the strongest noise contribution which is the pump stroke. If measurements are however only performed during the quiet phase of the cryostat, it could be advantageous to trigger the feedback such that it is only active during this very time frame. This would allow one to optimize the stability without being concerned of short term vibrations that are almost as large or larger than the cavity linewidth.

6. Collective Purcell enhancement of Nitrogen Vacancy centers

In the previous chapters, we have addressed the technical and conceptual challenges that one faces when integrating a diamond membrane into an optical cavity under cryogenic conditions. The building blocks that are necessary are the understanding of the influence of the membrane on the optical properties of the cavity and the technical development of a cavity platform that is capable of retaining a very high stability at cold temperatures. We now want to bring them together and use the insight that we gained to showcase its applicability by investigating cavity-enhanced fluorescence from small ensembles of NV centers.

I shall thereby focus on two main aspects: the increased emission rate due to the Purcell effect and the emergence of collective effects like superfluorescence or photon bunching that can be observed on short time scales. While the former is crucial to enhance the fraction of coherent photon emission of NV centers (see chapter 2), the latter provides a very nice way to understand the fundamental interactions between NV centers in small ensembles which opens up a variety of new applications like superradiant lasers [56, 57] or quantum memories [58, 59, 60, 61].

The results shown in this chapter are currently prepared for publication. The majority of the measurements and analyses were done jointly with Kerim Köster. The diamond membranes that were used in this chapter were etched by Julia Heupel.

6.1. Membrane characterization

Similarly to chapter 4, we start by characterizing the optical performance of the cavity with the integrated membrane using laterally resolved scanning cavity measurements. This is essential in order to gauge the losses in the cavity and thus the expected Purcell factor. As we have seen in ch. 4, the most prominent influences of the membrane on the cavity are the increased losses, mostly by the alternation of the mirror transmission and scattering on the diamond interfaces.

6.1.1. Material properties of the sample

The sample that was used is an electronic grade single crystal CVD-grown diamond with a (100) surface orientation. The orientation is irrelevant for the optical performance of the cavity, but defines the dipole orientation of the implanted NV centers that directly determines the interaction strength with the cavity field (see sec. 3.2.2). The sample was initially cut and polished to an average thickness of $40 \pm 10 \mu\text{m}$ and a thickness variation of $< 1 \mu\text{m}/\text{mm}$. Afterwards, the sample was shallowly implanted by the manufacturer⁵⁵ with nitrogen ions, leading to a high density of NV centers ($10 \pm 4 \text{NV}/\mu\text{m}$, as stated by the manufacturer) at a depth of 10 nm. Therefore, we are restricted to ensemble spectroscopy as individual emitters cannot be separated when excited off-resonantly.

The surface roughness of the sample is specified by the manufacturer to be $< 3 \text{ nm rms}$. Later measurements have shown that the surface roughness over areas of $(4 \times 4) \mu\text{m}^2$ is as low as 0.7 nm rms, even before the first etching step. While the former value mainly determines how suitable the sample is for van der Waals bonding, the roughness that is important for cavity experiments is the one on the scale of the mode area (which is expected to be $< 10 \mu\text{m}^2$ and thus considerably smaller than $(4 \times 4) \mu\text{m}^2$).

Initially, the sample had a footprint of $(3 \times 3) \text{ mm}^2$ and was later cut⁵⁶ laterally into four equally sized pieces with a footprint of $(1.5 \times 1.5) \text{ mm}^2$, which makes the bonding more likely to succeed due to the smaller area. Afterwards, the sample was bonded onto a plane mirror with coating C_C (see tab. 4.1). Figure 6.1 shows microscope images of the sample before and after the etching process that was used to create a membrane with a minimal thickness of $\sim 3 \mu\text{m}$. The etching process leads to a further smoothing of the surface, which was quantified using AFM measurements of $(4 \times 4) \mu\text{m}^2$ large areas, yielding values as low as 0.3 nm rms (see fig. 6.1(d), blue marked area in (b)). More details about the etching process and the surface characterization have been published in references [73] and [74].

Choice of the mirror coating The mirror coating has a major impact on the experimental results: since the characterization in chapter 4 revealed that air-like modes are capable of reaching higher finesse values, the coating was chosen such that it has a higher transmission than the fiber mirror when tuned to an air-like mode. This improves the directionality of the emitted photons as fluorescence was only measured on the plane mirror side (see sec. 6.2.1). As this particular coating was initially designated to be used with a different sample, it features a SiO_2 spacer layer, similar to the one used in chapter 4 for the electronic grade sample. The thickness of the spacer layer, however, is adjusted for a different wavelength and a different implantation depth. If one would bond the sample directly on such a mirror as it is, the electric field intensity at the position of the emitters would be far from its maximum, thereby heavily limiting

⁵⁵ Qnami, Basel

⁵⁶ Diamond materials, Freiburg

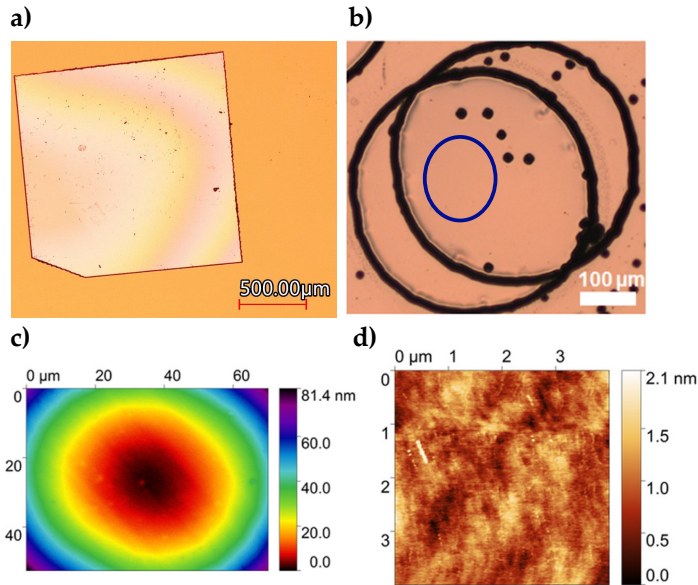


Figure 6.1: Microscope images of sample S_A . (a) Optical microscope image of the bonded sample before the first etching step. The interference fringes on the sample indicate a slight angular mismatch of the mirror and the bonded diamond surface. (b) Optical microscope image of the center region of the sample after the full etching procedure. The black dots are artifacts from the etching process, induced by micro-masking. The blue marker refers to the region where the lowest roughness of < 0.3 nm rms was measured and where the subsequently shown cavity measurements were performed. Since the mask slightly moved away from its initial position between two etching steps, only the overlapped region of both circles is fully etched down to the desired thickness of $3 - 5$ μm . (c) Interferometric image of the membrane after etching, showing the thickness gradient due to the uneven etching rate. (d) AFM measurement of a (4×4) μm^2 region in the blue region in (b). This measurement was used to extract the exact surface roughness. Images (b), (c) and (d) were recorded by Julia Heupel and are adapted from [74].

the coupling efficiency to the cavity mode. Therefore, a 40 nm thick layer of PMMA was added by spin coating before the membrane was bonded onto the mirror, as previously described in sec. 4.3.2. The influence of the additional spacer layer on the field intensity at the emitter's position is shown in fig. 6.2. While the field intensity only amounts to roughly half of its maximum without the use of an additional spacer layer, it is shifted close to the maximum with the additional PMMA layer. Note, that the refractive indices of SiO_2 and PMMA are almost identical, which prevents additional scattering loss at the mirror-PMMA interface. However, as a result of the shifted field intensity, scattering at the diamond-PMMA interface is not negligible anymore and has thus to be considered when modeling the expected losses in the system.

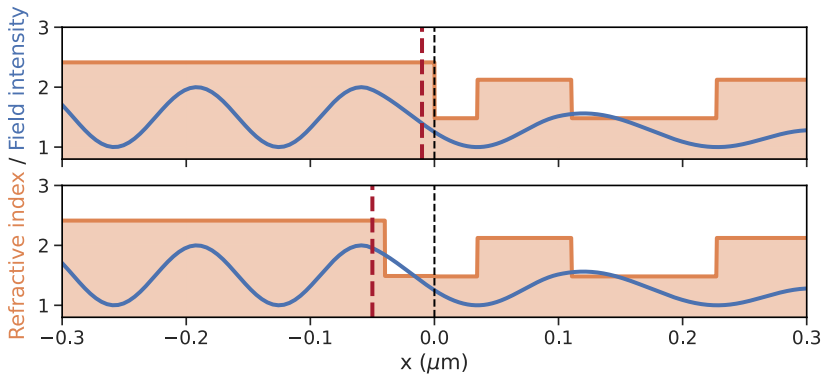


Figure 6.2: Impact of an additional PMMA spacer layer on the field distribution. Upper panel: the membrane is bonded directly onto the mirror surface, indicated by the black dashed line. The electric field intensity at the depth of the implanted NV centers (red dashed line) is at about half of its maximum value. Lower panel: a 40 nm thick PMMA layer is added between the diamond and the mirror coating. The phase of the electric field at the mirror surface stays the same, but the emitters are effectively shifted further away from the interface, leading to a higher field intensity at their position.

6.1.2. Performance of the sample in the cavity and modeling of losses

Similar to the evaluation in chapter 4, the first step is to investigate the optical properties of the cavity with the integrated membrane. For this, a transmission map as well as a finesse map is recorded near the center region of the membrane, where the lowest diamond thickness is expected. This measurement is shown in fig. 6.3. Since the very center shows an almost pure diamond-like mode character and hence a low finesse, the scanned region is slightly shifted laterally in order to include regions with an air-like character. The result is thereby consistent with the behaviour that was observed on other samples, i.e. regions where air-like modes are present show a high transmission and finesse, and vice versa for diamond-like modes. The measured finesse spans between 2000 for the diamond-like and 12000 for the air-like modes. This approaches the expected values if one only considers the bare coatings, where we calculate $\mathcal{F}_a = 15200$ and $\mathcal{F}_d = 2900$, but deviates significantly from the simulation, when the additional PMMA layer is taken into account. Then, the reflectivity of the plane mirror increases and the optimal finesse becomes $\mathcal{F}_a = 21800$ and $\mathcal{F}_d = 4400$. There are two reasonable explanations for these deviations: either, the system is limited by major losses that affect both air-like and diamond-like modes, such as absorption in the diamond or scattering at the diamond-PMMA interface. Or, the PMMA layer is considerably thicker than expected or missing completely. The latter case could originate from the etching process, if the diamond sample is undercut by the plasma. In order to further examine

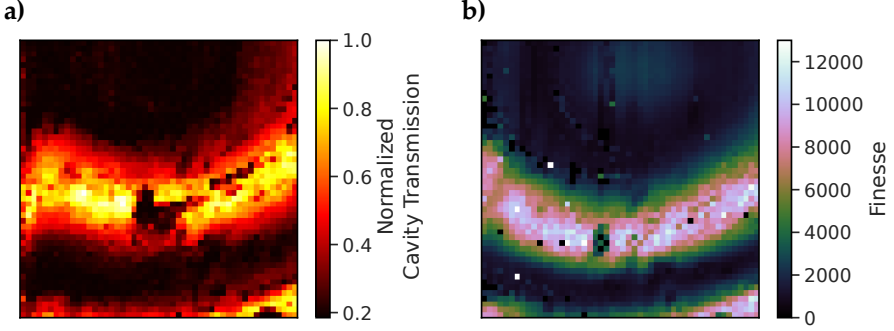


Figure 6.3: (a) Transmission and (b) finesse map of sample S_A , recorded at room temperature. The lateral position was chosen to be close to the center of the membrane such that the diamond thickness is as thin as possible while still being able to resolve multiple alternations between air-like and diamond-like modes.

the present losses, we apply the same loss model as in eq. 4.2.12. However, for this sample, the model has to be extended by scattering at the diamond-PMMA interface and the curvature-induced loss (see 4.5.2 for details). Both sources of loss are expected to be more severe compared to the cavity examined in ch. 4: as stated above, scattering at the diamond-PMMA interface is not negligible anymore due to the shifted electric field phase at the interface. The mode curvature effect could be more impactful since the fiber mirror profile of the fiber used here (F_C) has a smaller radius of curvature, leading to a stronger mode curvature at the diamond-air interface.

As we want to avoid any distortion of the recorded image and move the fiber perpendicular to the contour lines, we move the fiber mirror to a position where the contour lines are as straight as possible. The finesse map is shown in fig. 6.4(a). Since there is a high amount of failure measurements that yield NaN-values in the scan, they are removed and the mean value of each column is used instead of a cut along the x-axis. This results in a much smoother progression, see fig. 6.4(b).

The model that is used as a fit function for the data is a modified version of eq. 4.2.12, which describes the total loss for a specific membrane thickness as

$$\mathcal{L}_{\text{tot}} = \mathcal{L}_M + \mathcal{L}_{\text{scat}}(\sigma_{\text{rms}}) + \mathcal{L}_{\text{scat}}(\sigma_{\text{rms,backside}}) + \mathcal{L}_{\text{abs}}(\alpha_d), \quad (6.1.1)$$

where the factor $\mathcal{L}_{\text{scat}}(\sigma_{\text{rms,backside}})$, which describes the scattering loss on the backside of the membrane, is added. The surface roughness of this surface was not measured separately and is therefore estimated to be equal to the roughness of the other side before etching which was measured as 0.7 nm rms. The total effective loss is then a combination of the total loss for the physical diamond thickness, modified by the curvature-induced shift of the mode composition which considers a diamond thickness altered by $\lambda/4n_d$:

$$\mathcal{L}_{\text{tot,eff}} = \mathcal{L}_{\text{tot}}(t_d)(1 - C_{\text{curv}}) + \mathcal{L}_{\text{tot}}(t_d - \lambda/4n_d)C_{\text{curv}}. \quad (6.1.2)$$

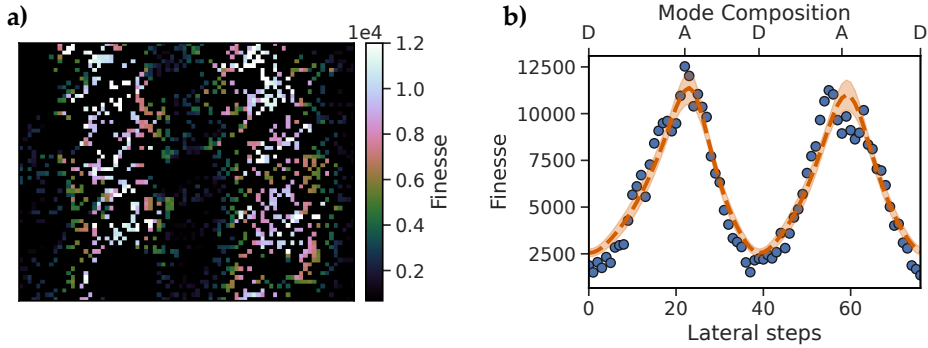


Figure 6.4: Modeling of the cavity losses on sample S_A. (a) Lateral finesse scan of the investigated region. Pixels where the finesse measurement was not successful were excluded from the model. (b) Loss modeling of the cavity. Blue circles: column-wise mean finesse values for the scan in (a). Orange line: fit of the data using eq. 6.1.2. "A" and "D" refer to air-like and diamond-like modes, respectively.

This expression affects both air-like and diamond-like modes: air-like modes face an increased total loss due to loss contributions such as scattering while the loss of diamond-like modes is reduced by the leaking air-like character of the mode. The resulting loss model is represented by the dashed line in fig. 6.4(b), returning $\sigma_{\text{rms}} = 0.86$ nm rms and $\sigma_{\text{rms,backside}} \approx 0.65$ nm rms as fit parameters. The value for σ_{rms} is thereby significantly higher than the value of 0.3 nm rms which was obtained via AFM microscopy. This discrepancy is an indication that the PMMA layer could indeed be thinner than expected, which would increase the transmission of the flat mirror. The fit result for $\sigma_{\text{rms,backside}}$, however, is close to the estimated roughness. Note, that the effective area in which roughness affects the cavity mode is smaller at the diamond-PMMA interface as the mode radius decreases when approaching the beam waist at the mirror surface. Since absorption in such a pure diamond is rather weak compared to the other loss contributions, the absorption coefficient was excluded from the fit and therefore set to the literature value for electronic grade diamond of $\alpha_d = 0.008 \text{ cm}^{-1}$ [185]. The deviation of the measured finesse to the expected finesse for the coating with the additional PMMA layer translates to a loss discrepancy of ~ 235 ppm. As we have seen in chapter 4, the quality of the fiber mirror profile can lead to significantly increased losses which are not considered in our model. Furthermore, the PMMA layer is rather thin, which could lower the reliability of the spin coating process. The increased loss could therefore be a combination of both effects.

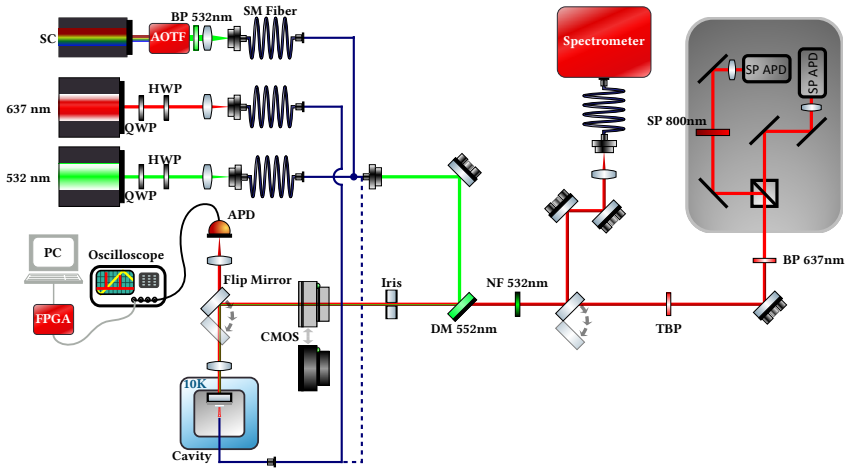


Figure 6.5: Schematic drawing of the optical setup. QWP: Quarter-wave plate. HWP: Half-wave plate. BP: Band-pass filter. SM Fiber: Single-mode fiber. DM: Dichroic mirror. NF: Notch filter. TBP: Tunable band-pass filter. SP: Short-pass filter. SP APD: Single-photon count APD.

6.2. Cavity-enhanced ensemble fluorescence from NV centers

In this section, the fluorescence of incoherently excited NV centers in sample S_A is investigated. For this, we use the cryogenic cavity platform that was introduced in the previous chapter.

6.2.1. Optical setup

The optical setup that was used in this chapter is an extension of the cavity setup in chapter 5 and is shown schematically in fig. 6.5.

Excitation path Three different laser sources can be coupled into the cavity: for off-resonant excitation, a diode-pumped solid-state laser⁵⁷ with a wavelength of 532 nm is used. The laser is first coupled into a fiber and can then either be connected directly to the cavity fiber, or coupled into the cavity through the plane cavity mirror. While this laser was predominantly used to excite the NV centers in the cavity, it can also be

⁵⁷ Cobolt Samba 532 100 (DPSSL), Hübner Photonics

conveniently used to align the optical beam paths, as the cavity mirrors are only partly reflective for this wavelength. Secondly, a tunable diode laser (TDL) with a wavelength of 637 nm can be used⁵⁸. As the design wavelength of the laser matches the ZPL of NV centers, it can be used for resonant excitation schemes that were not part of this thesis, but can be implemented later. Here, it was mainly used for finesse and cavity transmission measurements. The third laser source is a supercontinuum laser⁵⁹ which can either be used as a white light source, or can be combined with an acousto-optic tunable filter (AOTF) to filter out nanometer-narrow wavelength bands. Due to its pulsed emission (50 ps pulse length), it can be used for lifetime measurements.

The excitation laser beam is overlapped with the collection path using a dichroic mirror that has a high transmission above 552 nm. An iris can be inserted behind the dichroic mirror to define the beam path precisely and improve the reproducibility of the alignment. In order to excite the NV centers in the cavity as effectively as possible, the off-resonant excitation laser has to be overlapped with the Gaussian cavity mode. This can conveniently be achieved by maximizing the residual excitation light that is transmitted through the cavity and out of the cavity fiber.

Collection path For the detection of transmitted light from the cavity, mainly the free space channel of the cavity was used. This has multiple reasons: firstly, the choice of the mirror coatings leads to a higher transmission on the plane mirror side compared to the fiber mirror. It is therefore advantageous to collect the light on this side in order to maximize the number of collectable photons. Secondly, the transmission through an optical fiber can lead to fiber fluorescence, especially at cryogenic temperatures (the same principle of course applies for the excitation laser). The main disadvantage of the collection via the free space path is that the beam alignment strongly depends on the lateral position and hence on the angle of the fiber mirror. This becomes more severe the longer the geometrical distance from the cavity to the collection devices is. The divergent cavity mode is first collimated with an aspheric lens⁶⁰. The light is then either collected directly using an avalanche photodiode⁶¹ or coupled to the collection path with a flip mirror. A complementary metal–oxide–semiconductor (CMOS) camera⁶² can be added to the beam path to either observe the transverse shape of the cavity mode directly on the sensor, or to find out the exact position of the fiber mirror with respect to the sample. The same dichroic mirror that is used for the excitation path now acts as a spectral filter for the green excitation light. Since the extinction ratio of a dichroic mirror is not high enough to completely filter out the excitation laser, an additional notch filter for 532 nm is added to the beam path. A second flip mirror leads the

⁵⁸ *DLC DL pro HP 637*, Toptica

⁵⁹ *SC450*, Fianium

⁶⁰ *25 mm 0.40 NA, VIS coated*, Edmund optics

⁶¹ *APD410A2/M*, Thorlabs

⁶² *UI-1480LE Rev.2*, iDS

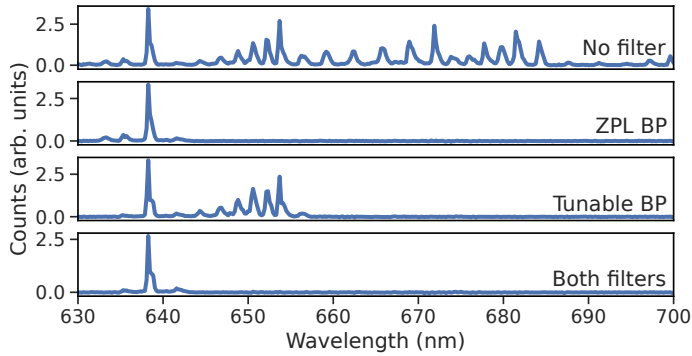


Figure 6.6: Fluorescence spectra of NV centers under the use of different optical filters. Two band-pass (BP) filters are combined in a way, such that the transmission edges of the respective filters form a very narrow band-pass filter that is tailored tightly around the ZPL.

fluorescence to a fiber coupling setup that is connected to a commercial spectrometer⁶³. Note, that one does not need additional spectral filters here as the different wavelengths are separated in the spectrometer itself. For further measurements such as the recording of the second-order auto-correlation function of the fluorescence, a Hanbury Brown and Twiss (HBT) setup is used. For these measurements, mostly the photons from the ZPL are of interest. Since the ZPL itself is narrower than commercial band-pass filters, a combination of two band-pass filters is used to tailor the transmission band such that only the fundamental cavity mode that matches the ZPL gets transmitted to the HBT setup. The choice of the used filters is motivated in fig. 6.6. When no filter is used (upper panel), the uncorrelated PSB dominates the spectrum which would heavily influence the subsequent measurements. Hence, a narrow band-pass filter with the center wavelength of 637 nm is added⁶⁴. As shown in the second panel of fig. 6.6, this filters out the PSB almost entirely. However, the higher order transverse modes of the central cavity mode lie within the transmission band of the band-pass. These residual counts can be filtered with a tunable band-pass filter⁶⁵ which has a rather broad transmission band that can be tuned by changing the incidence angle of the filter with respect to the beam path. By tuning this filter such that the ZPL is close to the edge of the transmission band, we can avoid the higher order transverse modes. With both filters combined, the photons from the ZPL are effectively separated from the uncorrelated part, as shown in the lower panel of fig. 6.6.

The HBT setup itself consists of a 50:50 beam splitter that distributes the photons equally

⁶³ Shamrock 500, Andor

⁶⁴ FF01-637/7-25, Semrock

⁶⁵ SEM-TBP01-704/13-25x36, Semrock

onto two single-photon count APD's^{66 67}. To shield the APD's from unwanted photons that do not originate from the cavity, the setup is surrounded by a black box that lets photons enter through a pin hole. The two beam path arms are designed such that their length is comparable in order to avoid any artificial delay between photon events. When a photon is detected on one APD, an unwanted infrared photon can be created and scattered back into the beam path. When it is detected by the second APD, it might be falsely interpreted as a correlation, leading to strong bunching peaks in the autocorrelation function (for more details, see sec. 6.3.2). To prevent this, a 800 nm short-pass filter is placed in front of one of the APD's. The detection events are then analyzed using a time-to-digital converter (TDC)⁶⁸.

6.2.2. Fluorescence spectra

To record fluorescence spectra, the sample is cooled down to 11 K and the cavity length is pre-set such that one of its resonances overlaps coarsely with the ZPL of the NV centers. The cavity finesse of 11000 corresponds to a linewidth of $\delta\nu = 1.1$ GHz and is thus expected to be narrower than the inhomogeneously broadened ZPL. This means that the cavity length jitter is not particularly impactful in this case, given that the passive stability of the setup is significantly better than one cavity linewidth. The lateral position of the fiber mirror is chosen such that the cavity shows an air-like mode character for the NV ZPL at 637 nm in order to reach the highest possible finesse. We then use the fine piezo to decrease the mirror separation step wise and thereby scan the cavity resonance slowly over the ZPL. While exciting the NV centers off-resonantly, the fluorescence is continuously monitored using the spectrometer. An exemplary fluorescence spectrum in which the cavity is on resonance with the ZPL is shown in fig. 6.7. In the cavity-enhanced spectrum, two things stand out. Firstly, the ratio of ZPL to PSB photons in the resonant case shows an up to 5-fold increase when the sample is incorporated into the cavity. For comparison, a fluorescence spectrum, recorded with a confocal microscope at room temperature, is added (not normalized). The inset shows two subsequent spectra with slightly different cavity lengths which showcases the effect of the cavity: the ZPL counts increase as the cavity becomes resonant with the transition while the PSB stays unaffected. The increased ZPL count rate with respect to the confocal measurement is in fact a manifestation of the cavity enhancement on one side, but also of the cryogenic environment, on the other side. The ZPL becomes more narrow as the temperature decreases (see sec. 2.1.3) [93], but its appearance is limited by the cavity linewidth. Secondly, the cavity acts as a spectral filter for the otherwise broad fluorescence spectrum, meaning that frequencies that are not on resonance with the cavity are suppressed. As a result, one can observe the cavity resonances in the

⁶⁶ *SPCM-AQRH-12-TR*, Excelitas

⁶⁷ *COUNT-T100*, Laser components

⁶⁸ *TimeTagger 20*, Swabian Instruments

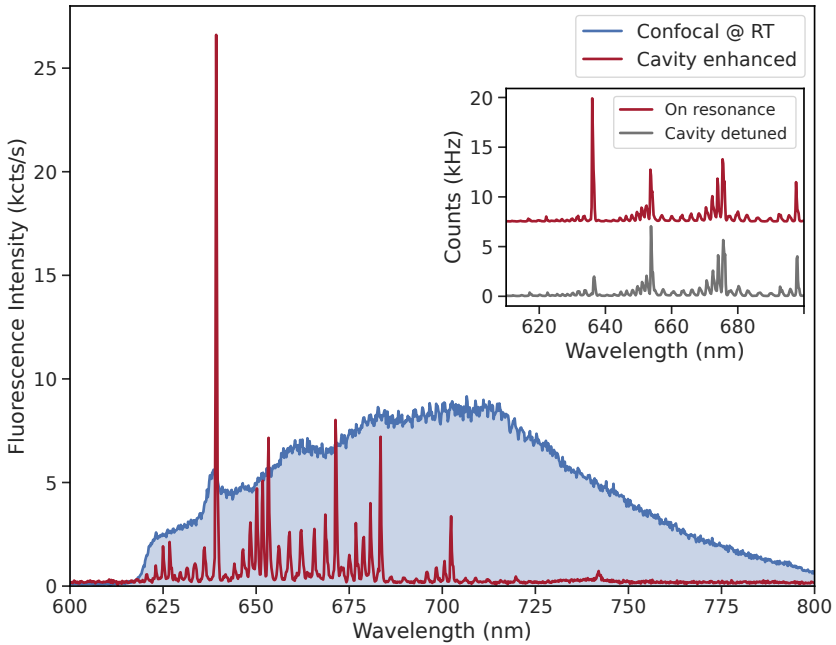


Figure 6.7: Fluorescence spectra under off-resonant excitation, either cavity-enhanced at 11 K (red) or as seen in confocal measurements at room temperature (blue). Note that the y-axis scaling refers to the counts of the cavity measurement, while the confocal scan is scaled such that the PSB count rates of both measurements roughly match for a better comparison of the ratio between ZPL and PSB photons. The inset shows two subsequent spectra where the cavity is either on resonance with the ZPL (red) or slightly detuned (grey).

spectrum. The Gaussian fundamental modes are thereby dominant. This depends on the wavelength due to the fact that the collection efficiency and fiber coupling to the spectrometer differs for different wavelengths. What stands out is that the free spectral range in frequency space is not constant and varies between 14 nm and 18 nm. Moreover, also the spacing between the higher order transverse modes depends on the wavelength. This is caused by the mode hybridization and the resulting avoided crossings of air-like and diamond-like modes in the mode dispersion, as simulated before in fig. 4.8. Due to this spectral filtering effect, only those NV centers contribute to the ZPL emission rate that emit within the cavity linewidth, while the PSB consists of fluorescence from all NV centers that are located in the spatial cavity mode. Hence, the ZPL enhancement is in fact much stronger than it appears in the fluorescence spectrum, as we shall quantify later.

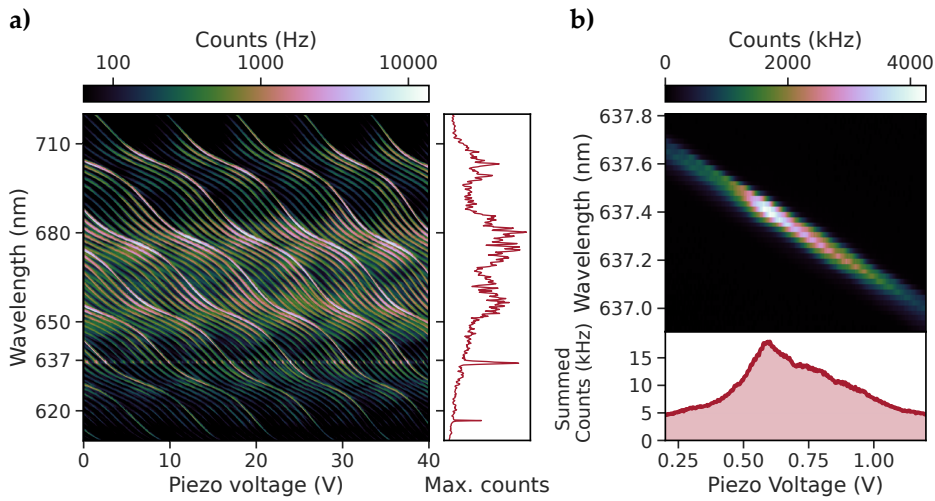


Figure 6.8: (a) Cavity mode dispersion of an ensemble of NV centers. The piezo voltage is swept while the fluorescence is recorded continuously with the spectrometer (3 s acquisition time per spectrum). The right panel shows the maximum count rates for each row, i.e. for each wavelength, yielding the full cavity-enhanced fluorescence spectrum. Note that the colorbar has a logarithmic scale such that also the higher order transverse modes become visible. A high resolution plot of the entire scanning range can be found in appendix B. (b) High-resolution spectroscopy of the inhomogeneous ZPL. The scan resolution was increased to acquire the inhomogeneous ZPL linewidth by integrating the counts over the piezo voltage.

Mode dispersion and inhomogeneous linewidth The width of the ZPL peak in fig. 6.7 is given by the spectral linewidth of the cavity, as only resonant photons are transmitted. In order to observe the full width of the ZPL inside the cavity, we perform the same procedure that was used to find the center frequency of the ZPL, i.e. the mirror separation is again tuned slowly over the ZPL while continuously recording fluorescence spectra. The mode dispersion for a larger spectral and scanning range is depicted in fig. 6.8(a). Several findings can be extracted from this figure:

- The spectra are dominated by the PSB which features the characteristic wavy structure due to hybridized cavity modes. In this picture it becomes clear that the cavity has indeed an air-like mode character for 637 nm, indicated by the steeper slope of the dispersion.
- The ZPL appears as a horizontal line as its wavelength is independent from the cavity length.
- Overall, the slope of the dispersion becomes steeper as the piezo voltage is increased, i.e. for shorter cavity lengths. This is in accordance to the expected

behaviour for a bare cavity (without diamond), as the FSR stays constant in frequency space, but not in terms of mirror separation.

- Analyzing the maximum count rate for each wavelength in the whole spectrum allows us to extract the full cavity enhanced spectrum of the NV centers while omitting the spectral filtering by the cavity resonances. This is shown on the right hand panel. The resulting spectrum reveals the periodic variation of the cavity transmission for different wavelengths as the cavity oscillates between air-like and diamond-like modes. The count rate is thereby higher for diamond-like modes which could be caused by the increased mirror transmission that diamond-like modes face. The cavity enhanced spectrum shows a sharp and prominent peak at 637 nm, as expected.

Since the cavity linewidth is considerably narrower than the inhomogeneous linewidth of the ensemble, it can be used to resolve the ZPL. Therefore, we repeat the dispersion measurement, but use a finer grating of the spectrometer for a better spectral resolution and restrict the piezo voltage to a narrow window around a ZPL while scanning the cavity length in much finer steps. The resulting dispersion scan is shown in fig. 6.8(b). When the cavity resonance overlaps with the center of the ZPL, the count rate shows a local maximum and declines again afterwards. It should be noted that the counts are not expected to go down to zero since other NV centers that lie within the spatial cavity mode can be spectrally shifted such that their PSB leaks into the ZPL of the NV centers that are resonant with the cavity. While only those NV centers contribute to the ZPL counts that are resonant with the cavity, the PSB consists of the photons emitted by all emitters that lie within the spatial cavity mode, adding up to a significant count rate when the cavity is off-resonant with respect to the ZPL.

When the counts are integrated over the recorded spectral range for each cavity length, we obtain the inhomogeneous ZPL. Integrating the counts over the piezo voltage for each wavelength bin of the spectrometer would of course yield the same result, but the spectral resolution of the spectrometer is about a hundred times coarser than the cavity linewidth. The integrated counts are shown in the lower panel of fig. 6.8(b) and correspond to a full width at half maximum (FWHM) of ~ 400 GHz. This is orders of magnitude larger than the natural linewidth of single NV centers, but corresponds well to the expected inhomogeneous broadening, mainly caused by local varying electric fields due to the high emitter density and strain in the diamond host. Especially the Stark-shift-induced broadening can already be in the range of several hundred GHz for a single nearby charge[97, 94]. Note that the straightness of the line in the ZPL dispersion is a sign of the exceptional mechanical stability of the cavity setup. As every voltage step corresponds to an exposure time of 3 s on the spectrometer - resulting in measurement times of hours - the cavity length drift has to be very low on these time scales.

Power dependence Measuring the fluorescence for different excitation laser powers allows us to get a better understanding of the dynamics which the system underlies,

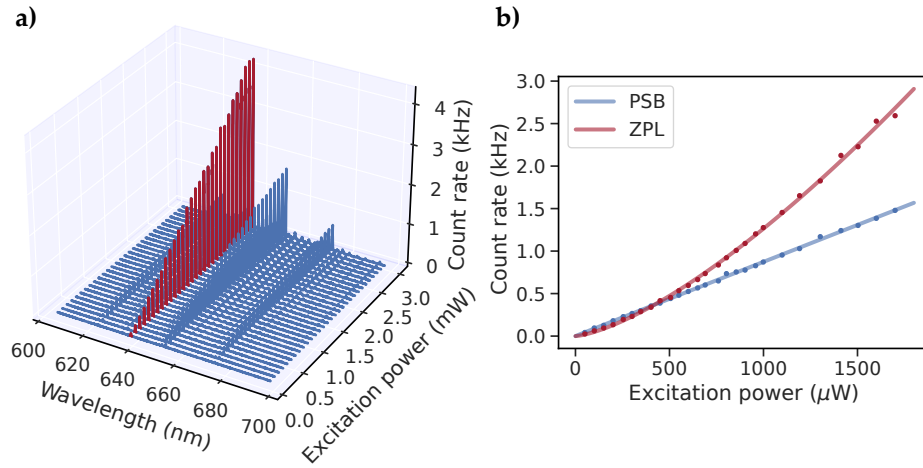


Figure 6.9: (a) Power dependence of fluorescence spectra under off-resonant excitation. The ZPL is highlighted in red. (b) Maximum ZPL and PSB count rates for different laser powers, far from saturation. The measurement data is fitted using a power law function. The fit yields $k = 1.01$ for the PSB and $k = 1.42$ for the ZPL.

as the rate with which NV centers get excited is altered. The expected behavior is a linear increase for the count rate for excitation powers that are far from saturation. This means that the excited states are decaying faster than they are repopulated by the laser. If the laser approaches the saturation power, the pump rate is higher than the emission rate and a further increase of the laser power has no impact. Fluorescence spectra for different laser powers are shown in fig. 6.9(a) where the cavity length is tuned to be on resonance with the ZPL. The spectral range is limited to the area around the ZPL which is highlighted in red. In addition to the ZPL, three fundamental cavity modes in the PSB are visible. As expected, the overall count rate increases for higher excitation powers. However, the count rate of the ZPL seems to grow faster than the PSB. This becomes more apparent when the maximum count rates of the ZPL and the next nearby PSB mode are compared directly, as can be seen in fig. 6.9(b). While the PSB follows an almost perfectly linear trend, the ZPL grows with a super-linear slope. To quantify this behavior, a power law function, given by

$$I = \beta \cdot P^k \quad (6.2.1)$$

is used as a fit function. Here, I is the count rate, β is a proportionality factor, and P^k is the excitation laser power that contributes exponentially with the power of k . In this case, the fit yields $k = 1.42$. Repeating the measurement under different conditions like cavity length or the lateral position on the sample leads to similar results. Such a super-linear relationship between the emitted intensity and the excitation power is a strong sign of collective effects between the emitters such as superradiance or superfluorescence. As described in section 3.3, a purely superradiant ensemble in the half-excited state would

exhibit a N^2 -scaling, i.e. $k = 2$. This scaling is diminished, if the system deviates from the half-excited state. Furthermore, any incoherent photon, in particular PSB photons from other NV centers, lowers the scaling factor as well. The appearance of superradiant or superfluorescent emission in this setting is in fact somewhat surprising as several requirements for superfluorescent emission are typically missing for NV centers. Firstly, the emitters need to have a very close spatial proximity of under one ZPL wavelength. This is not the case for this sample, as the NV centers are distributed over the whole spatial cavity mode. Secondly, a common transition frequency of the emitters is essential. Hence, the presence of inhomogeneous broadening that shifts the transition frequencies of the NV centers with respect to each other hinders the build-up of superfluorescence. Thirdly, the dephasing mechanisms have to be slower than the formation and the decay of the superfluorescent state. This also contradicts the expected fast dephasing, especially for shallowly implanted NV centers with a high emitter density. Finally, the probability of coherent emission, i.e. the branching ratio into the ZPL, has to be significant. For NV centers that are not affected by Purcell-enhancement, this is only 3 %.

In the following, I shall discuss how the cavity can mediate collective effects that would otherwise remain unobservable.

6.3. Cavity-mediated collective emission from few NV centers in a diamond membrane

6.3.1. Superfluorescence in an optical cavity

As described above, NV centers are very unlikely to show collective emission since it requires the emitters to share a coherent optical transition combined with a high spatial density such that the average distance between two emitters is smaller than the transition wavelength. This can be overcome if the emitters are coupled to each other via the cavity light field which can then act as a common radiation mode for spatially separated NV centers. This principle is shown schematically in fig. 6.10(a). Initially, the NV centers are excited incoherently⁶⁹, leading to a random phase distribution of their dipoles. There is no coherence in the system. The emission of photons is then started by spontaneous emission, it is therefore an intrinsically quantum mechanical process. Those photons that are resonant with the cavity mode are emitted into the cavity and the radiation field builds up. Note that the dipoles are still completely uncorrelated. Once the cavity light field is present, the individual NV centers that are coincidentally degenerate have a channel via which they can couple to each other. A random process called "spontaneous synchronization" occurs. This self-organization can also be observed in the classical

⁶⁹ Hence, we are talking about superfluorescence, as opposed to superradiance, which is the correct term if the emitters are excited coherently (see sec 3.3).

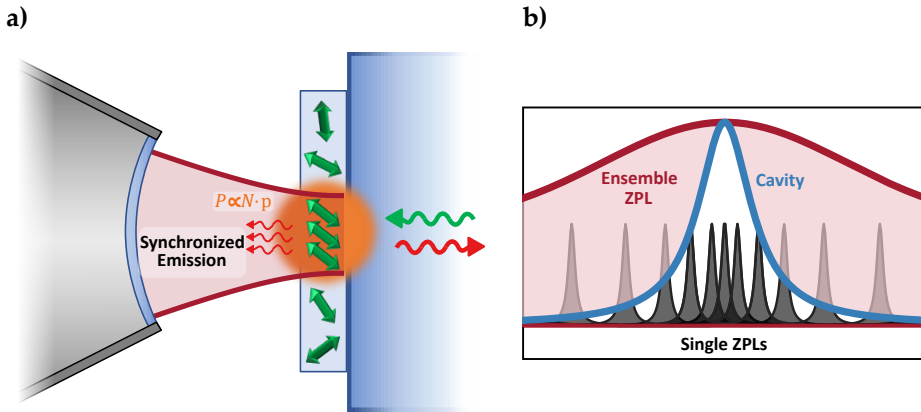


Figure 6.10: (a) Schematic depiction of cavity-mediated superfluorescence. (b) Schematic of multiple narrow emitters that form the broad inhomogeneous ZPL. The cavity linewidth (blue) acts as a spectral filter such that only few emitters are able to emit into the cavity mode.

equivalent of coupled quantum emitters, namely two or more coupled (mechanical) harmonic oscillators. The most commonly known example is the self-organization of multiple metronomes that are coupled to each other via a movable plank. Even if they are started asynchronously, the metronomes will adapt their oscillation phases after a short while and then stay synchronized. The same explanation can be used for the underlying principle in the quantum mechanical case. The cavity light field takes the role of the plank, allowing the dipoles to transition to synchronized oscillation. The ensemble now behaves the same way as in the free space case (but with close proximity): a macroscopic dipole is formed that features an increased decay rate, leading to emission in the form of short pulses that are the shorter the more NV centers are involved. One important difference to the typical superfluorescence is the fact that those emitters that emit collectively are not necessarily the very same NV centers the whole time. In fact, this would be very unlikely due to the significant frequency fluctuations due to spectral diffusion. Since the cavity acts as a spectral filter, the collectively coupled emitters can be "exchanged", and only the average number of coherent dipoles defines the superfluorescent emission, see fig. 6.10(b). Therefore, we need a way to validate whether the super-linear power dependence is in fact caused by collective effects and if so, how many NV centers are involved in the emission. One possible way to do so is by measuring the second-order autocorrelation function $g^{(2)}(\tau)$ of the cavity transmission which can reveal possible photon bunching.

6.3.2. Rate equations and the second-order correlation function

The second-order correlation function of a stream of photons gives rise to its temporal structure by describing the time-dependent intensity fluctuations. Intuitively, the $g^{(2)}(\tau)$ -function describes the likeliness with which a photon is emitted with a certain time delay τ after a first photon was detected. It was first measured by R. Hanbury Brown and R. Q. Twiss in the 1950s, the setup that is used is hence called Hanbury Brown-Twiss (HBT) setup [186, 187]. As described in sec. 6.2.1, it consists of a 50:50 beam splitter and two single-photon detectors, allowing for a measurement of the photon statistics.

The theoretical derivation of the second-order correlation function can be found in several textbooks, e.g. by M. Fox [126]. Mathematically, $g^{(2)}(\tau)$ is defined as

$$g^{(2)}(\tau) = \frac{\langle \mathcal{E}^*(t)\mathcal{E}^*(t+\tau)\mathcal{E}(t)\mathcal{E}(t+\tau) \rangle}{\langle \mathcal{E}^*(t)\mathcal{E}(t) \rangle \langle \mathcal{E}^*(t+\tau)\mathcal{E}(t+\tau) \rangle} = \frac{\langle I(t)I(t+\tau) \rangle}{\langle I(t) \rangle \langle I(t+\tau) \rangle} \quad (6.3.1)$$

where $\mathcal{E}(t)$ and $I(t)$ are the electric field amplitude and intensity of the light beam at time t , respectively. $\langle \dots \rangle$ denotes the time average. If the averaged intensity is constant for long integration times, $\langle I(t) \rangle = \langle I(t+\tau) \rangle$, and eq. 6.3.1 becomes

$$g^{(2)}(\tau) = \frac{\langle I(t)I(t+\tau) \rangle}{\langle I(t) \rangle^2}. \quad (6.3.2)$$

For a classical light source, we know that

$$\langle I(t) \rangle^2 \leq \langle I(t)^2 \rangle \quad (6.3.3)$$

which means that

$$g^{(2)}(0) \geq 1. \quad (6.3.4)$$

This is usually not the case in the quantum mechanical case, where the electric field amplitude is replaced by the electric field operator

$$E(t) \propto \hat{a}e^{-i\omega t} + \hat{a}^\dagger e^{i\omega t} \quad (6.3.5)$$

with the photon creation and destruction operators $\hat{a}^\dagger(t)$ and $\hat{a}(t)$. Eq. 6.3.1 then becomes

$$g^{(2)}(\tau) = \frac{\langle \hat{a}^\dagger(t)\hat{a}^\dagger(t+\tau)\hat{a}(t+\tau)\hat{a}(t) \rangle}{\langle \hat{a}^\dagger(t)\hat{a}(t) \rangle^2}, \quad (6.3.6)$$

which leads to the correlation function for $n \geq 1$ and zero time delay,

$$g^{(2)}(0) = \frac{\langle n(n-1) \rangle}{\langle n \rangle^2} = 1 - \frac{1}{n}. \quad (6.3.7)$$

This means that a single photon source should satisfy $g^{(2)}(0) = 0$ in the ideal case. Since a photon number state with $n = 2$ yields $g^{(2)}(0) = 0.5$, the condition $g^{(2)}(0) < 0.5$ can

be used as a requirement for a single emitter. Moreover, the second-order correlation function can thus be used to determine the number of emitters that are involved. For a more detailed description of the $g^{(2)}$ -function, in particular for three-level systems like the NV center in its simplified version, we start by investigating the rate dynamics of such a system.

Rate equations The simplest form of a quantum emitter is a two-level system, which is used here to derive a basic understanding of the underlying physics. It consists of a ground state **1** that is linked to the excited state **2** via an optical transition. In the case of the NV center, the excited state is additionally coupled to a continuum of states via phonons and a meta stable state **3**, see fig. 6.11(a). The latter is first ignored and will be added to the calculation later. Since the relaxation of the phonon states is fast compared to the lifetime of state **2**, it can be omitted as well. The transition is driven with the excitation laser power P_{ex} . As a consequence, the system is excited at a rate k_{12} , given by

$$k_{12} = a \cdot P_{\text{ex}} \quad (6.3.8)$$

with the proportionality constant a . The system then decays back into the ground state with rate k_{21} by emitting a photon. The population of the respective states are given by ρ_1 and ρ_2 , satisfying the condition

$$\rho_1 + \rho_2 = 1. \quad (6.3.9)$$

The temporal dynamics of the two states are described by the rate equations,

$$\begin{pmatrix} \dot{\rho}_1 \\ \dot{\rho}_2 \end{pmatrix} = \begin{pmatrix} -k_{12} & k_{21} \\ k_{12} & -k_{21} \end{pmatrix} \cdot \begin{pmatrix} \rho_1 \\ \rho_2 \end{pmatrix}. \quad (6.3.10)$$

When the transition is pumped continuously, the system will eventually reach a steady state where $\dot{\rho}_1 = \dot{\rho}_2 = 0$. This, combined with equations 6.3.9 and 6.3.10, yields for the excited state population:

$$\rho_2(t \rightarrow \infty) = \frac{k_{12}}{k_{12} + k_{21}}. \quad (6.3.11)$$

The emission rate $I(P_{\text{ex}}) = k_{21}\rho_2(t \rightarrow \infty)$ then amounts to

$$I(P_{\text{ex}}) = \frac{k_{21}P_{\text{ex}}}{P_{\text{ex}} + k_{21}/a} = \frac{k_{21}P_{\text{ex}}}{P_{\text{ex}} + P_{\text{sat}}} \quad (6.3.12)$$

with P_{sat} the saturation power, i.e. the excitation power that is needed to bring the excited state population to its maximum value. From this follows the expected linear power dependence for low excitation powers. The rate at which photons are emitted at saturation power is described by

$$I(P_{\text{ex}} \rightarrow \infty) = k_{21}. \quad (6.3.13)$$

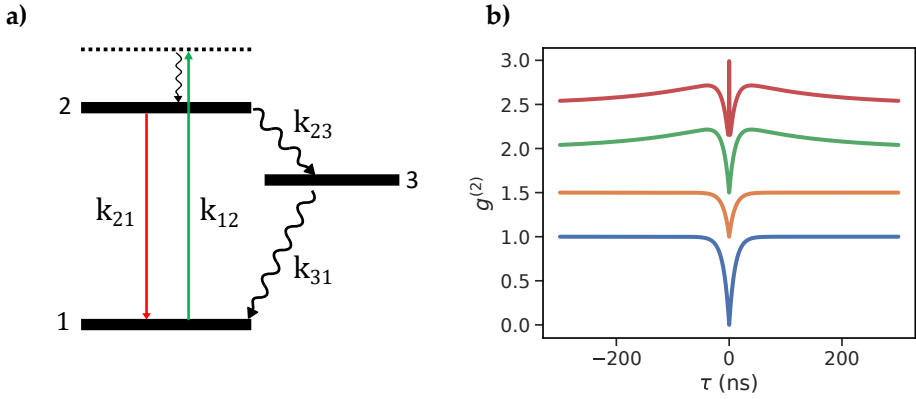


Figure 6.11: (a) Level scheme of the NV center, showing the most important rates. Note that the shelving states are depicted as a single state here for the sake of simplicity. (b) Simulated $g^{(2)}$ -functions, following eq. 6.3.19 for different sets of parameters, respectively shifted by 0.5 for visibility. Blue: $N = 1, a = b = 0, \tau_1 = 10$ ns. Orange: $N = 2, a = b = 0, \tau_1 = 10$ ns. Green: $N = 2, a = 0.3, b = 0, \tau_1 = 10$ ns, $\tau_2 = 150$ ns. Red: a second bunching term was added. $N = 2, a = 0.1, b = 1, \tau_1 = 10$ ns, $\tau_2 = 150$ ns, $\tau_{\text{SF}} = 0.5$ ns.

In order to describe NV centers, a third level **3** that represents the shelving state has to be included in the model. As the shelving state can "trap" excited electrons for a certain time, meaning that they are unable to contribute to photon emission, the emission can show a bunched behavior. In principle, an electron can also transition back from the shelving state to the excited state, but this is rather unlikely and is therefore not considered here. To derive the full dynamics of the state populations, it is necessary to solve the rate equations for all three levels.

Eq. 6.3.10 is extended by the additional level **3** and the respective rates k_{23} and k_{31} , leading to the rate equations of a three-level system:

$$\begin{pmatrix} \dot{\rho}_1 \\ \dot{\rho}_2 \\ \dot{\rho}_3 \end{pmatrix} = \begin{pmatrix} -k_{12} & k_{21} & k_{31} \\ k_{12} & -k_{21} - k_{23} & 0 \\ 0 & k_{23} & -k_{31} \end{pmatrix} \cdot \begin{pmatrix} \rho_1 \\ \rho_2 \\ \rho_3 \end{pmatrix}. \quad (6.3.14)$$

These equations can similarly be solved as eq. 6.3.10, yielding the steady state population for the excited state,

$$\rho_2(t \rightarrow \infty) = \frac{k_{12}}{\left(1 + \frac{k_{23}}{k_{31}}\right) k_{12} + k_{21} + k_{23}} \quad (6.3.15)$$

and the power-dependent emission rate,

$$I(P_{\text{ex}}) = \frac{\xi k_{12} P_{\text{ex}}}{P_{\text{ex}} + P_{\text{sat}}}. \quad (6.3.16)$$

Eq. 6.3.16 differs from the respective expression for a two-level system by the factor $\xi = \frac{1}{1 + \frac{k_{23}}{k_{31}}}$ which also changes the saturation power $P_{\text{sat}} = \xi(k_{21} + k_{23})/a$. Furthermore, eq. 6.3.13 is modified to

$$I(P_{\text{ex}} \rightarrow \infty) = \xi k_{21}. \quad (6.3.17)$$

Second-order correlation function The analytical expression for the complete second-order correlation function for an ensemble of N emitters can be obtained by once again normalizing $\rho_2(t)$ to $\rho_2(t \rightarrow \infty)$, resulting in [188]

$$g^{(2)}(\tau) = 1 - \left(\frac{1}{N} + a\right) \exp\left(-\frac{|\tau|}{\tau_1}\right) + a \exp\left(-\frac{|\tau|}{\tau_2}\right). \quad (6.3.18)$$

Here, a is the bunching amplitude with the time constant τ_2 due to the presence of the shelving state, $1/N$ describes the antibunching amplitude on the time scale τ_1 . An additional superfluorescent contribution can be expressed by adding a second bunching term, defined by the amplitude b and time constant τ_{SF} , to the $g^{(2)}$ -function which then becomes

$$g^{(2)}(\tau) = 1 - \left(\frac{1}{N} + a\right) \exp\left(-\frac{|\tau|}{\tau_1}\right) + a \exp\left(-\frac{|\tau|}{\tau_2}\right) + b \exp\left(-\frac{|\tau|}{\tau_{\text{SF}}}\right). \quad (6.3.19)$$

Note that with the presence of the second bunching term, eq. 6.3.7 is not applicable anymore as the value for $g^{(2)}(0)$ is "overwritten" by the bunching at zero time delay. Several simulated second-order correlation functions for different sets of parameters are shown in fig. 6.11(b). For just a single emitter, $g^{(2)}(0) = 0$ (blue line), which reduces when more emitters are involved at the same time (orange line). The green plot shows the same parameters as the orange one but with shelving state bunching taken into account. Note that the antibunching contrast i.e. the value of $g^{(0)}(0)$ remains the same as it is defined by the number of emitters. If a second bunching term with a much shorter time constant is added (representing collective photon bunching), the correlation function exhibits the characteristic sharp peak at zero time delay.

Uncorrelated background The main reason why the antibunching (and bunching) contrast of a $g^{(2)}$ -function might decrease is the number of emitters involved, as we saw above. A second reason, however, is the presence of uncorrelated background counts. In solid state emitters, these are quite prominent. In particular, fluorescence counts from the PSB, mainly from other color centers that are spectrally shifted with respect to the cavity resonance, can have a large share.

Generally, the collected photons can be split up into the signal (S) and background counts (B). From this, we can define a purity parameter of the counted photons,

$$p_e = \frac{S}{S + B}. \quad (6.3.20)$$

As p_e normalizes the signal counts to the total registered counts, it can be considered as the probability that a collected photon indeed originates from the ZPL of a color center that is coupled to the cavity mode. If one assumes that the ZPL and the background counts are uncorrelated, eq. 6.3.20 can be used to correct the measured correlation function, leading to [189]

$$g^{(2)}(\tau) = \left[\left(g_m^{(2)} - 1 - \Delta y \right) \frac{1}{p_e^2} \right] + 1. \quad (6.3.21)$$

Here, Δy denotes an offset of the baseline with respect to $g^{(2)}(\tau) = 1$.

Instrument response The dynamics in a cavity can happen on a very short time scale, especially for quantum emitters with short excited state lifetimes like NV or Silicon-vacancy (SiV) centers. For these fast dynamics, the instrument response of the measurement modules can become relevant as it limits the minimum time scale that can be resolved. Especially the collective effects mentioned above have time scales comparable to the instrument response time constant. The response function can be described by a Gaussian

$$j(\tau) = \frac{1}{\sqrt{2\pi}\sigma} \exp\left(-\frac{\tau^2}{\sigma^2}\right) \quad (6.3.22)$$

with σ the FWHM of the response function. A measurement of the system response is shown later in sec. 6.3.2.

As a result, the exponential decay of the central bunching peak in eq. 6.3.19 must be replaced by a Gaussian function if the signal is limited by the timing jitter of the setup. The expected instrument response can be gauged via the convolution of every single timing jitter contribution. The instrument response in this experiment is dominated by the timing jitter of the two photon count modules used in the HBT setup ($\sigma_{\text{APD1}} = 242$ ps, $\sigma_{\text{APD2}} = 352$ ps) and the time-to-digital converter ($\sigma_{\text{TDC}} = 34$ ps). The overall timing jitter is hence given by

$$\sigma = \sqrt{\sigma_{\text{APD1}}^2 + \sigma_{\text{APD2}}^2 + \sigma_{\text{TDC}}^2} \quad (6.3.23)$$

as the convolution of multiple Gaussian functions has again a Gaussian shape with the widths adding up quadratically. With this, the expected timing jitter of the detection setup can be determined to be $\sigma \approx 430$ ps. Any bunching on a shorter time scale should therefore be described using a Gaussian function.

Connection of decay rates and the second-order correlation function From the second-order correlation function given in eq. 6.3.19, one can find expressions that link the $g^{(2)}$ -parameters with the respective rates. This is very useful as it allows one to extract e.g. the excited state lifetime of the emitter from the measurement.

All the parameters then can be described by the correlation function are given by [190] as

$$\tau_{1,2} = 2/\left(A \pm \sqrt{A^2 - 4B}\right) \quad (6.3.24)$$

$$A = k_{12} + k_{21} + k_{23} + k_{31} \quad (6.3.25)$$

$$B = k_{12}k_{23} + k_{12}k_{31} + k_{21}k_{31} + k_{23}k_{31} \quad (6.3.26)$$

$$a = \frac{1 - \tau_2 k_{31}}{k_{31}(\tau_2 - \tau_1)}. \quad (6.3.27)$$

For the rates k_{12} , k_{23} and k_{32} , one finds a power dependency which let's us write

$$k_{12} = \sigma P_{\text{ex}} \quad (6.3.28)$$

$$k_{32} = d P_{\text{ex}} \quad (6.3.29)$$

$$k_{23} = e P_{\text{ex}} + k_{23}^0 \quad (6.3.30)$$

where σ , d and e are the respective proportionality constants. k_{23}^0 denotes the rate k_{23} at zero power. The constant rates k_{21} and k_{31} can be used to find an expression for the time constants in the $g^{(2)}$ -function:

$$k_{21} = 1/\tau_1^0 - k_{23}^0 \equiv \gamma \quad (6.3.31)$$

$$k_{31} = 1/\tau_2^0. \quad (6.3.32)$$

Hence, one can use the correlation function to find the different rates as fit values and extrapolate the respective time constants to zero power in order to obtain the excited state lifetimes.

Furthermore, the bunching amplitude should approach a constant value a^∞ for very large excitation powers, from which one can describe the proportionality constant e via

$$e = \frac{-a^\infty d^2 + a^\infty d \sigma}{a^\infty d + \sigma}. \quad (6.3.33)$$

From this, together with the rates, one gets the (equilibrium) population of the excited state and the total de-excitation rate Γ :

$$\rho_2 = \frac{k_{12}(k_{31} + k_{132})}{k_{23}k_{31} + k_{21}(k_{31} + k_{32}) + k_{12}(k_{23} + k_{31} + k_{32})} \quad (6.3.34)$$

$$\rho_2^\infty = \lim_{P_{\text{ex}} \rightarrow \infty} \rho_2 = \frac{1}{1 + e/d} \quad (6.3.35)$$

$$\Gamma = \rho_2^\infty k_{21}. \quad (6.3.36)$$

6.3.3. $g^{(2)}$ -measurements: photon bunching and the Purcell effect

As we have established a theoretical description of the second-order correlation function of an ensemble of NV centers that is expected to show photon bunching, we shall now

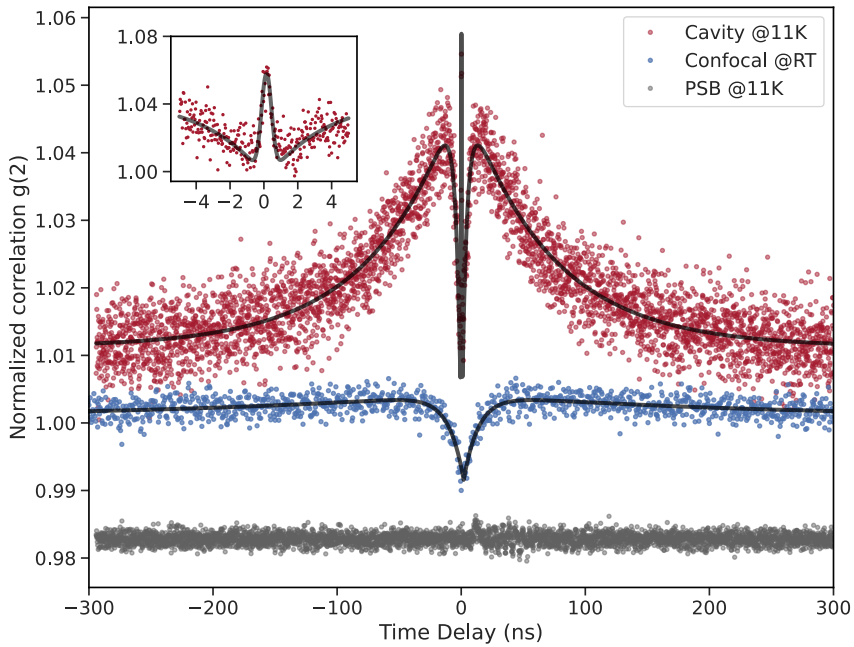


Figure 6.12: Second-order autocorrelation function of the emitted photons. The cavity-enhanced fluorescence (red data points) reveals bunching on a sub-ns time scale, as opposed to the fluorescence recorded in a confocal microscope (blue data points). The antibunching as well as the long-term bunching parts are linked to the lifetimes of the optical excited state and the non-radiative decay via the metastable singlet state. The PSB emission in the cavity setup (grey data points, shifted by 0.02 for clarity) does not show any bunching or antibunching, according to its uncorrelated nature and the much larger number of involved emitters. The inset shows a zoom of the bunching peak around $\tau = 0$.

analyze $g^{(2)}$ -measurements under different conditions such as varying excitation power or temperature. All $g^{(2)}$ -functions are recorded with continuous wave excitation.

Fig. 6.12 shows $g^{(2)}$ -functions for three different cases: first, the cavity-enhanced $g^{(2)}$ is measured with an excitation power of 4 mW (measured in front of the cavity). The cavity was thereby tuned manually to be resonant with the ZPL, where the count rate shows its maximum. For the duration of the measurement, the cavity was passively stable, slow drifts were compensated manually⁷⁰. The thermal drifts of the cavity are heavily suppressed due to the (stabilized) cryogenic temperature of the setup. Note that the slightly different cable length of the respective connections from the APD's to the TDC leads to an offset in the measured time delay and therefore shifts the correlation function.

⁷⁰ Here, the locking schemes presented in chapter 5 are not feasible since the cavity must be tuned to the center of the resonance rather than one of the fringes.

Moreover, artifacts from the collection optics like reflexes can lead to a distortion of the correlation function. To counteract this, the light of a broadband flashlight was used to record a reference with which the $g^{(2)}$ -functions can be corrected.

Number of emitters In the cavity correlation function, one can clearly identify the three different terms. The photon bunching at zero time delay is thereby a strong indicator for collective emission or interference effects. We use eq. 6.3.19 to fit the measured data, where the central bunching peak has been replaced by a Gaussian function with a time scale that is in the range of the expected instrument response. The fit function yields a bunching contrast of $\sim 7\%$ and a FWHM of the Gaussian function of 420 ps which matches the expected instrument response almost perfectly. The presence of this narrow bunching peak is an important verification that a fraction of the cavity-enhanced fluorescence might originate from collective emission. Consequently, the collective bunching cannot be observed when the measurement is repeated either in a confocal microscope (blue data points in fig 6.12) or if the photons emitted into the PSB are recorded instead of just the ZPL (grey data points). This suggests the assumption that the collective bunching is indeed a cavity-mediated effect which stems exclusively from coherent emitters. The collective effects in this experiment shall be discussed in more detail in sec. 6.3.4.

Following eq. 6.3.19, the number of emitters that couple to the cavity mode can be extracted from the antibunching contrast. Since the signal is mixed with uncorrelated background, the correlation function has first to be corrected using eq. 6.3.21. The background-corrected correlation function is shown in fig. 6.13, together with the uncorrected $g^{(2)}$ -function from fig. 6.12. The combination of the fit from eq. 6.3.19 and eq. 6.3.21 yields the contrast of the corrected $g^{(2)}$ -function of $\sim 6.7\%$ which corresponds to a number of 15 individual NV centers contributing to the ZPL fluorescence.

When the same measurement is performed at room temperature in a confocal microscope, the correlation function features a much smaller antibunching contrast. This is mostly caused by the fact that the spectral filtering from the cavity is missing. Thus, not only those NV centers that are spectrally degenerate contribute to the correlation function, but instead, the fluorescence from all emitters that lie within the spatial point spread function (PSF) of the confocal microscope is recorded. The background-corrected antibunching contrast of the confocal correlation function is $\sim 1.5\%$ which translates to roughly 67 ± 6 emitters in the confocal PSF. For the background correction, a saturation measurement of the NV fluorescence using varying excitation powers was performed. Note that the PSF of the confocal microscope has a radius of 448 nm [191] and is hence significantly smaller than the spatial size of the cavity mode which has a beam waist radius of $\sim 1.5\ \mu\text{m}$. In order to directly compare both measurements, we need to scale the number of emitters in the confocal scan up to the size of the cavity mode. From this, we can gauge a number of ~ 750 NV centers in the spatial cavity mode. Unsurprisingly, the contrast of the $g^{(2)}$ -function vanishes completely when the whole PSB from the cavity emission is recorded, as the expected antibunching contrast of $\sim 0.1\%$ is smaller than the measurement noise. The fact that only about one hundredth of the emitters

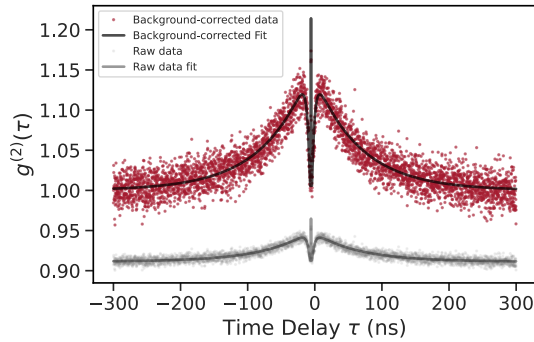


Figure 6.13: Background-corrected correlation function, according to eq. 6.3.21. The grey data points show the original $g^{(2)}$ -function as shown in fig. 6.12. The uncorrected data was shifted by 0.1 for better visibility.

that lie within the spatial cavity mode feature a ZPL frequency that overlaps with the spectral cavity mode emphasizes the heavy filtering effect of the cavity.

Power dependence and Purcell enhancement The decay time constants of the antibunching and the shelving-state-bunching in fig. 6.12 are given by the fit as $\tau_1 = 3.9$ ns and $\tau_2 = 69$ ns, respectively. Since the measurement was recorded under continuous-wave excitation, the time constants also depend on the excitation rate k_{12} . The excited state lifetime can therefore be determined by repeating the measurement for varying excitation laser powers such that the power dependency can be quantified. Fig. 6.14(a) shows the fit function of several correlation measurements. Here, some general trends can be identified:

- The central bunching peak is visible for all excitation powers and stays roughly the same for all measurements (6 – 8 %, uncorrected). The time constant remains almost unchanged for all measurements, fluctuating around 400 ps.
- The shelving-state-bunching decreases for increasing laser powers. This is somewhat surprising, as one would expect the exact opposite due to the linear power dependence of the rate k_{23} which causes this bunching. A clear explanation for this phenomenon could not be found in the course of this work.
- The antibunching contrast decreases for higher excitation powers. The contrast decrease for both the bunching and the antibunching could be caused by the increased amount of background that arises for higher excitation powers.

The antibunching time constants are shown in fig. 6.14(b). The measurement reveals an exponential decrease of the time constant for increasing laser powers. We can now

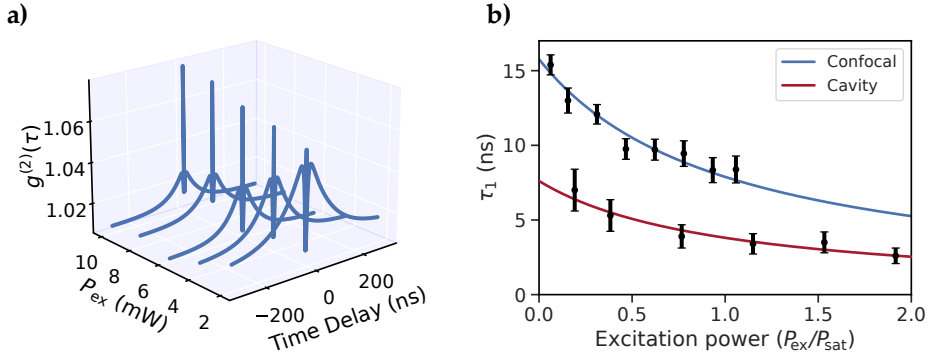


Figure 6.14: Power dependence of the correlation function. (a) Fitted $g^{(2)}$ -functions for changing excitation laser powers. (b) Time constants of the antibunching term for the cavity-enhanced (red) and the confocal (blue) measurements. Both data sets were fitted using a global fit of the rate model introduced in sec. 6.3.2. The excitation powers are normalized to the respective saturation power.

use the rate equations that were introduced in sec. 6.3.2 as a global fit to extract the time constant at zero laser power. The fit yields the excited state lifetime in the cavity of $\tau_c = 7.6 \pm 0.9$ ns. The fact that this lifetime is shorter than the expected free space excited state lifetime is a manifest of the cavity enhancement due to the Purcell effect. To quantify this effect, the measurement is repeated in the confocal microscope where the NV centers show their natural lifetime. Note that the excitation powers for the data sets in fig. 6.14(b) are normalized to their respective saturation power, since the spatial mode size is different for both cases.

The confocal measurement yields $\tau_0 = 15.8 \pm 0.8$ ns, which translates to a Purcell factor of

$$C_{\text{eff}} = \frac{\tau_0}{\tau_c} - 1 = 1.1 \pm 0.3. \quad (6.3.37)$$

When we only consider the ZPL, the emission enhancement is given by the ideal Purcell factor which is given by

$$C = C_{\text{eff}}/\zeta = 36 \pm 11. \quad (6.3.38)$$

This value leads to an increased probability for the emission into the ZPL from $\sim 3\%$ to $\sim 53\%$ of which almost the entirety ($> 97\%$) is emitted into the cavity mode, following eq. 3.2.43.

Interestingly, the free space lifetime measured in the confocal microscope is slightly higher than the literature value of 12 ns [24]. This deviation is caused by the structure of the dielectric environment surrounding the emitters. As opposed to the high refractive index of the diamond host of NV centers in a bulk environment, the shallowly implanted

NV centers in this case are very close (~ 10 nm) to the mirror surface, i.e. a diamond-silica interface. This difference leads to a longer lifetime, as described in refs. [192] and [193]. The time constant of the shelving-state-bunching at zero laser power is given by the fit as $\tau_2 \approx 200$ ns which is consistent with the literature value of 219 ns [82, 83]. Note that the bunching time constant is not altered by the cavity as the decay via the shelving states is not affected by the Purcell effect. The measured time constant thus refers to the free space decay, even when measured in a cavity.

6.3.4. Interpretation of the collective bunching peak

Influence of the instrument response To verify that the central bunching peak is indeed limited by the instrument response as proposed in the previous section, we record the correlation function of a pulsed laser source⁷¹ with very short pulses of 50 ps that should be limited entirely by the timing jitter. The resulting correlation function should then reveal the instrument response. As shown in fig. 6.15(a), it almost perfectly matches the central bunching peak from the NV emission. For this depiction, the background--corrected $g^{(2)}$ -function of the cavity-enhanced ZPL emission was fitted while omitting the central bunching peak, i.e. only antibunching and shelving-state-bunching were considered. The resulting fit function was then subtracted from the data, yielding the isolated bunching peak. The measured FWHM of the instrument response is 410 ps and is therefore close to the theoretical value of 430 ps, obtained via the single timing jitter constants.

The information obtained from this measurement can now be used to extract the "real" bunching peak as the measured peak is a convolution of the actual photon bunching peak and the instrument response. This is shown in fig. 6.15(b). The dynamics that lead to the bunching are expected to be faster than the photon ring-down time of the cavity, given by $\tau_{rd} = d\mathcal{F}/\pi c = 155$ ps (see eq. 3.1.7). Hence, we can estimate the deconvolved peak as an exponential decay with a linewidth of two times the ring-down time. The peak is then convolved with the measured instrument response, which was normalized such that the area under the curve is 1 and therefore does not change the integral of the convolved peak. The amplitude of the cavity-limited peak is then adjusted so as to match the measured bunching contrast after the convolution. Indeed, the resulting convolution describes the bunching peak almost perfectly. This corroborates the assumption that the collective decay of NV centers in the cavity is faster than the decay of the cavity itself. Moreover, it reveals the unconvolved bunching contrast of ~ 70 %.

Temperature dependence The theoretical interpretation of collectively coupling emitters suggests that the occurrence of such depends on the dephasing dynamics of the system. To probe this experimentally, we change the temperature of the sample which

⁷¹ WL-SC-450-2-PP, Fianium

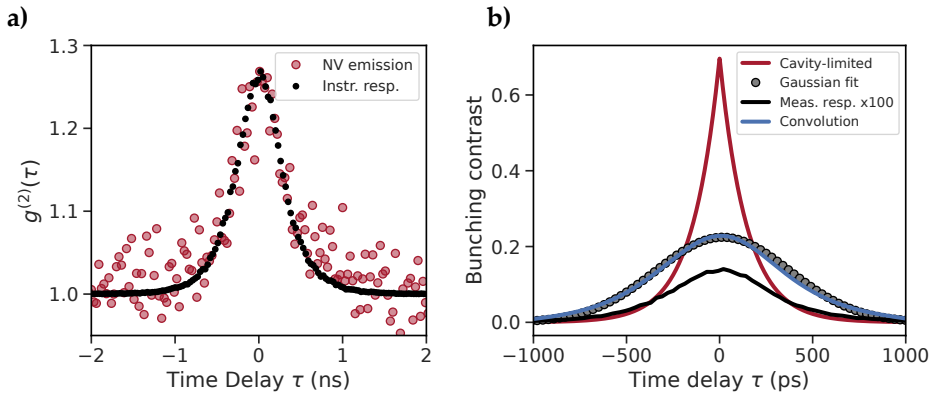


Figure 6.15: (a) Measured instrument response, compared to the background-corrected collective bunching peak after subtraction of the fitted antibunching and shelving-state-bunching terms. The instrument response refers to the correlation function of 50 ps short laser pulses that were heavily attenuated and forwarded directly onto the count APD's. (b) Convolution of a cavity-limited exponential decay, representing the photon ring-down time, with the measured and normalized instrument response. The normalized response function is rescaled by a factor of 100 for better visibility.

leads to a broadening of the homogeneous linewidth, hence to a shorter dephasing time. For this measurement, the sample temperature is increased stepwise from 10.6 K up to room temperature. At each temperature, the $g^{(2)}$ -function is recorded, similarly to previous correlation measurements. Fig. 6.16(a) shows a selection of the resulting correlation functions. The contrasts of the central bunching peak and the antibunching caused by the individual emitters are shown in fig. 6.16(b). Unsurprisingly, the contrast from individual NV centers, i.e. the antibunching and shelving-state-bunching gradually decreases until it completely vanishes around 100 K. As the homogeneous linewidth of the NV centers increases with temperature (see ref. [93]), more and more emitters overlap spectrally with the cavity resonance which leads to a decrease of the contrast. The collective bunching, on the other side, is visible for all temperatures except for room temperature, with an almost constant amplitude. This implies that this effect is very robust against dephasing and suggests that it is limited by the cavity photon lifetime. It should be stated that the measurement at room temperature has to be treated with caution as the ZPL becomes so broad that the count rate does not change when scanning the cavity length, making it virtually impossible to keep the cavity resonant with the ZPL. Furthermore, the temperature sensor is attached to the mirror holder, rather than to the sample itself. This leads to a possibly inaccurate temperature measurement, where the actual temperature of the NV centers might be higher than the measured value. Another possible source of error is the alignment of the optical setup, especially the lateral position of the fiber mirror on the sample. When the temperature of the setup is changed, the position of the fiber slightly drifts. The change of the position on the

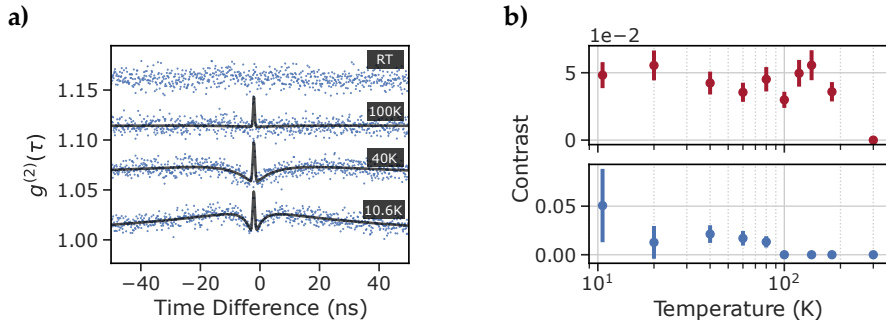


Figure 6.16: (a) Temperature dependence of the correlation function. The temperature was increased in steps of 10 to 20 K, a representative selection is shown here. The scan at room temperature was not fitted as no bunching or antibunching features were visible. The respective data sets are shifted for better visibility. (b) Contrast of the central bunching peak (red) and the surrounding antibunching (blue) for different sample temperatures. The respective errors are extracted from the fits of the $g^{(2)}$ -functions.

sample can be compensated using the x-axis motor (as the lateral drift is mainly limited to this direction, see sec. 5.2.1). However, also the angular alignment of the fiber changes, which leads to a slightly different cavity mode and hence to an altering angle of the cavity transmission. The resulting changes in the optical beam path were compensated after every temperature step.

Interpretation of the photon bunching The measurements shown in this chapter clearly indicate the emission of bunched light on very short time scales which can be observed with any excitation laser power or sample temperature. However, it is not trivial to identify in which regime the system can be described. According to the work of Auffèves et al. [64], the collective behavior of individual emitters strongly depends on the cavity parameters such as finesse, atom-cavity coupling strength, and emitter properties like dephasing. In the case of our experiment, one has $\frac{\kappa}{g_0} = \frac{1.1 \text{ GHz}}{180 \text{ MHz}} \approx 6.1$. From this alone, one would expect a much stronger bunching as well as an oscillatory dependence on N , as shown in fig. 3.7. Both were not observed in the experiment, which is due to the strong dephasing in the investigated sample.

A system with a high ratio of κ to g_0 can still show collective emission. This, however, is only the case for small pure dephasing rates, given by γ^* . When the dephasing approaches $\gamma^* = g_0$, the system again shifts to the uncorrelated regime, and finally shows thermal behavior for large γ^* . The pure dephasing rate cannot be measured in our experiment, but is estimated to be smaller than the cavity linewidth. For $\gamma^* = 500 \text{ MHz} \approx 2.8 \cdot g_0$, the system is already heavily dominated by dephasing. No bunching contrast larger than two would then be expected, similar to the bad cavity limit. The photon bunching is then a result of the interference of several individual, yet

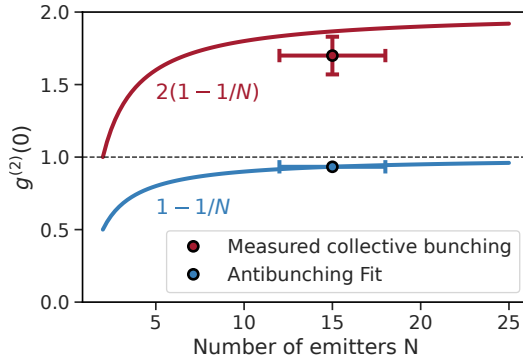


Figure 6.17: Theoretical contrast of the antibunching and the central bunching peak as a function of the number of particles, as described in ref. [64]. The data point of the bunching refers to the deconvolved bunching peak of the measurement shown in fig. 6.12, the antibunching contrast is extracted from the fit of the correlation function. The error for the number of emitter is given by the uncertainty of the antibunching fit, the error of the bunching peak results from the error of the cavity ring-down time τ_{rd} which influences the deconvolved peak.

indistinguishable emitters.

In the simulations for a weak emitter-cavity coupling or strong dephasing, $g^{(2)}(0)$ shows a $2(1 - 1/N)$ -dependence. For the previously gauged number of emitters of $N = 15$, one would therefore anticipate a value of $g^{(2)}(0) \approx 1.87$. From the deconvolution in fig. 6.15(b), we extract $g^{(2)}(0) \approx 1.7$, which comes reasonably close to the theoretically predicted value, but would translate to $N \approx 7$, if $g^{(2)}(0) = 2(1 - 1/N)$ is assumed to be valid. Both scaling laws are depicted in fig. 6.17, together with the values that were extracted from our measurements. What contradicts the emission of thermal light, is the fact that the fast bunching can only be observed in the ZPL emission, while it completely disappears when investigating the PSB. For a thermal light source, this should not be relevant.

Another dynamic that could mitigate superfluorescent emission is the number of emitters that is excited at the same time. As shown in fig. 3.6, the correlation between individual emitters in a system described by the Dicke model becomes the strongest for a half-excited system, i.e. for $|J, M = 0\rangle$. Only then, the emission rate scales with N^2 . For the fully excited or de-excited system, this effect is lost and the N^2 -scaling becomes a linear N -scaling.

One characteristic of the second-order correlation functions measured in the course of this thesis is that we are able to observe the single particle nature (antibunching, shelving-state-bunching) and collective effects from the ensemble (bunching on short times scales) at the same time. The question of terminology remains unsolved for the time being, especially since the different regimes discussed above are not always clearly distinct. However, the most reasonable explanation of the observed effects is that the photon bunching stems from interference effects while the super-linear power depen-

dence of the ZPL is indeed caused by superfluorescent emission. To our knowledge, these results have never been shown before using NV centers in a cavity.

6.3.5. Outlook

In this section, the Purcell-enhanced emission from ensembles of NV centers in a diamond membrane and therefore the most prioritized goal of this work was successfully demonstrated. Nevertheless, some open questions and possible improvements remain. The bunching at short time delays in the correlation function is still not fully understood. In order to narrow down possible explanations, a full theoretical description of the experiment is needed. This would allow for a full evaluation and a clear description of the mechanisms in the system. A limiting factor is the strong dephasing in the sample, which is partly due to the shallow depth of the implantation. The experiment would possibly benefit greatly from a more "bulk-like" environment of the emitters.

Another way of revealing collective effects in a NV ensemble is by using a pulsed excitation laser instead of the continuous wave excitation laser that was used in this work. With that, it should be possible to directly record the exponential decay of the fluorescence count rate, featuring an increased decay rate, if additional, fast decay channels are present. This was attempted in the scope of this work, but the fast decay could not be observed, as background noise dominated on the relevant time scale.

In this experiment, off-resonant excitation was used exclusively. However, with a resonant excitation laser, it could be possible to resolve single NV centers also in these large inhomogeneous ensembles by scanning the narrow laser line over the ZPL and resolving the individual emitters spectrally. Thereby, one could either collect the emission from the PSB or the ZPL directly. The latter requires either pulsed excitation or a cross-polarization scheme.

Considering the cavity setup itself, major redesigns could improve the robustness of the cavity against thermal drifts. This would expedite the $g^{(2)}$ -measurements with changing temperature greatly, as the repeating realignment of the cavity is very time-consuming.

7. Conclusion

In the course of this work, the effective integration of micrometer thick diamond membranes into a fiber-based microcavity was achieved, followed by the demonstration of Purcell-enhanced emission from ensembles of NV centers. We have identified influences on the performance of a cavity that the integration of such a dielectric layer has, that have been either underestimated or omitted completely in the past. To quantify this, we have investigated key parameters of the cavity such as the transmitted power and the cavity finesse in fully spatially resolved measurements.

In order to maximize the Purcell effect, the design of a mechanically stable cavity platform suitable for a cryogenic environment was crucial. As we have seen, the mechanical stability as well as negligible thermal drifts when cooled down enable us to keep the cavity on resonance with the coherent optical transition of the NV centers and thus observe Purcell-enhanced fluorescence. Moreover, this allowed us to measure the second-order correlation function of the emission over long periods of time and reveal photon bunching at short time scales.

The most significant difference to previously published results was thereby that ensemble effects from only a few emitters are observed, as opposed to the much larger emitter numbers of other experiments that can easily exceed 10^3 emitters [69, 70]. While the investigation of ensemble-based fluorescence and cavity effects gives great insight into the emitter-cavity coupling for multiple emitters, a primal goal of the project that this thesis and its successors are assigned to is to build an efficient spin-photon interface for a quantum repeater [194]. The basic structure of such a repeater is shown in fig. 7.1, containing multiple segments and quantum repeater cells. The latter is the perspective

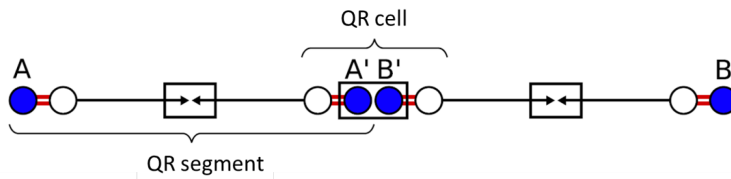


Figure 7.1: Basic structure of a quantum repeater as proposed in the course of the project *Quantenrepeater.Link*. It aims for a connection of two nodes, A and B, via the intermediate connection A'B'. The blue circles thereby represent "stationary qubits" (spins), the white circles denote the so called "flying qubits", i.e. photons. An entanglement between a stationary and a flying qubit is represented by the red double-line connections.

application of the developments that were achieved within this thesis. There, the control and readout of single NV centers is the central aspect of the device. As the technological parts of the experiment have been designed with the eventual goals in mind, the transition to single emitters could be realized, if a sample with sufficiently narrow, isolated NV centers is available.

Efficiency of the spin-photon interface For applications in the field of quantum communication, the efficiency of a device is one of its central quality attributes. As the main goal of the NV-based spin-photon interface is the emission of photons that are entangled to the electron or nuclear spin of the NV center, a high probability for the creation of indistinguishable photons is necessary. This, of course, does not only involve the emission itself, but also the collection efficiency that is defined via a combination of properties like the probability that a photon can be extracted out of the cavity and is then actually measured by the photon detector.

The efficiency can be gauged by combining the most limiting factors. We define P_{link} as the probability that a coherent (i.e. ZPL) photon is emitted into the cavity mode, transmitted out of the cavity through the desired cavity mirror (combined under η_{creation}), reaches and finally triggers the photodetector ($\eta_{\text{detection}}$). If the photon is not collected in free space but is instead coupled into a fiber network, the efficiency of the fiber coupling η_{fiber} has to be included as well. P_{link} is therefore given by

$$P_{\text{link}} = \eta_{\text{creation}} \cdot \eta_{\text{fiber}} \cdot \eta_{\text{detection}}. \quad (7.0.1)$$

$\eta_{\text{creation}} = \beta \cdot \eta_c$ is described via the product of the already derived factor β which defines the fraction of coherent photons that are emitted into the cavity mode (see eq. 3.2.43) and the fraction of photons that are transmitted through the desired cavity mirror (i.e. into the "right" direction) $\eta_c = T_2 / \mathcal{L}_{\text{tot}}$, see sec. 3.1.1. \mathcal{L}_{tot} denotes the overall effective losses in the system, resulting in the measured cavity finesse, T_2 is the transmissivity of the outcoupling mirror. It is thus advantageous to design a cavity with asymmetric mirror transmissions. Note that the Purcell factor for diamond membranes that have been cut along the (100)-crystal surface is further decreased by a factor of 1/3 due to the lower coupling efficiency of the NV dipole to the cavity light field⁷². $\eta_{\text{detection}}$ is mostly defined by the quantum efficiency of the detector, which is typically in the range of 70 % for the transition wavelength.

Inserting the values that have been extracted from the measurements in chapter 6 into eq. 7.0.1 yields an expected link efficiency of 0.16. This value as well as the theoretical estimated values for different Purcell factors are illustrated in fig. 7.2. Here, the color of the different curves describes the directionality of the emission, i.e. η_c . From this, we can see that the efficiency of a spin-photon interface can benefit significantly from a

⁷² In the case presented here, this effect is already included in the Purcell factor, as we consider the value that was extracted from the measured lifetime reduction.

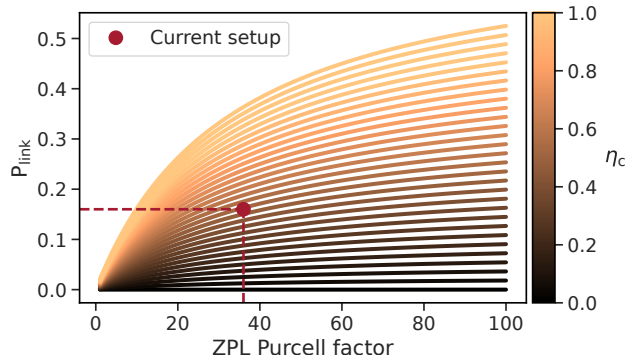


Figure 7.2: Theoretical estimation of the achievable link efficiency under varying cavity properties, in comparison to the current setup.

higher Purcell factor, but is ultimately also limited by the mirror transmissions. Ideally, one would conceptualize the cavity in a way that one of the mirrors is almost perfectly reflective. Furthermore, a lower \mathcal{L}_{tot} of course also leads to a higher cavity finesse and therefore to a higher Purcell factor. Note that this estimation completely omits the protocol for the entanglement of photons to the electron spin of the NV and its probability to succeed.

Potential improvements As indicated by the above-shown evaluation, the most obvious improvement that can be realized is to operate the cavity with a higher finesse. While this sounds rather straightforward, it comes along with other challenges. In chapter 5, we have seen that a higher finesse at the same time requires a better mechanical stability in order to fully utilize the narrower cavity line. The achieved cavity stability of under one picometer is more than sufficient for a much higher finesse, but requires an improved locking scheme such as stabilization on a double resonance, or temporal gating of the lock, as shown in ref. [49]. Another way to increase the impact of the Purcell effect is by minimizing the beam waist. It can be manipulated via the fiber machining as a mirror profile with a smaller radius of curvature leads to a smaller beam waist (see eq. 4.5.4). However, the ROC cannot be chosen arbitrarily small as the profile becomes steeper for smaller radii of curvature. This can impact the coating as well as the cavity stability range. Furthermore, the additional losses induced by the presence of the diamond membrane have to be avoided as much as possible. This can be accomplished by a very well machined and pure sample. Moreover, fig. 7.2 indicates that even a moderate Purcell factor can lead to reasonable efficiencies if the total loss is dominated by the transmission through the outcoupling mirror.

Finally, the cutting axis of the sample can improve its performance greatly. By using a sample cut along the (111) surface, one "loses" 75 % of the potential emitters since their dipole axes are lying along the electric field vector of the excitation field. However, one

7. Conclusion

of the NV orientation axes matches the (111)-vector perfectly and can therefore couple efficiently to the cavity mode. This means that the Purcell factor is increased by a factor of 3 for those NV centers. For a system with identical properties as the one in chapter 6, this would increase the link efficiency from 0.16 to 0.24. Ultimately, the link efficiency is limited by the quantum efficiency of the detector.

Concluding words The research field of light-matter interaction in optical cavities is still growing as new experimental approaches are proposed and new emitters are discovered that might improve the potential of such systems immediately. In order to further push the progress, it is crucial to develop an understanding of its technological as well as fundamental boundaries. The results that are presented in this thesis can certainly help to show the potential of our approach and open up new possible experiments or applications.

The road that has to be taken to successfully achieve the goals of the second quantum revolution might be a lengthy one. The progress that was made in the last years, however, is astonishing and holds promise to result in many new technologies that can improve our society, our industries, and, eventually, our everyday life.

Appendices

A. Transmission scans during a cooldown

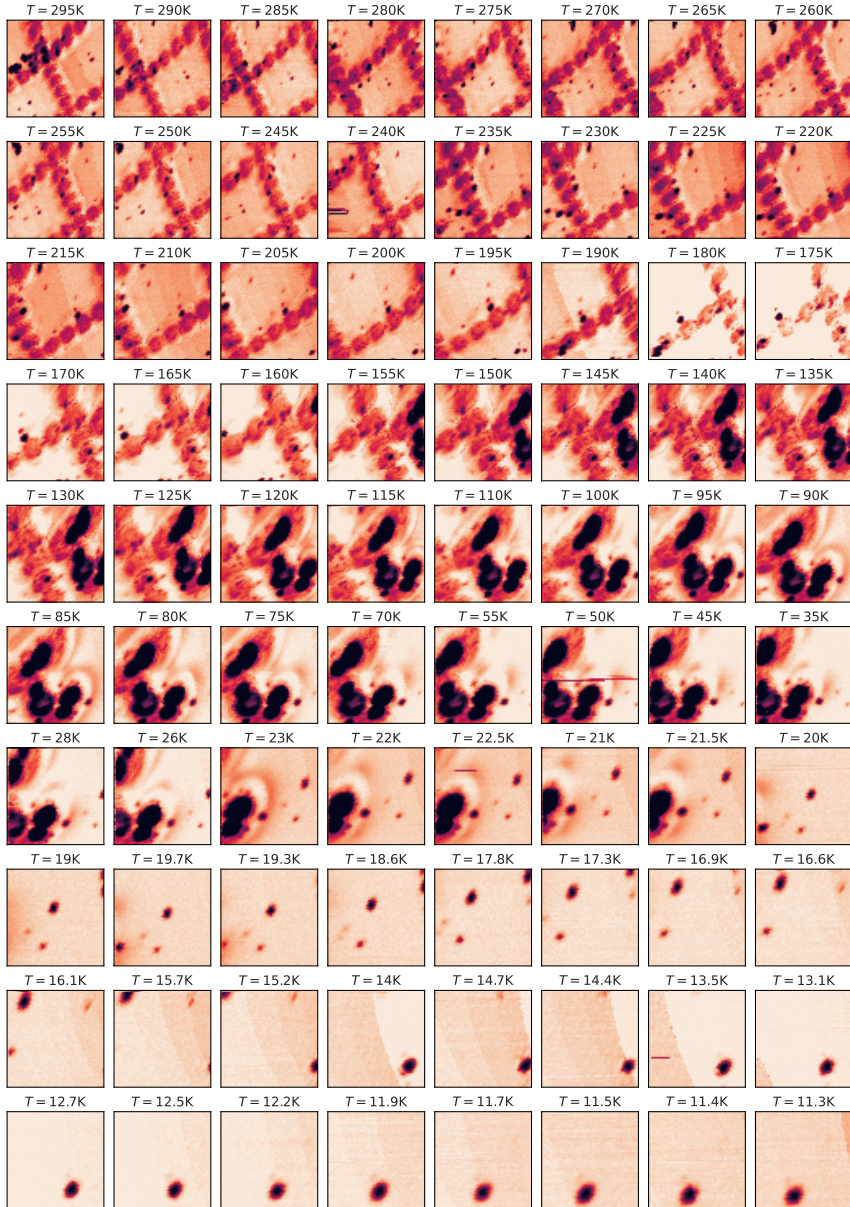


Figure A.1: Full set of the cavity transmission scans during the cooldown shown in fig. 5.4.

B. Dispersion measurement

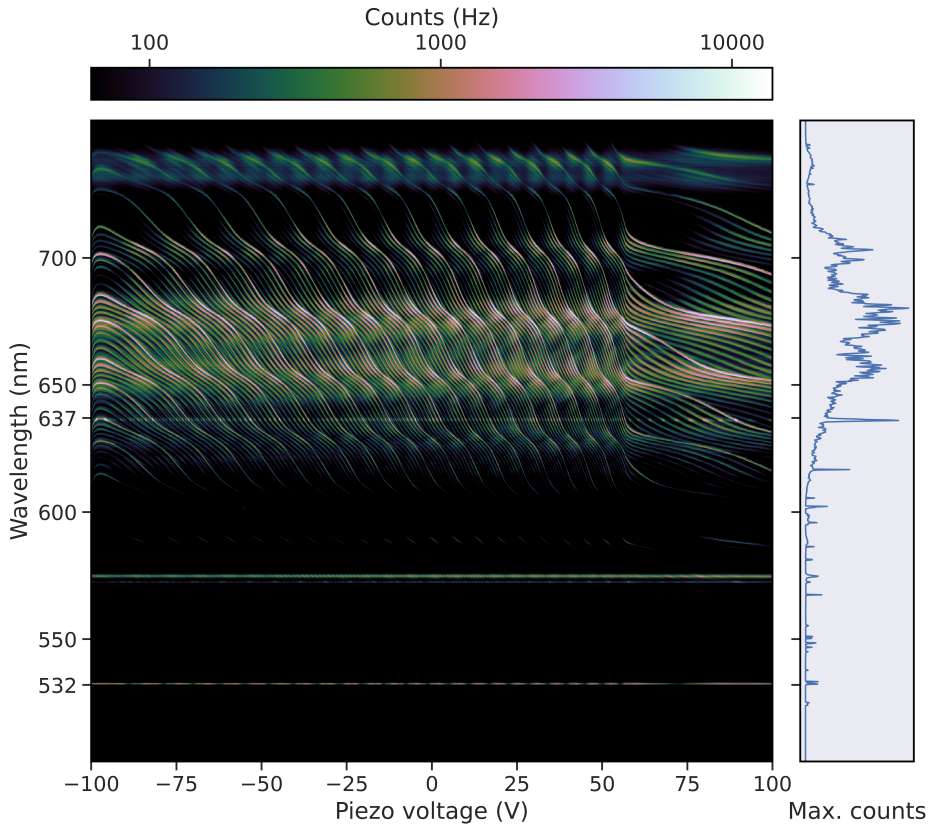


Figure B.2: Mode dispersion over the full scanning range. Several wavelengths are independent from the cavity length and hence appear as straight horizontal lines in the dispersion. The most prominent ones are the residual signal from the excitation laser at 532 nm, the first order Raman peak at 572 nm [195], and the ZPL at 637 nm.

C. Overview of the cavity parameters

From the measurements that were performed in chapter 6, one can extract a full set of parameters that describe the cavity itself as well as the light-matter interaction in the resonator. In tab. C.1, an overview of these parameters is given. Note that some of these values are valid exclusively for these measurements, like e.g. the cavity length, beam waist or the mode volume.

Parameter	Symbol	Value
Cavity finesse	\mathcal{F}	11000
Optical cavity length	d	12.5 μm
Cavity quality factor	Q	430 000
Cavity linewidth	$\delta\nu$	1.1 GHz
Cavity decay rate	κ	$2\pi \cdot 1.1$ GHz
Cavity ringdown time	τ_{rd}	145 ps
Beam waist	w_0	1.5 μm
Mode Volume	V_m	22 μm^3
Homogeneous emitter linewidth	$\delta\nu_e$	< 1 GHz
Emitter dephasing	$\gamma + \gamma^*$	< $2\pi \cdot 1$ GHz
Inhomogeneous emitter linewidth @11 K	$\delta\nu_{e,\text{inh.}}$	400 GHz
Number of NV's in the spatial cavity mode	-	750
Number of NV's in the spectral cavity mode	-	15
Free space lifetime	τ_0	15.8 ns
Cavity-enhanced lifetime	τ_c	7.6 ns
Effective Purcell factor	C_{eff}	1.1
ZPL Purcell factor	C	36
Cavity-emitter coupling strength	g	$2\pi \cdot 180$ MHz

Table C.1: Overview of the relevant cavity parameters as measured in chapter 6

D. Abbreviations and symbols

Abbreviations

NV	nitrogen-vacancy
ZPL	zero-phonon line
hBN	hexagonal boron nitride
SiV	silicon-vacancy
SnV	tin-vacancy
GeV	germanium-vacancy
PSB	phonon-side band
SIL	solid immersion lens
SR	superradiance
SF	superfluorescence
LCAO	linear combination of atomic orbitals
ODMR	optically detected magnetic resonance
PDMR	photoelectric detected magnetic resonance
ND	nanodiamonds
RIE	reactive-ion etching
CVD	chemical vapor deposition
HTA	high temperature annealing
FSR	free spectral range
TEM	transverse electromagnetic (modes)
cQED	cavity quantum electrodynamics
JC	Jaynes-Cummings

DoS	density of states
QE	quantum efficiency
TC	Tavis-Cummings
ASE	amplified spontaneous emission
PC	photonic crystal
WGM	whispering gallery mode
AOM	acousto-optic modulator
WLI	white light interferometer
DBR	distributed Bragg reflector
PMMA	Polymethylmethacrylat
ROC	radius of curvature
GRIN	graded-index
MM	multimode
ICP-RIE	inductively-coupled plasma reactive-ion etching
TDL	tunable diode laser
FPGA	field-programmable gate array
FWHM	full width at half maximum
PID	proportional-integral-derivative
PDH	Pound-Drever-Hall
SOF	side of fringe
EOM	electro-optic modulator
APD	avalanche photodiode
CMOS	metal-oxide-semiconductor
PSD	power spectral density

ASD	amplitude spectral density
FFT	fast Fourier transform
AOTF	acousto-optic tunable filter
HBT	Hanbury Brown and Twiss
TDC	time-to-digital converter

Symbols

$\delta\nu$	Linewidth
\mathcal{L}_{tot}	Total loss
\mathcal{F}	Finesse
$\Delta\nu$	Free spectral range
τ_{rd}	Cavity ringdown time
κ	Cavity decay rate
Q	Quality factor
P_{peak}	Maximum intra-cavity power
η_{c}	Outcoupling efficiency
$T_{(1,2)}$	Mirror transmissions
$R_{(1,2)}$	Radii of curvature
q	Longitudinal mode order
g	Cavity-emitter coupling strength
V_{m}	Mode volume
w_0	Beam waist
T_1	Excited state lifetime

T_2^*	Pure dephasing time
γ	Spontaneous emission rate
γ^*	Pure dephasing rate
M_{12}	Transition matrix element
$\rho(\omega)$	Density of states
$\Lambda(\omega)$	Emitter density of states
ξ	Dipole orientation factor
C	Purcell factor
C_0	Ideal Purcell factor
C_{eff}	Effective Purcell factor
ζ	Branching ratio
β	Emission efficiency
τ_0	Free-space lifetime
τ_c	Cavity-enhanced lifetime
R	Cavity-emitter coupling rate
QE	Quantum efficiency
γ_N	Collective emission rate
P	Macroscopic dipole moment
ROC	Radius of curvature
ϵ	Mode matching factor
\mathcal{L}_m	Mirror losses
t_a	Cavity air gap
t_d	Diamond thickness
n_d	Refractive index of diamond

$\mathcal{L}_{\text{scat}}$	Scattering loss
\mathcal{L}_{abs}	Absorption loss
σ_{rms}	RMS surface roughness
α_{d}	Absorption coefficient of diamond
C_{curv}	Curvature-induced loss factor
δ	Polarization frequency splitting
δd	Mirror separation linewidth
Δz	Cavity length jitter
$\tau_{1,2}$	Bunching/Antibunching time constant
p_e	Signal-to-noise ratio
σ	Timing jitter
P_{link}	Link efficiency
η_{fiber}	Fiber coupling efficiency
$\eta_{\text{detection}}$	Detection efficiency

E. Publications and conference contributions

Publications

- *"Fabrication and Characterization of Single-Crystal Diamond Membranes for Quantum Photonics with Tunable Microcavities"*
J. Heupel, M. Pallmann, J. Körber, R. Merz, M. Kopnarski, R. Stöhr, J. Reithmaier, D. Hunger, C. Popov
2020, Micromachines 11(12) (2020) [73]
- *„Scanning cavity microscopy of a single-crystal diamond“*
J. Körber, M. Pallmann, J. Heupel, R. Stöhr, E. Vasilenko, T. Hümmer, L. Kohler, C. Popov, D. Hunger
Preprint (2022), DOI:10.48550/arXiv.2210.05514 [45]
- *„Fabrication of High-Quality Thin Single-Crystal Diamond Membranes with Low Surface Roughness“*
J. Heupel, M. Pallmann, J. Körber, D. Hunger, J. Reithmaier, C. Popov
Physica Status Solidi (A) Application and Materials (2022) [74]
- *„A highly stable and fully tunable open microcavity platform at cryogenic temperatures“*
M. Pallmann, T. Eichhorn, J. Benedikter, B. Casabone, T. Hümmer, D. Hunger
APL Photonics (2022) [75]
- *“Cavity-mediated collective emission from few inhomogeneous color centers in a diamond membrane”*
M. Pallmann, K. Köster, Y. Zhang, J. Heupel, C. Popov, K. Mølmer, D. Hunger
currently being prepared for publication (2023)

Conference Contributions

- *"Development of a coherent spin-photon interface for quantum repeaters using NV centers in diamond"*
Latsis Symposium Diamond Photonics, Poster
Lausanne, Switzerland, May 2019
Awarded with 3rd place "Best Student Poster"
- *"Development of a coherent spin-photon interface for quantum repeaters using NV centers in diamond"*
Summer school "Quantum devices for non-classical light generation and manipulation", Poster
Erice, Italy, September 2019
- *"Development of a coherent spin-photon interface for quantum repeaters using NV centers in diamond"*
DPG-Tagung der Sektion AMOP, Poster
Rostock, Germany, March 2019
- *"Development of a coherent spin-photon interface for quantum repeaters using NV centers in diamond"*
718. WE-Heraeus-Seminar, Poster
Bad Honnef, Germany, August 2021
- *"Development of a coherent spin-photon interface for quantum repeaters using NV centers in diamond"*
DPG-Tagung der Sektion AMOP, Poster
virtual, September 2021
- *"Nitrogen-vacancy centers in diamond membranes coupled to an optical microcavity"*
DPG-Tagung der Sektion AMOP, Talk
virtual, March 2022
- *"Superfluorescence of cavity-enhanced NV centers in diamond membranes"*
DPG-Tagung der Sektion KM, Talk
Regensburg, Germany, September 2022
- *"Superfluorescence of cavity-enhanced NV centers in diamond membranes"*
Frontiers in Optics, Talk
Rochester (New York), USA, October 2022

Bibliography

- [1] A. L. Schawlow and C. H. Townes, “Infrared and Optical Masers,” *Physical Review*, vol. 112, pp. 1940–1949, Dec. 1958.
- [2] L. J. Edgar, “Method and apparatus for controlling electric currents,” Jan. 1930.
- [3] C. Degen, F. Reinhard, and P. Cappellaro, “Quantum sensing,” *Reviews of Modern Physics*, vol. 89, p. 035002, July 2017.
- [4] A. Barenco, C. H. Bennett, R. Cleve, D. P. DiVincenzo, N. Margolus, P. Shor, T. Sleator, J. A. Smolin, and H. Weinfurter, “Elementary gates for quantum computation,” *Physical Review A*, vol. 52, pp. 3457–3467, Nov. 1995.
- [5] A. Steane, “Quantum computing,” *Reports on Progress in Physics*, vol. 61, pp. 117–173, Feb. 1998.
- [6] C. H. Bennett and D. P. DiVincenzo, “Quantum information and computation,” *Nature*, vol. 404, pp. 247–255, Mar. 2000.
- [7] H. J. Kimble, “The quantum internet,” *Nature*, vol. 453, pp. 1023–1030, June 2008.
- [8] J. L. O’Brien, A. Furusawa, and J. Vučković, “Photonic quantum technologies,” *Nature Photonics*, vol. 3, pp. 687–695, Dec. 2009.
- [9] P. W. Shor and J. Preskill, “Simple Proof of Security of the BB84 Quantum Key Distribution Protocol,” *Physical Review Letters*, vol. 85, pp. 441–444, July 2000.
- [10] C. H. Bennett and G. Brassard, “Quantum cryptography: Public key distribution and coin tossing,” *Theoretical Computer Science*, vol. 560, pp. 7–11, Dec. 2014.
- [11] J. P. Dowling and G. J. Milburn, “Quantum technology: the second quantum revolution,” *Philosophical Transactions of the Royal Society of London. Series A: Mathematical, Physical and Engineering Sciences*, vol. 361, pp. 1655–1674, Aug. 2003.
- [12] J. I. Cirac and P. Zoller, “Quantum Computations with Cold Trapped Ions,” *Physical Review Letters*, vol. 74, pp. 4091–4094, May 1995.

- [13] J. Kim, O. Benson, H. Kan, and Y. Yamamoto, "A single-photon turnstile device," *Nature*, vol. 397, pp. 500–503, Feb. 1999.
- [14] M. B. Ward, T. Farrow, P. See, Z. L. Yuan, O. Z. Karimov, A. J. Bennett, A. J. Shields, P. Atkinson, K. Cooper, and D. A. Ritchie, "Electrically driven telecommunication wavelength single-photon source," *Applied Physics Letters*, vol. 90, p. 063512, Feb. 2007.
- [15] W. P. Ambrose and W. E. Moerner, "Fluorescence spectroscopy and spectral diffusion of single impurity molecules in a crystal," *Nature*, vol. 349, pp. 225–227, Jan. 1991.
- [16] T. Basché, W. E. Moerner, M. Orrit, and H. Talon, "Photon antibunching in the fluorescence of a single dye molecule trapped in a solid," *Physical Review Letters*, vol. 69, pp. 1516–1519, Sept. 1992.
- [17] M. Zhong, M. P. Hedges, R. L. Ahlefeldt, J. G. Bartholomew, S. E. Beavan, S. M. Wittig, J. J. Longdell, and M. J. Sellars, "Optically addressable nuclear spins in a solid with a six-hour coherence time," *Nature*, vol. 517, pp. 177–180, Jan. 2015.
- [18] A. Högele, C. Galland, M. Winger, and A. Imamoğlu, "Photon Antibunching in the Photoluminescence Spectra of a Single Carbon Nanotube," *Physical Review Letters*, vol. 100, p. 217401, May 2008.
- [19] S. Castelletto and A. Boretti, "Silicon carbide color centers for quantum applications," *Journal of Physics: Photonics*, vol. 2, p. 022001, Apr. 2020.
- [20] S. Häußler, G. Bayer, R. Waltrich, N. Mendelson, C. Li, D. Hunger, I. Aharonovich, and A. Kubanek, "Tunable Fiber-Cavity Enhanced Photon Emission from Defect Centers in hBN," *Advanced Optical Materials*, vol. 9, p. 2002218, Sept. 2021.
- [21] I. Aharonovich, S. Castelletto, D. A. Simpson, C.-H. Su, A. D. Greentree, and S. Praver, "Diamond-based single-photon emitters," *Reports on Progress in Physics*, vol. 74, p. 076501, July 2011.
- [22] I. Aharonovich, D. Englund, and M. Toth, "Solid-state single-photon emitters," *Nature Photonics*, vol. 10, pp. 631–641, Oct. 2016.
- [23] F. Jelezko and J. Wrachtrup, "Single defect centres in diamond: A review," *physica status solidi (a)*, vol. 203, pp. 3207–3225, Oct. 2006.
- [24] M. W. Doherty, N. B. Manson, P. Delaney, F. Jelezko, J. Wrachtrup, and L. C. L. Hollenberg, "The nitrogen-vacancy colour centre in diamond," *Physics Reports*, vol. 528, pp. 1–45, July 2013. arXiv: 1302.3288.

- [25] J. P. Goss, R. Jones, S. J. Breuer, P. R. Briddon, and S. Öberg, “The Twelve-Line 1.682 eV Luminescence Center in Diamond and the Vacancy-Silicon Complex,” *Physical Review Letters*, vol. 77, pp. 3041–3044, Sept. 1996.
- [26] A. E. Rugar, C. Dory, S. Aghaeimeibodi, H. Lu, S. Sun, S. D. Mishra, Z.-X. Shen, N. A. Melosh, and J. Vučković, “Narrow-Linewidth Tin-Vacancy Centers in a Diamond Waveguide,” *ACS Photonics*, vol. 7, pp. 2356–2361, Sept. 2020.
- [27] A. E. Rugar, H. Lu, C. Dory, S. Sun, P. J. McQuade, Z.-X. Shen, N. A. Melosh, and J. Vučković, “Generation of Tin-Vacancy Centers in Diamond via Shallow Ion Implantation and Subsequent Diamond Overgrowth,” *Nano Letters*, vol. 20, pp. 1614–1619, Mar. 2020.
- [28] M. E. Trusheim, B. Pingault, N. H. Wan, M. Gündoğan, L. De Santis, R. Debroux, D. Gangloff, C. Purser, K. C. Chen, M. Walsh, J. J. Rose, J. N. Becker, B. Lienhard, E. Bersin, I. Paradeisanos, G. Wang, D. Lyzwa, A. R.-P. Montblanch, G. Malladi, H. Bakhru, A. C. Ferrari, I. A. Walmsley, M. Atatüre, and D. Englund, “Transform-Limited Photons From a Coherent Tin-Vacancy Spin in Diamond,” *Physical Review Letters*, vol. 124, p. 023602, Jan. 2020.
- [29] T. Iwasaki, F. Ishibashi, Y. Miyamoto, Y. Doi, S. Kobayashi, T. Miyazaki, K. Tahara, K. D. Jahnke, L. J. Rogers, B. Naydenov, F. Jelezko, S. Yamasaki, S. Nagamachi, T. Inubushi, N. Mizuochi, and M. Hatano, “Germanium-Vacancy Single Color Centers in Diamond,” *Scientific Reports*, vol. 5, p. 12882, Aug. 2015.
- [30] P. Siyushev, M. H. Metsch, A. Ijaz, J. M. Binder, M. K. Bhaskar, D. D. Sukachev, A. Sipahigil, R. E. Evans, C. T. Nguyen, M. D. Lukin, P. R. Hemmer, Y. N. Palyanov, I. N. Kupriyanov, Y. M. Borzdov, L. J. Rogers, and F. Jelezko, “Optical and microwave control of germanium-vacancy center spins in diamond,” *Physical Review B*, vol. 96, p. 081201, Aug. 2017.
- [31] M. H. Aboobeih, J. Cramer, M. A. Bakker, N. Kalb, M. Markham, D. J. Twitchen, and T. H. Taminiau, “One-second coherence for a single electron spin coupled to a multi-qubit nuclear-spin environment,” *Nature Communications*, vol. 9, p. 2552, June 2018.
- [32] G. Balasubramanian, P. Neumann, D. Twitchen, M. Markham, R. Kolesov, N. Mizuochi, J. Isoya, J. Achard, J. Beck, J. Tissler, V. Jacques, P. R. Hemmer, F. Jelezko, and J. Wrachtrup, “Ultralong spin coherence time in isotopically engineered diamond,” *Nature Materials*, vol. 8, pp. 383–387, May 2009.
- [33] M. Pompili, S. L. N. Hermans, S. Baier, H. K. C. Beukers, P. C. Humphreys, R. N. Schouten, R. F. L. Vermeulen, M. J. Tiggeleman, L. Dos Santos Martins, B. Dirkse, S. Wehner, and R. Hanson, “Realization of a multinode quantum network of remote solid-state qubits,” *Science*, vol. 372, pp. 259–264, Apr. 2021.

- [34] A. Faraon, P. E. Barclay, C. Santori, K.-M. C. Fu, and R. G. Beausoleil, “Resonant enhancement of the zero-phonon emission from a colour centre in a diamond cavity,” *Nature Photonics*, vol. 5, pp. 301–305, May 2011. Number: 5 Publisher: Nature Publishing Group.
- [35] S. M. Mansfield and G. S. Kino, “Solid immersion microscope,” *Applied Physics Letters*, vol. 57, pp. 2615–2616, Dec. 1990.
- [36] M. Jamali, I. Gerhardt, M. Rezai, K. Frenner, H. Fedder, and J. Wrachtrup, “Microscopic diamond solid-immersion-lenses fabricated around single defect centers by focused ion beam milling,” *Review of Scientific Instruments*, vol. 85, p. 123703, Dec. 2014.
- [37] J. P. Hadden, J. P. Harrison, A. C. Stanley-Clarke, L. Marseglia, Y.-L. D. Ho, B. R. Patton, J. L. O’Brien, and J. G. Rarity, “Strongly enhanced photon collection from diamond defect centers under microfabricated integrated solid immersion lenses,” *Applied Physics Letters*, vol. 97, p. 241901, Dec. 2010.
- [38] E. M. Purcell, H. C. Torrey, and R. V. Pound, “Resonance Absorption by Nuclear Magnetic Moments in a Solid,” *Physical Review*, vol. 69, pp. 37–38, Jan. 1946.
- [39] D. Hunger, T. Steinmetz, Y. Colombe, C. Deutsch, T. W. Hänsch, and J. Reichel, “A fiber Fabry–Perot cavity with high finesse,” *New Journal of Physics*, vol. 12, p. 065038, June 2010.
- [40] H. Kaupp, T. Hümmer, M. Mader, B. Schleder, J. Benedikter, P. Haeusser, H.-C. Chang, H. Fedder, T. W. Hänsch, and D. Hunger, “Purcell-Enhanced Single-Photon Emission from Nitrogen-Vacancy Centers Coupled to a Tunable Microcavity,” *Physical Review Applied*, vol. 6, p. 054010, Nov. 2016.
- [41] J. Hessenauer, K. Weber, J. Benedikter, T. Gissibl, J. Höfer, H. Giessen, and D. Hunger, “Laser written mirror profiles for open-access fiber Fabry–Pérot microcavities,” 2022. Publisher: arXiv Version Number: 1.
- [42] B. J. M. Hausmann, B. J. Shields, Q. Quan, Y. Chu, N. P. de Leon, R. Evans, M. J. Burek, A. S. Zibrov, M. Markham, D. J. Twitchen, H. Park, M. D. Lukin, and M. Lončar, “Coupling of NV Centers to Photonic Crystal Nanobeams in Diamond,” *Nano Letters*, vol. 13, pp. 5791–5796, Dec. 2013.
- [43] E. Janitz, M. Ruf, M. Dimock, A. Bourassa, J. Sankey, and L. Childress, “Fabry-Perot microcavity for diamond-based photonics,” *Physical Review A*, vol. 92, p. 043844, Oct. 2015.
- [44] S. B. van Dam, M. Ruf, and R. Hanson, “Optimal design of diamond-air microcavities for quantum networks using an analytical approach,” *New Journal of Physics*,

- vol. 20, p. 115004, Nov. 2018.
- [45] J. Körber, M. Pallmann, J. Heupel, R. Stöhr, E. Vasilenko, T. Hümmer, L. Kohler, C. Popov, and D. Hunger, “Scanning cavity microscopy of a single-crystal diamond membrane,” Oct. 2022. arXiv:2210.05514 [cond-mat, physics:physics, physics:quant-ph].
- [46] P. Tamarat, T. Gaebel, J. R. Rabeau, M. Khan, A. D. Greentree, H. Wilson, L. C. L. Hollenberg, S. Prawer, P. Hemmer, F. Jelezko, and J. Wrachtrup, “Stark Shift Control of Single Optical Centers in Diamond,” *Physical Review Letters*, vol. 97, p. 083002, Aug. 2006.
- [47] D. Najer, I. Söllner, P. Sekatski, V. Dolique, M. C. Löbl, D. Riedel, R. Schott, S. Starosielec, S. R. Valentin, A. D. Wieck, N. Sangouard, A. Ludwig, and R. J. Warburton, “A gated quantum dot strongly coupled to an optical microcavity,” *Nature*, vol. 575, pp. 622–627, Nov. 2019. Number: 7784 Publisher: Nature Publishing Group.
- [48] B. Merkel, A. Ulanowski, and A. Reiserer, “Coherent and Purcell-Enhanced Emission from Erbium Dopants in a Cryogenic High-Q Resonator,” *Physical Review X*, vol. 10, p. 041025, Nov. 2020. Publisher: American Physical Society.
- [49] B. Casabone, C. Deshmukh, S. Liu, D. Serrano, A. Ferrier, T. Hümmer, P. Goldner, D. Hunger, and H. de Riedmatten, “Dynamic control of Purcell enhanced emission of erbium ions in nanoparticles,” *Nature Communications*, vol. 12, p. 3570, June 2021.
- [50] M. Ruf, M. Weaver, S. van Dam, and R. Hanson, “Resonant Excitation and Purcell Enhancement of Coherent Nitrogen-Vacancy Centers Coupled to a Fabry-Perot Microcavity,” *Physical Review Applied*, vol. 15, p. 024049, Feb. 2021.
- [51] Y. Fontana, R. Zifkin, E. Janitz, C. D. Rodríguez Rosenblueth, and L. Childress, “A mechanically stable and tunable cryogenic Fabry-Pérot microcavity,” *Review of Scientific Instruments*, vol. 92, p. 053906, May 2021.
- [52] R. H. Dicke, “Coherence in Spontaneous Radiation Processes,” *Physical Review*, vol. 93, pp. 99–110, Jan. 1954.
- [53] N. Skribanowitz, I. P. Herman, J. C. MacGillivray, and M. S. Feld, “Observation of Dicke Superradiance in Optically Pumped HF Gas,” *Physical Review Letters*, vol. 30, pp. 309–312, Feb. 1973.
- [54] R. Bonifacio, P. Schwendimann, and F. Haake, “Quantum Statistical Theory of Superradiance. I,” *Physical Review A*, vol. 4, pp. 302–313, July 1971.

- [55] R. Bonifacio and L. A. Lugiato, “Cooperative radiation processes in two-level systems: Superfluorescence,” *Physical Review A*, vol. 11, pp. 1507–1521, May 1975. Publisher: American Physical Society.
- [56] D. Meiser, J. Ye, D. R. Carlson, and M. J. Holland, “Prospects for a Millihertz--Linewidth Laser,” *Physical Review Letters*, vol. 102, p. 163601, Apr. 2009.
- [57] J. G. Bohnet, Z. Chen, J. M. Weiner, D. Meiser, M. J. Holland, and J. K. Thompson, “A steady-state superradiant laser with less than one intracavity photon,” *Nature*, vol. 484, pp. 78–81, Apr. 2012.
- [58] G. Ferioli, A. Glicenstein, L. Henriot, I. Ferrier-Barbut, and A. Browaeys, “Storage and Release of Subradiant Excitations in a Dense Atomic Cloud,” *Physical Review X*, vol. 11, p. 021031, May 2021.
- [59] Z. Shen and A. Dogariu, “Subradiant directional memory in cooperative scattering,” *Nature Photonics*, vol. 16, pp. 148–153, Feb. 2022. Number: 2 Publisher: Nature Publishing Group.
- [60] M. Lei, R. Fukumori, J. Rochman, B. Zhu, M. Endres, J. Choi, and A. Faraon, “Many-body cavity quantum electrodynamics with driven inhomogeneous emitters,” Aug. 2022. arXiv:2208.04345 [physics, physics:quant-ph].
- [61] A. Rastogi, E. Saglamyurek, T. Hrushevskiy, and L. J. LeBlanc, “Superradiance-Mediated Photon Storage for Broadband Quantum Memory,” *Physical Review Letters*, vol. 129, p. 120502, Sept. 2022.
- [62] V. Paulisch, M. Perarnau-Llobet, A. González-Tudela, and J. I. Cirac, “Quantum metrology with one-dimensional superradiant photonic states,” *Physical Review A*, vol. 99, p. 043807, Apr. 2019.
- [63] N. Barnes and B. Walsh, “Amplified spontaneous emission-application to Nd:YAG lasers,” *IEEE Journal of Quantum Electronics*, vol. 35, pp. 101–109, Jan. 1999. Conference Name: IEEE Journal of Quantum Electronics.
- [64] A. Auffèves, D. Gerace, S. Portolan, A. Drezet, and M. França Santos, “Few emitters in a cavity: from cooperative emission to individualization,” *New Journal of Physics*, vol. 13, p. 093020, Sept. 2011.
- [65] M. A. Norcia, R. J. Lewis-Swan, J. R. K. Cline, B. Zhu, A. M. Rey, and J. K. Thompson, “Cavity-mediated collective spin-exchange interactions in a strontium superradiant laser,” *Science*, vol. 361, pp. 259–262, July 2018.
- [66] J. A. Muniz, D. Barberena, R. J. Lewis-Swan, D. J. Young, J. R. K. Cline, A. M. Rey, and J. K. Thompson, “Exploring dynamical phase transitions with cold atoms in

- an optical cavity,” *Nature*, vol. 580, pp. 602–607, Apr. 2020.
- [67] M. Scheibner, T. Schmidt, L. Worschech, A. Forchel, G. Bacher, T. Passow, and D. Hommel, “Superradiance of quantum dots,” *Nature Physics*, vol. 3, pp. 106–110, Feb. 2007.
- [68] K. Miyajima, Y. Kagotani, S. Saito, M. Ashida, and T. Itoh, “Superfluorescent pulsed emission from biexcitons in an ensemble of semiconductor quantum dots,” *Journal of Physics: Condensed Matter*, vol. 21, p. 195802, May 2009.
- [69] A. Angerer, “Superradiant emission from colour centres in diamond,” *Nature Physics*, vol. 14, p. 7, 2018.
- [70] C. Bradac, M. T. Johnsson, M. v. Breugel, B. Q. Baragiola, R. Martin, M. L. Juan, G. K. Brennen, and T. Volz, “Room-temperature spontaneous superradiance from single diamond nanocrystals,” *Nature Communications*, vol. 8, p. 1205, Dec. 2017.
- [71] T. Hümmer, *Cavity-enhanced hyperspectral Raman and Absorption Microscopy*. PhD thesis, 2019.
- [72] J. Benedikter, *Microcavity enhancement of silicon vacancy centres in diamond and europium ions in yttria*. PhD thesis, Ludwig-Maximilians-Universität München, 2019. Medium: application/pdf.
- [73] J. Heupel, M. Pallmann, J. Körber, R. Merz, M. Kopnarski, R. Stöhr, J. P. Reithmaier, D. Hunger, and C. Popov, “Fabrication and Characterization of Single-Crystal Diamond Membranes for Quantum Photonics with Tunable Microcavities,” *Micromachines*, vol. 11, p. 1080, Dec. 2020. Number: 12 Publisher: Multidisciplinary Digital Publishing Institute.
- [74] J. Heupel, M. Pallmann, J. Körber, D. Hunger, J. P. Reithmaier, and C. Popov, “Fabrication of High-Quality Thin Single-Crystal Diamond Membranes with Low Surface Roughness,” *physica status solidi (a)*, vol. n/a, no. n/a, p. 2200465. _eprint: <https://onlinelibrary.wiley.com/doi/pdf/10.1002/pssa.202200465>.
- [75] M. Pallmann, T. Eichhorn, J. M. H. Benedikter, B. Casabone, T. Hümmer, and D. Hunger, “A highly stable and fully tunable open microcavity platform at cryogenic temperatures,” *APL Photonics*, p. 5.0139003, Mar. 2023.
- [76] J. R. Weber, W. F. Koehl, J. B. Varley, A. Janotti, B. B. Buckley, C. G. Van de Walle, and D. D. Awschalom, “Quantum computing with defects,” *Proceedings of the National Academy of Sciences*, vol. 107, pp. 8513–8518, May 2010.
- [77] S. Mukherjee, *Applied mineralogy: applications in industry and environment*. Dordrecht: Springer, 2011.

- [78] W. Kaiser and W. L. Bond, "Nitrogen, A Major Impurity in Common Type I Diamond," *Physical Review*, vol. 115, pp. 857–863, Aug. 1959.
- [79] J. R. Maze, A. Gali, E. Togan, Y. Chu, A. Trifonov, E. Kaxiras, and M. D. Lukin, "Properties of nitrogen-vacancy centers in diamond: the group theoretic approach," *New Journal of Physics*, vol. 13, p. 025025, Feb. 2011.
- [80] M. W. Doherty, N. B. Manson, P. Delaney, and L. C. L. Hollenberg, "The negatively charged nitrogen-vacancy centre in diamond: the electronic solution," *New Journal of Physics*, vol. 13, p. 025019, Feb. 2011.
- [81] D. Riedel, *Engineering of the photonic environment of single nitrogen-vacancy centers in diamond*. PhD Thesis, University_of_Basel, 2017.
- [82] V. M. Acosta, E. Bauch, M. P. Ledbetter, C. Santori, K.-M. C. Fu, P. E. Barclay, R. G. Beausoleil, H. Linget, J. F. Roch, F. Treussart, S. Chemerisov, W. Gawlik, and D. Budker, "Diamonds with a high density of nitrogen-vacancy centers for magnetometry applications," *Physical Review B*, vol. 80, p. 115202, Sept. 2009.
- [83] V. M. Acosta, A. Jarmola, E. Bauch, and D. Budker, "Optical properties of the nitrogen-vacancy singlet levels in diamond," *Physical Review B*, vol. 82, p. 201202, Nov. 2010.
- [84] G. Zhang, Y. Cheng, J.-P. Chou, and A. Gali, "Material platforms for defect qubits and single-photon emitters," *Applied Physics Reviews*, vol. 7, p. 031308, Sept. 2020.
- [85] K. Huang and A. Rhys, "Theory of light absorption and non-radiative transitions in F -centres," *Proceedings of the Royal Society of London. Series A. Mathematical and Physical Sciences*, vol. 204, pp. 406–423, Dec. 1950.
- [86] M. de Jong, L. Seijo, A. Meijerink, and F. T. Rabouw, "Resolving the ambiguity in the relation between Stokes shift and Huang–Rhys parameter," *Physical Chemistry Chemical Physics*, vol. 17, no. 26, pp. 16959–16969, 2015.
- [87] M. Born and R. Oppenheimer, "Zur Quantentheorie der Molekeln," *Annalen der Physik*, vol. 389, no. 20, pp. 457–484, 1927.
- [88] E. W. Schlag and G. Drechsler, "H. Haken, H.C. Wolf: Molekülphysik und Quantenchemie, 2. Auflage, Springer-Verlag, 1994, ISBN 3-540-57460-3, 429 Seiten, Preis: DM 74,-," *Berichte der Bunsengesellschaft für physikalische Chemie*, vol. 99, pp. 692–693, Apr. 1995.
- [89] V. Hizhnyakov, H. Kaasik, and I. Sildos, "Zero-Phonon Lines: The Effect of a Strong Softening of Elastic Springs in the Excited State," *physica status solidi (b)*, vol. 234, no. 2, pp. 644–653, 2002.

-
- [90] K. Lee, B. J. Sussman, J. Nunn, V. Lorenz, K. Reim, D. Jaksch, I. Walmsley, P. Spizzirri, and S. Praver, "Comparing phonon dephasing lifetimes in diamond using Transient Coherent Ultrafast Phonon Spectroscopy," *Diamond and Related Materials*, vol. 19, pp. 1289–1295, Oct. 2010.
- [91] A. T. Collins, M. F. Thomaz, and M. I. B. Jorge, "Luminescence decay time of the 1.945 eV centre in type Ib diamond," *Journal of Physics C: Solid State Physics*, vol. 16, pp. 2177–2181, Apr. 1983.
- [92] G. Davies, "The Jahn-Teller effect and vibronic coupling at deep levels in diamond," *Reports on Progress in Physics*, vol. 44, pp. 787–830, July 1981.
- [93] K.-M. C. Fu, C. Santori, P. E. Barclay, L. J. Rogers, N. B. Manson, and R. G. Beausoleil, "Observation of the Dynamic Jahn-Teller Effect in the Excited States of Nitrogen-Vacancy Centers in Diamond," *Physical Review Letters*, vol. 103, p. 256404, Dec. 2009.
- [94] J. Wolters, N. Sadzak, A. W. Schell, T. Schröder, and O. Benson, "Measurement of the Ultrafast Spectral Diffusion of the Optical Transition of Nitrogen Vacancy Centers in Nano-Size Diamond Using Correlation Interferometry," *Physical Review Letters*, vol. 110, p. 027401, Jan. 2013.
- [95] L. C. Bassett, F. J. Heremans, C. G. Yale, B. B. Buckley, and D. D. Awschalom, "Electrical Tuning of Single Nitrogen-Vacancy Center Optical Transitions Enhanced by Photoinduced Fields," *Physical Review Letters*, vol. 107, p. 266403, Dec. 2011.
- [96] Z. Yuan, M. Fitzpatrick, L. V. H. Rodgers, S. Sangtawesin, S. Srinivasan, and N. P. de Leon, "Charge state dynamics and optically detected electron spin resonance contrast of shallow nitrogen-vacancy centers in diamond," *Physical Review Research*, vol. 2, p. 033263, Aug. 2020.
- [97] V. M. Acosta, C. Santori, A. Faraon, Z. Huang, K.-M. C. Fu, A. Stacey, D. A. Simpson, K. Ganesan, S. Tomljenovic-Hanic, A. D. Greentree, S. Praver, and R. G. Beausoleil, "Dynamic Stabilization of the Optical Resonances of Single Nitrogen-Vacancy Centers in Diamond," *Physical Review Letters*, vol. 108, p. 206401, May 2012.
- [98] N. Manson, L. Rogers, M. Doherty, and L. Hollenberg, "Optically induced spin polarisation of the NV- centre in diamond: role of electron-vibration interaction," 2010. Publisher: arXiv Version Number: 1.
- [99] P. Neumann, R. Kolesov, V. Jacques, J. Beck, J. Tisler, A. Batalov, L. Rogers, N. B. Manson, G. Balasubramanian, F. Jelezko, and J. Wrachtrup, "Excited-state spectroscopy of single NV defects in diamond using optically detected magnetic resonance," *New Journal of Physics*, vol. 11, p. 013017, Jan. 2009.

- [100] L. Robledo, L. Childress, H. Bernien, B. Hensen, P. F. A. Alkemade, and R. Hanson, “High-fidelity projective read-out of a solid-state spin quantum register,” *Nature*, vol. 477, pp. 574–578, Sept. 2011. Number: 7366 Publisher: Nature Publishing Group.
- [101] L. Rondin, J.-P. Tetienne, T. Hingant, J.-F. Roch, P. Maletinsky, and V. Jacques, “Magnetometry with nitrogen-vacancy defects in diamond,” *Reports on Progress in Physics*, vol. 77, p. 056503, May 2014.
- [102] C. L. Degen, “Scanning magnetic field microscope with a diamond single-spin sensor,” *Applied Physics Letters*, vol. 92, p. 243111, June 2008.
- [103] J. M. Taylor, P. Cappellaro, L. Childress, L. Jiang, D. Budker, P. R. Hemmer, A. Yacoby, R. Walsworth, and M. D. Lukin, “High-sensitivity diamond magnetometer with nanoscale resolution,” *Nature Physics*, vol. 4, pp. 810–816, Oct. 2008.
- [104] B. Shields, Q. Unterreithmeier, N. de Leon, H. Park, and M. Lukin, “Efficient Read-out of a Single Spin State in Diamond via Spin-to-Charge Conversion,” *Physical Review Letters*, vol. 114, p. 136402, Mar. 2015.
- [105] E. Bourgeois, A. Jarmola, P. Siyushev, M. Gulka, J. Hruby, F. Jelezko, D. Budker, and M. Nesladek, “Photoelectric detection of electron spin resonance of nitrogen-vacancy centres in diamond,” *Nature Communications*, vol. 6, p. 8577, Oct. 2015.
- [106] C. T. Nguyen, D. D. Sukachev, M. K. Bhaskar, B. Machielse, D. S. Levonian, E. N. Knall, P. Stroganov, R. Riedinger, H. Park, M. Lončar, and M. D. Lukin, “Quantum network nodes based on diamond qubits with an efficient nanophotonic interface,” *Physical Review Letters*, vol. 123, p. 183602, Oct. 2019. arXiv:1907.13199 [quant-ph].
- [107] R. E. Evans, M. K. Bhaskar, D. D. Sukachev, C. T. Nguyen, A. Sipahigil, M. J. Burek, B. Machielse, G. H. Zhang, A. S. Zibrov, E. Bielejec, H. Park, M. Lončar, and M. D. Lukin, “Photon-mediated interactions between quantum emitters in a diamond nanocavity,” *Science*, vol. 362, pp. 662–665, Nov. 2018. Publisher: American Association for the Advancement of Science.
- [108] E. Neu, C. Arend, E. Gross, F. Guldner, C. Hepp, D. Steinmetz, E. Zscherpel, S. Ghodbane, H. Sternschulte, D. Steinmüller-Nethl, Y. Liang, A. Krueger, and C. Becher, “Narrowband fluorescent nanodiamonds produced from chemical vapor deposition films,” *Applied Physics Letters*, vol. 98, p. 243107, June 2011.
- [109] J. Benedikter, H. Kaupp, T. Hümmer, Y. Liang, A. Bommer, C. Becher, A. Krueger, J. M. Smith, T. W. Hänsch, and D. Hunger, “Cavity-Enhanced Single-Photon Source Based on the Silicon-Vacancy Center in Diamond,” *Physical Review Applied*, vol. 7, p. 024031, Feb. 2017.

- [110] N. Mohan, C.-S. Chen, H.-H. Hsieh, Y.-C. Wu, and H.-C. Chang, "In Vivo Imaging and Toxicity Assessments of Fluorescent Nanodiamonds in *Caenorhabditis elegans*," *Nano Letters*, vol. 10, pp. 3692–3699, Sept. 2010.
- [111] K. Tews, "On the variation of luminescence lifetimes. The approximations of the approximative methods," *Journal of Luminescence*, vol. 9, pp. 223–239, Sept. 1974.
- [112] M. Ruf, M. Ijspeert, S. van Dam, N. de Jong, H. van den Berg, G. Evers, and R. Hanson, "Optically Coherent Nitrogen-Vacancy Centers in Micrometer-Thin Etched Diamond Membranes," *Nano Letters*, vol. 19, pp. 3987–3992, June 2019.
- [113] R. Hanson, "Mother Nature outgrown," *Nature Materials*, vol. 8, pp. 368–369, May 2009. Number: 5 Publisher: Nature Publishing Group.
- [114] J. Isberg, J. Hammersberg, E. Johansson, T. Wikström, D. J. Twitchen, A. J. Whitehead, S. E. Coe, and G. A. Scarsbrook, "High Carrier Mobility in Single-Crystal Plasma-Deposited Diamond," *Science*, vol. 297, pp. 1670–1672, Sept. 2002.
- [115] S. Pezzagna, D. Rogalla, D. Wildanger, J. Meijer, and A. Zaitsev, "Creation and nature of optical centres in diamond for single-photon emission—overview and critical remarks," *New Journal of Physics*, vol. 13, p. 035024, Mar. 2011.
- [116] Y. Chu, N. de Leon, B. Shields, B. Hausmann, R. Evans, E. Togan, M. J. Burek, M. Markham, A. Stacey, A. Zibrov, A. Yacoby, D. Twitchen, M. Loncar, H. Park, P. Maletinsky, and M. Lukin, "Coherent Optical Transitions in Implanted Nitrogen Vacancy Centers," *Nano Letters*, vol. 14, pp. 1982–1986, Apr. 2014.
- [117] D. Riedel, I. Söllner, B. J. Shields, S. Starosielec, P. Appel, E. Neu, P. Maletinsky, and R. J. Warburton, "Deterministic Enhancement of Coherent Photon Generation from a Nitrogen-Vacancy Center in Ultrapure Diamond," *Physical Review X*, vol. 7, p. 031040, Sept. 2017.
- [118] Y.-C. Chen, P. S. Salter, S. Knauer, L. Weng, A. C. Frangeskou, C. J. Stephen, S. N. Ishmael, P. R. Dolan, S. Johnson, B. L. Green, G. W. Morley, M. E. Newton, J. G. Rarity, M. J. Booth, and J. M. Smith, "Laser writing of coherent colour centres in diamond," *Nature Photonics*, vol. 11, pp. 77–80, Feb. 2017. Number: 2 Publisher: Nature Publishing Group.
- [119] K. C. Wong, S. L. Ng, K. O. Ho, Y. Shen, J. Wu, K. T. Lai, M. Y. Leung, W. K. Leung, D. B. R. Dasari, A. Denisenko, J. Wrachtrup, and S. Yang, "Microscopic Study of Optically Stable Coherent Color Centers in Diamond Generated by High-Temperature Annealing," *Physical Review Applied*, vol. 18, p. 024044, Aug. 2022.

- [120] L. Orphal-Kobin, K. Unterguggenberger, T. Pregolato, N. Kemf, M. Matalla, R.-S. Unger, I. Ostermay, G. Pieplow, and T. Schröder, “Optically coherent nitrogen--vacancy defect centers in diamond nanostructures,” Mar. 2022. arXiv:2203.05605 [physics, physics:quant-ph].
- [121] J. Meijer, B. Burchard, M. Domhan, C. Wittmann, T. Gaebel, I. Popa, F. Jelezko, and J. Wrachtrup, “Generation of single color centers by focused nitrogen implantation,” *Applied Physics Letters*, vol. 87, p. 261909, Dec. 2005. Publisher: American Institute of Physics.
- [122] A. T. Collins, “Vacancy enhanced aggregation of nitrogen in diamond,” *Journal of Physics C: Solid State Physics*, vol. 13, p. 2641, May 1980.
- [123] L. A.-M. Kohler, *Characterization and tracking of the three-dimensional translational motion and rotation of single nanoparticles using a fiber-based microcavity with high finesse*. PhD thesis, 2021.
- [124] B. E. A. Saleh and M. C. Teich, *Fundamentals of Photonics*. Wiley Series in Pure and Applied Optics, New York, USA: John Wiley & Sons, Inc., Aug. 1991.
- [125] D. Meschede, *Optik, Licht und Laser*. Wiesbaden: Vieweg+Teubner, 2008.
- [126] M. Fox, *Quantum optics: an introduction*. No. 15 in Oxford master series in physics, Oxford ; New York: Oxford University Press, 2006.
- [127] M. Mader, *A scanning cavity microscope*. PhD thesis, 2018.
- [128] H. Kaupp, *Coupling Nitrogen-Vacancy Centers in Diamond to Fiber-based Fabry-Pérot Microcavities*. PhD thesis, 2017.
- [129] A. M. De Riva, G. Zavattini, S. Marigo, C. Rizzo, G. Ruoso, G. Carugno, R. Onofrio, S. Carusotto, M. Papa, F. Perrone, E. Polacco, G. Cantatore, F. Della Valle, P. Micossi, E. Milotti, P. Pace, and E. Zavattini, “Very high Q frequency-locked Fabry–Perot cavity,” *Review of Scientific Instruments*, vol. 67, pp. 2680–2684, Aug. 1996.
- [130] A. Meldrum, P. Bianucci, and F. Marsiglio, “Modification of ensemble emission rates and luminescence spectra for inhomogeneously broadened distributions of quantum dots coupled to optical microcavities,” *Optics Express*, vol. 18, pp. 10230–10246, May 2010. Publisher: Optica Publishing Group.
- [131] T. Grange, G. Hornecker, D. Hunger, J.-P. Poizat, J.-M. Gérard, P. Senellart, and A. Auffèves, “Cavity-Funneled Generation of Indistinguishable Single Photons from Strongly Dissipative Quantum Emitters,” *Physical Review Letters*, vol. 114, p. 193601, May 2015.

-
- [132] A. Auffèves, D. Gerace, J.-M. Gérard, M. F. Santos, L. C. Andreani, and J.-P. Poizat, “Controlling the dynamics of a coupled atom-cavity system by pure dephasing,” *Physical Review B*, vol. 81, p. 245419, June 2010. Publisher: American Physical Society.
- [133] A. Auffèves, J.-M. Gérard, and J.-P. Poizat, “Pure emitter dephasing: A resource for advanced solid-state single-photon sources,” *Physical Review A*, vol. 79, p. 053838, May 2009. Publisher: American Physical Society.
- [134] E. Jaynes and F. Cummings, “Comparison of quantum and semiclassical radiation theories with application to the beam maser,” *Proceedings of the IEEE*, vol. 51, pp. 89–109, Jan. 1963. Conference Name: Proceedings of the IEEE.
- [135] M. Tavis and F. W. Cummings, “Exact Solution for an N-Molecule—Radiation-Field Hamiltonian,” *Physical Review*, vol. 170, pp. 379–384, June 1968.
- [136] M. Tavis and F. W. Cummings, “Approximate Solutions for an N-Molecule-Radiation-Field Hamiltonian,” *Physical Review*, vol. 188, pp. 692–695, Dec. 1969.
- [137] M. G. Raizen, R. J. Thompson, R. J. Brecha, H. J. Kimble, and H. J. Carmichael, “Normal-mode splitting and linewidth averaging for two-state atoms in an optical cavity,” *Physical Review Letters*, vol. 63, pp. 240–243, July 1989.
- [138] R. J. Thompson, G. Rempe, and H. J. Kimble, “Observation of normal-mode splitting for an atom in an optical cavity,” *Physical Review Letters*, vol. 68, pp. 1132–1135, Feb. 1992.
- [139] P. A. M. Dirac and N. H. D. Bohr, “The quantum theory of the emission and absorption of radiation,” *Proceedings of the Royal Society of London. Series A, Containing Papers of a Mathematical and Physical Character*, vol. 114, no. 767, pp. 243–265, 1927. Publisher: Royal Society.
- [140] E. A. Hinds, “Cavity Quantum Electrodynamics,” in *Advances In Atomic, Molecular, and Optical Physics* (D. Bates and B. Bederson, eds.), vol. 28, pp. 237–289, Academic Press, Jan. 1990.
- [141] I. P. Radko, M. Boll, N. M. Israelsen, N. Raatz, J. Meijer, F. Jelezko, U. L. Andersen, and A. Huck, “Determining the internal quantum efficiency of shallow-implanted nitrogen-vacancy defects in bulk diamond,” *Optics Express*, vol. 24, p. 27715, Nov. 2016.
- [142] L. Novotny and B. Hecht, *Principles of nano-optics*. Cambridge: Cambridge University Press, 2nd ed ed., 2012.

- [143] B. M. Garraway, “The Dicke model in quantum optics: Dicke model revisited,” *Philosophical Transactions of the Royal Society A: Mathematical, Physical and Engineering Sciences*, vol. 369, pp. 1137–1155, Mar. 2011.
- [144] K. Cong, Q. Zhang, Y. Wang, G. T. Noe, A. Belyanin, and J. Kono, “Dicke super-radiance in solids [Invited],” *Journal of the Optical Society of America B*, vol. 33, p. C80, July 2016.
- [145] M. Gross and S. Haroche, “Superradiance: An essay on the theory of collective spontaneous emission,” *Physics Reports*, vol. 93, pp. 301–396, Dec. 1982.
- [146] A. E. Siegman, *Lasers*. Mill Valley, Calif: Univ. Science books, 1986.
- [147] R. Florian, L. O. Schwan, and D. Schmid, “Time-resolving experiments on Dicke superfluorescence of O_2^+ centers in KCl. Two-color superfluorescence,” *Physical Review A*, vol. 29, pp. 2709–2715, May 1984. Publisher: American Physical Society.
- [148] C. Cohen-Tannoudji, “Emission et détection de rayonnement : approches semi-classiques et approches quantiques,” 1979.
- [149] A. Kuhn, M. Hennrich, and G. Rempe, “Deterministic Single-Photon Source for Distributed Quantum Networking,” *Physical Review Letters*, vol. 89, p. 067901, July 2002.
- [150] C. Arnold, V. Loo, A. Lemaître, I. Sagnes, O. Krebs, P. Voisin, P. Senellart, and L. Lanco, “Optical bistability in a quantum dots/micropillar device with a quality factor exceeding 200 000,” *Applied Physics Letters*, vol. 100, p. 111111, Mar. 2012.
- [151] D. W. Vernooy, V. S. Ilchenko, H. Mabuchi, E. W. Streed, and H. J. Kimble, “High-Q measurements of fused-silica microspheres in the near infrared,” *Optics Letters*, vol. 23, p. 247, Feb. 1998.
- [152] M. Mader, J. Reichel, T. W. Hänsch, and D. Hunger, “A scanning cavity microscope,” *Nature Communications*, vol. 6, p. 7249, June 2015.
- [153] L. Kohler, M. Mader, C. Kern, M. Wegener, and D. Hunger, “Tracking Brownian motion in three dimensions and characterization of individual nanoparticles using a fiber-based high-finesse microcavity,” *Nature Communications*, vol. 12, p. 6385, Nov. 2021.
- [154] M. Mader, J. Benedikter, L. Husel, T. W. Hänsch, and D. Hunger, “Quantitative Determination of the Complex Polarizability of Individual Nanoparticles by Scanning Cavity Microscopy,” *ACS Photonics*, vol. 9, pp. 466–473, Feb. 2022.

- [155] Y. Zhi, X.-C. Yu, Q. Gong, L. Yang, and Y.-F. Xiao, "Single Nanoparticle Detection Using Optical Microcavities," *Advanced Materials*, vol. 29, p. 1604920, Mar. 2017.
- [156] Y. Colombe, T. Steinmetz, G. Dubois, F. Linke, D. Hunger, and J. Reichel, "Strong atom–field coupling for Bose–Einstein condensates in an optical cavity on a chip," *Nature*, vol. 450, pp. 272–276, Nov. 2007.
- [157] F. Haas, J. Volz, R. Gehr, J. Reichel, and J. Estève, "Entangled States of More Than 40 Atoms in an Optical Fiber Cavity," *Science*, vol. 344, pp. 180–183, Apr. 2014.
- [158] T. Hümmer, J. Noe, M. S. Hofmann, T. W. Hänsch, A. Högele, and D. Hunger, "Cavity-enhanced Raman microscopy of individual carbon nanotubes," *Nature Communications*, vol. 7, p. 12155, July 2016.
- [159] B. Casabone, J. Benedikter, T. Hümmer, F. Oehl, K. d. O. Lima, T. W. Hänsch, A. Ferrier, P. Goldner, H. d. Riedmatten, and D. Hunger, "Cavity-enhanced spectroscopy of a few-ion ensemble in $\text{Eu}^{3+}:\text{Y}_2\text{O}_3$," *New Journal of Physics*, vol. 20, p. 095006, Sept. 2018.
- [160] R. Høy Jensen, E. Janitz, Y. Fontana, Y. He, O. Gobron, I. P. Radko, M. Bhaskar, R. Evans, C. D. Rodríguez Rosenblueth, L. Childress, A. Huck, and U. Lund Andersen, "Cavity-Enhanced Photon Emission from a Single Germanium-Vacancy Center in a Diamond Membrane," *Physical Review Applied*, vol. 13, p. 064016, June 2020.
- [161] S. Häußler, J. Benedikter, K. Bray, B. Regan, A. Dietrich, J. Twamley, I. Aharonovich, D. Hunger, and A. Kubanek, "Diamond photonics platform based on silicon vacancy centers in a single-crystal diamond membrane and a fiber cavity," *Physical Review B*, vol. 99, p. 165310, Apr. 2019.
- [162] D. Hunger, C. Deutsch, R. J. Barbour, R. J. Warburton, and J. Reichel, "Laser micro-fabrication of concave, low-roughness features in silica," *AIP Advances*, vol. 2, p. 012119, Mar. 2012.
- [163] R. Kitamura, L. Pilon, and M. Jonasz, "Optical constants of silica glass from extreme ultraviolet to far infrared at near room temperature," *Applied Optics*, vol. 46, p. 8118, Nov. 2007.
- [164] B. Schlederer, "Development of a CO₂ laser setup for fiber end facet machining and characterization," Master's thesis, Ludwig-Maximilians-Universität München, 2014.
- [165] C. J. R. Sheppard, "Approximate calculation of the reflection coefficient from a stratified medium," *Pure and Applied Optics: Journal of the European Optical Society Part A*, vol. 4, pp. 665–669, Sept. 1995.

- [166] J. Benedikter, T. Hümmer, M. Mader, B. Schlederer, J. Reichel, T. W. Hänsch, and D. Hunger, “Transverse-mode coupling and diffraction loss in tunable Fabry–Pérot microcavities,” *New Journal of Physics*, vol. 17, p. 053051, May 2015.
- [167] J. Benedikter, T. Moosmayer, M. Mader, T. Hümmer, and D. Hunger, “Transverse-mode coupling effects in scanning cavity microscopy,” *New Journal of Physics*, vol. 21, p. 103029, Oct. 2019.
- [168] G. K. Gulati, H. Takahashi, N. Podoliak, P. Horak, and M. Keller, “Fiber cavities with integrated mode matching optics,” *Scientific Reports*, vol. 7, p. 5556, Dec. 2017.
- [169] H. E. Bennett and J. O. Porteus, “Relation Between Surface Roughness and Specular Reflectance at Normal Incidence,” *Journal of the Optical Society of America*, vol. 51, p. 123, Feb. 1961.
- [170] P. Hill, E. Gu, M. D. Dawson, and M. J. Strain, “Thin film diamond membranes bonded on-demand with SOI ring resonators,” *Diamond and Related Materials*, vol. 88, pp. 215–221, Sept. 2018. Num Pages: 7.
- [171] M. Karplus and H. J. Kolker, “Van der Waals Forces in Atoms and Molecules,” *The Journal of Chemical Physics*, vol. 41, pp. 3955–3961, Dec. 1964.
- [172] I. Friel, S. Clewes, H. Dhillon, N. Perkins, D. Twitchen, and G. Scarsbrook, “Control of surface and bulk crystalline quality in single crystal diamond grown by chemical vapour deposition,” *Diamond and Related Materials*, vol. 18, pp. 808–815, May 2009.
- [173] P.-N. Volpe, P. Muret, F. Omnes, J. Achard, F. Silva, O. Brinza, and A. Gicquel, “Defect analysis and excitons diffusion in undoped homoepitaxial diamond films after polishing and oxygen plasma etching,” *Diamond and Related Materials*, vol. 18, no. 10, pp. 1205–1210, 2009.
- [174] J. M. Dodson, J. R. Brandon, H. K. Dhillon, I. Friel, S. L. Geoghegan, T. P. Mollart, P. Santini, G. A. Scarsbrook, D. J. Twitchen, A. J. Whitehead, J. J. Wilman, and H. de Wit, “Single crystal and polycrystalline CVD diamond for demanding optical applications,” (Orlando, Florida, United States), p. 80160L, May 2011.
- [175] J. C. Sankey, C. Yang, B. M. Zwickl, A. M. Jayich, and J. G. E. Harris, “Strong and tunable nonlinear optomechanical coupling in a low-loss system,” *Nature Physics*, vol. 6, pp. 707–712, Sept. 2010.
- [176] M. Uphoff, M. Brekenfeld, G. Rempe, and S. Ritter, “Frequency splitting of polarization eigenmodes in microscopic Fabry–Pérot cavities,” *New Journal of Physics*, vol. 17, p. 013053, Jan. 2015.

- [177] H. Pinto and R. Jones, "Theory of the birefringence due to dislocations in single crystal CVD diamond," *Journal of Physics: Condensed Matter*, vol. 21, p. 364220, Sept. 2009.
- [178] W. M. Haynes, D. R. Lide, and T. J. Bruno, eds., *CRC Handbook of Chemistry and Physics*. CRC Press, 97 ed., June 2016.
- [179] G. Martinet, S. Blivet, F. Chatelet, M. Fouaidy, N. Hammoudi, A. Olivier, and H. Sagnac, "Low Temperature Properties of Piezoelectric Actuators Used in SRF Cavities Cold Tuning Systems," 2006.
- [180] R. W. P. Drever, J. L. Hall, F. V. Kowalski, J. Hough, G. M. Ford, A. J. Munley, and H. Ward, "Laser phase and frequency stabilization using an optical resonator," *Applied Physics B Photophysics and Laser Chemistry*, vol. 31, pp. 97–105, June 1983.
- [181] E. D. Black, "An introduction to Pound–Drever–Hall laser frequency stabilization," *Am. J. Phys.*, vol. 69, no. 1, 2001.
- [182] L. Neuhaus, R. Metzdorff, S. Chua, T. Jacqmin, T. Briant, A. Heidmann, P.-F. Cohadon, and S. Deléglise, "PyRPL (Python Red Pitaya Lockbox) – An open-source software package for FPGA-controlled quantum optics experiments," in *2017 Conference on Lasers and Electro-Optics Europe & European Quantum Electronics Conference (CLEO/Europe-EQEC)*, pp. 1–1, June 2017.
- [183] R. G. Budynas and J. K. Nisbett, *Shigley's mechanical engineering design*. McGraw-Hill series in mechanical engineering, New York: McGraw-Hill, 9th ed ed., 2011.
- [184] C. Woolger, "Properties: Invar - Nickel Iron Alloy."
- [185] A. M. Bennett, B. J. Wickham, H. K. Dhillon, Y. Chen, S. Webster, G. Turri, and M. Bass, "Development of high-purity optical grade single-crystal CVD diamond for intracavity cooling," (San Francisco, California, United States), p. 89590R, Feb. 2014.
- [186] R. H. Brown and R. Twiss, "LXXIV. A new type of interferometer for use in radio astronomy," *The London, Edinburgh, and Dublin Philosophical Magazine and Journal of Science*, vol. 45, pp. 663–682, July 1954.
- [187] R. H. Brown and R. Q. Twiss, "Correlation between Photons in two Coherent Beams of Light," *Nature*, vol. 177, pp. 27–29, Jan. 1956.
- [188] C. Kurtsiefer, S. Mayer, P. Zarda, and H. Weinfurter, "Stable Solid-State Source of Single Photons," *PHYSICAL REVIEW LETTERS*, vol. 85, no. 2, p. 4, 2000.

- [189] R. Brouri, A. Beveratos, J.-P. Poizat, and P. Grangier, “Photon antibunching in the fluorescence of individual color centers in diamond,” *Optics Letters*, vol. 25, p. 1294, Sept. 2000.
- [190] C. Wang, *A solid-state single photon source based on color centers in diamond*. PhD thesis, Ludwig-Maximilians-Universität München, 2007.
- [191] J. Resch, “Spin manipulation of Nitrogen-Vacancy centers in diamond for cavity-enhanced spin-photon interfaces,” Master’s thesis, Karlsruher Institut für Technologie, 2021.
- [192] M. Radtke, E. Bernardi, A. Slablab, R. Nelz, and E. Neu, “Nanoscale sensing based on nitrogen vacancy centers in single crystal diamond and nanodiamonds: achievements and challenges,” *Nano Futures*, vol. 3, p. 042004, Dec. 2019.
- [193] M. Zahedian, J. Liu, R. Vidrio, S. Kolkowitz, and J. T. Choy, “Modeling of Radiative Emission from Shallow Color Centers in Single Crystalline Diamond,” *Laser & Photonics Reviews*, p. 2200529, Feb. 2023.
- [194] “Verbundprojekt Quantenrepeater.Link, <https://quantenrepeater.link/>.”
- [195] S. A. Solin and A. K. Ramdas, “Raman Spectrum of Diamond,” *Physical Review B*, vol. 1, pp. 1687–1698, Feb. 1970.

List of Figures

1.1.	3D rendering of the fiber-based microcavity used in this thesis	3
2.1.	Introduction of the NV center	10
2.2.	Level scheme and vibronic structure of the NV center	12
2.3.	Temperature dependence of spectral diffusion	13
2.4.	Influence of a magnetic field on the level structure	16
2.5.	Creation of NV centers by electron irradiation	20
3.1.	Basic principle of optical resonators	24
3.2.	Schematic drawing of a Gaussian beam	28
3.3.	Introduction of Hermite-Gauss modes	30
3.4.	Schematic of the relevant cavity parameters	31
3.5.	Dicke "ladder" for N emitters	42
3.6.	Spontaneous emission rate in the Dicke model	44
3.7.	Numerical simulation of the bunching for different parameters.	46
4.1.	Simplified sketch of a fiber-based microcavity	49
4.2.	Optical microscope images of the laser-machined fibers	50
4.3.	WLI image and height profiles of machined fibers	51
4.4.	Fiber machining overview	52
4.5.	Simulated transmission profile of two different DBR coatings	54
4.6.	Simulation of a DBR coating with a spacer layer	55
4.7.	Simulated electric field intensity for different diamond thicknesses	58
4.8.	Simulated mode dispersion for different diamond thicknesses	59
4.9.	Influence of the hybridized mode structure on the mirror coating	61
4.10.	Simulated finesse for a system including transmission and scattering	63
4.11.	Schematic drawing of the cleaning and bonding process	67
4.12.	Microscope images of different diamond membranes during the bonding process	68
4.13.	Schematic drawing of the room temperature cavity setup	70
4.14.	3D rendering of a CAD model of the cavity platform	71
4.15.	Schematic drawing of the optical configuration	72
4.16.	Cavity transmission scans of a marked mirror	75
4.17.	WLI measurements and height map of a diamond membrane	77
4.18.	Dispersion measurements of the hybrid diamond-air cavity	78

List of Figures

4.19. Transmission and finesse scans on a small area	79
4.20. Cut along a line in the finesse map	80
4.21. Dependence of the finesse of a bare cavity on the cavity length	81
4.22. Modeling of the loss in a hybrid cavity	82
4.23. Experimental evidence of transverse mode-mixing	83
4.24. Transmission maps for different cavity air gaps	84
4.25. Finesse scans for different cavity lengths	85
4.26. Dependence of the maximum finesse on the diamond thickness	86
4.27. Schematic drawing of the geometrical parameters leading to curvature-induced loss	87
4.28. Calculated curvature-induced loss	88
4.29. Polarization splitting on a diamond membrane	89
4.30. Cavity measurements of the polarization splitting	90
5.1. Dependence of the Purcell factor to the rms cavity length jitter	95
5.2. Photographs of the cavity platform	97
5.3. Temperature of the setup during a cooldown	99
5.4. Transmission maps during a cooldown	101
5.5. Simulation of a cavity transmission signal	103
5.6. Schematic drawing of the locking setup	106
5.7. Mechanical transfer functions of the cavity	108
5.8. Amplitude spectral density of the cavity at room temperature	110
5.9. Comparison of the ASD of the cavity for different environments	111
5.10. ASD of the actively stabilized cavity in contact mode	112
5.11. ASD of the actively stabilized cavity in contact mode at cryogenic temperatures	114
5.12. Time-resolved measurement of the cavity length jitter	115
6.1. Microscope images of sample S_A	121
6.2. Impact of an additional spacer layer on the field distribution.	122
6.3. Transmission and finesse map of sample S_A	123
6.4. Modeling of the cavity losses on sample S_A	124
6.5. Schematic drawing of the optical setup.	125
6.6. Combination of optical filters for the NV ZPL.	127
6.7. Cavity-enhanced NV fluorescence spectrum	129
6.8. Mode dispersion of the ensemble fluorescence in the cavity.	130
6.9. Power dependence of the fluorescence rate.	132
6.10. Schematic depiction of cavity-mediated superfluorescence.	134
6.11. Three-level scheme and simulated second-order correlation functions	137
6.12. Temporal photon statistics of ensemble NV fluorescence	141
6.13. Background-corrected correlation function	143
6.14. Power dependence of the correlation function	144
6.15. Influence of the instrument response on the bunching.	146
6.16. Temperature dependence of the correlation function.	147

6.17. Theoretical contrast of the antibunching and the central bunching peak as a function of the number of particles	148
7.1. Basic structure of a quantum repeater	151
7.2. Theoretical estimation of the achievable link efficiency	153
A.1. Full set of the cavity transmission scans during a cooldown	157
B.2. Mode dispersion over the full scanning range	158

List of Tables

4.1. Overview of the different coatings ($C_{(A,B,C)}$), fibers ($F_{(A,B,C)}$) and samples ($S_{(A,B,C)}$) used in this thesis	65
5.1. Summary over the values for the cavity length jitter that have been recorded for different approaches in the course of this work	116
C.1. Overview of the cavity parameters	159

Danksagung

Am Ende einer solch langen Zeit gibt es natürlich viele Menschen, denen man viel zu verdanken hat, die einen unterstützt haben, besonders, wenn es mal nicht so lief. Ich möchte mich bei vielen Leuten bedanken (von denen ich auch bestimmt ein paar vergesse), einigen möchte ich jedoch einen persönlichen Dank aussprechen.

David, vielen Dank, dass du mich als deinen Doktoranden betreut hast. Du hast immer ein offenes Ohr und hast für deine Arbeitsgruppe eine sehr angenehme und respektvolle Arbeitsatmosphäre geschaffen. Du warst dir nie zu schade, auch mal selbst im Labor zu stehen, wenn es der Terminkalender zulässt und deinen Mitarbeitern und Studenten mit Rat und Tat zur Seite zu stehen. Ich bin froh, bei dir am KIT gelandet zu sein!

~~~~~  
*"Kollegen sind wie Pickel, die hat man auch, ob man will oder nicht."*

- Bernd Stromberg -

~~~~~

Meinen lieben Kollegen, den *Hungerhaken*, möchte ich zunächst im Kollektiv danken. Ihr seid eine tolle Rasselbande, die mir nach meiner Zeit am KIT sehr fehlen wird. Seien es die teils hitzigen Diskussionen bei der Kaffeepause, gemeinsame Ausflüge oder feucht-fröhliche Feiern, oder einfach der alltägliche Wahnsinn im Labor. Ich wünsche euch, dass ihr diesen Team-spirit auch in Zukunft beibehalten werdet!

Einige meiner Kollegen möchte ich hier namentlich erwähnen, da sie eine besonders große Rolle in meinem Leben während der Promotion gespielt haben.

Timon, du warst in den letzten fünf Jahren mein Weg- und Leidensgefährte, besonders während der Corona-Zeit, als wir mit unserer *Uschi* quasi im Labor eingesperrt waren und an der Tücke des Objekts halb verzweifelt sind :). Wir hatten viele schöne fachliche und private Gespräche, die den Berufsalltag bereichert haben.

Larissa, du warst meine Kollegin der ersten Stunde. Du hast mir so gut wie alles gezeigt, von den ersten Abläufen im Labor bis hin zum Schreiben der Doktorarbeit. Ich bin sehr froh, in dir auch eine tolle Mitmusikerin gefunden zu haben, sei es gemeinsam auf den Badischen Bühnen, oder beim wilden Jammen auf der Weihnachtsfeier!

Kerim, du bist quasi mein Nachfolger und hast mich während meiner heißen Laborphase enorm unterstützt. Ich werde die langen Mess-Sessions mit 80er-Jahre-Playlists sehr vermissen! Mein Experiment (und dessen Nachfolger) ist bei dir in sehr guten Händen. Weiterhin erwähnen möchte ich meine Mitdoktoranden Eugen, Jannis, Jeremias, Jonas, Shalom, Sören, Nick (not a phd student anymore, but your cakes alone deserve a big THANK YOU!). Teilweise durfte ich euch schon als Masterstudenten betreuen, die dann zu Kollegen und Freunden wurden (Falls ich jemanden von den Doktoranden vergessen habe, sorry! Die Zeit war knapp ;)).

Von meinen ehemaligen Masterstudenten möchte ich noch Jonathan Körber namentlich erwähnen. Wir haben sehr viel gemeinsame Zeit verbracht beim Reinraum-Wahnsinn oder dann beim paper-Schreiben, danke für die schöne Zusammenarbeit!

Weiterhin möchte ich mich bei meinen Münchner Kollegen Julia Benedikter, Thomas Hümmel und Matthias Mader bedanken. Ihr habt mir den Einstieg in die Promotion sehr leicht gemacht, an meinen Aufenthalt an der LMU denke ich sehr gerne zurück!

Ein großer Dank geht an meine Familie, besonders meine Eltern, die mich - nicht nur während der Promotion - bedingungslos unterstützt hat. Ihr habt mir ermöglicht, in einem liebevollen Umfeld aufzuwachsen, meine Interessen zu entwickeln und auch zu verfolgen. Das hat mich schließlich zur Physik und somit hierher gebracht.

Ein letzter Dank geht an meine Frau Maren. Du hast mich immer unterstützt, an mich geglaubt und so manche Widrigkeit wie eigenartige Arbeitszeiten oder einen genervten Mann während der Schreibzeit ertragen. Mein Leben wäre nicht halb so schön ohne dich an meiner Seite, du machst mich zu dem Menschen, der ich bin!

...

So, wie sagt man in der Pfalz so schön?

Genug gebabbelt.

Ich habe fertig.